Novel porous membranes with enhanced stability as lithium ion battery separator

Dissertation

zur Erlangung des akademischen Grades eines
Doktors der Naturwissenschaften
– Dr. rer. nat. –

vorgelegt von

Thomas Knoche

geboren in Essen

Institut für Technische Chemie II
der
Universität Duisburg-Essen

2016

Die vorliegende Arbeit wurde im Zeitraum von Januar 2012 bis Februar 2016 im Arbeitskreis von Prof. Dr. Mathias Ulbricht am Institut für Technische Chemie II der Universität Duisburg-Essen in Kooperation mit der Fa. Brückner Maschinenbau GmbH & Co. KG durchgeführt.

Gutachter:	Prof. Dr. Mathias Ulbricht
	Prof. Dr. Matthias Epple
Vorsitzender:	Prof. Dr. Eckhard Spohr
Disputation am:	14. November 2016 in Essen

Hiermit versichere ich, dass ich die vorliegende Arbeit mit dem Titel

„Novel porous membranes with enhanced stability as lihtium ion battery separators"

selbst verfasst und keine außer den angegebenen Hilfsmitteln und Quellen benutzt habe, und dass die Arbeit in dieser oder ähnlicher Form noch bei keiner anderen Universität eingereicht wurde.

Essen, 29. Februar 2016

DANKSAGUNG

Mein erster Dank gilt Prof. Dr. Mathias Ulbricht für die Möglichkeit der Promotion in der Technischen Chemie II und die gute Unterstützung über die Jahre hinweg. Danken möchte ich auch Prof. Dr. Matthias Epple für die Übernahme des Zweitgutachtens und der Möglichkeit einer gemeinsamen Zusammenarbeit im Rahmen der Promotion. Im dem Zuge möchte ich auch Dr. Oleg Prymak danken, für die gute Zusammenarbeit und aufwendigen Auswertung bei der Texturanalyse.

Ebenso gilt mein Dank an die Firma Brückner Maschinenbau, insbesondere an Herrn Dr. Breil für die interessante Aufgabenstellung und die Möglichkeit der Promotion im Rahmen einer Kooperation mit der Technischen Chemie II der UDE. Ich möchte auch meinen Kollegen bei Brückner, insbesondere Herrn Roland Lund und Maximilian Armbruster für die gute Betreuung und die vielen Diskussionsrunden danken.

Mein besonderer Dank geht an meine Familie, die mich während des Studiums und der Promotion immer unterstützt und motiviert hat. Ich möchte mich auch bei meinen ehemaligen Studienkollegen und Freunden bedanken für die gegenseitige Hilfe, Motivation und den einen oder anderen Brettspielabend. Insbesondere möchte ich mich bei „dem einen der zwei Beiden“ für seine Geduld bedanken, da PBr4Ve im letzten Jahr mehr in den Hintergrund treten musste. Zu guter Letzt möchte ich mich bei Mel bedanken, die mir in der schwierigen und ungewissen Zeit während des Umzugs und des Ankommens bei Brückner zur Seite stand und mir die Motivation gegeben hat jeden Tag aufs Neue anzupacken.

TABLE OF CONTENTS

ABSTRACT

With the recent advance in consumer devices such a smartphones, tablets, laptops and power tools, and the future potential growth of the electric vehicle market, energy storage is of global interest, with the Li-ion technology showing the highest potential. Many research groups are working on the development of new materials for electrode materials in hopes of increasing energy density. Less research is committed to separators which are a crucial part in state of the art Li-ion batteries as they prevent contact between anode and cathode and therefore avoid short-circuiting of the battery while at the same time allowing sufficient flow of Li-ions. Especially for electric vehicles, safety is an integral part of the viability of this technology, requiring separators that combine high performance and high mechanical and thermal stability. This work outlines the current state of the art manufacturing process of battery separator membranes as well as the new EVAPORE® process developed by Brückner. The EVAPORE® process is used as a basis for the research presented herein. As this process was previously only possible in large scale on Brückners pilot line, a laboratory method was developed as a quick and cost-effective alternative. Using this method, an in-depth analysis of the morphology of separator membranes and pore formation mechanisms was carried out and is presented herein, deepening the general understanding of the EVAPORE® process.

On the basis of the EVAPORE® process, a range of commercial temperature stable polymers were screened for their applicability in the process with the ultimate goal of increasing thermal stability of the separator. To that end, polymers were first evaluated based on their stability in typical battery electrolyte LP71, a requirement for use in modern Li-ion batteries. The most promising candidates were then used in the laboratory method to identify a suitable polymer-solvent combination which was then extruded and processed on a laboratory line and analyzed in terms of their crystalline morphology and typical separator membrane properties.

In addition, to increase mechanical strength of a separator, high density polyethylene (HDPE) was in part replaced by different ultrahigh molecular weight polyethylene grades (UHMWPE). By processing UHMWPE on the laboratory as well as the pilot line it could be proven that mechanical strength could potentially be improved, similar to the well-established wet process. However, optimization of all line parameters is necessary, to achieve a high performance film fitting all application related requirements.

ABSTRACT (GERMAN)

Durch die Verbreitung von Smartphones, Tablets, Laptops und Elektrowerkzeugen sowie dem erwarteten Wachstum der Elektromobilität in naher Zukunft ist Energiespeicherung von wachsender globaler Bedeutung. Die Li-Ionen Technologie weißt dabei die größten Potentiale auf. Aktuelle Forschungen sind zumeist auf der Entwicklung neuer Materialien für Elektroden fokussiert mit dem Ziel einer gesteigerten Energiedichte. Weitaus weniger Beachtung findet die Separator Membran, die einen wichtigen Beitrag zur Funktion einer typischen Li-Ionen Batterie beiträgt indem diese den Kontakt zwischen den Elektroden und damit einen Kurzschluss der Batterie verhindert und zeitgleich Li-Ionen Diffusion ermöglicht. Die Durchsetzung der Elektromobilität ist im großen Maße von der Sicherheit dieser Technologie abhängig und erfordert Separatoren, die sowohl hohe Leistung als auch hohe mechanische und thermische Stabilität aufweisen.

In der vorliegenden Arbeit werden die etablierten Herstellungsverfahren nach dem Stand der Technik als auch der von der Firma Brückner neu entwickelte EVAPORE® Prozess vorgestellt. Die Grundlage für die in dieser Arbeit präsentierten Ergebnisse bildet der EVAPORE® Prozess. Da dieser Prozess bisher nur auf der Pilotanlage der Firma Brückner möglich war, wurde eine schnelle und kosteneffiziente Labormethode entwickelt, die für tiefgehende Analysen der Separator Morphologie und des Porenformierungsprozesses verwendet wurde.

Zur Verbesserung der thermischen Eigenschaften wurden typische kommerzielle temperaturbeständige Polymere hinsichtlich ihrer Übertragbarkeit in den EVAPORE® Prozess evaluiert. Um eine ausreichende Stabilität in modernen Li-Ionen Batterien zu gewährleisten wurden ausgewählte Polymere zunächst auf ihre Stabilität in Batterieelektrolyt LP71 geprüft. Die chemisch stabilen Polymere wurden dann mittels der Labormethode mit verschiedenen Lösemitteln verarbeitet mit dem Ziel eine geeignete Materialkombination zu identifizieren, die eine Verarbeitung nach dem EVAPORE® Prozess ermöglicht und gleichzeitig eine poröse Struktur ausbildet. Im letzten Schritt wurde die potentiell beste Materialkombination auf Brückners Laboranlage extrudiert und verstreckt. Die erhaltenen Filme und Separator Membranen wurden auf ihre Morphologie und typische Separator Eigenschaften untersucht.

Neben der Erhöhung der thermischen Eigenschaften wurde eine Verbesserung der mechanischen Integrität angestrebt durch Einsatz von „ultrahigh molecular

polyethylene“ (UHMWPE) statt dem standardmäßig verwendetem „high-density polyethylene“ (HDPE). Durch Übertragung des EVAPORE® Prozesses auf UHMWPE auf Brückners Laboranlage konnte nachgewiesen werden, dass eine Erhöhung der mechanischen Eigenschaften vergleichbar mit dem etablierten Nass-Prozess möglich ist. Es sind jedoch weitgehende Optimierungen der komplexen Anlageneinstellungen nötig um sowohl eine hohe Leistung als auch alle anwendungsbezogenen Anforderungen an den Separator zu erfüllen.

List of Abbreviations

DEC	Diethyl carbonate
DMC	Dimethyl carbonate
DSC	Differential scanning calorimetry
EC	Ethylene carbonate
EV	Electric vehicle
EVOH	Ethylene vinyl alcohol
HDPE	High-density polyethylene
LIB	Lithium-ion battery
LISIM	Linear Motor Simultaneous Stretching
MD	Machine direction
MDO	Machine direction orientation
MFR	Melt flow rate
MVR	Melt volume rate
PC	Propyl carbonate
PE	Polyethylene
PET	Polyethylene terephthalate
PMP	Poly(4-methyl-1-pentene)
PP	Polypropylene
SEM	Scanning electron microscopy
TC	Texture coefficient
TD	Transverse direction
TDO	Transverse direction orientation
TIPS	Thermally induced phase separation
UHMWPE	Ultra-high molecular weight polyethylene
XRD	X-ray powder diffraction

LIST OF FIGURES

LIST OF TABLES

1 INTRODUCTION

The development and subsequent commercialization of secondary Lithium Ion Batteries (LIB) by Sony in 1991 has led to their widespread application in consumer handheld devices including cell phones, camcorders and notebooks[1-3]. Most notable advantages of LIBs compared to conventional energy storage devices are high specific energy, energy density and cycle life[4-9]. Since the introduction of LIBs, the market has grown considerably in the last decade from 5 Billion $ in 2005 to 15 Billion $ in 2012 and is estimated to reach 33 Billion $ in 2020. While growth in the portable market is relatively stagnant at an annual growth rate of 3 %, highest growth is expected for automotive applications at a rate of 20 % per year. This includes hybrid electric vehicles (HEV), plug-in hybrid EVs (PHEV) and full EVs. A significant driving force are regulations in CO_2 emissions in light of global climate change that is associated with increasing CO_2 emission worldwide[2, 10-12]. It is estimated that demand for EVs will grow slowly but steady and will reach 1 to 5 Million units sold worldwide in 2020. Aside from automotive applications there is also growing interest for stationary and industrial energy storage solutions[13-14]. The market is estimated to grow at 16 % annually to 10 Billion $ in 2020.

To meet the increased demand in energy density a great amount of research committed to the development of next generation LIBs is made[9]. Promising new technologies include Lithium-Air[9, 15-17], Lithium-Sulfur[16, 18-22] or Sodium-Ion Batteries[23-25] as well as continued developments in new active materials of battery electrodes, electrolytes and separator films[8, 26-29]. Theoretical specific energy density increases by a factor of 8 for Li-Air Batteries and a factor of 5 for Li-Sulfur Batteries[16, 22]. These are strong contenders to meet the increasing demands for electrified road travel in the future. Commercialization has been hindered due to unsolved challenges concerning electrolyte decomposition and capacity retention[9, 16]. While performance of LIBs is an important factor for the energy demand of next generations, battery cell safety especially in EV and stationary applications is of great interest for current LIBs[11, 30]. In that regard the separator membrane plays an important role in the battery cell. Situated between anode and cathode the separator is necessary to prevent contact of electrodes and a subsequent short-circuiting of the cell while still enabling sufficient flow of Li-Ions[7-8, 31-32]. State-of-the-art materials used for separators are Polyethylene (HDPE, UHMWPE) and Polypropylene, while different processes are used in terms of

actual membrane production. Major processes on the market are the wet process (Asahi Kasei, Toray) in which the polymer is processed with a high-boiling paraffinic solvent that is washed out after stretching of the film thus generating a porous structure and the dry process (Celgard), in which the pores are formed due to consecutive monoaxial stretching and annealing steps[7-8, 31-32]. The global need for separator film was estimated to be 585 Million m² in 2013, resembling approx. 19 % in cell material cost. The market for separator film reached 1 Billion $ in 2013 and is estimated to grow by 17 %. The market leader in the battery separator business are Asahi Kasei, Toray and Celgard with market shares in 2012 of 26 %, 23 % and 19 % respectively. In 2015 Asahi Kasei announced and completed the acquisition of Polypore including the business of Celgard, increasing market share significantly[33-34].

In any case separators with thicknesses of lower than 20 μm are required with market demand tending to thicknesses of <10 μm to increase packing and energy density in battery cells. The requirements for separator films are therefore manifold and increasing steadily[7, 31-32]. For EV applications higher temperature stability is required that can be achieved by coating a conventional polyolefinic separator with an inorganic layer on one or both sides[7-8, 32, 35-36]. Due to the trend to lower thicknesses the requirements in mechanical integrity increase correspondingly. To that end HDPE is increasingly substituted by UHMWPE.

The company Brückner Machinery, market leader in film stretching technology, has developed a new process called EVAPORE®, which uses a solvent during extrusion similar to the wet process, but avoids an expensive extraction step. The solvent is instead carefully evaporated during the stretching and pore formation steps, thus making it a semi-wet or semi-dry process. The first two production lines utilizing the EVAPORE® process have been started in 2015. As the current process has been focused on HDPE, Brückner is also looking at alternative materials to meet market demands and requirements for EV applications. Thermal and mechanical stability are key points in the development of next-generation separators.

This work focuses on the evaluation of alternative high temperature materials for the use in the EVAPORE® process aiming to increase thermal and mechanical stability of the final separator, while simultaneously trying to deepen the understanding of the underlying principles of the process. To this end, a laboratory method was developed to evaluate various prospective polymers for their potential in the EVAPORE® process. A selection of these materials was then evaluated on Brückners laboratory and pilot line.

2 THEORY AND STATE OF THE ART

2.1 LITHIUM ION BATTERY TECHNOLOGY

Since the commercialization of the Li-Ion battery in the early 90s the technology has found widespread application in consumer devices all over the world (Laptops, Cell Phones, Power tools, etc.). A scheme of a typical battery cell is given in Figure 2.1.

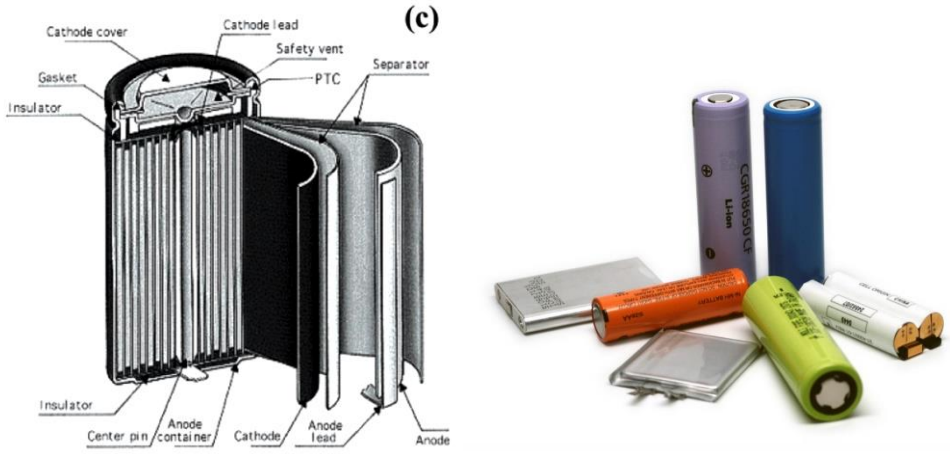

Figure 2.1: Schematic overview of a spirally-wound battery cell (left)[31]. Different types of battery cells: Spirally wound cylindrical and prismatic as well as stacked pouch cells (right)[37].

Battery cells consist, in its most basic form, of alternating layers of anodic and cathodic active materials that are sandwiched between an electrolyte-filled porous separator membrane. A multitude of these layers are stacked together to achieve the desired capacity. Stacks are packed into containers that can be classified into three major types: spirally-wound cylindrical and prismatic cells and stacked pouch cells[38]. Cylindrical and prismatic cells are inserted into a steel container while pouch cells use a laminate of nylon/aluminum/polypropylene. Many different cell chemistries using Lithium as charge carrier have been studied over the past, but only few were actually commercialized.

2.1.1 ELECTRODE MATERIALS

The first primary Lithium batteries were developed and commercialized in the 1970s using metallic Lithium as the anode and several different materials for the cathode[38]. Major cathode materials include SO_2 $SOCl_2$, SO_2Cl_2, $(CF_x)_n$ and MnO_2. Today MnO_2 is used in most consumer applications (button cells). For secondary LIBs the cathode was replaced by intercalation materials such as TiS_2, MoS_2, V_2O_5 and V_6O_{13}[38]. Due to safety issues with metallic Lithium, these types of batteries did not gain much significance. In modern rechargeable LIBs, intercalation materials are used for both electrodes, allowing repeated charging and discharging while avoiding metallic Lithium altogether. Common materials are graphite (mesocarbon microbeads, MCMB) for the anode and $LiCoO_2$ or $LiM_xNi_{1-x}O_2$ for the cathode[3, 10]. Figure 2.2 shows the electrochemical process during discharging.

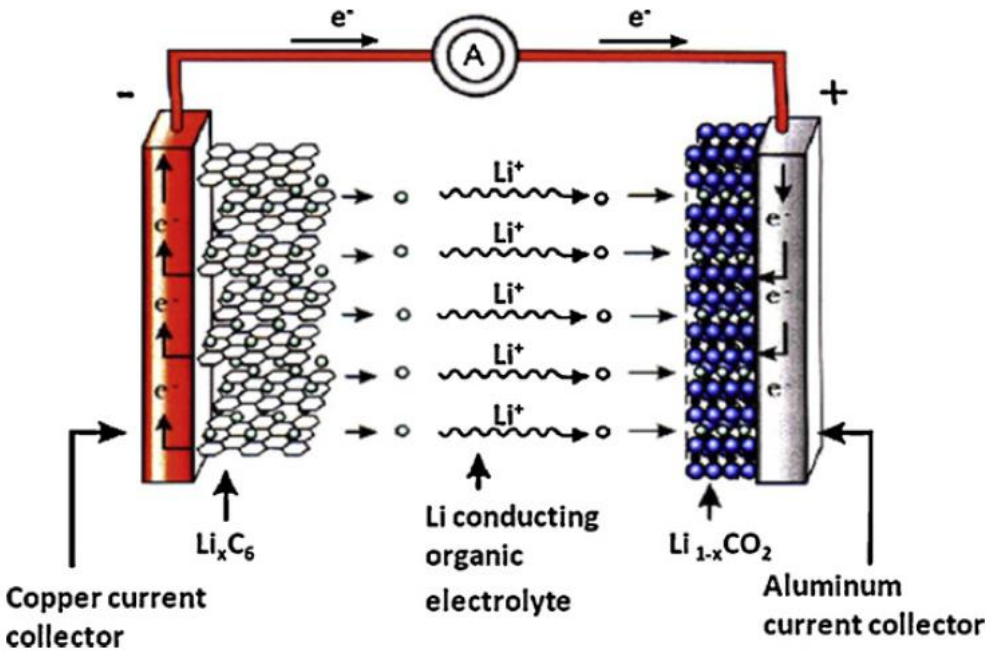

Figure 2.2: Scheme of the electrochemical process in a Li-Ion battery.[10]

Charging and discharging of a typical LIB can be described according to equation 2.1.

$$yC + LiMO_2 \rightleftharpoons Li_xC_y + Li_{(1-x)}MO_2 \qquad 2.1$$

With an operational voltage of 3,5 to 4 V Li-Ions move into the carbon structure during charging with $LiMO_2$ acting as a Li-source. The ratio of x to y is approximately 0,5 to 6.[10]

2.1.2 ELECTROLYTES

Electrolytes play an important role in LIBs as they must allow a rapid flow of Li-Ions and as such must work in tandem with a battery separator. Different types of electrolytes and electrolyte/separator combinations are used including non-aqueous liquid electrolytes, polymer electrolytes and solid electrolytes[39]. Liquid as well as polymeric electrolytes contain Li-salt of the type LiX and more uncommonly LiX_2. The salt is required to have thermal and electrochemical stability, good solubility in the solvent or polymer system, high conductivity and low molecular weight as well as low cost and non-toxicity. As of yet no salt is available that sufficiently satisfies all required criteria. The most common salt used in modern LIBs is $LiPF_6$[40-43] with a conductivity of 10,7 mS/cm^{-1} in 1 M electrolyte solution[39]. Drawbacks are lower thermal stability as well as sensitivity to water which leads to degradation of the salt to HF, CO_2 and PF_5 which polymerizes typical organic solvents and leads to a reduction in conductivity[40-43]. As a solvent, organic carbonates such as cyclic ethylene carbonate (EC), propyl carbonate (PC) and linear dimethyl carbonate (DMC), diethyl carbonate (DEC) are widely used. Requirements for good solvent are thermal and chemical stability, good solvating properties, low vapor pressure and low viscosity[39]. While vapor pressure can be decreased by using heavier molecular derivatives, viscosity will increase appropriately, reducing ionic conductivity of the electrolyte solution.

In light of high-voltage application using voltages above 5 V, typical organic carbonate electrolytes reach their limit, as they suffer from relatively low anodic stability vs Li/Li^+[39, 44-45]. Alternatives are sulfone- or nitrile-based solvents as well as ionic liquids[44-45]. While sulfone-based solvents are available at low cost, drawbacks include a higher melting point and low wettability in typical polyolefin separators. Nitrile-based solvents exhibit excellent electrochemical stability at high potentials up to 7 V and high thermal stability[44]. It has not reached much significance due to its instability at lower potentials and its inability to form a stable passivation layer on graphite anodes. Much research has been invested into the usage of ionic liquids (IL) as electrolytes for LIBs, due to their outstanding electrochemical and thermal stability. Non-Flammability and low vapor pressure are key aspects for increased safety. Due to their nature ILs suffer from higher viscosities compared to conventional organic carbonate electrolytes and thus potentially lower conductivities. Similar to nitrile based solvents, IL are incompatible to carbon electrodes and need additional film forming additives to increase battery life[44].

2.1.3 BATTERY SEPARATOR

A key component in most batteries is the separator which electrically insulates anode and cathode while simultaneously allowing sufficient ionic flow. In the past many different types of separators where used including paper, nonwovens and flat-sheet membranes[31]. In modern LIBs, porous stretched films made from Polyethylene or Polypropylene or laminates are the most widely used. Figure 2.3 shows a representative scheme of a typical LIB cell.

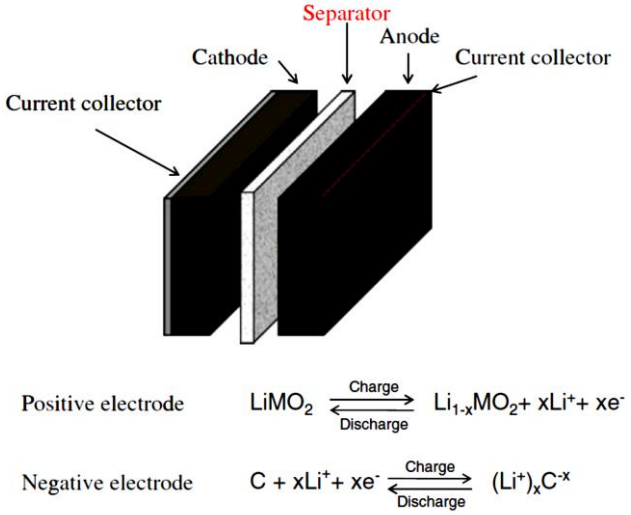

Figure 2.3: Composition of a typical Li-Ion battery cell. A polymeric separator membrane is placed between electrodes to prevent electrical short circuiting.

2.1.3.1 Properties and Requirements

Properties of LIB separators are high porosity, low ionic resistance, low shrinkage, good mechanical stability and low thickness[7-8, 31-32]. Porosity is one of the most important parameters for battery performance as it corresponds to the ionic flow and charging and discharging rates. On the other hand, higher porosities are detrimental to the mechanical properties as well as to the dimensional stability when heat is applied. Generally a porosity between 40 – 70 % is used in modern separators. Pore sizes should be in the submicron range to prevent Li-dendrites to grow into the separator[7-8, 31-32].

Shrinkage describes the change in dimensions when the separator is exposed to heat and is very important in regards to the safety of a LIB. During failure of a battery cell, the cell temperature will usually rise due to uncontrollable chemical reactions caused by charge and discharge processes. A separator is required to keep its mechanical integrity such as not to allow contact between electrodes and to prevent further

damage. Typically shrinkage is measured at 90 °C for one hour and should be < 5 % in machine direction (MD) and transverse direction (TD)[31-32]. No uniform procedure is used in the industry. Brückners standard for measurement of shrinkage is 105 °C for 1 hour.

Mechanical stability is expected to be as high as 98 MPa during tensile stretching in either MD or TD[7-8]. While tensile strength is less important once the separator is put into a cell, it is more important during the manufacture of a LIB as the separator needs to withstand winding tensions[31]. Instead a high puncture strength is a requirement to prevent puncture by the electrode surfaces during manufacture and operation of a LIB. A value of 240 g for a 20 μm thick separator is accepted as the minimum value in literature[7, 31-32], although market demand has significantly increased by then, now demanding 500 g for a separator membrane thickness of 16 μm.

Finally thickness determines the other parameters indirectly as lower thickness reduces the mechanical strength while increasing ion flux. As the separator is estimated to be about 20 % of the final cell cost[32], the demand is high for separators with lower thicknesses. In this way the packing density of a cell can also be increased, improving energy capacities. While most common separators in the consumer market have a thickness of 20-25 μm[7-8, 31], separators with thickness of 9-16 μm will be preferred in the future. To achieve this goal, new materials and process optimizations are necessary to keep all other properties on a sufficient level. Additionally, with the electrification of automotive transport, requirements for next generation batteries and separators are even higher in regard to battery safety, which is mostly expressed in higher demand for thermal and mechanical stability. Shrinkage for separators applicable for EV is required to be less than 5 % at 200 °C according to the United States Advanced Battery Consortium (USABC)[7]. Even though commercial separators use materials such as PE and PP which melt at 137 °C and 167 °C respectively, higher thermal stability can be achieved by coating one or both surfaces of separator with a heat resistant layer.

2.1.3.2 Manufacturing Process

Two major processes are currently used to manufacture porous stretched separator membranes: the wet and the dry process[7, 31-32]. In the wet process a polyolefin is mixed with a mineral oil in an extrusion system and cast into a film which is then oriented either in machine direction (MD) only or biaxially. After extraction of the oil in a volatile solvent such as DMC, the final stretched film has a distinct porous sponge-like structure. Material used in this process is mainly PE, which is increasingly replaced

by Ultra High Molecular Weight PE in order to increase mechanical properties[8]. A typical morphology of a wet separator is shown in Figure 2.4.

The dry process, as the name suggests, does not need any additional solvent during extrusion. Instead the pores are formed through one or multiple orientation and annealing steps in which a stacked lamellar structure is produced that forms slit-like pores during subsequent orientation in the machine direction. For this process PP or multilayers consisting of PP and PE are widely used[8, 31]. In contrast to the wet process, biaxial orientation is not applied as it does not achieve the desired results. Due to monoaxial stretching, properties of such separators are distinctly anisotropic[31], with lower mechanical strength in the transverse direction and a slit-like pore structure as shown in Figure 2.4.

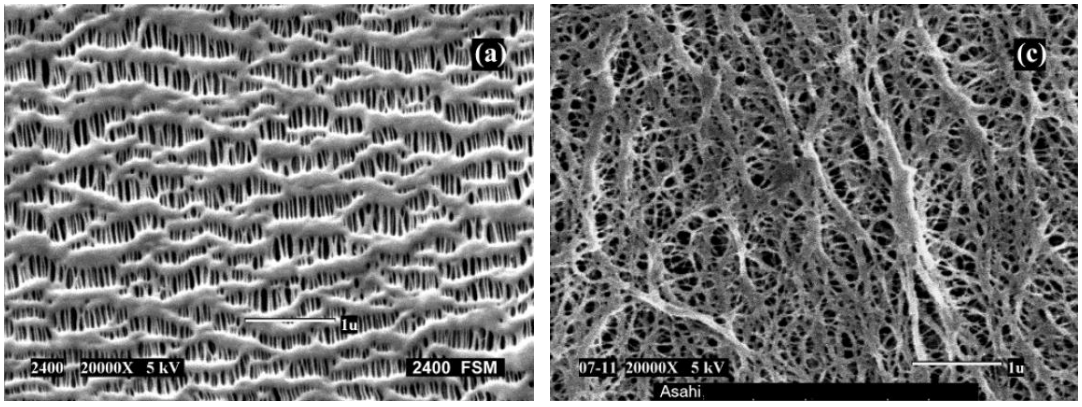

Figure 2.4: SEM images of commercial battery separators produced in the dry process (left, Celgard 2400, PP) and the wet process (right, Asahi, HiPore, PE)[31].

When β-nucleated PP is used, a sequential biaxial stretching process can be applied, which does not need a stacked-lamellar crystal structure, but relies on the density change during phase change of β-PP to α-PP during the first orientation step[31]. In this way micro crazes are formed which propagate during subsequent orientation in transverse direction (TD, perpendicular to MD).

In light of the recent advances of LIB technology in automotive applications, greater emphasis is put on the safety and durability of LIBs. Thus many separator manufacturers have begun to increase thermal stability of the separator by coating the separator with a heat resistant layer[35, 46-58]. This is typically done in an additional step where an inorganic or organic coating with a thickness of approximately 2-3 μm is applied on one or both sides of the separator. While the aim is reduced shrinkage of the film, careful tuning is necessary to ensure a sufficient high ionic flux. In most cases inorganic nanoparticles are used in combination with a polymeric binder such as PVDF.

2.2 EVAPORE® PROCESS

The EVAPORE® process is developed by Brückner as a cost efficient alternative to the wet and dry process. Called semi-dry or semi-wet process, the EVAPORE® process is a sequential biaxial process which uses low boiling aliphatic hydrocarbons during the extrusion, similar to the use of mineral oils in the wet process, while avoiding the expensive extraction of solvent after film stretching. The solvent is simply evaporated during the second stretching step, thereby giving the process its name. Using thermal regenerative systems, energy can be regenerated from the evaporated solvent which is reintroduced into the EVAPORE® process. An overview of a typical sequential line as is similarly used in the EVAPORE® process is given in Figure 2.5.

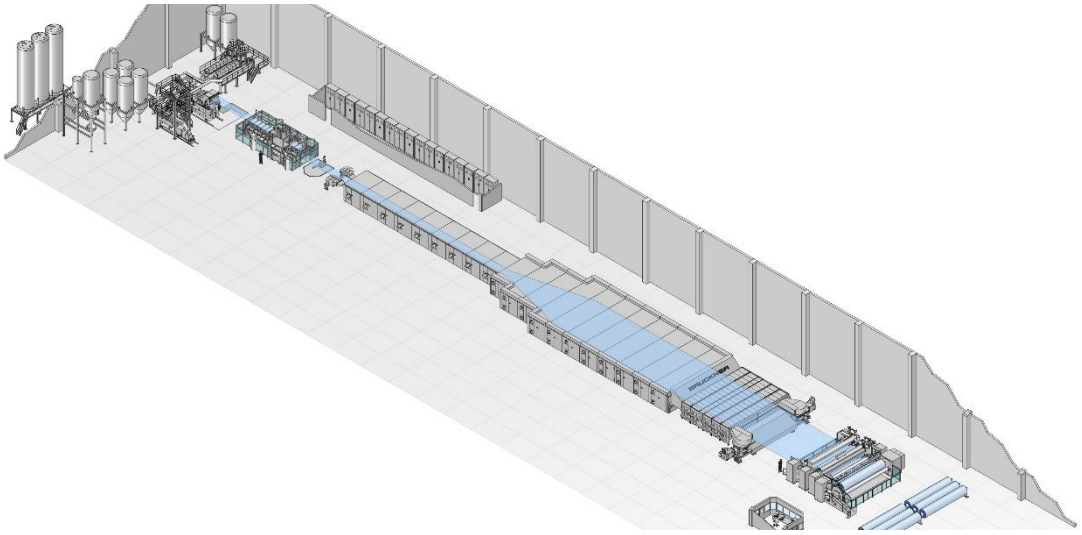

Figure 2.5: Isometric visualization of a typical sequential line from Brückner. From left to right: Material Dosing and Extrusion, MDO, TDO and winder.

With a film width of 4 m approximately 30 Mm^2/a can be produced on a typical EVAPORE® production line. A high yield in combination with high line speed and film width as well as energy recovery from evaporated solvent lead to a significant advantage in production costs compared to other processes. Typical film properties of a Brückner and commercial separators are given in Table 2.1.

Table 2.1: Comparison of commercial battery separators for 3C application.

		Brückner	Asahi	Celgard	Exxon Mobile / Tonen
Product Name		n/A	NH316C	A273	F16BME
Material		PE	PE	PP	-
Process		EVAPORE®	Wet	Dry	Wet
Thickness [μm]		16	16	16	16
Porosity [%]		44	40	40	38
Gurley (100 cc) [s]		215	240	345	280
Tensile Strength [N/mm²]	MD	116	157	157	132
	TD	111	128	13	108
Puncture Strength [g]		387	377	300	350
Shrinkage [%]	MD	4,1[a]	2[b]	3[c]	3[d]
	TD	0[a]	0[b]	0[c]	2[d]

[a] Measured at 105 °C for 1 hour.
[b] Measured at 90 °C for 1 hour.
[c] Measured at 100 °C for 1 hour.
[d] Measured at 105 °C for 8 hours.

Comparison to commercial separators shows similar values with slightly lower tensile strength for Brückners separator. As many separator manufacturers have already started to use UHMWPE in their process, mechanical integrity is expected to be increased. As separators in the dry process are only stretched in machine direction, tensile strength is very low in transverse direction. SEM (Scanning electron microscopy) images of an EVAPORE® separator are shown in Figure 2.6.

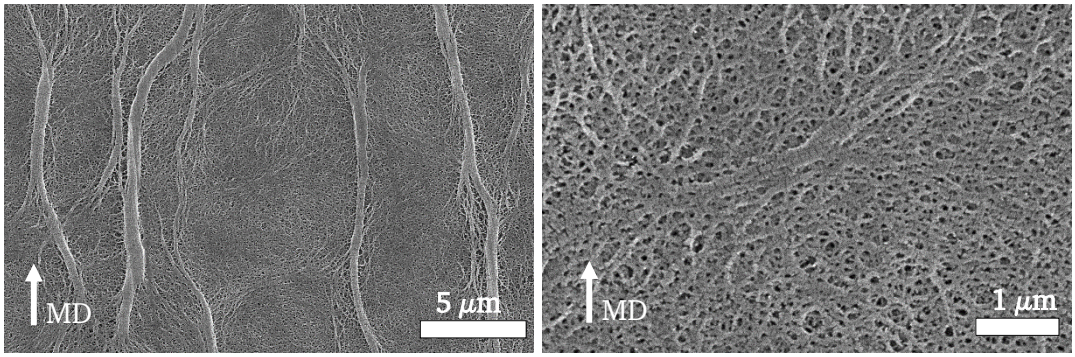

Figure 2.6: SEM images of the film surface of an EVAPORE® separator.

Characteristic for a sequential stretching process are the oriented thick crystalline strands. Generally, these structures are detrimental to the battery performance and a homogeneous surface morphology is preferred.

2.3 FILM STRETCHING

Thermoplastic materials, at higher temperatures, can be plastically formed in a variety of ways. For the manufacturing of polymer films, calender, flat sheet film extrusion and bubble film extrusion are the most important technologies[59-60]. While the calender has lost much of its significance for polymeric films, it is still used for the production of Polyvinyl chloride (PVC)-films. Typically a calender has multiple rolls in different configurations that apply pressure on the film such that it is milled into the desired form. The melt is supplied by an extrusion system to the calender. Afterwards the film can be stretched and conditioned in additional steps. Flat sheet film and bubble film extrusion are the major technologies used today for the production of all major film types[59]. Both technologies use an extrusion system to supply the molten resin, but differ significantly in the film forming instrument.
Bubble films are extruded through a tubular die in an upward vertical fashion. A schematic overview of a bubble film production line is given in Figure 2.7.

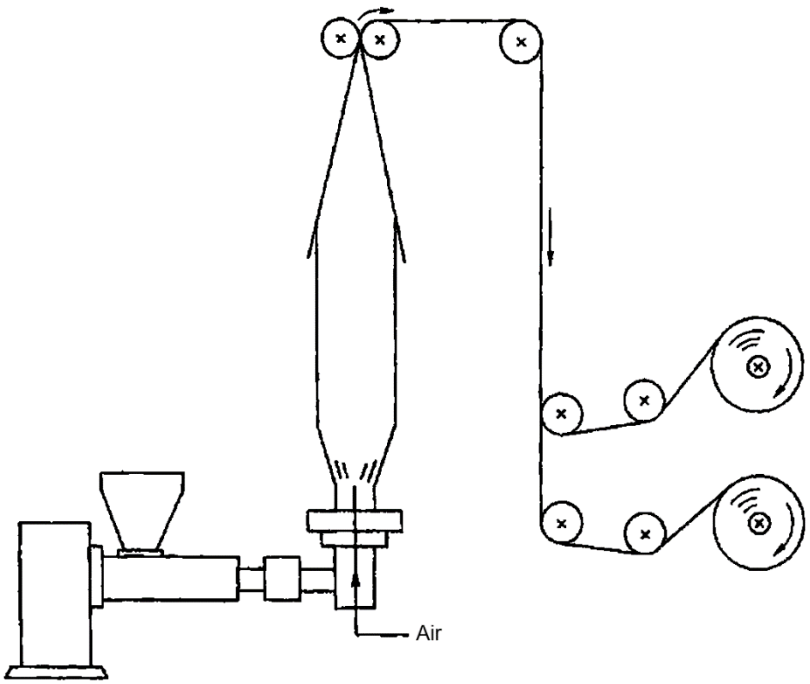

Figure 2.7: A tyipcal line layout of a blown film line using an extrusion system in conjunction with a tubular die[59].

As the film exits the die, it is blown-up from the inside and successively cooled by air from both inside and outside. The speed of which the film is transported is usually higher than the exit speed at the die. In this way the film is stretched both in machine direction (MD) due to the take-up speed and in transverse direction (TD) due to the

blow-up. When the film temperature falls below the melting point of the resin the film is fixed and will be folded by rolls to avoid the inclusion of air. The folded tube is then slit at the edges to receive two films that are then wound up[59-60].

As the name suggest flat sheet films are produced by extrusion of the melt through a flat die and subsequent cooling of the formed melt on a chill roll as shown in Figure 2.8.

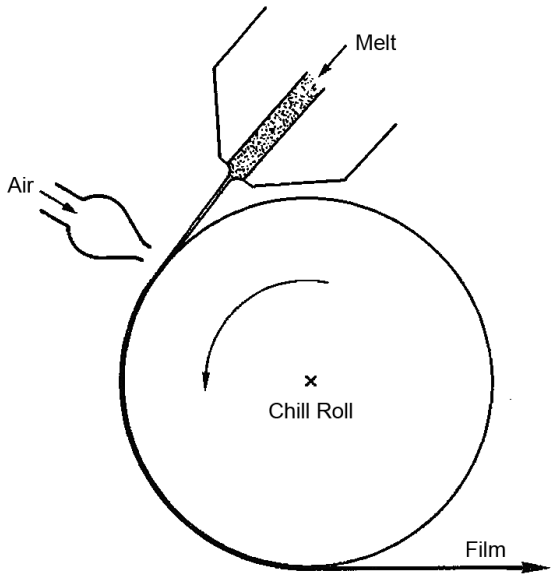

Figure 2.8: Casting of a melt onto a chilled roll. One way of ensuring contact to the roll is pinning by high pressurized air[59].

The die can be adjusted for film thickness and more importantly film thickness profiles. Today automatic adjustment systems use inline thickness measuring devices as an input to correct thickness profile when necessary. The chill roll temperature plays an important role during cooling of the melt and heavily influences crystallinity of semi-crystalline materials. To ensure good contact between film and chill roll, typically pinning systems, including high pressure air knifes, electrostatic pinning, vacuum pinning or pinning rolls are used. The so called cast film is then transported to one or multiple stretching devices[59-60].

Lithium Ion Battery separators are exclusively manufactured using flat sheet film technology. The main process steps are detailed further in the following chapters in view of flat sheet film technology.

2.3.1 EXTRUSION

Extrusion is a classic casting process to form resins into shape. It uses an extrusion system that usually entails accurate dosing of the materials, melting and densification of the resins and extrusion through a shaping tool. The main part is a series of temperature controlled hollow cylinders in which one or two screws are rotating and transporting the material from the feeding zone to the extrusion exit[60-61]. Figure 2.9 shows a typical single-screw extrusion system.

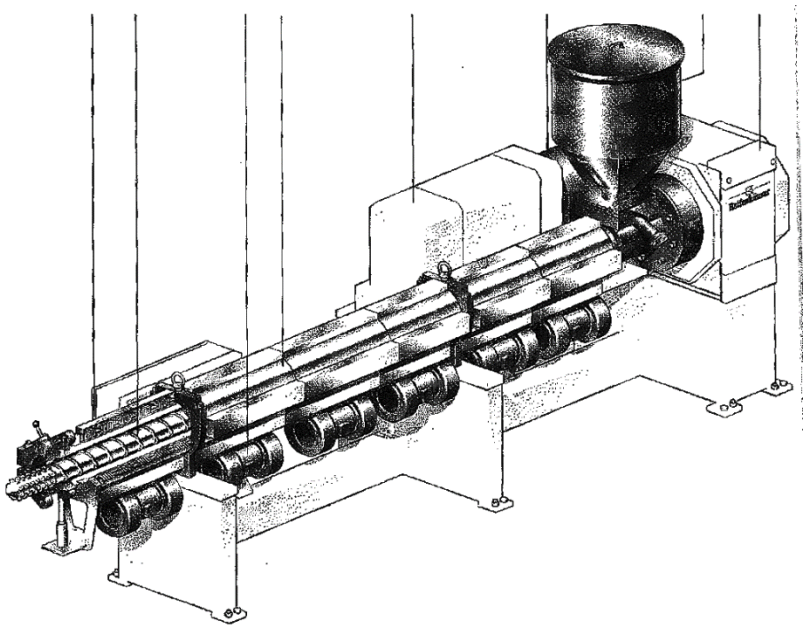

Figure 2.9: Typical single screw extrusion system[61].

The screw is defined by its specific geometry that is individually tailored to each process and material. A main characteristic of an extrusion system is its L/D number, which is a ratio of extrusion length to screw diameter. Each extrusion system is divided into multiple zones that each are comprised of an individually heated cylinder. Typically the material is first heated in the first parts of the extrusion, compressed and molten in the middle part and lastly homogenized and pressurized in the last part. High pressure is needed to achieve homogenous melt quality and to push melt through further heated pipes as well as through the film forming die. For each part the screw uses specialized elements to achieve the desired conditions[61].

After exiting the extrusion, the melt is transported through heated pipes using a melt pump to control extrusion head pressure on one hand and to gain enough pressure for consecutive filter elements on the other. Finally the polymer melt will reach the film forming die, which can be a one- or multilayer die, in the latter case combining multiple polymer melts from different extrusion systems into a layered sheet structure.

Typical thicknesses of such dies for film application range from 0,5 to 1 mm. Different geometries are available such as a T-die or a coat-hanger die shown in Figure 2.10.[61]

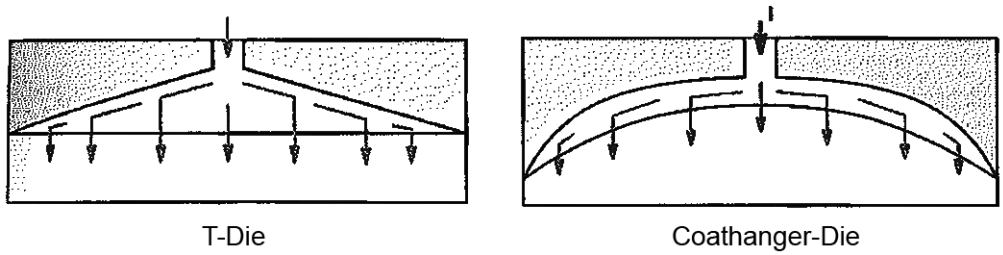

Figure 2.10: Common Die geometries[61].

The challenge of such a die is to distribute the melt evenly over the working width, which requires careful consideration of the geometry as well as the viscosities of the melt that is to be used. While coat-hanger dies are typically more expensive than T-dies, they allow for a better distribution with sensitive materials[61].

2.3.1.1 Melt Flow Instabilities

Instabilities in melt flow at the die exit can limit the upper throughput of an extrusion line[62-63]. Early reports of melt instabilities date back to the 1960s and can be classified according to their severity and include surface-distortions, stick-slip fracture and gross melt fracture. In literature the appearance of surface-distortions is called sharkskin effect or sharkskin melt fracture. It is generally agreed that the appearance of sharkskin is correlated to the flow dynamics at the capillary die exit and the transition from laminar flow to plug flow[62, 64-65]. Figure 2.11 shows a schematic overview of melt flow near a capillary exit, as well as a photograph of pronounced sharkskin on a polymer melt.

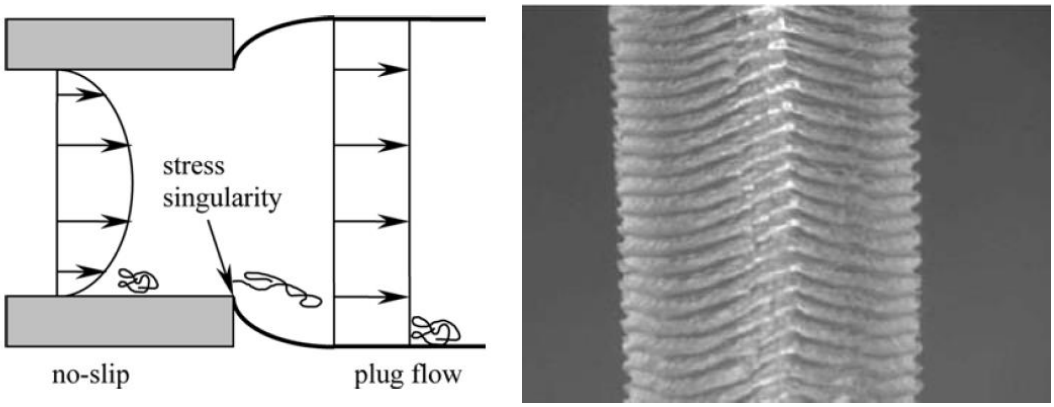

Figure 2.11: Schematic of melt flow at the die exit (left). Photograph of pronounced sharkskin (right)[66].

As can be seen from the picture, sharkskin can occur as oscillating ridges on the melt surface. During melt flow inside capillary restraints, a laminar flow can be assumed fulfilling a no-slip condition at the wall boundary. When the melt exits the die, the flow abruptly transitions to a plug flow, which induces a large stress at the contact point between melt surface and die exit, called a stress singularity[66]. At higher throughputs, and therefore higher shear rates, molecular chains at the die wall start to disentangle due to the high tensile stress and at some point will slip from the wall boundary due to their high extension. At this point the entangled chains will relax into an entangled form. This mechanism leads to an oscillating stick-slip behavior of molecular chains near the die exit and will consequently lead to the formation of surface distortions (sharkskin). At even higher shear rates, this phenomenon will be so pronounced that no cohesive melt can be produced (gross melt fracture).

Several studies have reported on the influence of molecular weight and polymer chain configuration on the onset of sharkskin formation[64-65, 67-68]. Ansari et al. studied the influence of various Ziegler-Natta and Metallocene HDPEs with varying molecular weight and molecular weight distribution[65, 68]. They found that an increase in molecular weight lowers the onset of melt instabilities and attributed this to an increase in chain entanglement that leads to abrupt stick-slip mechanisms. Consequently they found, that an increase in polydispersity lowers the effect of sharkskin formation as the shorter chains contribute to less entanglements. Yoo et al. investigated the effect of long chain branching of LLDPE on the severity of the sharkskin effect and found a decrease of the critical shear stress with increasing amount of long chain branching[64].

To avoid melt instabilities, several approaches can be used to decrease shear stress below the critical value. The most common approach is to either increase melt temperature in bulk, or more energy efficient, to increase the die temperature at the die exit[62-63, 65-66, 68]. As polymer melts are typically insufficient thermal conductors, only the melt surface will be heated, leading to a decrease in viscosity and reduction of the stick and slip mechanism. Alternatively fluorinated processing aids can be used that migrate to the die wall during extrusion and limit the effect of sticking of polymer melt to the wall[62, 68-69]. Arda et al. reported a decrease in melt flow instabilities by using a die with a curved exit, attributing the improvement to a delay in the melt separation point from the die, allowing the stresses in the melt to relax[70].

2.3.2 STRETCHING

One of the most important biaxially stretched films is BOPP (Biaxially Oriented Polypropylene), as it is used heavily in the packaging industry. Oriented films offer increased mechanical strength, optimized transparency, thermal stability as well as increased barrier properties. Stretched films can be produced either sequentially, using a two-step stretching process or simultaneously[59-60]. A schematic overview of a sequential production line is given in Figure 2.12.

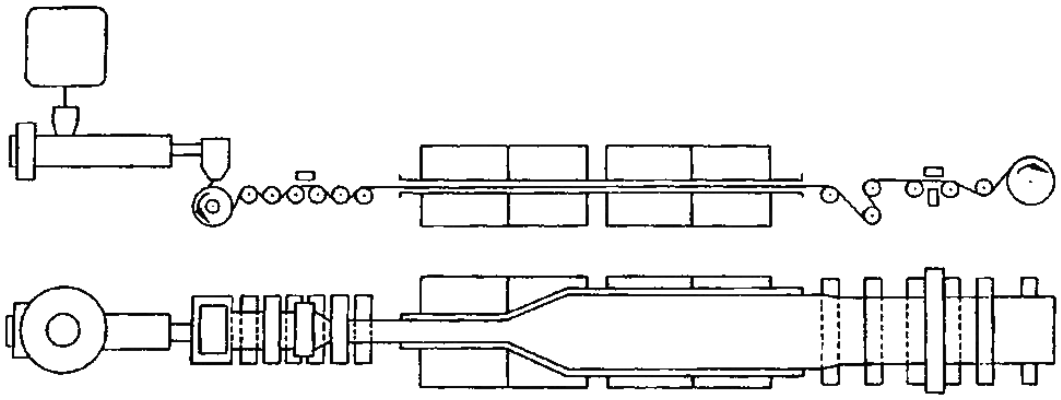

Figure 2.12: Line overview of a biaxial film stretching line comprising extrusion, machine direction orientation, transverse direction orientation as well as winding[59].

After extrusion the cooled cast film is transported to a series of rolls that typically consist of several preheating rolls, drawing rolls and annealing rolls. During the preheating the film is slowly heated to the required temperature and is consecutively stretched between two or more drawing rolls with a defined gap between the rolls. A smaller gap is usually beneficial for even film properties. After stretching, the film is exposed to annealing rolls, where the molecular orientation is fixed thermally to reduce film stress. When orientation on transverse direction is required, a tenter frame is used which uses clips mounted on a chain to grip the film at its edges and stretch the film in a V-shaped manner. This process is done in a large oven with controlled temperatures for preheating, stretching and heat-setting of the film[59-60].

As an alternative, simultaneous stretching is possible with Brückners LISIM® (Linear Motor Simultaneous Stretching) technology, which enables contact free stretching by avoiding rolls during machine direction stretching and achieves isotropic film properties. The LISIM® process is shown in Figure 2.13.

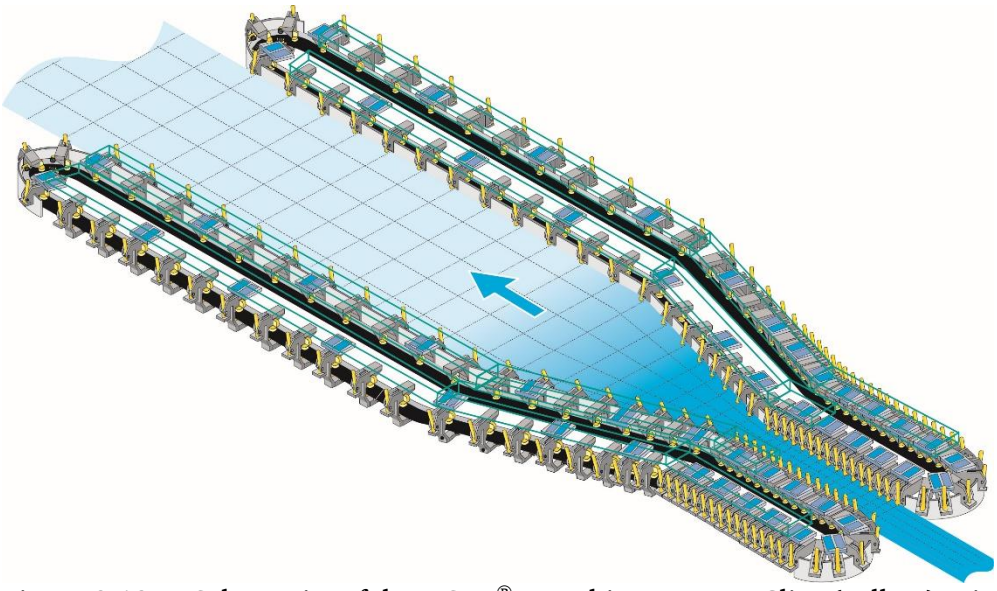

Figure 2.13: Schematics of the LISIM® stretching process. Clips (yellow) grip the film at the edges and stretch it in both machine and transverse direction, resulting in a biaxially oriented film.

Contrary to standard transverse direction stretching, clips used in the LISIM® run on linear motors that can speed up independently from each other, thereby achieving stretching in machine direction.

2.3.3 WINDING

In a winding unit the stretched film is conditioned before being wound up under controlled film tension. Conditioning of the film includes cutting off of the edges as well as optional corona or plasma treatment to increase surface hydrophilicity. Film thickness and other properties of the final film can also be measured in the winding unit, to create a feedback loop for the running process.

2.4 POLYMER CRYSTALLIZATION

Semi-crystalline polymers consist of two phases, an amorphous phase of randomly oriented and entangled molecular chains and a highly ordered crystalline phase. The fraction of crystalline phase is described by the crystallinity, with typical values between 60 % and 80 % for High Density Polyethylene (HDPE)[71],which is one of the main materials used for battery separator films. The crystalline unit cell of Polyethylene is shown in Figure 2.14

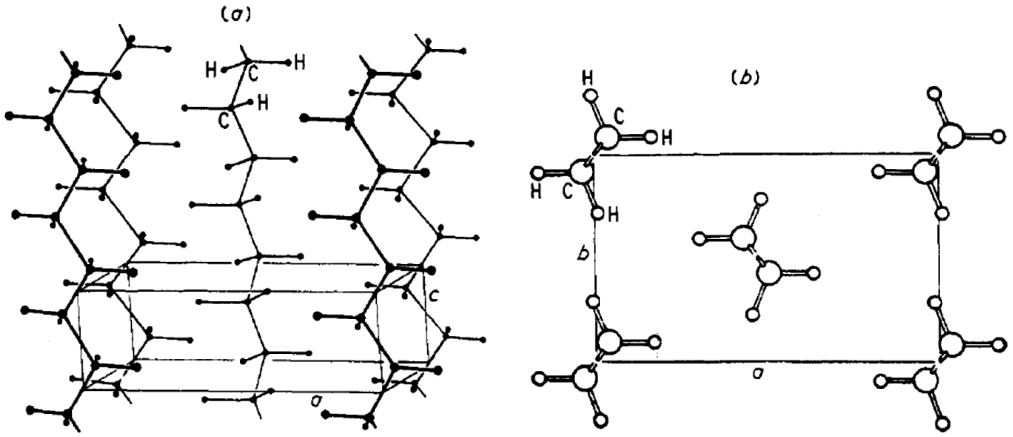

Figure 2.14: Crystal structure and unit cell of orthorhombic Polyethylene[72]. a=0,74 nm, b=0,493 nm, c=0,254 nm[73].

2.4.1 CHAIN-FOLDING

Polymer chains crystallize via a chain-folding mechanism, where chains are aligned in parallel and fold back when they reach the end of a crystalline phase. Some chains will not fold back into the same crystal, and can instead be part of a multitude of crystals as can be seen in Figure 2.15[73].

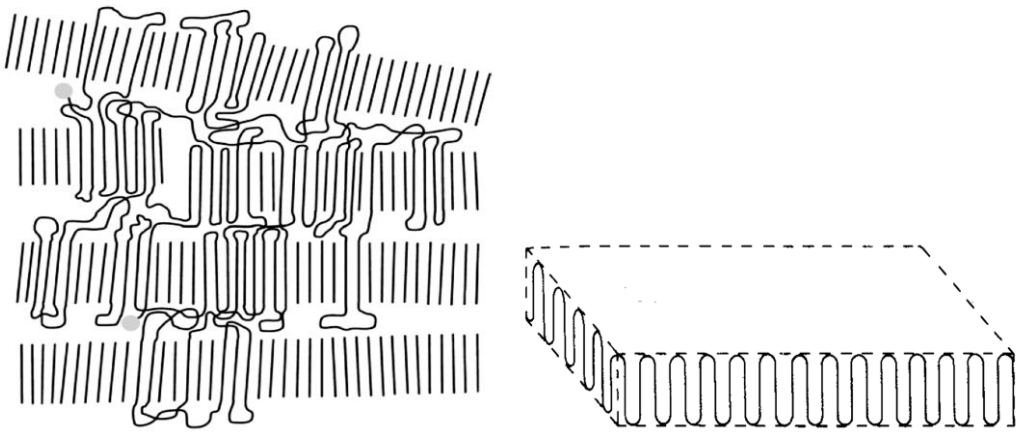

Figure 2.15: Schematic representation of chain folding of a polymer chain into crystalline regions interconnected by an amorphous phase (left)[71]. Idealized representation of a chain-folded lamellar crystal (right)[60].

The direction of chain-folding and lamellar thickness corresponds to the c-axis of the polymer crystal and the molecular backbone. Amorphous material can be found in between adjacent crystalline regions and serves as a linkage between them. These crystalline regions, also called lamellae, propagate in two dimensions, with fold-length being equal to lamellae thickness. Chain-folding is a consequence of the material striving to reduce free energy of the chain surfaces with the folding length being a

function of crystallization temperature[72]. Low undercooling leads to longer folding length, while a high undercooling results in thinner crystals and overall lower crystallinity[74]. Interestingly, annealing of semi-crystalline polymers results in a thickening of lamellae as the polymer chain tries to reduce free energy further by extending its length. The mechanism of thickening has been proposed to be due to local melting and recrystallization as well as due to a concerted movement of multiple chain segments.

2.4.2 SPHERULITES

The formation of crystalline lamellae proceeds in a radial fashion during polymer crystallization. The so generated morphology is called a spherulite, and in the absence of boundaries, typically growths outward in a three dimensional fashion. Spherulites can reach diameters up to 1 cm depending on crystallization temperature and number of nucleation sites. A schematic illustration of a spherulite structure is shown in Figure 2.16.

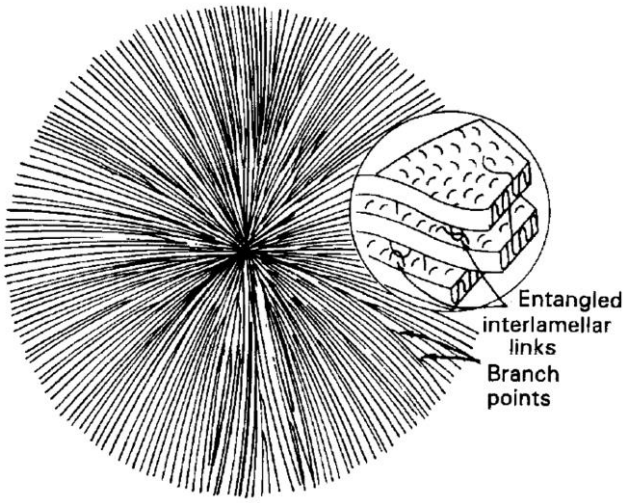

Figure 2.16: Illustration of a spherulitic crystal structure[73].

During growth of the crystalline phase, lamellae will grow out from the nucleation site and branch regularly, leading to spherulitic morphology. The space between the individual lamellae is filled with amorphous intercrystalline connections. Depending on the impingement with other spherulites, the boundaries are typically straight. The formation of spherulites is illustrated in Figure 2.17.

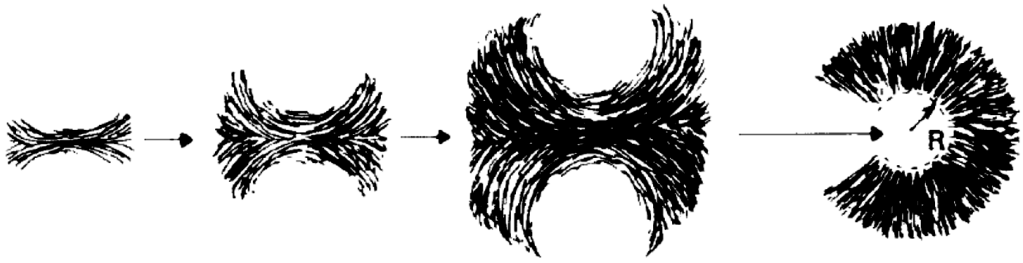

Figure 2.17: Illustration of spherulitic growth[73].

After the initial nucleation, lamellae start to grow outward in a sheaf-like morphology. Low angle branching of the lamellae leads to spreading and ultimately to radial growth.

2.4.3 PLASTIC DEFORMATION

One of the most important aspects of film stretching of semi-crystalline materials is the plastic deformation, which occurs during the application of sufficient shear stress. During stretching, the material passes the elastic region, in which only the amorphous interlamellar tie-molecules will be pulled taut. If the stress is high enough, irreversible plastic deformation of the crystalline regions will occur. These deformations can potentially occur in multiple ways from a crystallographic point of view, but are dominantly of a shear type mechanism. These can be described as a crystallographic slip of distinct crystallographic planes, avoiding a disruption of chain folds. It is well known that during tensile deformation, the slip direction and chain axis rotates towards the tensile direction, resulting in an orientation of the crystalline structure. This process is mainly dependent on temperature and strain rate, as the crystal deformation is a thermally activated process. The deformation of spherulites can be divided in polar and equatorial deformation, depending on the alignment of the chain axis to the tensile direction[73, 75]. The process of deformation is shown schematically in Figure 2.18.

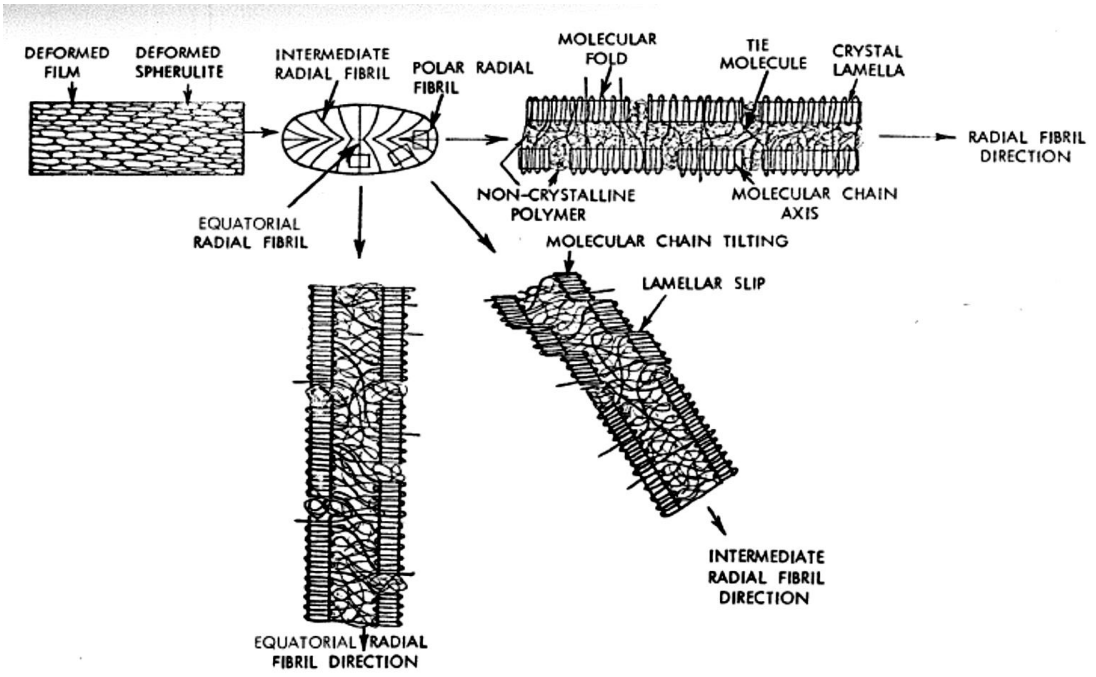

Figure 2.18: Schematic illustration of spherulitic deformation[75].

In the equatorial regions, the chain axis is aligned parallel to the tensile direction and simple chain slip mechanisms prevail. On the other hand, the polar regions consist of chains aligned perpendicular to the tensile direction, therefore exerting higher resistance to deformation. The predominant mode of deformation in the intermediate regions is transverse slip and micro-necking, where crystalline regions break off, rotate and realign themselves into the tensile direction[73, 75]. The stress-strain diagram for a stretched semi-crystalline sample with spherullitic morphology is shown in Figure 2.19.

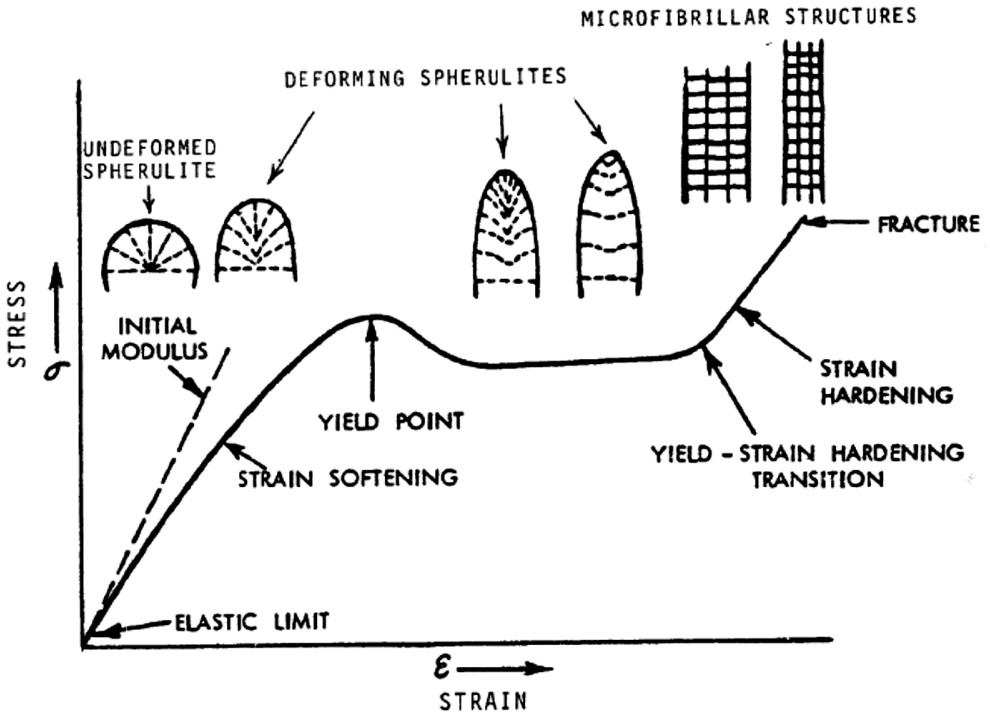

Figure 2.19: Idealized Stress-strain diagram for a semi-crystalline material.[75]

Initially, at low strains, the material will exhibit viscoelastic behavior with linear correlation of the stress-strain curve. Stresses will start to temper off during further stretching as the spherulite will start to deform by rotating crystallites and straightening of some of the amorphous regions. This so-called strain softening will occur until the yield point is reached, which marks the onset of significant crystal deformation through chain slip and crystal shear mechanisms. As more and more crystallites are disrupted, the resistance to deformation is lowered and stress falls to a nearly constant level due to the occurrence of necking which reduces the cross-section of the material. Once all lamellae have been rotated and aligned parallel to the deformation direction, further deformation will become more difficult and crystal fracture is dominant. This is called strain hardening, which results in a transition from spherulitic to microfibrilar structure[75].

2.4.4 SHISH-KEBAB MORPHOLOGY

Under elongational flow, a different mode of crystallization can occur. Molecular chains will first extend under flow conditions, leading to the formation of elongated crystal blocks of various lengths depending on the crystallization temperature[60]. These blocks of aligned molecular chains serve as nuclei for the overgrowth of lateral crystals forming a stacked lamellar morphology as shown in Figure 2.20.

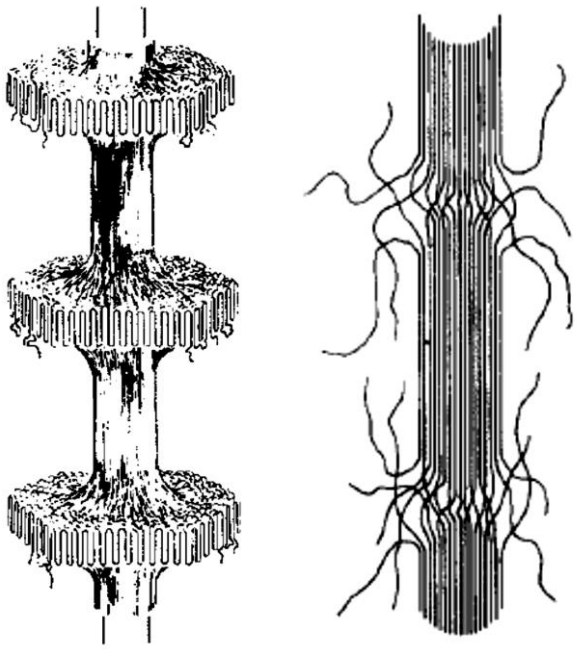

Figure 2.20: Illustration of a final shish-kebab crystal morphology (left) and the elongated crystal block precursor of the shish-kebab (right)[60].

This morphology is also named shish-kebab in literature as it resembles blocks of meat on a skewer. While the precursor core structure of elongated molecular chains is called the shish, the platelet overgrowths are called kebab. Formation of kebabs is possible due to the nature of the central core. Depending on the temperature, the crystal blocks in the shish can be of various length with alternating amorphous regions between each individual block. It is at these regions that loose molecular chains extend outward and form, under given cooling conditions, micro-kebabs that serve as nucleation sites for further crystalline growth. The chain axis in these overgrowths is parallel to the central core structure[60, 76-78].

The shish-kebab morphology has been widely found in solution crystallization for polyethylene, where a crystalline precipitate has been observed to form on a stirrer of a solution at slightly higher temperature than the typical crystallization temperature of static solutions. This has been attributed to the formation of a shish-kebab morphology due to the extensional flow field generated by vigorous stirring. As these elongated shish-kebab morphology exhibit significant higher tensile moduli, they have been widely used in the production of fibers by the solution growth and gel-spinning process. Tensile Moduli of 100 to 150 GPa can be achieved by adjusting the temperature of crystallization, which has been attributed to an increase in crystal block length in the core of the shish-kebab crystallites[60].

The formation of a shish-kebab morphology is not limited to polymer solutions, as it can also occur under shear flow of a pure melt as well as under uniaxial extension. Flow-induced crystallization, as it is also called, is dependent on four major parameters: shear rate, strain, molecular weight and temperature. For crystallization to occur, a certain critical strain of the molecular chains is required. Because the extension of chains is countered by polymer relaxation, the shear rate needs to be high enough to maintain and propagate further extension. Molecular weight and molecular weight distribution play an important role, with longer chains needing more time for relaxation due to their increased weight. Therefore, the higher molecular weight fraction of a given molecular weight distribution is more readily extended and a certain critical molecular weight is required for flow-induced crystallization at a given shear rate and strain. With increasing shear rate, the critical molecular weight can be reduced to some extent. The effect of temperature is tied to movement and relaxation phenomena of polymers, with increased temperature leading to reduced relaxation times. Nonetheless, flow-induced crystallization can also occur above the melting point of a given polymer, when shear stress and molecular weight are sufficiently high[60, 76-80].

2.4.5 CAVITATION

Tensile deformation of semi-crystalline polymers can be accompanied by cavitation, which can be described as the generation of voids in the amorphous phase. A significant amount of research has been invested mainly by Pawlak et al. and Galeski et al. into the cavitation of common polymers such as HDPE and PP[79-95]. The phenomenon of cavitation occurs during the initial deformation of polymers, as the amorphous phase is extended between adjacent crystalline regions. This leads to a thinning of material in the amorphous region, resulting in a build-up of negative pressure that can, theoretically, only be countered by flow-in of surrounding material, voiding of the amorphous phase or deformation of the crystalline phase. Flow-in of material seems highly unlikely, as the surrounding amorphous phase is entangled and connected to the crystalline regions. The formation of voids and crystalline deformation are competing processes. If the coherent strength of the amorphous phase is lower than the strength of the crystalline phase, voiding will preferably occur. As the crystalline strength is connected to the yield point, with it marking the onset of crystalline deformation, cavitation typically occurs slightly before the yield point has been reached. It is also evident, that by changing crystallization conditions, the crystal

strength can be changed to allow for more or less cavitation. For example, polymers exhibiting strong crystals such as PP and HDPE readily show cavitation while materials comprised of small and defected crystals such as LDPE or ethylene-copolymers do not show cavitation at all[82, 87]. For PE and PP, negative pressure needed for cavitation reaches values between -13 MPa and -16 MPa[83].

The process of cavitation is dependent on a variety of parameters, such as molecular weight, chain branching, temperature, strain rate and lamellae orientation. With increasing molecular weight or increasing chain branching, the number of entanglements and general cohesive strength of the amorphous phase is increased, leading to a lesser extent of voiding. This is also true for increased temperature and lower strain rates, as it allows for easier activation of the necessary crystal deformation processes such as crystal slip and shear. Lamellae orientation on the other hand can lead to increased cavitation, when lamellae are oriented with their normal parallel to the tensile direction[87]. This is the case for flow-induced shish-kebab structure that is further deformed parallel to the shish direction, leading to the formation of voids between adjacent kebab overgrowths. This mechanism is used for the production of porous separator membrane by the dry process[89, 93].

3 AIM OF THIS WORK

The aim of this work is separated into several issues, with the most important aspect being the production of a novel, high temperature stable battery separator membrane via the EVAPORE® process. With the market demand for electric vehicles (EV) expected to grow rapidly in the coming years, emphasis is put on safety of the battery device. Separators made of HDPE and UHMWPE are limited in their temperature stability due to a low melting point of about 137 °C. Therefore, current state of the art battery separators are coated with a ceramic layer, before being used in a battery. The idea behind this study is to avoid an additional coating step by using a high temperature stable polymer as an alternative to the currently used HDPE. Additionally, higher mechanical strength is an important key property of the separator that is connected to safety of not only EV but 3C applications as well. Special emphasis is put on the puncture strength of a separator, as the current trend is going towards thinner membranes without losing mechanical integrity. The requirements defined by Brückner for a novel separator are summarized in Table 3.1.

Table 3.1: Actual and target values for separators produced by the EVAPORE® process.

Film Property		Actual	Target
Thickness [μm]		16	16
Porosity [%]		44	>45
Gurley (100 cc) [s]		215	210
Puncture Strength [g]		387	>500
Tensile Strength [N/mm²]	MD	116	>150
	TD	111	>150
Shrinkage (3C) [%] 105 °C/1 h	MD	4,1	<2
	TD	0	<0,5
Shrinkage (EV) [%] 160 °C/1 h	MD	-	<5
	TD	-	<5

To achieve sufficient temperature stability for EV applications, a range of common high temperature polymers were to be evaluated as an alternative to HDPE for use in the EVAPORE® process. All polymers were first to be checked for their stability in common battery electrolyte by submersing pristine samples of the respective polymer in the electrolyte LP71 (1:1:1 of dimethyl carbonate, diethyl carbonate and ethylene carbonate containing 1 M of $LiPF_6$) for up to seven days. To further evaluate the polymers, a laboratory method was to be developed with the aim of producing cast film and stretched membrane samples in a small and cost efficient scale. This method was to be established by using HDPE and an aliphatic hydrocarbon solvent as used by the EVAPORE® process. Using the laboratory method, high temperature polymers were to be processed with compatible solvents as determined by Hansen parameters with the aim of identifying a suitable polymer-solvent combination for the EVAPORE® process. Suitable solvents were to be chosen not only according to their miscibility with the respective polymers, but also based on cost, boiling point and health hazards. Finally, the identified polymer-solvent mixtures were to be adapted to the EVAPORE® process on Brückners laboratory and pilot line in a larger scale.

Increased mechanical strength of the state of the art battery separator membrane using polyethylene was to be another aspect of this work. By using UHMWPE instead of HDPE, the EVAPORE® process was to be scaled-down and established on Brückners new laboratory line with the aim of increasing tensile strength as well as puncture strength of the separator membrane. Several UHMWPE polymer grades with molecular weight ranging from 0.7 Mg/mol to 5 Mg/mol were to be evaluated.

In addition, as the EVAPORE® process is not fully understood, the newly developed laboratory method was to be used to deepen the understanding of the pore formation mechanism. HDPE cast films from the laboratory line were to be used for stretching trials on Brückners KARO IV machine to elucidate the effect of the stretching conditions on membrane morphology, polymer chain orientation as well as on pore formation and final separator performance. To that end, scanning electron microscopy (SEM), X-ray powder diffraction (XRD), differential scanning calorimetry (DSC) as well as porosity and air permeability measurements were to be used to analyze the stretched membranes.

4 MATERIALS AND METHODS

In this work the following polymeric and chemical substances were used. The methods used for characterization of materials and produced separators are also described further.

4.1 MATERIALS

In general, polymeric materials will be listed in more detail in the corresponding chapters. Table 4.1 lists all polymers that were used for the production of films by the EVAPORE® process and can be used as a quick reference to the corresponding sections. Technical Data Sheets can be found in appendix 8.3. In addition, Table 4.2 provides information about the solvents used in conjunction with the polymers, most important the boiling range of the respective solvent, which is an important criteria for extrusion temperature limit and evaporation rate.

Table 4.1: List of polymers used for the production of films by the EVAPORE® process.

Polymer name	Manufacturer	Type	T_m [°C]	Reference
Alathon L5906	LyondellBasell	HDPE	137	Chapter 5.1 Chapter 5.4.1
Sunfine SH800	Asahi	HDPE	137	Chapter 5.5
PP-A[a]	NDA[a]	PP	167	Chapter 5.4.2
PP-B[a]	NDA[a]	PP	167	Chapter 5.4.2
PP-C[a]	NDA[a]	PP	167	Chapter 5.4.2
RT31	Mitsui Chemicals	PMP (TPX™)	240	Chapter 5.4.3
DX845	Mitsui Chemicals	PMP (TPX™)	240	Chapter 5.4.3
MX002	Mitsui Chemicals	PMP (TPX™)	240	Chapter 5.4.3
HiZex 145M	Mitsui Chemicals	UHMWPE	137	Chapter 5.5
GUR4018	Celanese	UHMWPE	137	Chapter 5.5
GUR4012	Celanese	UHMWPE	137	Chapter 5.5
GUR4120	Celanese	UHMWPE	137	Chapter 5.5
GUR2122	Celanese	UHMWPE	137	Chapter 5.5

[a] Development material, protected by non-disclosure-agreement

The solvents used in this study for the production of cast and stretched films are summarized in Table 4.2.

Table 4.2: List of solvents used and their boiling range. Values from MSDS or TDS.

Solvent name	Manufacturer	Boiling Range [°C]	Flash Point [°C]
Solvent 142	Sunnyside	188-194	62
SiSol D60	Silbermann	180-220	>62
Exxsol D80	Exxon Mobile	200-250	>77
Exxsol D100	Exxon Mobile	210-280	>100
Exxsol D140	Exxon Mobile	260-370	>100
ShellSol T	Shell	189-215	61
Dibutyl Adipate	Sigma-Aldrich	305	>113
Diethyl Adipate	Sigma-Aldrich	245	>100
Dimethyl Phthalate	Sigma-Aldrich	282	146

4.2 METHODS

4.2.1 MELT FLOW RATE / MELT VOLUME RATE (MFR / MVR)

MFR was measured using Petflow@on (KARG Industrietechnik, Germany). According to ISO1133[96] samples were measured at a predefined temperature and pressure (i.e. weight of cylinder). The capillary flow is measured for a certain amount of time and the MFR can then be calculated.

4.2.2 ELECTROLYTE TESTS

To test a range of common polymeric materials for their chemical stability in electrolytes used in Li-Ion Batteries, the following procedure was used. Sheets of polymers (150 mm x 15 mm) of various thicknesses were dried in an oven at elevated temperatures and their weight measured. Each sheet was sealed in a glass bottle and the air was exchanged with an Argon atmosphere through a septum. About 50 ml of LP71 (DMC, DEC, EC (1:1:1); 1 M $LiPF_6$) was filled through the septum and the polymer thus completely immersed in electrolyte. For each material, four glass bottles were prepared in this manner and kept at room temperature and at 60 °C for one and seven days for each temperature. After that the polymer sheet was removed, shortly

rinsed in a small amount of fresh DMC and the surface carefully dried with a laboratory grade paper towel. Dimensions and weight of these samples were measured to calculate the degree of swelling. Finally the samples were washed in ethanol for 30 minutes and dried in a vacuum oven. The dried samples were again measured in their dimensions as well as weight and also characterized by IR spectroscopy and tensile testing.

4.2.3 THERMALLY INDUCED PHASE SEPARATION (TIPS)

TIPS experiments were done with small amounts of shredded polymer granules that were mixed with varying contents of solvents in a sealed and with N_2-filled test tube under elevated temperatures typically in the range of the melting point of the polymer. After 30 minutes a small sample from the visually homogeneous melt was scraped out of the tube and sealed between two glass slides. Using optical light microscopy with an integrated hot stage (see 4.2.10), a thin layer of material was observed during melting and crystallization at a non-constant cooling rate of 9 K/min ± 1 K/min. Pictures were captured with the video system in defined intervals.

4.2.4 DIFFERENTIAL SCANNING CALORIMETRY (DSC)

Analysis of crystallinity of solvent-filled and dried samples were carried out in a DSC200 F3 Maia (Netzsch, Germany) at heating rates of 10 K/min. Sealed aluminum pans were used to contain samples of 5-10 mg. The samples were first heated to about 180 °C and kept at this temperature for 10 minutes to erase thermal history and subsequently cooled to room temperature at a cooling rate of 10 K/min.

4.2.5 CAPILLARY FLOW POROMETRY

Analysis of pore size distribution was carried out on a Porometer 3G zh (Quantachrome, USA) using high pressured N_2 as a displacing gas and Porofil® as a wetting agent. Two runs, wet and dry, were carried out in this order. The pressure range used was 6 bar to 25 bar. Mean flow pore size, defined as the pore size corresponding to a wet flow that is half the dry flow, was used for comparison.

4.2.6 PUNCTURE STRENGTH

Puncture strength was measured on a Z005 (Zwick GmbH & Co. KG, Germany) using a 1 mm rounded tip, a speed of 120 mm/min and a free clamping diameter of 17 mm.

4.2.7 TENSILE TESTING

Samples of 15 mm x 170 mm were measured on a Z0.5 (Zwick GmbH & Co. KG, Germany) at a speed of 100 mm/min according to ASTM D882[97]. The free clamping length of the sample was fixed at 100 mm. For measuring of the E-Modulus a speed of 1 mm/min was used in the range of 0,05 % - 0,25 % elongation.

4.2.8 FILM THICKNESS

Film thickness was measured on a hand device 1202 D (Mahr GmbH, Germany). Larger samples from the pilot line were measured automatically in a GPA-CAP (Octagon, Germany) according to DIN53370[98] using a combination of mechanical caliper and a capacitive sensor at fixed distances.

4.2.9 SCANNING ELECTRON MICROSCOPY (SEM)

A JSM-6510 (JEOL, Japan) with a tungsten cathode was used for characterization of surface morphologies of film samples. Samples were sputtered with gold for 20 s at 20 mA prior to measurement and measured in SE mode using a working distance of 9 mm.

4.2.10 OPTICAL LIGHT MICROSCOPY

A light microscope Laborlux 12 Pol (Leica, Germany) with an integrated hot-stage and video system was used to visualize phase changes in polymeric mixtures. Melting point as well as crystallization and cloud points were observed. Heating rate was adjusted manually by setting the current. Over a wide temperature difference the heating rate is not constant, but can be approximated as linear for a narrower range (i.e., in the range of crystallization). For the observation of crystallization a cooling rate of 9 K/min ± 1 K/min was used.

4.2.11 ATTENUATED TOTAL REFLECTANCE IR SPECTROSCOPY (ATR-FTIR)

For characterization of film samples an FT-ATR-IR 3100 from Varian was used at room temperature. The analysis was done in a spectral range of 650 to 4000 cm^{-1} at a rate of 2 cm^{-1} per step. Four scans were done for each sample with the background signal subtracted from the results.

4.2.12 X-RAY POWDER DIFRACTION

Samples of MD stretched film were analyzed by X-ray diffraction in cooperation with Prof. Dr. Mathias Epple and Dr. Prymak at the Institute of Inorganic Chemistry at the University Duisburg-Essen. Each sample was measured three times with a different incident plane for each measurement. The three planes used were the film surface and cross-sections along both machine and transverse direction. As the area provided by the cross-section of these thin films (with a thickness of approx. 100 μm) was too small, 32 pieces of film were manually stacked upon each other using Pattex plastics glue (Henkel AG & Co. KGaA) as described in Figure 4.1, making sure that MD and TD direction was the same for each piece of film. Measurement of the glue yielded no significant response that would alter the analysis. The layered sample was then cut to reveal clean surfaces for X-ray powder diffraction.

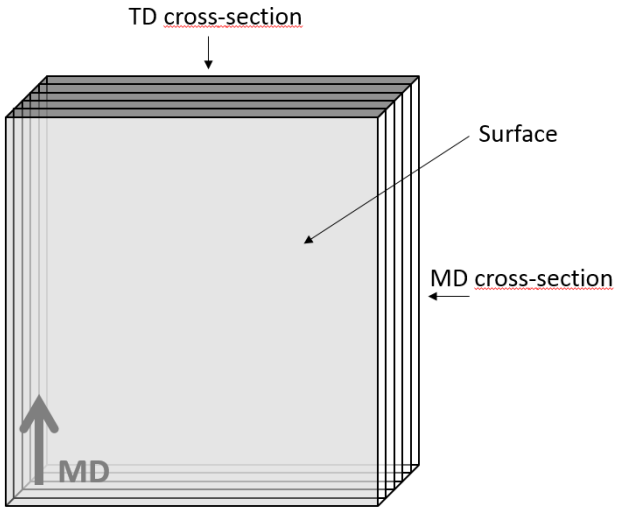

Figure 4.1: Sample preparation for x-ray powder diffraction. 32 pieces cut from the MD stretched sample were glued to a layered cube of a thickness of about 5 mm. The layered sample was then cut along MD and TD to reveal clean surfaces for X-ray analysis. The surfaces were named MD and TD cross-section respectively. The initial stretching direction (MD) is indicated in the lower left.

X-ray powder diffraction was carried out on a Bruker D8 Advance instrument in Bragg−Brentano mode with Cu Kα radiation (1.54 Å; 40 kV and 40 mA) using a PMMA sample holder rings with 8.5 mm height. All samples were investigated in the range from 5 to 90° 2θ with a step size of 0.01° 2θ with a counting time of 0.6 s. Rietveld refinement with the program package TOPAS 4.2 from Bruker was performed to determine the average crystallite size, micro strain and the lattice parameters. For each Rietveld refinement, the instrumental correction as determined with a standard powder sample LaB_6 from NIST (National Institute of Standards and Technology) as standard reference material (SRM 660b; a(LaB_6) = 4.15689 Å) was taken into account. For the refinement a CIF-structure of polyethylene from the Cambridge Crystallographic Data Centre (#QILHUO01) was used.

A texture coefficient TC was calculated using the peak intensity of the hkl planes for each sample using the relationship defined by Barret and Massalski[23-24] given in equation 4.1.

$$TC_{(hkl)} = \frac{I_{(hk)}}{I^0_{(hkl)} \cdot n^{-1} \sum \frac{I_{(hkl)}}{I^0_{(hkl)}}} \qquad 4.1$$

$I_{(hkl)}$ is the experimental intensity of diffraction peak of the given hkl plane, $I^0_{(hkl)}$ represents the intensity of the peak of a non texturized sample and n is the number of diffraction peaks used for this calculation. In this study 18 hkl-planes were used which are summarized in Table 4.3.

Table 4.3: hkl planes used for TC calculation; relative intensity shown for a non-texturized HDPE sample from the Cambridge Crystallographic Data Centre (#QILHUO01).

hkl-plane	2-Theta [°]	Relative Intensity [%]
110	21.639	100
200	24.036	34.3
210	30.175	1.3
020	36.420	4.3
120	38.460	0.4
011	39.975	1.9
310	40.878	5.2
111	41.862	0.9
201	43.241	1.8
220	44.107	2.7
211	47.176	1.4
400	49.214	0.7
320	52.439	0.7
121	53.261	2.9
311	55.159	1.8
031	67.926	0.7
231	73.199	0.7
002	74.758	0.3

4.3 BRÜCKNER TECHNOLOGY CENTER

The Technology Center of Brückner is used extensively for the development of new film types and/or the improvement of existing film technologies. Apart from the wide range of methods used for the characterization of films and material types in the In-house film/chemical laboratory, the main development is focused around the fully equipped pilot line that is also used extensively by external companies. In addition to the pilot line, a smaller second line was installed in 2014 that can produce monoaxially oriented films. For many applications, first experiments can be done on Brückners proprietary laboratory stretching machine KARO IV which is a quick and cost-efficient alternative to the pilot line.

4.3.1 PILOT LINE

The Pilot line is at the core of Brückners R&D activities as it enables the production of all film types in a wide variety of processes. Trials on this line are usually the last step towards a full-scale production line. The line is equipped with several extrusion systems, casting units, machine direction orientation device (MDO), transverse direction orientation device (TDO) that can also work in simultaneous mode (LISIM®, Linear Motor Simultaneous Stretching), pull-roll and winding rolls. For battery separator film a twin-screw extrusion system is generally used to maximize homogeneity of the polymer-solvent mixture. The MDO is equipped with six pre-heating rolls, four stretching rolls (stretching is achieved by roll speed difference in a defined gap) and two annealing rolls. In the TDO the film edges are fixed into clips, which are driven apart in a customizable profile along the TDO. When simultaneous stretching is preferred clips will also be driven apart in MD direction using Brückners patented LISIM® technology. Temperatures can be adjusted in each of the nine zones and are typically grouped into pre-heating, stretching and annealing zones. The pull-roll is equipped with automatic thickness measuring systems (beta-ray or x-ray) and typical post treatments (corona treatment, flame treatment, edge trimming, etc.) are available. A Picture of Brückners pilot line is shown in Figure 4.2.

Figure 4.2: Pilot Line in Brückners technology center. MDO (right) and TDO/LISIM® (left). Film direction from right to left.

General technical specifications of the pilot line are listed in Table 4.4.

Table 4.4: Technical specification of Brückners pilot line.

Parameter	Limits
Film type	Up to 7 layers
Extrusion[a]	BTS-75-34D
Dosing	Granules, Powder, Liquids
MDO Stretching gaps	1 - 3
MDO temperatures	RT – 150 °C
MDO roll width	670 mm
MDO number of rolls	12 (6 pre heat, 4 stretching, 2 annealing)
TDO speed	3 – 85 m/min
TDO length	15 m
TDO temperatures	Up to 260 °C
Max. Film width	1650 mm
Stretching mode	Sequential, simultaneous

[a] Used for battery separator membranes

4.3.2 LABORATORY LINE

To cope with the increased demand for R&D on the pilot line, Brückner installed a new laboratory line in 2014. It is equipped with two twin-screw and one single-screw extrusion systems and is able to process a wide range of common as well as development materials. Cast films can be processed in the MDO, containing five pre heating rolls, two stretching rolls and two annealing rolls. In contrast to the pilot line, TD stretching is not supported. The produced films can be stretched in TD on the KARO IV or on the pilot line in a roll-to-roll process. A picture of the laboratory line is shown in Figure 4.3.

Figure 4.3: Casting unit (left) and MDO (right) of the laboratory line.

Technical specifications are listed in Table 4.5.

Table 4.5: Technical specification of Brückners laboratory line.

Parameter	Limits
Film type	Up to 3 layers
Extrusion[a]	ZSE 40HP-56D
Dosing	Granules, Powder, Liquids
MDO Stretching gaps	1
MDO temperatures	RT – 170 °C
MDO roll width	350 mm
MDO number of rolls	9 (5 pre heat, 2 stretching, 2 annealing)
MDO speed	0,2 – 30 m/min
Stretching mode	monoaxial
Max. Film width	320 mm

[a] Used for battery separator film

4.3.3 LABORATORY STRETCHER (KARO IV)

The KARO IV is an invaluable tool for the development of new films and processes as it allows for quick and cost-efficient stretching of all film types in a wide range of parameters. It is therefore not only extensively used at Brückner but also in research facilities around the world[99]. The KARO IV is equipped with a tenter frame and, in its basic version, with two ovens for stretching and annealing respectively. Sample size, stretching ratio and speed as well as oven temperatures and heating times can be easily adjusted to fit the process.

Figure 4.4: Sample loading into the tenter frame (left), film after stretching (right).

Technical specifications are listed in Table 4.6.

Table 4.6: Technical specification of Brückners KARO IV.

Parameter	Limits
Sample thickness	20 – 4000 μm
Min. Sample dimension	90 mm x 90 mm
Stretching ratio	Up to 10 x 10
Stretching speed	5 – 500 mm/s
Operation temperature	RT – 400 °C
Stretching forces per axis	2000 N
Stretching mode	Sequential, simultaneous

4.4 SEPARATOR TEST METHODS

A range of specific separator tests have been widely adopted in the separator industry as the standard methods for characterization.

4.4.1 GURLEY

One of the most important specifications of a separator is its Gurley value, which describes the time in seconds needed for a specified volume (usually 100 ml) of air to flow through a circular separator sample with a diameter of 2,54 cm at a constant pressure of 1,22 kPa. The method is described in more detail in ISO 5636-5[100]. As such it is an of the diffusion resistivity against Li-Ions. Lower Gurley value usually means lower resistivity and therefore higher performance for the battery using such separator. Typical values in the industry range from 200 to 400 s at 100 ml.

4.4.2 POROSITY

Porosity is usually directly related to the Gurley value and it gives important information about the structure of the final separator. High porosity typically equals lower Gurley values at a potential loss in mechanical integrity. Porosity can be estimated by measuring the mass and thickness of a film sample of defined size and calculating the free volume in relation to the standard density of a particular material as given in equation 4.2.

$$\text{Porosity in } \% = \frac{m}{\rho \cdot A \cdot d} \cdot 100\ \% \qquad 4.2$$

In equation 4.2, m is the mass of the sample, ρ is the density of the base material, A is the area of the sample and d is the measured thickness.

4.4.3 SHRINKAGE

When exposed to excessive heat (i.e., due to malfunction) the separator has to continue to separate both electrodes from each other or otherwise there is a high risk of the battery catching fire or exploding. Shrinkage is defined as the reduction in size under heat and is typically measured in MD and TD direction separately. In the industry, various temperature and time spans are used for these tests. In this work, when not otherwise noted, samples of 100 mm x 100 mm were heated for 60 min at 105 °C.

5 RESULTS AND DISCUSSION

5.1 EVAPORE® LABORATORY METHOD

Development of the EVAPORE® process on a pilot line is very expensive and requires a large amount of resources and time. For that reason a scaled-down version of this process is preferred to quickly and accurately test different combinations of materials before using the pilot line to optimize process conditions and film parameters. A laboratory method was therefore developed and will be further outlined in this chapter.

5.1.1 METHOD OVERVIEW

The basis for the laboratory method is Brückner's KARO IV laboratory stretching machine (see 4.3.3). The difficulty in this approach is to generate proper cast film samples without using an expensive extrusion system.

For this a simple compression moulding was used. First a set amount of shredded or powdered polymer and solvent are sealed in a test tube under inert atmosphere and heated in an oil bath at a temperature higher than the melting point of the given polymer. After 30 minutes the test tube is removed and slowly cooled. The resulting sample then has to be carefully removed from the test tube, sometimes by breaking the test tube itself. Forming a sheet out of the solid sample is then done in a heat press using circular aluminum moulds with a diameter of 140 mm and depth of 700 μm. The heat press is heated to an appropriate temperature for the given polymer/solvent mixture. After 5 minutes the aluminum mould is removed and quickly submersed in cold water for 5 minutes. After the mould has cooled down it can be carefully opened to reveal the final formed sheet of 700 μm thickness. This sheet can then be used on the KARO IV stretching machine to produce stretched film samples.

5.1.2 KARO IV SEQUENTIAL STRETCHING

Stretching on the laboratory stretching machine was done sequentially. An HDPE (Alathon L5906) and Solvent 142 (Sunnyside) was used for the laboratory method as well as for the production of cast films. The solvent content was kept at 50 % for both laboratory method and pilot line production. Sheets prepared by the laboratory method as well as cast films from the pilot line were first stretched monoaxially. The stretched films were then taken out of the KARO IV labstretcher, cut down to proper size and stretched monoaxially in a direction perpendicular to the first stretching step. As the concept of machine direction does not apply to the laboratory method, samples produced in this way were stretched in an arbitrary direction at the first stretching step. For better comparison and naming consistency the first and second stretching direction for the laboratory samples are also designated as MD and TD respectively.

5.1.2.1 MD Stretching

MD stretching was done using similar parameters to the pilot line settings. A stretching temperature of 100 °C was used at a stretching speed of 100 %/s. The stretched film samples surface morphology were observed in a SEM. A comparison of pilot line and laboratory samples is shown in Figure 5.1.

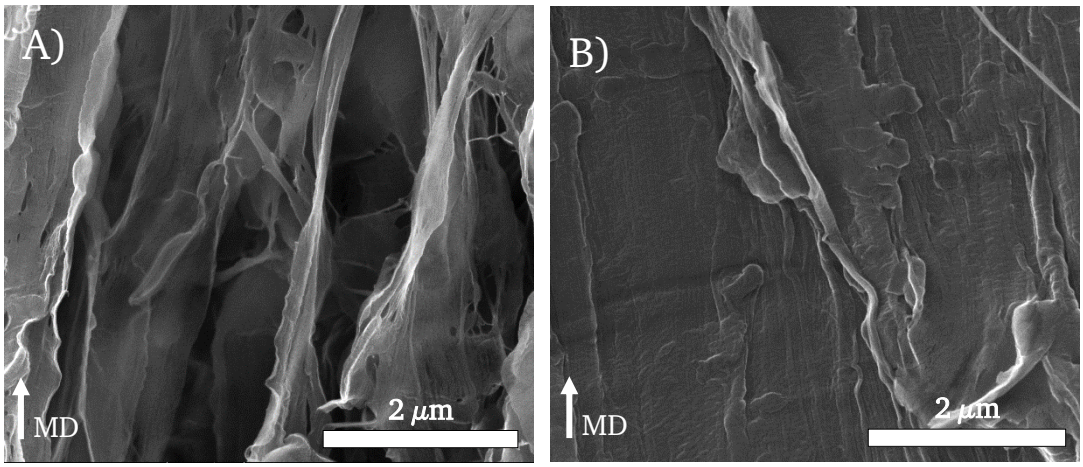

Figure 5.1: SEM Pictures of MD stretched film surface morphology without using a PET cover. MD ratio 5.5. A) Pilot line cast film; B) Laboratory scale cast film.

Due to the low solvent content of these stretched samples (19.5 % for laboratory scale samples; 14.6 % for the pilot line sample. Compared to approx. 40-45 % for a pilot MD film sample) additional stretching experiments were done using a PET cover on both sides of the cast film sheets to hinder the solvent from evaporation during

stretching. The PET covers were chosen with a thickness of about 100-250 μm each and stretched simultaneously to the samples covered within. The solvent content after stretching increased to the desired range of 40-45 %. Additionally with the PET covers in place the films were also annealed at a temperature of 120 °C without risk of solvent evaporation. SEM pictures of the resulting morphologies are shown in Figure 5.2.

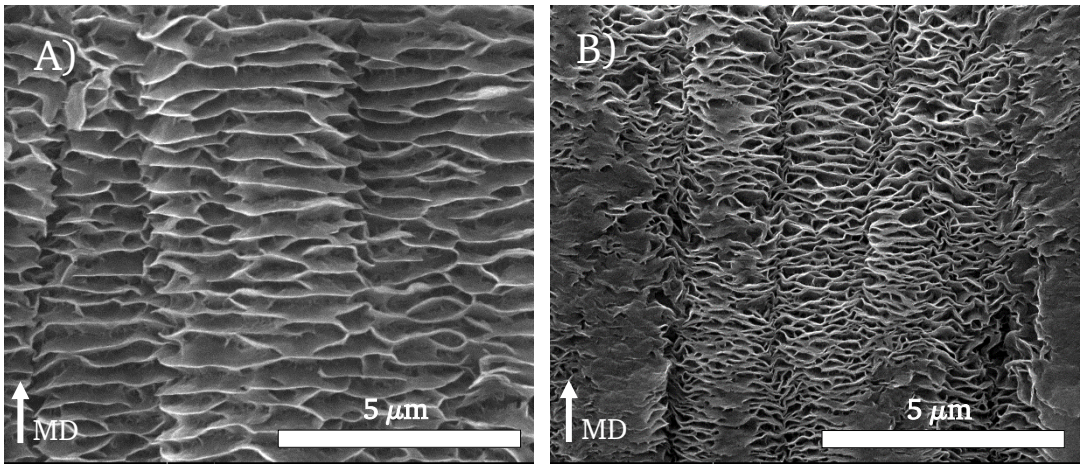

Figure 5.2: SEM pictures of MD stretched film surface morphology using a PET cover. MD ratio 5.5. A) Pilot line cast film (Annealing time 85 s); B) Laboratory scale cast film (Annealing time 60 s).

The pictures show highly crystalline stacked lamellar morphology (Shish-kebab structure) typical for uniaxially stretched and annealed samples[60, 76-78]. Crystal growth occurs laterally to the stretching direction.

Using the stretching experiments without PET cover the forces exerted onto the film during stretching were obtained. In Figure 5.3 the stress-strain curves for different MD ratios for both pilot line cast film and laboratory cast film are shown.

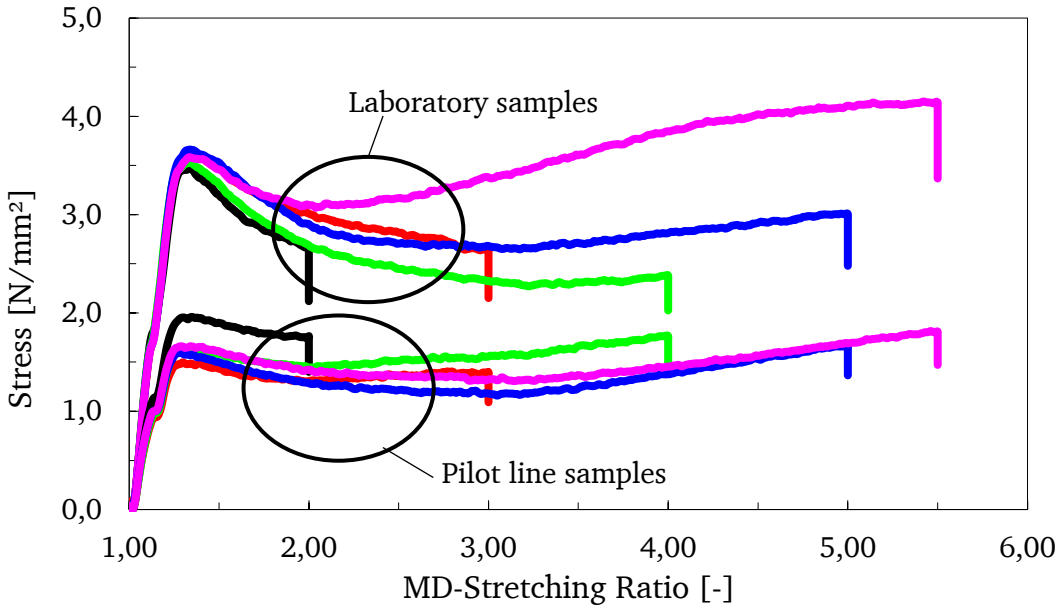

Figure 5.3: Stress-strain curves for pilot line and laboratory cast film for different MD ratios between 2.0 and 5.5.

Comparing pilot line and laboratory samples a distinct increase of stress needed for stretching can be observed for the laboratory samples (approx. 1.5 N/mm²). While the stress-strain curves for pilot line samples are relatively close with different ratios, a larger variation in stretching forces is visible for the laboratory samples.

5.1.2.2 TD Stretching

MD samples prepared from the previous step were taken out of the PET covers, cut back to proper dimensions and stretched at 70 °C in TD direction at 50 %/s. Due to the small size of the samples and machine limitations the samples could only be stretched to small ratios of 2.0. The resulting morphology was again analyzed in a SEM and is shown in Figure 5.4.

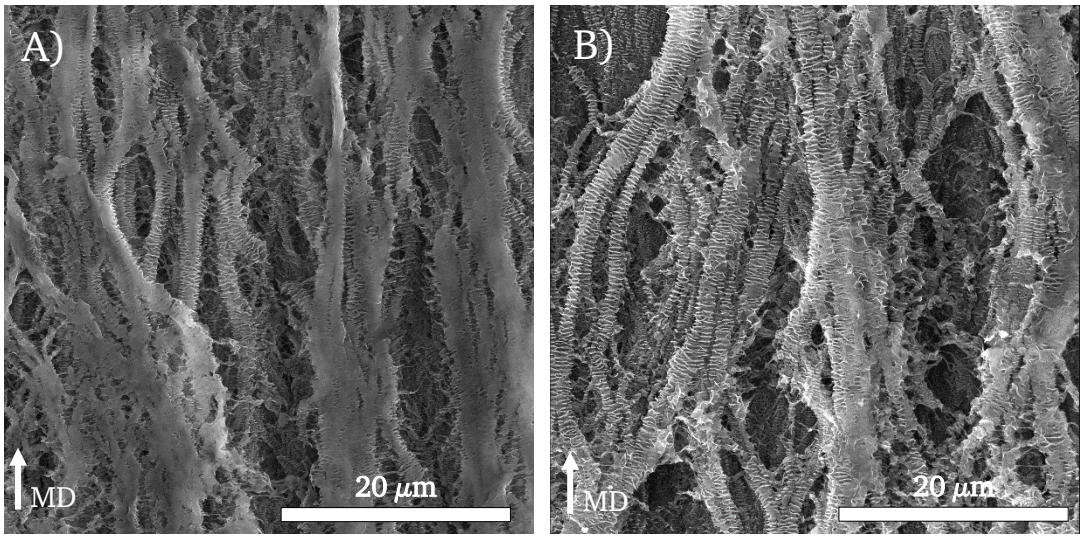

Figure 5.4: SEM pictures of TD stretched film surface morphology. TD ratio 2.0. A) Pilot line cast film; B) Laboratory scale cast film.

Both samples show the distinct stacked lamellar morphology that was slightly pulled apart during the TD stretching, creating pores in the process. While some of the lateral crystal structures (kebabs) have begun to unwind as a result of the stretching, many intact shish-kebab structures are still visible and easily distinguishable from each other. The Gurley value for these samples was also measured and values of 48 s for the pilot line sample and 34 s for the laboratory line sample were obtained.

5.1.3 DISCUSSION

Comparing pilot line and laboratory scale film samples, similar results and morphologies could be obtained. One of the difficulties in the beginning was the evaporation of solvent during the stretching procedure itself. MD stretching on the pilot line is done using heated rolls without the use of any additional air convection. With the KARO IV, however, stretching is done in a tenter frame and heated air is blown over the film to reach the desired stretching temperatures. As a side effect most of the solvent evaporates during the preheating step and also during stretching and annealing. Therefore PET covers were successfully used to retain a solvent level comparable to the pilot line. As can be seen from the SEM pictures of the MD stretched samples (Figure 5.1 and Figure 5.2) the higher amount of solvent in the film during stretching and annealing lead to a visibly more crystalline structure with a stacked lamellar morphology. This can be attributed to a lower melting point of the solvent rich polymer/solvent mixture compared to a solvent lean mixture. The larger size of

the lamellae for the pilot line sample can be attributed to the longer annealing time of 85 s compared to 60 s for the laboratory scale sample.

One of the main differences between pilot line and laboratory scale samples is the increased stress necessary for the laboratory films during stretching as shown in Figure 5.3. A reasonable explanation for this can be found in the orientation of the molecular chains in the cast film sheet itself. Extruding a polymer through a slit die, as it is done on the pilot line, generates shear forces that imparts orientation in MD direction which is subsequently frozen during cooling of the melt. While for the compression molded laboratory scale sample a certain orientation during the sheet forming process will certainly be imparted, it is much less anisotropic than for the extruded samples. A simple experiment was done to test the difference in orientation in regard to MD and TD direction. Pieces of cast film containing solvent were completely dried in an oven and the resulting shrinkage in MD and TD direction was measured. For the compression molded sample there is no distinction between MD and TD direction and the shrinkage was 18 % in two directions perpendicular to each other. For the pilot line cast film however shrinkage was observed at 28 % and 13 % for MD and TD direction respectively. This shows that there is a clear difference in orientation that cannot be overcome by compression molding. As a result of this orientation it is not unreasonable that stretching in MD direction requires less stress for a sample that is already pre-oriented in the same direction.

5.1.4 LIMITATIONS

Although this method works reasonable well and similar results can be obtained when comparing the stretched samples there still are some limitations. As there is no convection or shear used during the mixing/melting of the polymer/solvent mixture only a range of about 40-60 % solvent can be used or otherwise the mixture will be much less homogeneous. Still, without shearing the mixture will never be as homogeneous as with an extrusion system that is specially designed for mixing both component in a wide range of concentrations. This is mostly evident when comparing solvent content from a compression molded sample at different positions as shown in Figure 5.5.

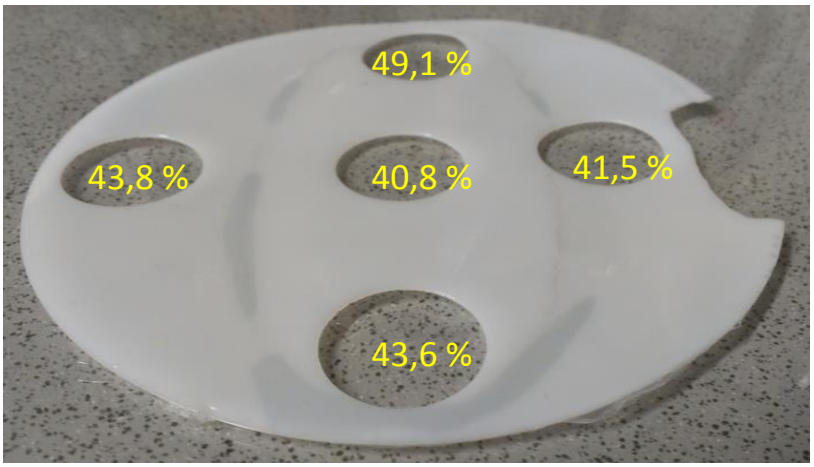

Figure 5.5: Solvent content at five positions of a compression molded sample.

Solvent content ranges between 40 and 49 % in this sample that was prepared with a mixture of 50 % solvent. For the given reason blending of different polymers is also impossible without mixing under shear.

5.1.5 CONCLUSION

With all its limitations, the results have shown that pilot line cast films and laboratory cast films behave similar during stretching and also show comparable morphologies. This method can therefore be used as a quick and low cost alternative to the pilot line. Stretching of solvent filled cast films was also made possible by using PET covers as a barrier for solvent evaporation. In this way extruded cast films either from the pilot line or similar extrusion lines can also be stretched.

5.2 PORE FORMATION

The KARO IV labstretching machine was used to further study the morphological changes in the film samples depending on the stretching conditions as well as their effect on final separator properties. For the morphological evaluation cast films produced on the pilot line were used. In addition MD film samples from the pilot line were TD stretched on the KARO IV machine and the formation of a porous morphology analyzed in a SEM. In the last part an in-depth analysis was done, to evaluate the effect of stretching conditions on final separator properties. By using two different cast films containing different UHMWPEs the effect of molecular weight was also investigated.

5.2.1 EFFECT OF MD STRETCHING CONDITIONS ON MORPHOLOGY

Stretching and annealing temperatures are key parameters for the EVAPORE® process to achieve sufficient porosity. Therefore, cast film samples, extruded with 50 % HDPE (Alathon L5906) and 50 % of Solvent 142, were taken from the pilot line and analyzed in a DSC. The resulting thermogram is shown in Figure 5.6. It is important to note that the actual cast film sample does not retain all of the used solvent and typically a solvent content of 45 % is achieved.

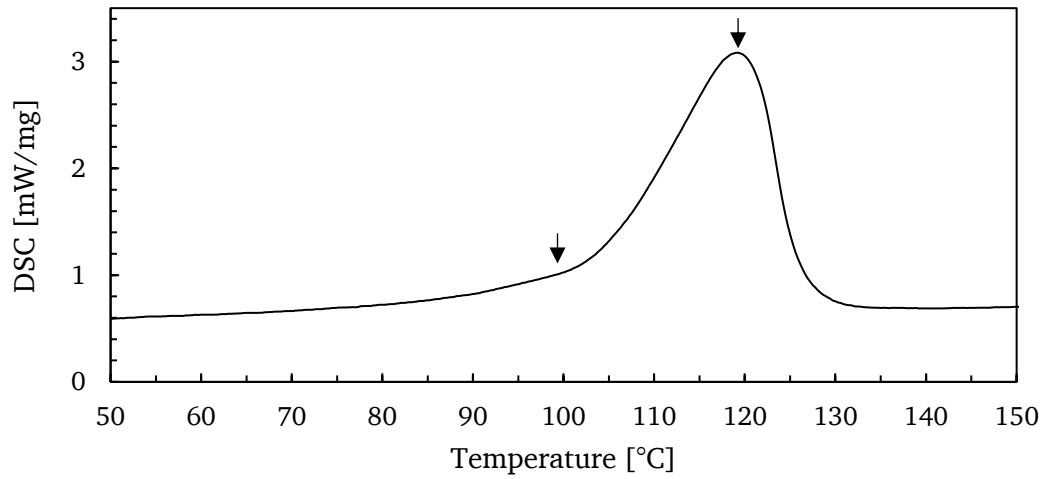

Figure 5.6: DSC thermogram of a cast film produced on the pilot line containing about 45 % of solvent. Heating rate 20 K/min. Base line is shown as a dotted line.

Compared to the melting point of pristine HDPE (137 °C) the melting point of a mixture of about 45 % solvent is shifted to 120 °C. The temperature of about 100 °C marks the onset of melting. These temperatures were then used for consecutive stretching trials, using two stretching temperatures (below and at the onset melting

temperature of 100 °C) as well as three different annealing temperatures ranging from below the onset melting temperature up to the actual melting temperature as indicated by the DSC result. The surface morphology of MD stretched samples prepared in this way are shown in Figure 5.7.

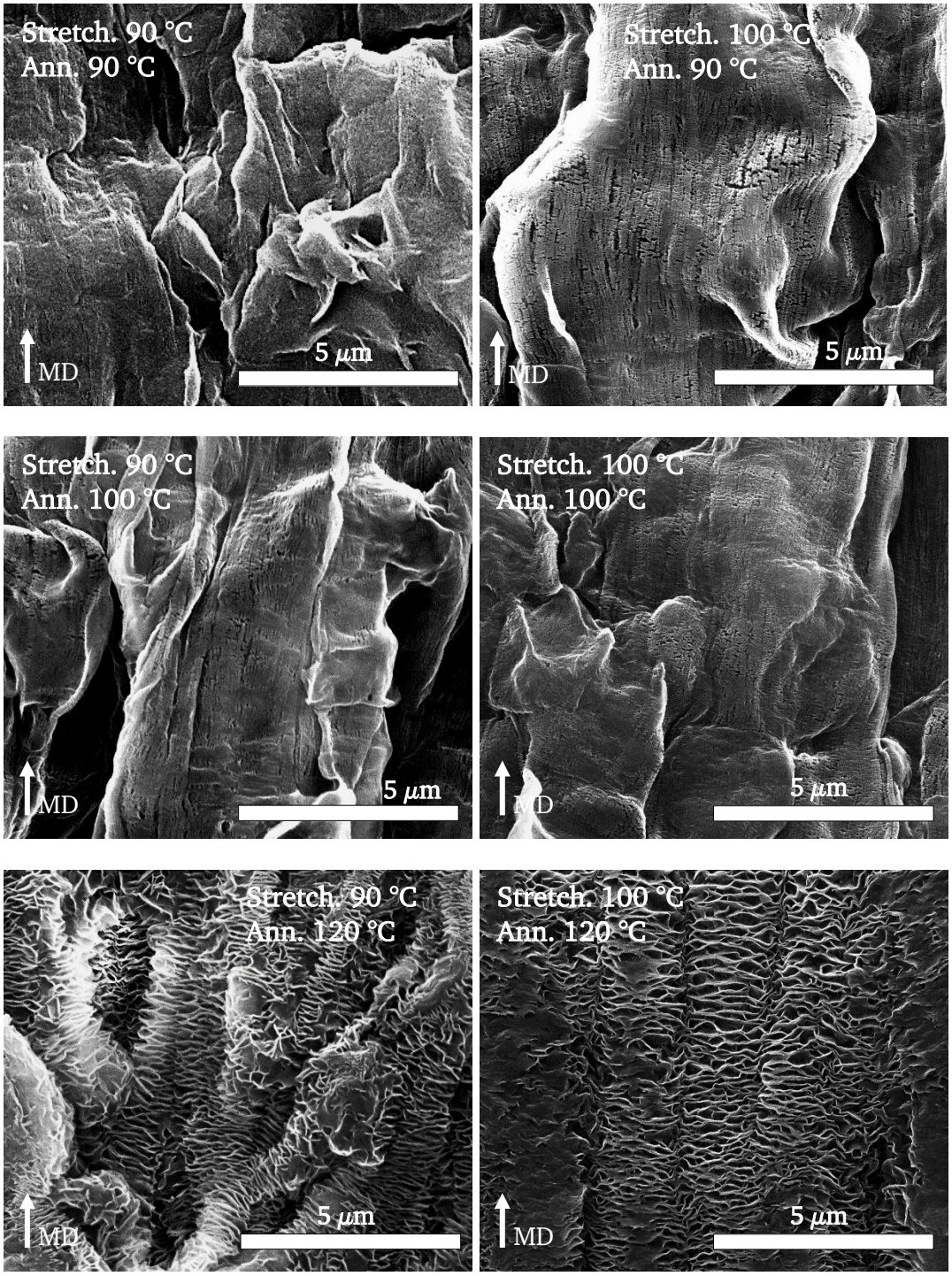

Figure 5.7: SEM images of MD films stretched and annealed at temperatures between 90 °C and 120 °C. Stretching Ratio 5.5. Annealing Time 60 s.

The SEM images indicate, that a higher stretching temperature of 100 °C leads to more evenly orientation of chains in the stretching direction, while a high annealing temperature of 120 °C leads to pronounced growth of lamellae, resulting in a shish-kebab morphology. As is known from literature, the development of a shish-kebab morphology is also dependent on molecular weight and strain rate[60, 76-78]. Figure 5.8 shows the surface morphology of MD stretched samples at different strain rates (expressed in MD ratio).

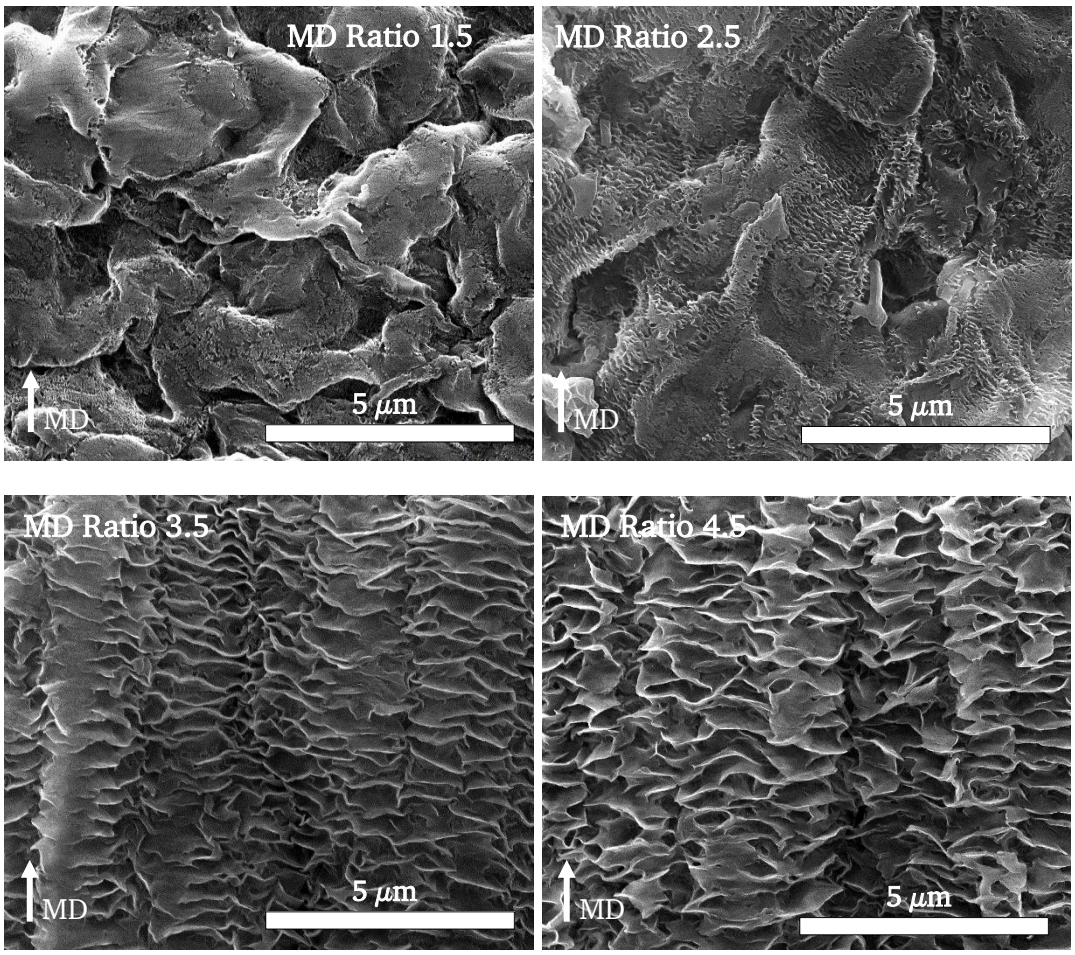

Figure 5.8: SEM images of MD films stretched at various stretching ratios between 1.5 and 5.5. Stretching Temperature 100 °C. Annealing Temperature 120 °C. Annealing Time 60s.

The SEM images show that stretching ratios below 3.5 do not lead to significant growth of a stacked lamellar structure. On the other hand, with a stretching ratio of 3.5 and higher a pronounced shish-kebab morphology is formed. The differences in stretching ratios of 3.5 and 4.5 seem negligible.

5.2.2 EFFECT OF TD RATIO ON SEPARATOR MORPHOLOGY

To study the pore formation process, MD samples from the pilot line, extruded with 50 % of Solvent 142 and 50 % of HDPE (Alathon L5906) were stretched in TD on the KARO IV machine at various stretching ratios. SEM images of these samples are shown in Figure 5.9.

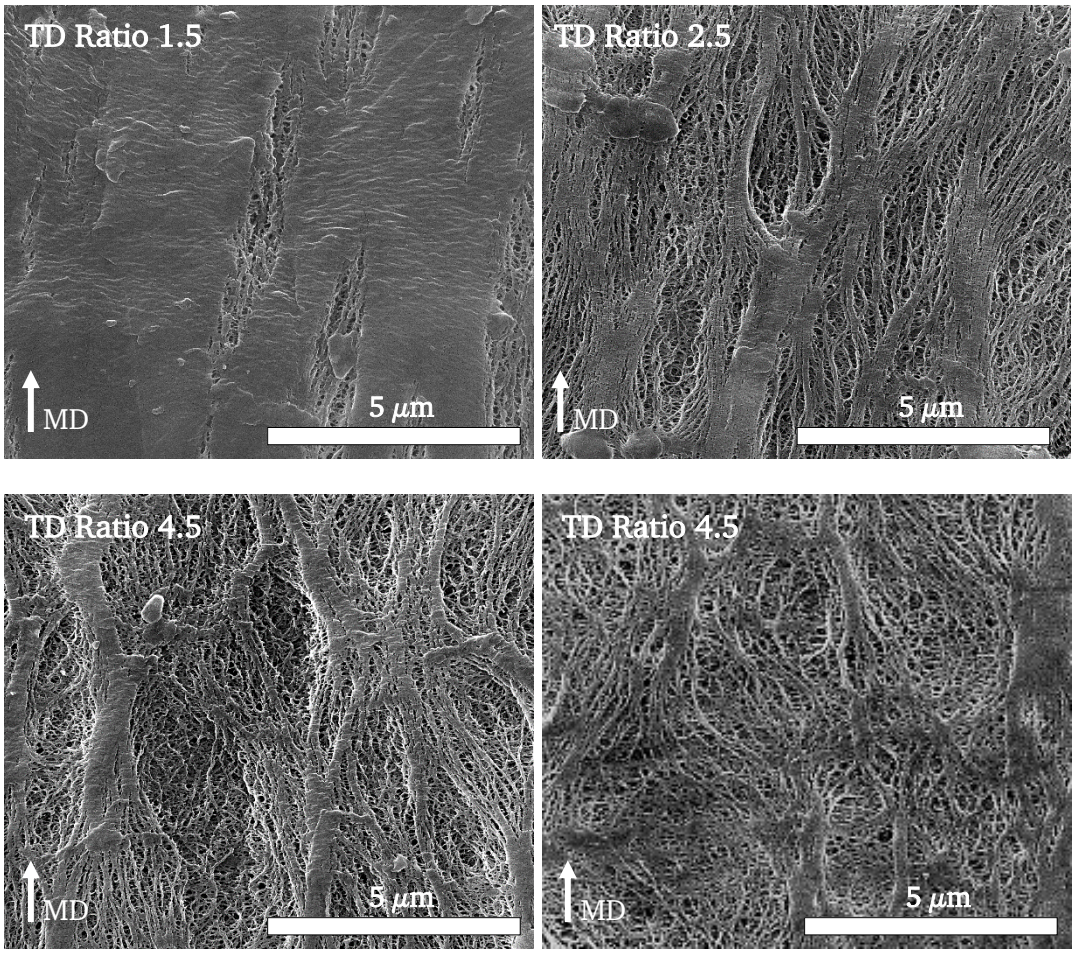

Figure 5.9: SEM images of TD films stretched at various stretching ratios between 1.5 and 4.5. Stretching Temperature 45 °C. Annealing Temperature 120 °C. Annealing Time 50 s. The MD film used was produced on the pilot line and stretched and annealed at about 100 °C.

With increasing stretching ratio, the dense surface of the MD film is changed into a porous network with strings of dense crystalline phases being pulled apart, fibrillating into smaller crystalline domains. While at a TD ratio of 1.5 the surface remains in large parts very dense, a stretching ratio of 2.5 is sufficient for the formation of many micro cracks which are eventually pulled apart at higher stretching ratios, leading to a more homogeneous network of pores.

With the TD stretching ratio having a pronounced effect on the surface porosity of the final separator film, it is expected that Gurley values will be affected as well. Therefore, Gurley measurements were done and the results are summarized in Figure 5.10.

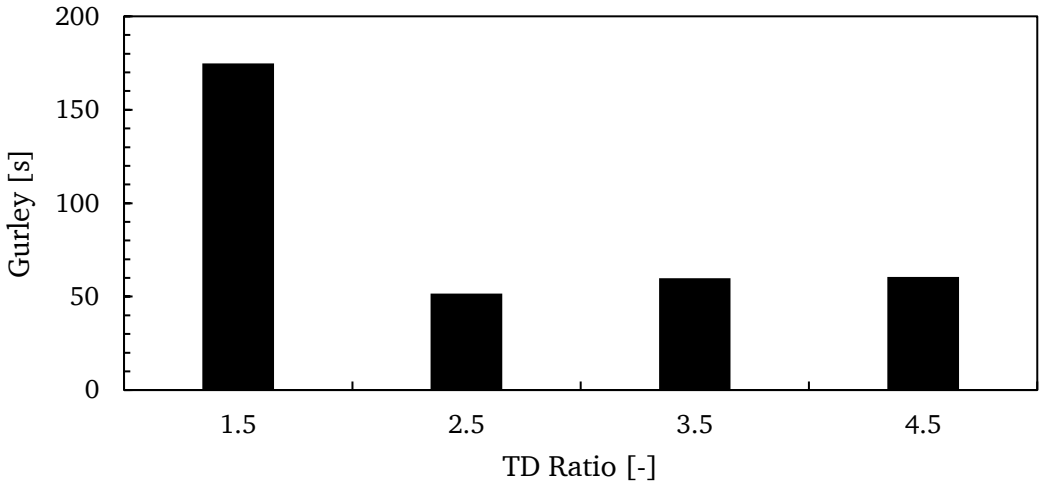

Figure 5.10: Gurley values for TD films stretched at various ratios between 1.5 and 4.5. Stretching Temperature 45 °C. Annealing Temperature 120 °C. Annealing Time 50s. The MD film used was produced on the pilot line and stretched and annealed at about 100 °C. Gurley measured with 10 ml.

A low TD stretching ratio leads to very high Gurley values of about 175 s for 10 ml of air, while 50-60 s can be achieved at stretching ratios ranging from 2.5 to 4.5, with no added benefit in Gurley values once a stretching ratio of 2.5 has been reached.

5.2.3 EFFECT OF MD STRETCHING CONDITIONS ON SEPARATOR PROPERTIES

Cast films from the laboratory line were used in conjunction with the KARO IV stretching machine to study the effect of MD annealing conditions on final separator film properties. By using two cast films made from different UHMWPE material grades, the effect of molecular weight was evaluated as well. The materials used were GUR4012 (1.8 Mio g/mol) and GUR2122 (5 Mio g/mol) and 65 % of SiSol D60 as a solvent to counter the increased viscosity of the materials. The UHMWPE was mixed with equal parts of a powdered HDPE (Asahi Sunfine SH800, 300.000 g/mol) before extrusion, leading to a total amount of 17.5 % of UHMWPE.

With different annealing conditions it is expected that crystalline growth is favored at higher temperatures. DSC analysis of dried MD stretched samples were used to determine the total crystallinity. The results are shown in Figure 5.11.

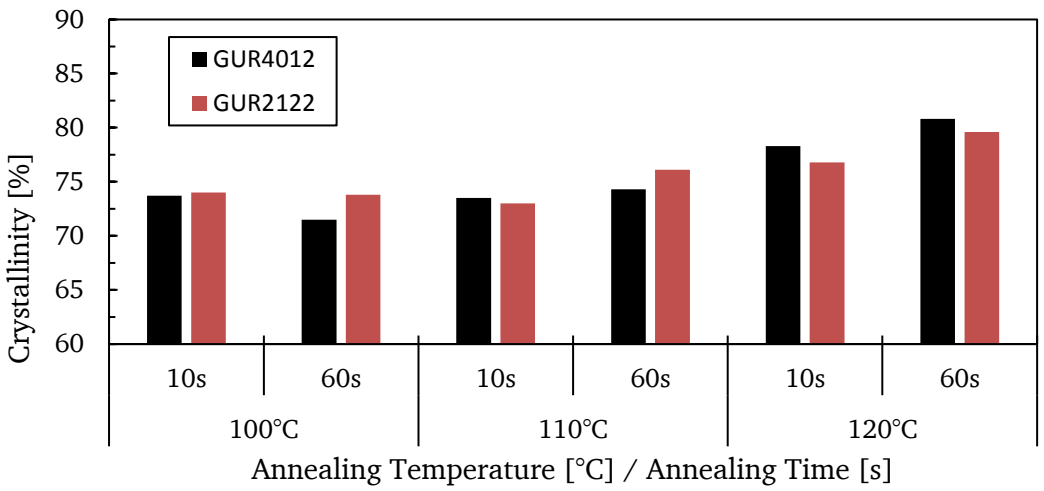

Figure 5.11: Crystallinity of MD stretched films produced by various MD annealing conditions.

The analysis reveals that higher crystallinity was achieved by using annealing temperatures of 120 °C leading to values ranging between 77 % and 81 %. At 100 °C and 110 °C crystallinity is slightly lower with values in the range of 71 % to 74 %, with the exception of GUR2122 that shows crystallinity of 76 % when annealed at 110 °C for 60 s. With the exception of high annealing temperatures, where GUR2122 shows slightly lower crystallinity, no significant difference can be found between both UHMWPE grades.

X-ray powder diffraction and texture analysis was carried out in collaboration with Prof. Dr. Epple and Dr. Prymak (Institute of Inorganic Chemistry at the University of Duisburg-Essen). The MD stretched samples annealed for 60 s were measured once from each of the respective sides, with one being the film surface and the other ones being cross-sections along MD and TD (see Figure 4.1). Figure 5.12 compares the diffractograms of each side using the example of a sample made of GUR4012 annealed at 100 °C.

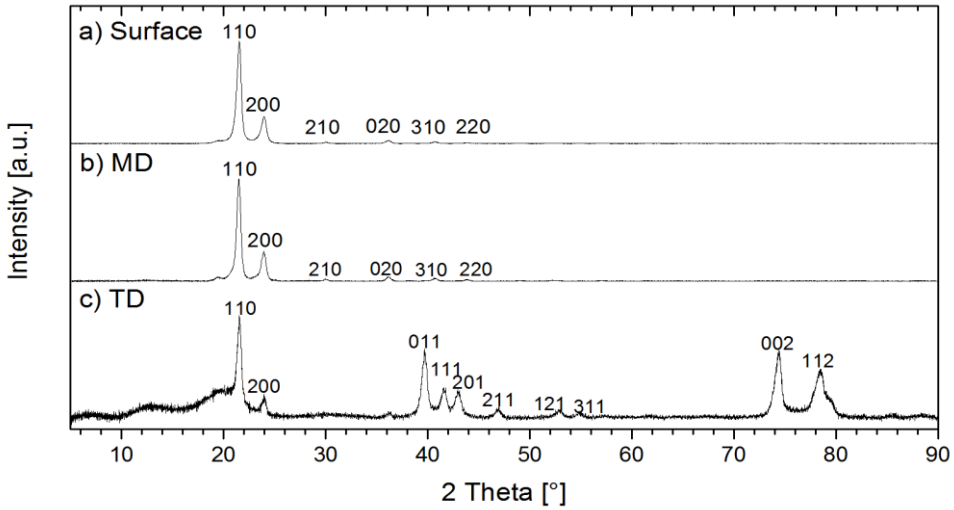

Figure 5.12: X-ray diffractograms of a sample containing GUR4012 measured from three different sides. The sample was stretched and annealed at 100 °C. The y-scaling was changed for easier comparison.

All samples show similar results, with nearly identical diffraction of the surface and MD cross-section and a distinct difference in diffraction for the TD cross-section, which lies perpendicular to the stretching direction. All spectra had been normalized to the intensity of the most prominent peak, and it is interesting to note, that the diffraction intensity was much lower for the TD cross-section as can be inferred from the low signal-to-noise ratio. The calculated lattice parameters also confirm a polyethylene crystal phase for all samples (see appendix 8.1). Using the same sample annealed at 100 °C, Figure 5.13 gives a comprehensive overview of the calculated texture coefficients (TC).

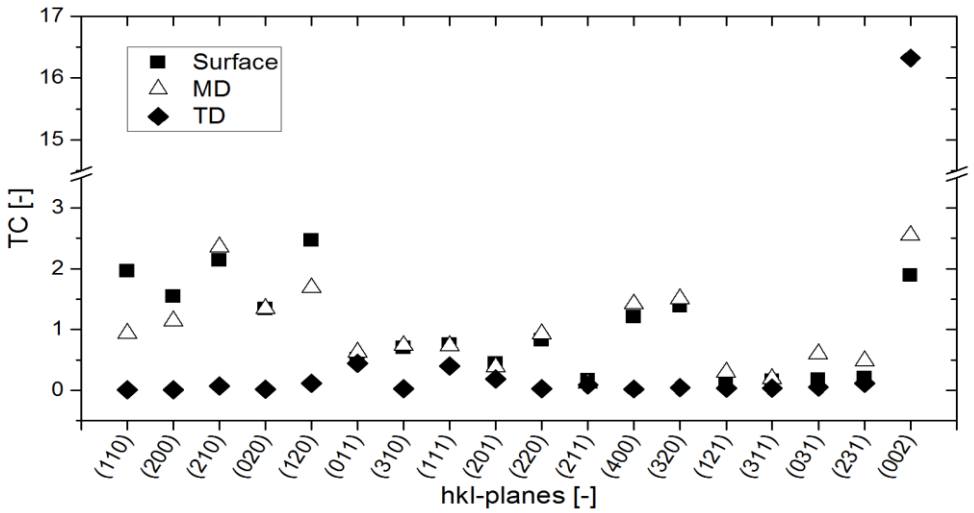

Figure 5.13: Comparison of calculated texture coefficients (TC) for sample containing GUR4012 measured from three different sides. The sample was stretched and annealed at 100 °C. A TC value of 1 indicates a non-texturized hkl plane.

The TC is a measure of the relative intensity of the diffraction of a hkl plane compared to a non-texturized sample, comprised of a randomly oriented crystalline phase. Therefore, a TC of 1 in a given hkl plane represents the absence of texture. The most striking information is the measurement along the TD cross-section, showing a TC of nearly 0 in all cases except for a few slightly higher TCs at (011), (111), (201) and most notably (002), which shows a very high value of 16.3. The TCs of the measurements along the surface and the MD cross-section are similar to each other and indicate hkl planes with reduced as well as increased texture. No specific hkl plane stands out when compared to the measurement along the TD cross-section. The TC of the (002) plane when measured along the TD cross-section is shown in Figure 5.14 and compares the different values to the annealing temperatures used during stretching.

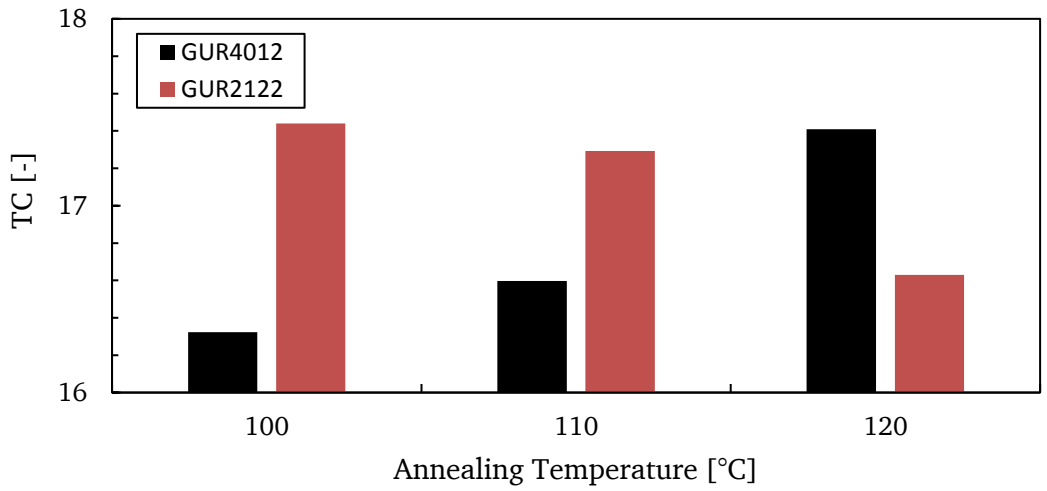

Figure 5.14: Comparison of texture coefficient of hkl-plane (002) for samples containing GUR4012 and GUR2122 annealed at various temperatures for 60 s.

A clear trend is obvious for both compositions. With GUR4012 an increase in TC from 16.3 to 17.4 is found, while the TC is reduced from 17.4 to 16.6 when using a composition containing GUR2122.

Two of the most important parameters concerning the performance of a battery separator are porosity and Gurley value. TD stretched separator samples were analyzed and the results are shown in Figure 5.15 and Figure 5.16.

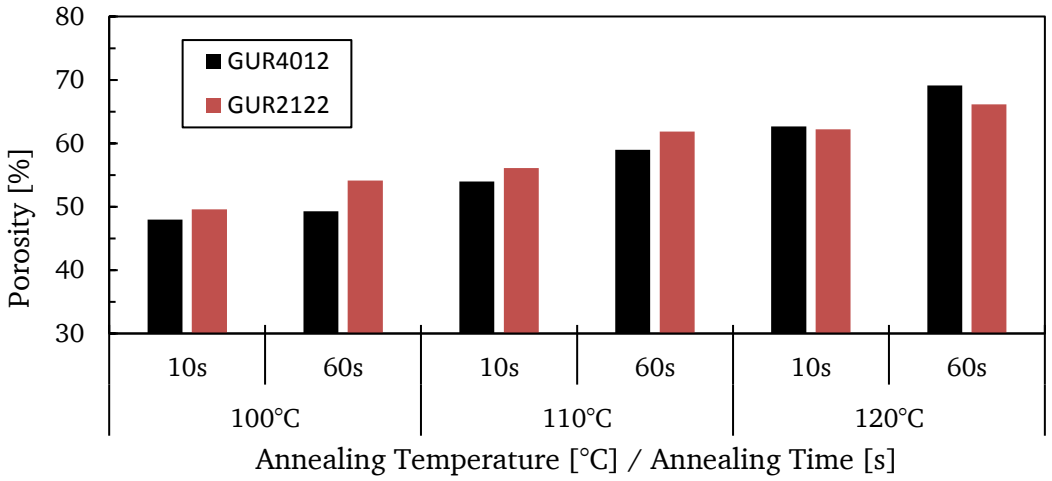

Figure 5.15: Porosity of separator samples of two different UHMWPE materials produced by varying MD annealing conditions.

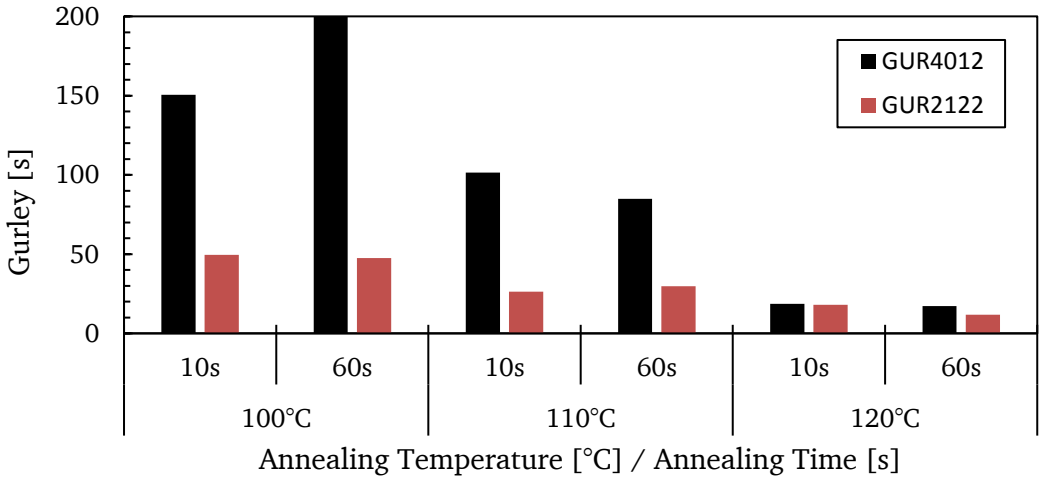

Figure 5.16: Gurley values of separator samples of two different UHMWPE materials produced by varying MD annealing conditions. Measurement was aborted when 200 s was not sufficient.

The porosity values in Figure 5.15 show a steady increase in porosity when the MD samples are annealed at higher temperatures ranging from 47 % to 63 % in the case of GUR4012 annealed for 10 s. In almost all cases, an increase in annealing time from 10 s to 60 s leads to an increase in porosity of 4-8 %. The results also indicate a slightly higher porosity for samples containing GUR2122, although this cannot be observed in all cases. The Gurley results mirror the obtained values from the porosity analysis, with lower Gurley values being achieved at higher annealing temperatures. For GUR4012 Gurley values range from 150 s to 19 s when annealed for 10 s. However, in contrast to the porosity results, annealing time does not have a significant effect on Gurley values. Comparing both materials, lower Gurley values were achieved with GUR2122 in all cases.

5.2.4 DISCUSSION

The SEM analysis has shown that careful consideration has to be done when deciding MD stretching and annealing temperatures. As seen from Figure 5.6 and Figure 5.7 the stretching temperature should be at least as high as the onset melting temperature to achieve sufficient homogeneous orientation of the molecular chains. At this temperature, marked as the beginning of melting of the smaller crystalline domains, viscosity is lowered and chain mobility is increased, allowing for easier stretching as well as reorientation of the crystalline phase. In this way, stretched chains will bundle up and form nuclei (shish) on which further crystalline growth (kebab) can occur during annealing, leading to a shish-kebab morphology. The extent of lamellar growth is dependent on the annealing temperature, with only little growth visible at the onset melting temperature. With higher temperatures up until the melting point, more energy is available for melting and recrystallization of smaller crystals, leading to pronounced growth of a stacked-lamellar morphology. As the melting point of the polymer/solvent mixture is reduced with increasing solvent content, careful consideration has to be taken when deciding stretching and annealing temperatures at a given material combination. Stretching ratio is another important aspect to consider, as sufficient orientation and subsequent lamellar growth is necessary for the pore formation process as well as for high mechanical strength in machine direction. Figure 5.8 shows that a stretching ratio of 3.5 and higher is necessary for sufficient orientation and crystalline growth. This is in line with the accepted theory of shish-kebab formation[60, 76-78], which describes a critical strain needed for the formation of shish. The reasoning behind this is, that relaxation of the molecular chains work against the orientation of the chains and therefore high enough strain is needed to compensate for the relaxation phenomenon. Consequently, the strain threshold can be lowered by using higher molecular weight materials, as relaxation proves more difficult due to the increased viscosity.

The data from the XRD analysis as shown in Figure 5.12 proves a pronounced orientation of the crystalline phase. First it is important to note from that the increase in diffraction intensity along the TD cross-section applies only in hkl-planes having a component of the c-axis of the polyethylene unit cell, which is also the chain direction of polyethylene as given in Figure 5.17.

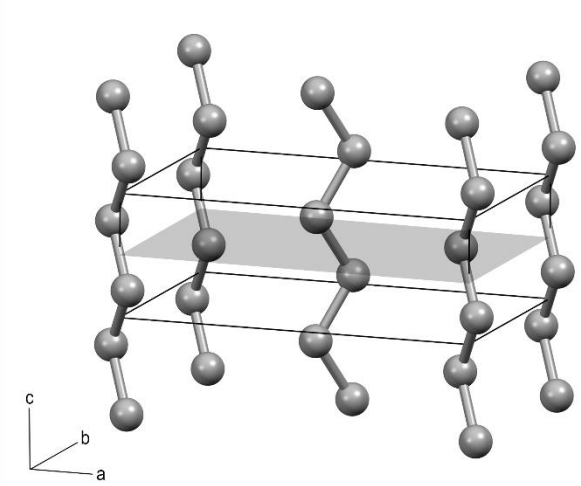

Figure 5.17: Unit cell of polyethylene. The shaded area represents the hkl-plane (002).

In other words, the direction perpendicular to the TD cross-section, in this case the stretching direction, aligns with the c-direction of the elemental cell, which equals the direction of the polyethylene chain backbone (compare Figure 4.1 and Figure 5.17). The texture coefficient of the (002) plane, which lies in the same plane as the TD cross-section, therefore represents the extent of the alignment of chains parallel to the stretching direction. As explained before, the polyethylene with higher molecular weight is expected to have increased orientation as the higher viscosity allows for less chain relaxation during stretching and annealing. As seen from Figure 5.14, that is indeed the case at annealing temperatures between 100 and 110 °C, but changes significantly at 120 °C. While the texture coefficient of the sample comprised of GUR4012 is steadily increasing due to a higher fraction of polyethylene crystallizing along the stretching direction, it is supposed that the high temperature is sufficient for the relaxation of the build-up stress in the composition using GUR2122, leading to a reduction in number of nucleation sites. Combined with the lower chain mobility, crystallinity as well as chain orientation are consequently lower when using GUR2122 annealed at a temperature of 120 °C for 60 s.

During TD stretching, as seen in Figure 5.9, the crystalline phase is pulled apart and the network formation propagates through the sample due to the formation of micro cracks. Initially, the MD sample shows a dense surface with few micro cracks visible at a low stretching ratio of 1.5 and pronounced pore formation at ratios at 2.5 and above. Consequently, air permeability, measured in terms of the Gurley value, is increased with increasing surface porosity of the samples. With increasing stretching ratio, the Gurley value only changes slightly while the network becomes more homogeneous due

to the continued deformation of the crystalline phase. The deformation is shown in more detail in Figure 5.18 on the example of a UHMWPE sample that was annealed at 120 °C during MD stretching.

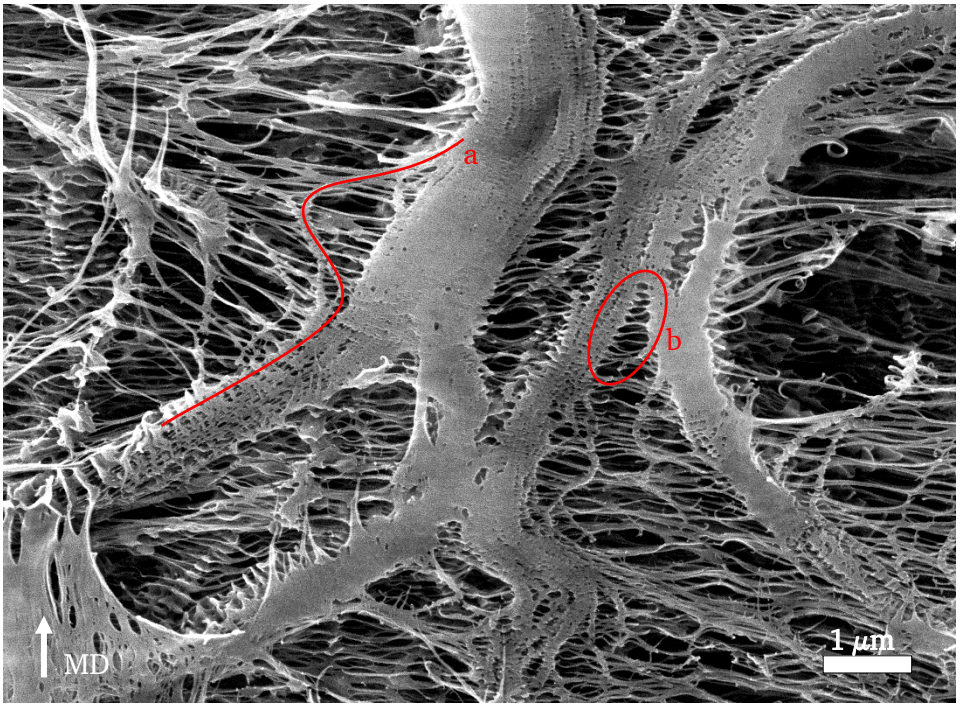

Figure 5.18: SEM image of a TD stretched UHMWPE sample showing the deformation of the shish-kebab morphology. TD stretching ratio 4.5. During the MD stretching the sample was annealed at 120 °C. a) Shish being pulled apart from a shish bundle. b) Unwinding and network formation of kebab crystals.

The SEM image shows a bundle of oriented chains (crystalline shish) being pulled apart due to the process of TD stretching. As stress is imparted into the material, crystal bundles will form micro cracks as individual shish or shish bundles are pulled apart from the crystalline phase (a). The lamellar overgrowths (kebabs) that generally cover a bundle of shish are unwound to cover the void created by micro crack formation (b), thus creating a network of smaller pores. Deformation of a crystalline phase in such a way is heavily dependent on crystalline thickness as well as the amount of crystallization defects. Therefore, annealing conditions during MD stretching play an important role in the overall network formation, with a much coarser morphology formed at higher annealing temperatures as evident by comparing Figure 5.18 (Annealing Temperature 120 °C) and Figure 5.9 (Annealing Temperature 102 °C). The same conclusion can be drawn from the results presented in Figure 5.11 to Figure 5.16, as a high annealing temperature leads to increased crystallinity and in turn to higher porosity and significantly reduced Gurley values. Generally, it is observed that an

increase in annealing temperature and chain orientation leads to increased porosity and decreased Gurley values, which is in line with the results presented above. As a result of increased chain orientation in machine direction, it is probable that stress imparted during TD stretching is increasingly aligned perpendicular to the oriented chains, leading to higher probability for micro crack formation which is the essential precondition for pore formation. In the case of less oriented samples, some of the stress is redirected along the chain backbone of the crystals depending on the angle between oriented chains and transverse stretching direction. Consequently, a higher porosity and lower Gurley values are achieved using GUR2122 compared to GUR4012.

5.2.5 CONCLUSION

Stretching and annealing conditions during the MD orientation step of the EVAPORE® process is a key aspect controlling the formation of a porous network. The temperatures need to be carefully tuned to fit the material combination as melting point of the mixture can be shifted by varying solvent content. For a standard mixture of 50 % Solvent and 50 % HDPE (extrusion settings), a stretching temperature of at least 100 °C, which marks the onset of melting, is recommended to achieve sufficient crystal orientation. Annealing temperature can then be varied between the onset of melting up to the melting temperature itself, with increasing porosity and lower Gurley values at higher temperatures. However, a coarser surface morphology, as achieved by higher annealing temperatures, is detrimental for the application in a Li-ion battery, where separators should be as homogeneous as possible. Therefore, careful consideration is needed when deciding annealing conditions. Incidentally, the empirically found process window used on the pilot line mirrors the findings from this study. Stretching temperature of about 100 °C and an annealing temperature of 102 °C is used to produce a separator that has good air permeability as well as a fine homogeneous surface morphology. The results presented in this chapter therefore help to substantiate and deepen the understanding of the effect of stretching conditions on the formation of a porous network.

5.3 MATERIAL EVALUATION

Battery separators for EV applications have higher thermal stability requirements than for 3C (Consumer, Communication, Computer) applications. Typical separator made from high density polyethylene do not fit these criteria. The current state of the art describes a refinement process by coating the separator with organic or inorganic layers of 1-3 μm thickness. Shrinkage of the separator can be reduced to below 1 %, even at temperatures higher than the melting point of polyethylene of 137 °C. Unfortunately, this requires another process step that increases cost and adds complexity to the production process. A different approach would be to use a thermally more stable material than HDPE. Several separators are already available on the market made out of PP or PVDF to increase thermal properties, yet the melting point of PP (167 °C) and PVDF (176 °C) still not fit the requirements (see chapter 3). For that reason, one of the aims of this work is the evaluation of high temperature polymers for use with the EVAPORE® process. A wide range of polymers were chosen based on their melting points, and non-porous cast- and stretched films were used for laboratory screening tests. Table 5.1 gives an overview of the materials used in this study.

Table 5.1: Overview of materials tested for chemical compatibility with electrolyte.

Material	Acronym	Manufacturer[a]	T_m[b] [°C]	T_g [°C]
Polyethylenterephthalate	PET	Invista	255	80
Polybutylenterephthalate	PBT		225	60
Polyethylennaphthalat	PEN		265	120
Poly (Ethylene Vinyl Alcohol)	EVOH		various	various
Polyvinyl Alcohol	PVOH		200	85
Polycarbonate	PC		-	150
Poly (Methyl Methacrylate)	PMMA	Lipp Terler	-	100

[a] Samples received from Brückners internal portfolio. Manufacturer given when available.
[b] Melting Temperature of crystalline phase

Table 5.1: Overview of materials tested for chemical compatibility with electrolyte. (continued)

Material	Acronym	Manufacturer[a]	T_m[b] [°C]	T_g [°C]
Polyoxymethylene	POM		175	-
Polyetheretherketone	PEEK	Lipp Terler	335	143
Polyethersulfone	PES	Lipp Terler	-	220
Polysulfone	PSU	Lipp Terler	-	185
Polyphenylene Sulfide	PPS	Lipp Terler	285	85
Polyamide 6	PA6		220	50
Polyimide	PI	Kaneka	-	360
Polyetherimide	PEI	Lipp Terler	-	217
Poly (Fluorinated Ethylene Propylene)	FEP	DuPont	258	60
Poly (Ethylene Tetrafluoroethylene)	ETFE	DuPont	267	-100
Cyclic Olefin Copolymer	COC	Topas Advanced Polymers	-	various
Polymethylpentene	PMP	Mitsui Chemicals	245	50

[a] Samples received from Brückners internal portfolio. Manufacturer given when available.
[b] Melting Temperature of crystalline phase

5.3.1 ELECTROLYTE COMPATIBILITY

One necessary requirement of the material is stability and compatibility with typical electrolytes currently used in Li-ion battery cells. To test the compatibility of the polymers, film samples were soaked in electrolyte at 60 °C for one day and seven days. The electrolyte used was LP71 from BASF and contained a mixture of Dimethyl Carbonate (DMC), Diethyl Carbonate (DEC) and Ethylene Carbonate (EC) in a ratio of 1:1:1 with 1 M of Lithium Hexafluorophosphate ($LiPF_6$) as the conducting agent. The polymer samples were inspected for mass, IR spectra, visual appearance and tensile strength.

For some samples further characterization was not possible as they either dissolved in the electrolyte or became very brittle after soaking. The dissolved polymers include PSU, PES, PMMA, PA6 and in some extent PC. POM strips on the other hand became very brittle after the soaking experiment and broke into multiple parts.

5.3.1.1 Swelling

Mass of the samples was measured in the swollen state directly after the soaking experiment and again after an additional washing and drying step. Ethanol was used as a washing agent. Swelling of cast films is presented in Figure 5.19.

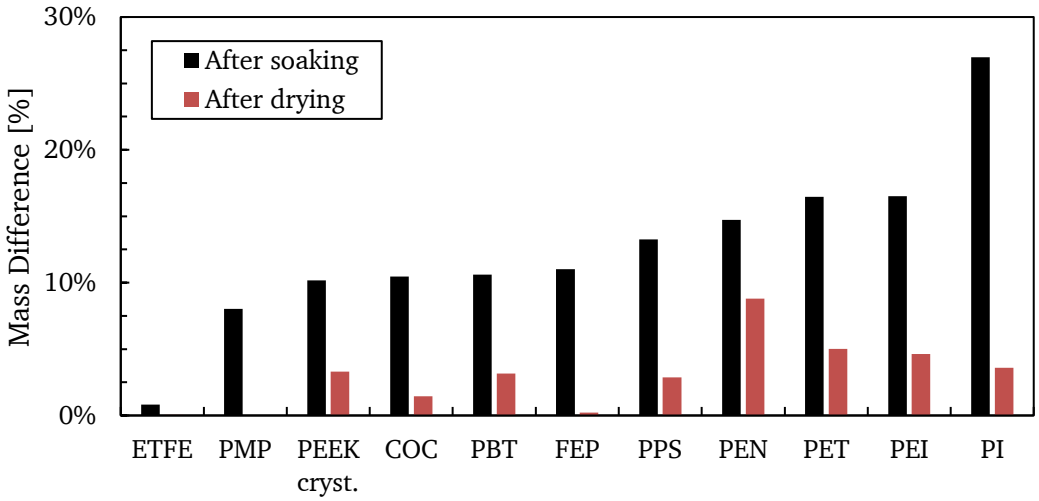

Figure 5.19: Mass difference of cast films stored in LP71 for 7 days at 60 °C.

As can be expected, swelling is lowest for hydrophobic materials ETFE, PMP, COC and FEP which show a swelling of up to 11 % and a total mass change after drying of lower than 2 %. ETFE shows the best result and is nearly unaffected by the treatment. Similar swelling at higher mass change after drying is exhibited by PEEK, PBT and PPS. With these materials, weight increases by approx. 3 %. Higher swelling of 16 % and mass increase of 9 % and 5 % can be seen for PEN and PET respectively. PI shows similar results to PET with 16 % swelling and 5 % mass change. With PI the swelling is as high as 27 %.

The same experiment was repeated with stretched samples when available. The results are summarized in Figure 5.20.

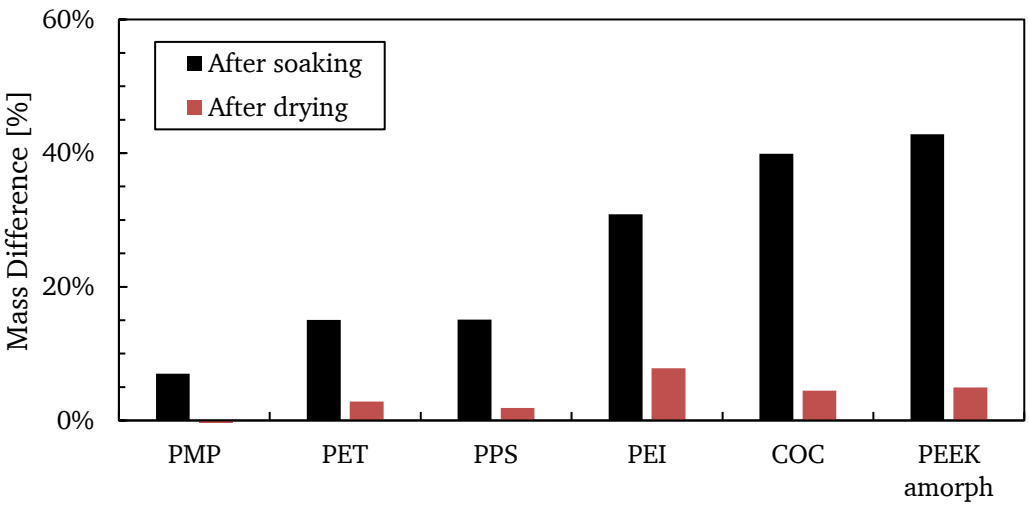

Figure 5.20: Mass difference of stretched films stored in LP71 for 7 days at 60 °C.

Results are similar for stretched films compared to cast films, with PMP showing the lowest swelling at 7 % and virtually no weight difference after drying. PET and PPS exhibit similar intake of LP71 at 15 %, although mass difference is lower than for cast films (e.g. PET cast film 5 %; PET stretched film 3 %). PEI and COC show increased swelling as well as increased mass after drying compared to the respective cast films. Surprisingly, COC swelling increased by a factor of 4 compared to cast film. Finally, amorphous PEEK is swelling significantly more than the highly crystalline cast film.

5.3.1.2 ATR-FTIR Analysis

Infrared analysis was used to characterize polymer samples prior and after treatment in LP71 at 60 °C. Comparing the results from treated samples with pristine ones, additional peaks could only be observed for PEEK (1560 cm^{-1}), PEN (1808, 1774, 1476, 1003 cm^{-1}), PET (1808, 1774, 1476, 972 cm^{-1}), and PES/PSU (1807, 1774, 1744, 1074, 968 cm^{-1}). For example, Figure 5.21 and Figure 5.22 show the IR spectra for PEN and PSU respectively.

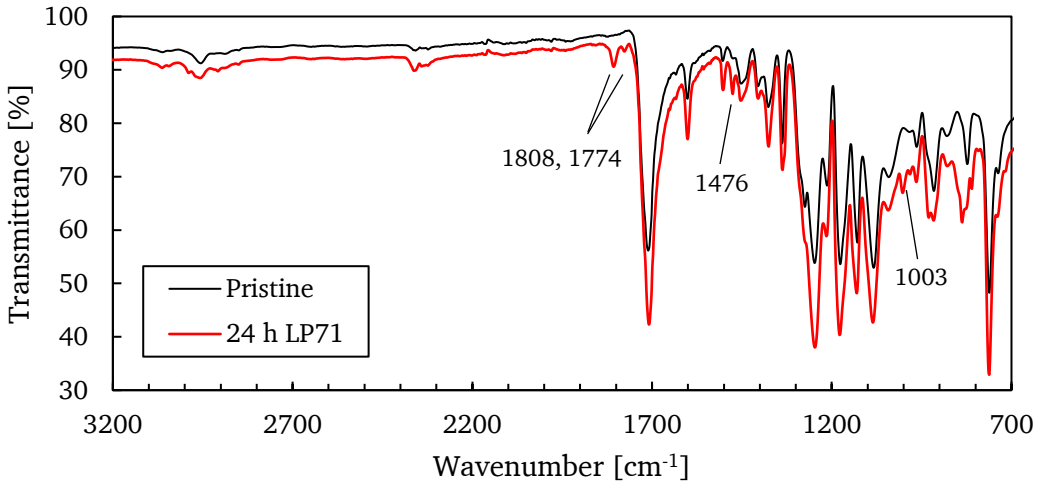

Figure 5.21: ATR-FTIR Spectra of PEN before and after submersion in LP71 for 24 h at 60 °C.

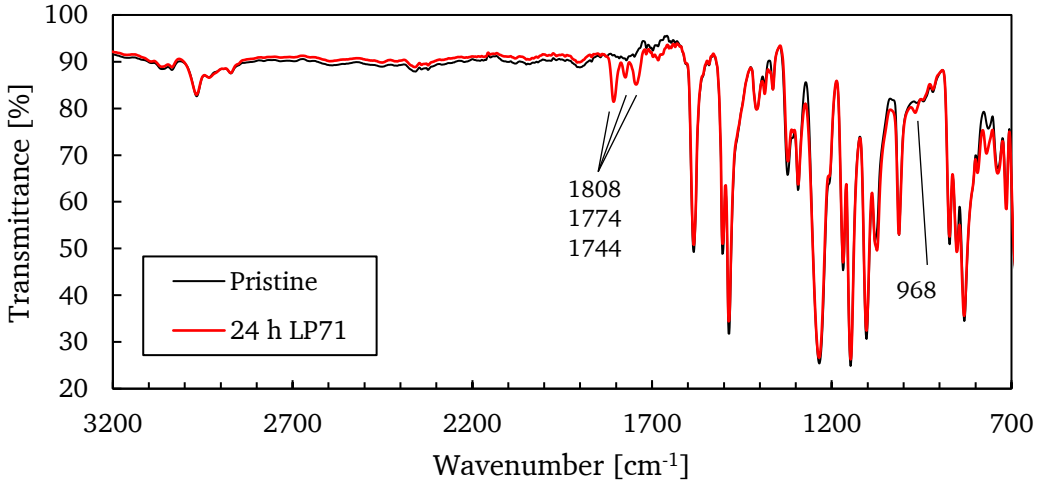

Figure 5.22: ATR-FTIR Spectra of PSU before and after submersion in LP71 for 24 h at 60 °C.

Generally, the intensities of the additional signals were very weak. For PES and PSU, however, higher intensities of the bands from 1700-1800 cm could be observed. The results were similar with 24 h and 7 days submersion as well as between cast films and stretched films. IR spectra comparing pristine and 24 h immersed cast films of all samples can be found in appendix 8.2.

5.3.1.3 Tensile Testing

Tensile testing was used to analyze degradation in mechanical properties due to the influence of electrolyte LP71. Pristine as well as treated polymer strips were tested. The mechanical properties of PMP, COC, ETFE, FEP, PI and PPS are not affected by

submersion in LP71. Tensile Strength and Elastic Modulus for samples showing significant differences are shown in Figure 5.23 and Figure 5.24.

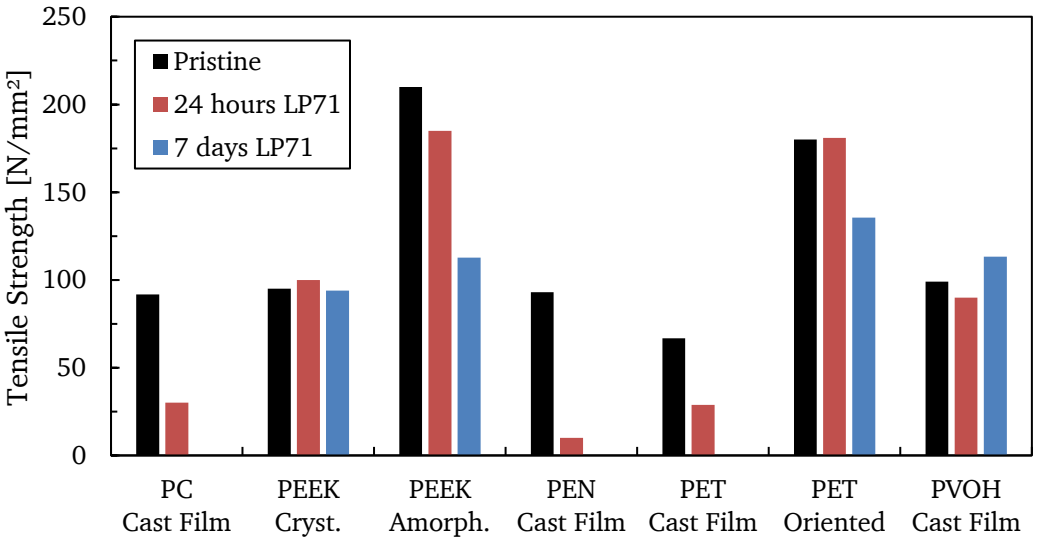

Figure 5.23: Tensile Strength for polymer samples before and after submersion in LP71 at 60 °C.

Heavily degraded samples PC, PEN and PET exhibit a drastic loss in tensile strength. The elongation at break is reduced to 2 % for PC and 1 % for PEN and PET when submersed in LP71 for 24 hours. Tensile testing for samples treated for 7 days was not possible. In contrast, stretched PET as well as amorphous stretched PEEK show a loss in tensile strength with increasing submersion time.

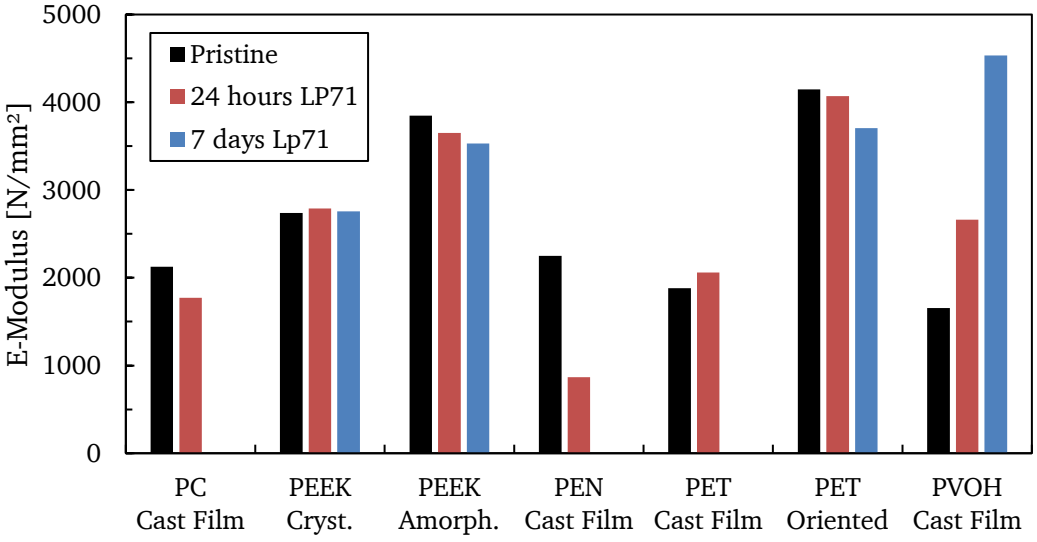

Figure 5.24: Elastic Modulus for polymer samples before and after submersion in LP71 at 60 °C.

In accordance with tensile strength, elastic modulus decreases for PC, PEEK, PEN and oriented PET when exposed to electrolyte. Crystalline PEEK and PET cast film show similar results compared to the pristine samples. In contrast, the elastic modulus for PVOH increases from 1655 N/mm² to 4535 N/mm² when treated for 7 days with LP71.

5.3.1.4 Discussion

Chemical stability in commercial electrolyte is one important requirement for polymers used as separator material. The results from the given experiments have shown that many materials tested in this study are not suitable for Lithium ion battery applications. First of all, materials such as PA, PMMA dissolve completely in LP71, while PSU, PES and POM are heavily dissolved, although not completely, over the timeframe of 7 days. The IR analysis of PSU and PES shows additional peaks at 1808, 1774, 1744 and 968 cm^{-1} that can be attributed to residue of ethylene carbonate (EC). IR spectra of EC reported by Fortunato et al.[101] are consistent with the observed signals. Taking the high boiling point of EC into account (248 °C), it is obvious that not all of EC was successfully removed by the washing and drying procedure. In contrast, no dimethyl carbonate (DMC) or diethyl carbonate (DEC) are found in the samples , their boiling point being 90 °C and 126 °C respectively.

The same reasoning can be applied to explain the additional signals observed in the IR spectra of PET, PEN and PEEK. In these cases the amount of EC residue is much lower as evidenced by the weak IR signals. The increase of sample weight after the electrolyte test is also consistent with residue on or in the films. Comparing PET cast and stretched films, swelling is comparable with 16 % and 15 % respectively, which is contrary to expectation as film thickness of the stretched sample is lower at 68 μm compared to 277 μm for the cast film. Considering that crystallinity increases during stretching[102] and orientation processes, and that swelling occurs in the amorphous regions of polymers[103-104], it is reasonable to conclude that diffusion of electrolyte into the material is slowed down for the stretched sample. The same reasoning can be applied to the difference in swelling of crystalline cast film and amorphous stretched film of PEEK, with 10 % swelling for the cast film and 43 % for the stretched sample. In this case the difference in thickness, 201 μm for cast film and 27 μm for stretched sample, also contributes to the higher swelling.

While many of the other materials, namely COC, PPS, PEI and PI, also show swelling and increase in weight after the experiment, no distinct differences in IR spectra can

be found, meaning that the concentration of EC residue for detection in IR was not sufficient.

When taking mechanical properties into account, it is obvious that for PET, PEN and PC, in addition to the take-up of EC, the materials are also heavily degraded after submersion in electrolyte. This is also immediately evident when looking at the visual appearance of the samples after the test as can be seen in Figure 5.25 on the example of PET.

Figure 5.25: Visual appearance of PET cast film after 7 days in LP71 at 60 °C.

It is easily visible that treatment in LP71 has led to clouding and defects in the sample. It is well known in literature that polyesters undergo hydrolysis when subjected to water in acidic or alkaline environment[105-107]. As the crystalline regions are impermeable to water, hydrolysis will occur mainly in the amorphous regions. During hydrolysis chain scission leads to rapid degradation of molecular weight as evidenced by the decrease in mechanical properties.

Due to the manner in which the electrolyte tests are carried out, water content in the presented experiments is below 50 ppm as measured by Karl-Fischer titration prior to storing the submersed samples at 60 °C. LP71 electrolyte, in addition to containing small amounts of HF, also contains $LiPF_6$ that will dissociate into PF_5 and LiF at elevated temperatures[40-41, 43, 108-109]. PF_5 in turn reacts to hydrofluoric acid according to equation 5.22.1[40, 43] and may also lead to ester exchange reactions of alkyl carbonates as seen in equation 5.3[43].

$$LiPF_6 \xrightarrow{\Delta} PF_5 + LiF \qquad 5.1$$

$$PF_5 + H_2O \rightarrow POF_3 + 2\ HF \qquad 5.2$$

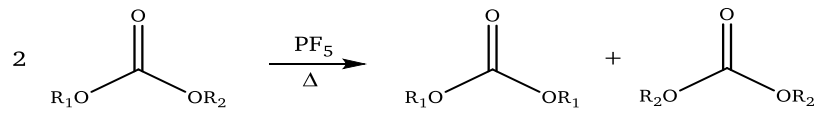

5.3

In light of this situation, it can be assumed that polyesters such as PET and PEN will also react in transesterification reactions with HF assuming the role of Lewis acid catalyst. The reaction to Hydrofluoric acid is partly due to the presence of residual amounts of water in the electrolyte but mostly due to the water content in the PET films prior to measurement. When subjected to ambient conditions, PET will take up water, making drying of the film necessary. When the PET film was dried beforehand, cloudiness and cracking could be reduced severely, making it a potential albeit challenging material for the EVAPORE® process.

5.3.1.5 Conclusion

Of all materials tested, more than half are not suitable for use in Lithium ion batteries using current state of the art electrolyte comprised of alkyl carbonates and $LiPF_6$. An overview of all materials not stable in electrolyte is given in Table 5.2.

Table 5.2: Overview of materials not stable in LP71 electrolyte.

Material	Tensile Strength	ATR-FTIR	Result
PMMA, PA6	-	-	Dissolved completely
PSU, PES	-	EC residue	Heavily dissolved, changed form
PC	decreased	OK	Partly dissolved, shrunk in size
POM	-	-	Heavily swollen, brittle sample
PET, PEN	decreased	EC residue	Clouding and cracking of sample, reaction with electrolyte, OK when dried beforehand
PEEK	decreased	EC residue	Visually OK, probable reaction with electrolyte
PEI	-	OK	Sample broke in electrolyte

Aside from chemical stability, raw material cost plays an important role. Currently, material cost makes up a small part of final separator cost, mostly due to inexpensive HDPE being used. With a targeted price of the final separator film of < 1 €/m² careful

consideration of potential candidates is important. Table 5.3 presents a rough estimation of material cost for all materials that were stable in LP71.

Table 5.3: Overview of materials stable in LP71 electrolyte and their corresponding prices.

Material	Price[a] [€/kg]	Yield[b] [m²/kg]	Price[b] [€/m²]
PI	25.00	69.9	0.358
FEP	25.00	46.5	0.538
ETFE	25.00	57,1	0.438
PPS	15.00	74.6	0.201
COC	7.00	98.0	0.071
PMP	6.50	120.5	0.054
PET	1.50	72.5	0.021
HDPE	1.50	105.3	0.014

[a] Based on prices obtained from manufacturers and distributors.
[b] Based on a theoretical separator film of 20 μm thickness and 50 % porosity.

In comparison, material cost for HDPE separator amounts to 0,014 €/m² only. As could be expected, fluorinated polymers as FEP and ETFE are very expensive compared to HDPE with a 38-fold increase in price of FEP over HDPE. Feasible prices can only be achieved by polyolefines COC and PMP, both showing a moderate increase in cost that can be justified by the potential for increased thermal stability. Despite its chemical stability and acceptable price, COC is not usable for the EVAPORE® process as it requires materials with sufficient crystallinity due to the mechanisms involved in the pore formation process. This leaves only PMP, a copolymer manufactured exclusively by Mitsui Chemicals under the trade name TPX. In addition to PMP, PP (Polypropylene) and UHMWPE (Ultra High Molecular Weight Polyethylene) were also included as potential candidates. Both PP and UHWMPE are already used in Lithium ion battery applications with low cost of 0,014 €/m² and 0,039 €/m² respectively. As the decomposition of PET could be avoided by removal of residual water beforehand and to further test the potential of high temperature stable polyesters, further experiments using dried PET were carried out.

5.3.2 SOLVENT EVALUATION

In the EVAPORE® process, solvent is the second important factor to be considered. Necessary requirements are miscibility with the polymer used, low melting point for liquid processing, a suitable boiling range for quick evaporation, while simultaneously being safe to use and low in cost. Safety includes aspects of both fire and explosion hazards as well as personal safety for all workers involved during production. With these stringent limitations, this chapter discusses a few prominent classes of solvents and their practicality for application in the EVAPORE® process.

5.3.2.1 Aliphatic Hydrocarbons

As a byproduct of the petroleum industry, aliphatic hydrocarbons are widely available in many different variations. Low cost dearomatized petroleum distillates containing linear, isoparafinic and cycloalkanes are trademarked as Exxsol or Shellsol and available from Exxon Mobile and Shell respectively. Many other such destillates are available on the market and are even mixed by redistributors and sold under different brands. Typically these solvent mixtures are classified by their flash point ranging from 40 °C to up to 140 °C with carbon chain lengths of C9 to C20. Therefore, appropriate boiling range can be selected by choosing the right solvent mixture, usually between 140 °C and 320 °C. Aside from danger of aspiration, which can easily be avoided, no other health risks are reported. Drawbacks are low flash point and a lower explosion limit of 0.6 vol%, which makes costly explosion protected equipment necessary. In addition, due to their nature as mixed aliphatic hydrocarbons, boiling points must be expressed as boiling ranges, meaning that different fractions will therefore evaporate at different rates, which affects processing. Despite these limitations, aliphatic hydrocarbons are already used successfully in the EVAPORE® process due to their excellent compatibility with HDPE and their low cost of 1-2 €/kg.

5.3.2.2 Fatty Alcohols

The second class of simple solvents are alcohols, which boiling point is dependent on the main chain length. Boiling points of 230 °C to 340 °C can be achieved with chains lengths between 10 and 18. Fatty alcohols are industrially used as precursors for derivatives used for hygienic applications. With prices ranging from 1-2 €/kg they are similar in cost to aliphatic hydrocarbons[110]. From a safety point of view, derivates of C10-C12 are reported to cause skin and eye irritation according to their safety data sheets[111] and are therefore less desirable. Auto-ignition temperature is slightly higher

than for aliphatic hydrocarbons (~250 °C) with lower explosion limit of 0.5 vol%, making explosion safety equipment necessary. When higher boiling points are required, alcohols containing 12 or more carbon atoms will be solid at ambient conditions and will need to be heated for liquid processing, increasing complexity of the dosing system.

5.3.2.3 Carboxylic Acids

Carboxylic acids such as caprylic, linoleic or oleic acid (also categorized as fatty acids) are used in the cosmetics and food industry. They are usually comprised of a linear aliphatic chain and one carboxylic acid group. As with fatty alcohols, boiling point is dependent on carbon chain length and ranges from C8 to C14 for boiling points of 238 °C to 326 °C respectively[111]. Explosion safety is also a concern with a lower explosion limit of 0.5 to 0.7 vol%. Additionally, these compounds are irritative and/or corrosive to skin and eyes. As the process requires these solvent to be evaporated, the use of acids is highly discouraged.

5.3.2.4 Phthalates

Phthalates are controversially used as plasticizers in plastics such as PVC. These plasticizers are not chemically bound and can therefore migrate into the environment, leading to contamination of rivers[112] and potential health risks when used for food packaging[113]. In addition, longer chain derivatives dibutyl phthalate and dioctyl phthalate are classified as carcinogenic[111]. This basically leaves only the short chain derivatives dimethyl phthalate and diethyl phthalate with high boiling points of 282 °C and 302 °C respectively. For these two compounds no safety risks are reported[111]. With a lower explosion limit of 0.9 vol%, explosion safety is increased by a small margin. Due to the high boiling points only dimethyl phthalate might be suitable for the EVAPORE® process, although evaporation rate may prove limiting.

5.3.2.5 Dicarboxylic Acid Esters

Dicarboxylic acid esters come in different derivatives depending on the number of carbon atoms between both ester groups as can be seen in Figure 5.26.

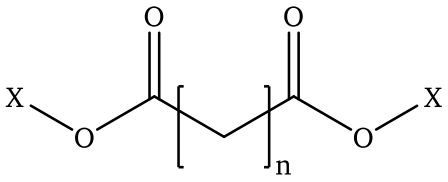

Figure 5.26: Chemical formula of typical dicarboxylic acids with n ranging from 1, 2, 4 and 8 for Malonate, Succinate, Adipate and Sebacate respectively.

These esters are typically used as plasticizers in industrial applications and due to their variable chain length offer boiling points between 180 °C and 340 °C, as well as varying compatibility with polar and unpolar materials. No safety hazards are reported, although lower explosion limit still needs to be kept in mind. With their varying properties and low cost of < 2 €/kg this class of solvent might contain adequate candidates for the EVAPORE® process.

5.3.2.6 Conclusion

Several solvents were chosen based on the classes of aliphatic hydrocarbons, phthalates and dicarboxylic acid esters. Alcohols and acids were not further used due to their increased safety concerns. Additionally, specific solvents were chosen based on their boiling point as well as good compatibility to the polymers PP, PMP, PET and EVOH estimated on their Hansen solubility parameters[114]. An overview of the chosen solvents is given in Table 5.4.

Table 5.4: Overview of solvent candidates for EVAPORE® process using PP, PMP, PET and EVOH.

Solvent	T_B [°C]	RED[a] PP	RED[a] PMP	RED[a] PET	RED[a] EVOH
Exxsol D80-D100	205-267	0,47	1,06	1,25	2,51
Dimethyl phthalate	282	1,44	1,21	0,60	1,14
Diethyl adipate	245	1,28	0,87	0,46	1,43
Dibutyl adipate	305	0,91	0,71	0,53	1,66

[a] Relative Energy Difference, calculated via Hansen Solubility Parameter software HSPiP. Values below 1 typically express good solubility.[114]

5.3.3 MISCIBILITY

Using the chosen polymers and solvents (see chapter 5.3.1.5 and 5.3.2.6) miscibility tests were done to confirm compatibility and solubility of polymers in the solvents under heat. In a first stage a small amount of polymer/solvent mixture at a ratio of 20 % polymer to 80 % solvent was heated in a sealed test tube for 30 minutes to confirm solubility. When the test was passed, the amount of polymer was varied and the resulting solidified mixture observed with an optical microscope and a hot stage to determine potential immiscibility gaps that may lead to thermally induced phase separation (TIPS)[115-121]. Additionally, dimethyl phthalate was tested on a Brabender kneader with various polymers to determine miscibility under shear force. UHMWPE was not further tested as the same solvent as for HDPE can be used.

5.3.3.1 Solubility tests

Initial tests showed that EVOH (32 % and 48 % ethylene content) as well as PET were not solved in either dimethyl phthalate, diethyl adipate or dibutyl adipate at temperatures as high as 220 °C. In the case of polyolefines PP and PMP, good solubility was found in aliphatic hydrocarbons, diethyl adipate and dibutyl adipate. On the other hand no solubility could be observed with dimethyl phthalate as solvent. Therefore, PP and PMP were further analyzed at varying solvent/polymer ratios and crystallization from the melt observed in an optical microscope. In all cases, except for a mixture of PP and dibutyl adipate, no miscibility gap was found. The phase diagram of PP/diethyl adipate is shown in Figure 5.27.

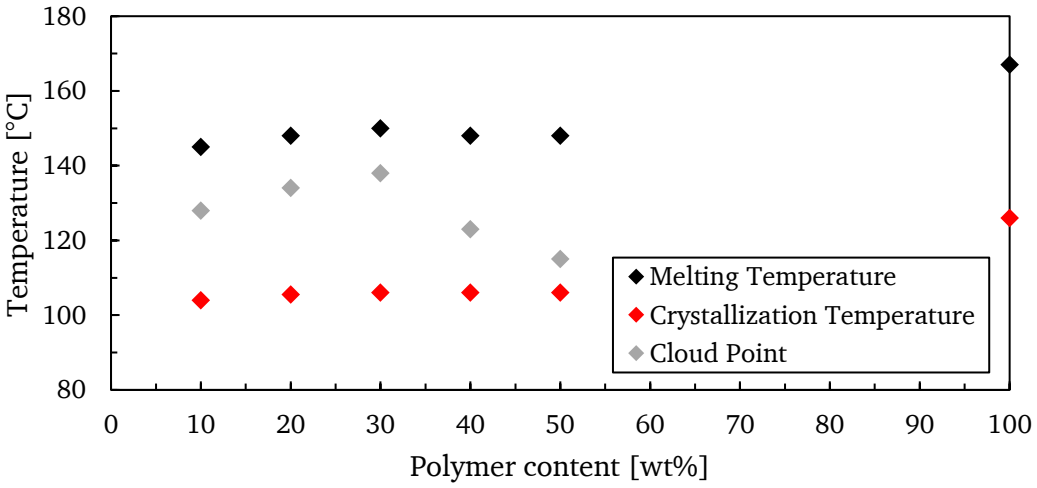

Figure 5.27: Phase diagram of PP (HP522P) and diethyl adipate mixtures over a range of 10-50 % polymer content. For reference pure PP is included as well.

As can be seen, melting temperature is lowered with increase in solvent content, while the temperature for the onset of crystallization remains nearly constant in the range tested. The cloud point, defined as the temperature at which phase separation first occurs during cooling of the melt, reaches its maximum at around 30 wt% polymer content. The monotectic point, defined as the intersection of cloud point curve and crystallization temperature curve[120-121], can be estimated to be between 50 and 60 wt% polymer content. The exact ratio was not further investigated as mixing of high amounts of polymer via this method is difficult due to high viscosity.

5.3.3.2 Solubility under shear

A kneading machine from the company Brabender (Duisburg, Germany) was utilized to do more extensive mixing experiments under shear, while simultaneously measuring temperature and torque. The machine and the kneading geometry used is shown in Figure 5.28.

Figure 5.28: Kneading chamber of Brabender kneading machine (left); Kneading geometry (right)

When mixing of PET and EVOH was done in a test tube without application of shear, no solubility was found. Therefore the focus of these additional mixing experiments was set on PET and EVOH with dimethyl phthalate as a solvent. In these experiments the polymer was added first and after plastification, solvent was added as well. The development of torque during the mixing experiments is shown in Figure 5.29 and Figure 5.30.

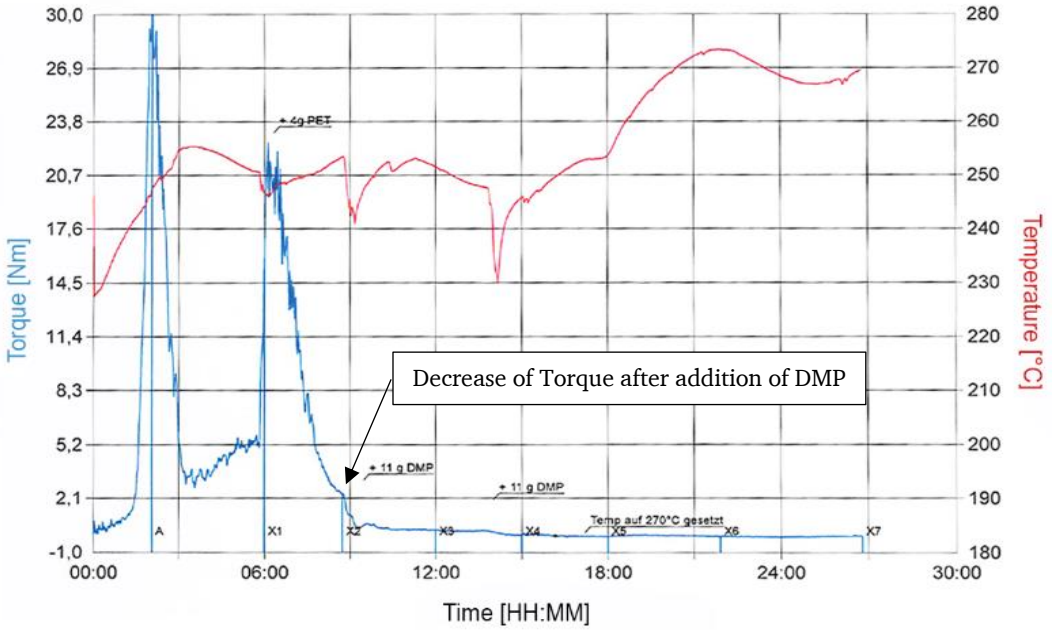

Figure 5.29: Development of torque during mixing of PET and DMP under shear in a Brabender kneader. The addition of polymer and solvent is marked. PET was added stepwise before DMP was added into the chamber.

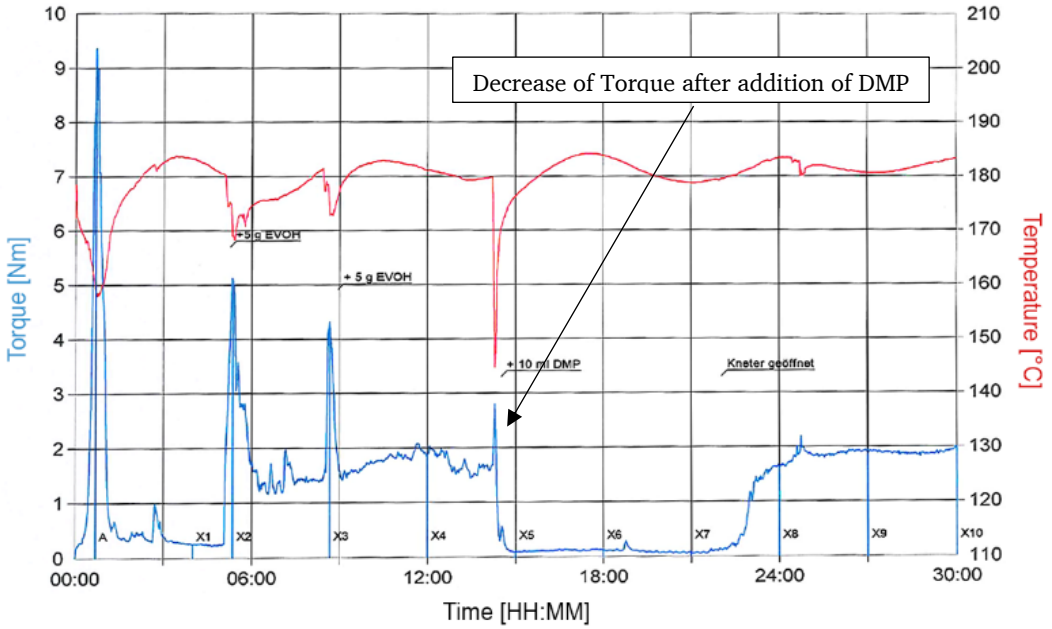

Figure 5.30: Development of torque during mixing of EVOH and DMP under shear in a Brabender kneader. EVOH was added stepwise before DMP was added into the chamber.

In both cases, after solvent was added, torque decreased to very low values of almost 0 Nm and no further increase could be observed. When the kneader was opened after the experiment, most of the solvent was not mixed with the polymer and leaked out of the chamber. In addition, PET as well as EVOH were strongly decomposed and/or oxidized as shown in Figure 5.31.

Figure 5.31: Decomposition of PET (left) and EVOH (right) after mixing with DMP on a Brabender kneading machine.

5.3.3.3 PP Crystallization

Although Polypropylene is soluble in aliphatic hydrocarbons as well as diethyl- and dibutyl adipate, the solidified material is often very brittle and, therefore, unsuitable for further processing. It is believed that the reason for this behavior can be found in the crystalline phase. Thermomicroscopy as well as DSC and SEM measurements were used to analyze crystallization of a PP/solvent mixture. Microscopic images during crystallization of thin films were obtained with a Leica Microscope equipped with a heating stage and video capture system. Figure 5.32 shows a comparison of crystallization of neat PP and mixtures with Exxsol D80, diethyl- and dibutyl adipate.

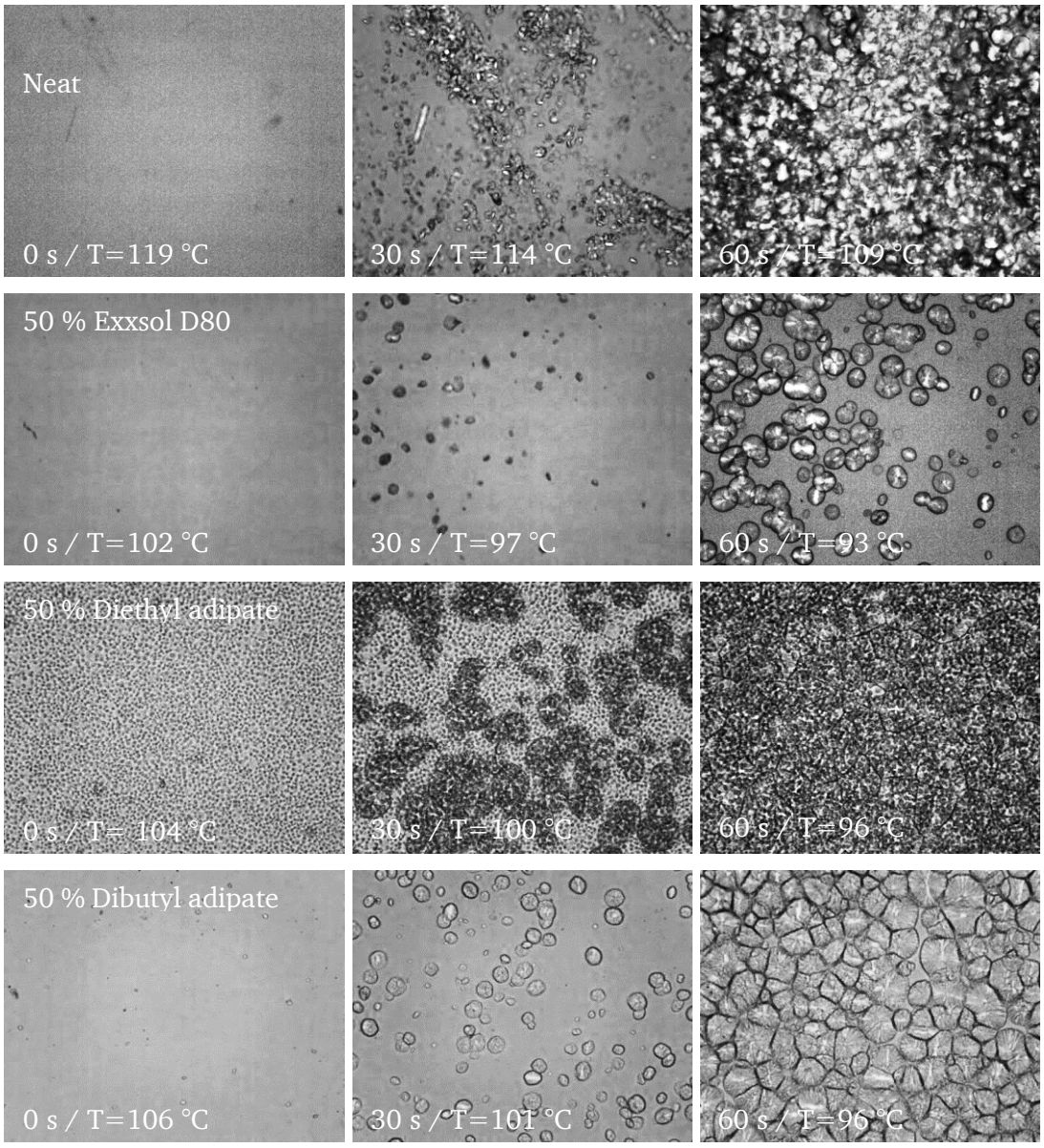

Figure 5.32: Microscopic images of polymer crystallization during cooling at a rate of 9 K/min ± 1 K/min. The onset of crystallization is defined as 0 s.

Crystallization for neat PP as well as mixtures with diethyl- and dibutyl adipate has proceeded to a high degree after 60 s. In comparison, in a mixture with 50 wt% of aliphatic hydrocarbon Exxsol D80, crystallization is much slower. In all cases, when mixed with solvent, fewer amount of nuclei can be observed and ultimately spherulite size is increased in comparison to neat PP. Crystallization was also investigated by DSC measurements of solvent filled samples at a cooling rate of 10 K/min. Figure 5.33 shows the development of relative crystallinity during cooling.

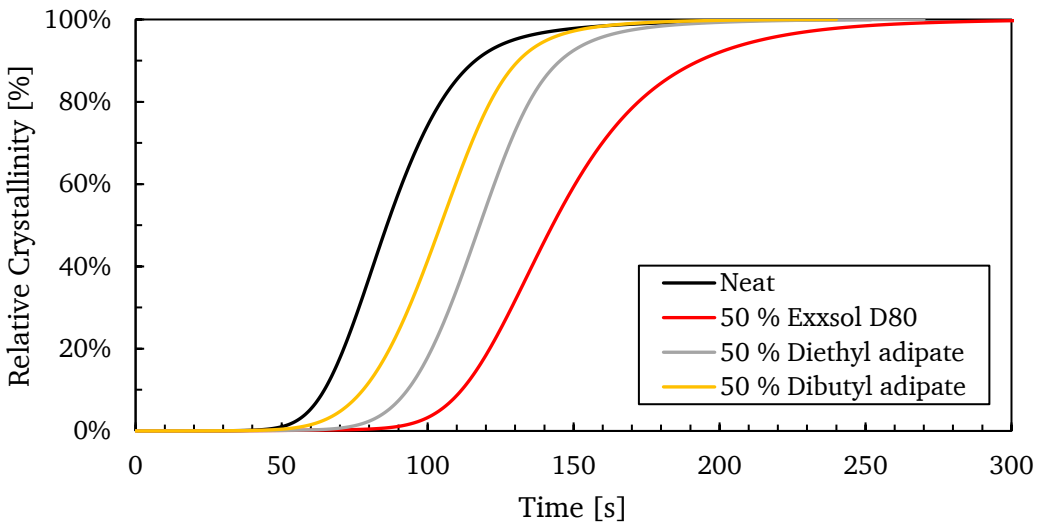

Figure 5.33: Relative crystallinity of neat PP (HP522H) as well as mixtures with different solvents as calculated from DSC analysis. Cooling rate: 10 K/min.

From the slope of the curves, it is clear that crystallization rate is slower for Exxsol D80, confirming the results from the microscopic analysis. A measure for crystallization rate is the time needed to reach 50 % relative crystallization $t_{½}$ and is shown in Table 5.5 along with crystallization enthalpy ΔH_C and crystallinity X_C.

Table 5.5: Crystallinity and crystallization half-time of PP and mixtures with solvent.

Material Combination	$t_{½}$[a] [s]	ΔH_C[b] [J/g]	X_C[c] [%]
Neat PP	37	102,8	49,7
PP + 50 % Exxsol D80	54	139,1	67,2
PP + 50 % Diethyl adipate	45	114,1	55,1
PP + 50 % Dibutyl adipate	48	120,4	58,2

[a] Crystallization half-time
[b] Enthalpy of crystallization disregarding weight of solvent
[c] Crystallinity calculated from ΔH_C using a heat of fusion of 207 J/g.

The results confirm that crystallization is slower when PP is mixed with solvent, most significantly for the mixture with Exxsol D80. Additionally, final crystallinity corresponds well with crystallization time, with highest crystallinity obtained when Exxsol D80 is used. Figure 5.34 shows a SEM cross-section of a cast film prepared with a PP/Exxsol D80 mixture.

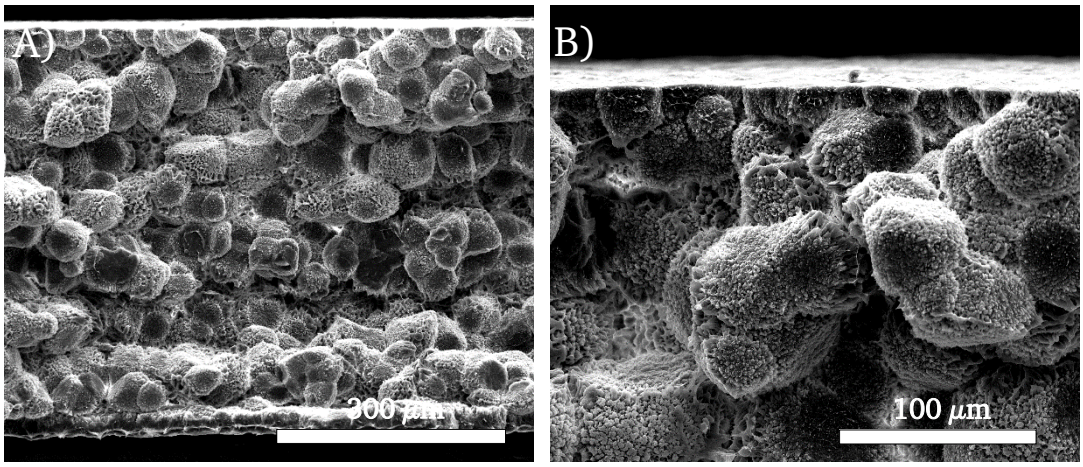

Figure 5.34: SEM image of a cross-section of a PP/Exxsol D80 (50:50) castfilm. Cross-section prepared in liquid Nitrogen.

The results are in line with thermomicroscopic analysis, with spherulites in the order of 50-100 μm are visible over the whole sample cross-section. Sample preparation was done by fracture method in liquid nitrogen and it is interesting to note that spherulites are mostly intact, i.e., not showing any intraspherulitic fracture.

5.3.3.4 Discussion

Results from the solubility tests are summarized in Table 5.6.

Table 5.6: Summary of solubility results.

Polymer	DMP[a]	DEA	DBA	D80
PP (HP522H)	x	TIPS[b]	✓	✓
PMP (DX 845)	x	✓	✓	✓
EVOH 32% (F101B)	x	x	x	x
EVOH 48% (G156B)	x	x	x	x
PET (Invista RT4027)	x	x		

[a] Additionally tested in Brabender kneader.
[b] Soluble with miscibility gap leading to temperature induced phase separation.
✓ Soluble in the range 10-50 wt% polymer without immiscibility gap

From the results it is clear that polyolefines PP and PMP were easily soluble in aliphatic hydrocarbons under heat even without applying shear, similar to HDPE mixtures already used in the EVAPORE® process. When more hydrophilic solvents such as diethyl- or dibutyl adipate are used, solubility is expected to decrease and indeed this can be observed when PP is mixed with diethyl adipate as this mixture will phase

separate in a range of 10 to approx. 50 wt% polymer when temperature of the melt is reduced (see Figure 5.27). When the solvent is changed to dibutyl adipate, no phase separation is observed and the mixture is miscible over the whole range of polymer content. In this case, a small increase in aliphatic chain length is enough to increase solubility significantly. When the integrity of the solidified mixture is taken into account, it becomes evident, that crystallization of the mixture is an important factor to consider. Due to the solvent, crystallization is slowed and final crystallinity is higher. This can be attributed to lower viscosity of the mixture and a longer crystallization time, which provides more time for crystallites to form. Unfortunately, the solvent inhibits the formation of nuclei, as statistically polymer molecules are less likely to randomly align themselves. This in turn leads to fewer but larger spherulites with weak interspherulitic bonding, resulting in brittleness of the solidified mixture or cast film.

Unexpectedly, PMP is soluble in both, diethyl- and dibutyl adipate, showing no phase separation. Considering that commercially available PMP, sold under the brand name TPX by Mitsui Chemicals, is a copolymer with its exact composition being proprietary information, and the fact the RED values from the Hansen Parameters are based on PMP homopolymer, the difference in estimated solubility as evidenced by the Hansen Parameters compared to the real solubility does not seem unreasonable. The reason that PMP is not commercially available as a homopolymer is its processability (e.g., stretchability). Due to its molecular structure, it is expected that crystallization of PMP would be similar to PP, or even slower, showing the same brittleness of the solidified mixture as PP. This is not observed, as cast films made from PMP are mechanically stable. The addition of co-monomers during the production process and the overall lower crystallinity of PMP is a probable reason for the increased stability of the solidified mixture.

For PET and EVOH, finding a suitable solvent proved to be unsuccessful. Experiments on a Brabender kneader showed that mixing under shear can lead to severe degradation of the polymers. It is well known, that processing of PET requires exclusion of moisture, usually achieved by pre-drying of the polymer and also by applying a vacuum in the extrusion system. Mixing of PET with solvent such as adipates or phthalate is therefore problematic, as no vacuum can be used and solvents might react with PET or EVOH and degrade the polymers. Aside from these difficulties, it was evident, that dimethyl phthalate, even though a potential solvent for PET or EVOH

according to Hansen Parameters (Table 5.4), was not sufficient. This can be seen from the torque measured during the mixing on a Brabender kneader. After the addition of solvent to the plasticized polymer, torque decreased to nearly 0 Nm, which means that solvent was functioning as a lubricant in the kneading chamber, without being mixed into the polymer itself.

5.3.4 CONCLUSION

A diverse set of materials, both polymers and solvents, were evaluated for the use in the EVAPORE® process. One of the main requirements of a polymeric material is sufficient chemical stability in commercial non-aqueous battery electrolytes, consisting of a mixture of organic carbonates and $LiPF_6$. Most of the materials used in this study dissolved partly or completely when immersed into electrolyte. A select set of materials proved to be stable under these conditions including PI, FEP, ETFE, PPS, COC, PMP and in parts also PET (low water content necessary). Based on material pricing, only PMP, PET and COC fall in range to the currently used HDPE (see Table 5.3). With COC, pore formation seems unlikely due to the amorphous nature of the material and it is therefore not further used. Instead PMP, PET as well as EVOH and PP were chosen as promising candidates. The evaluation continued with the search for a suitable solvent for the selected polymers and a small group of solvents, including aliphatic hydrocarbons, adipates and phthalates, was chosen for miscibility trials. PET and EVOH proved impossible to dissolve with these solvents even under shear in a Brabender kneader, where significant degradation of both the polymers occurred (see Figure 5.31). On the other hand PMP and PP were easily soluble in aliphatic hydrocarbons while a mixture of PP and diethyl adipate showed phase separation (see Figure 5.27). It was also observed that a mixture of PP and solvent produced brittle and unstable cast films, unsuitable for the EVAPORE® process (see Figure 5.34). In the end, a material combination of PMP and aliphatic hydrocarbons was chosen as the most promising to achieve stable cast films.

5.4 NOVEL SEPARATOR

Laboratory tests (see chapter 5.1.1) as well as trials on the laboratory line were carried out with the most promising material combination, in this case PMP and aliphatic hydrocarbons. In addition to the materials described before, several development polypropylene materials were tested as well, one of them containing alpha-nucleating agents to counteract slow crystallization of PP in solvent (see chapter 5.3.3.3). The effect of ceramic filler material on temperature stability was also investigated by compounding polyethylene with aluminum flame-retardants. Lastly various Ultra High Molecular Weight Polyethylenes (UHMWPE) were tested directly on the laboratory line.

5.4.1 CERAMIC FILLED HDPE

Two flame-retardants from Nabaltec AG (Germany) based on AlO(OH) (Boehmite) were compounded with HDPE (Alathon L5906) in Nabaltecs facilities on a twin screw extruder. The specifications for both materials are given in Table 5.7.

Table 5.7: Type of filler used for compounding with HDPE.

Material	Type	Particle size D50	Density
Actilox 200 SM	AlO(OH)	277 nm	3 g/cm³
Actilox 200 HS1	AlO(OH) – silane modified surface	405 nm	3 g/cm³

5.4.1.1 Compounding

Materials were compounded on an L/D 36 twin screw extruder with an output of 5 kg/h. For each composition 60 % of filler was added via main feeding and 40 % were added after plasticization via a side feeder. The melt was extruded cylindrically, cooled in water and granuled before packaging. A filler content of 50 wt% was targeted. Table 5.8 summarizes the results of the compounding tests as well as analysis of the compounded materials.

Table 5.8: Summary of compounding results.

Parameter/Result	Actilox 200 SM	Actilox 200 HS1
Filler content [%]	30	50
Extr. Pressure [bar]	41	32
Melt Temp. [°C]	212	211
Extrusion load [%]	58	44
MFR[a] [g/10min]	0,045[b]	0,086[b]
Melting Point [°C]	138	137
Crystallinity [%]	62	63

[a] Measured at 230 °C / 2,16 kg
[b] MFR for pure Alathon L5906: 0,13 g/10min

Two masterbatches with filler content of 30 wt% and 50 wt% were produced for Actilox 200 SM and Actilox 200 HS1 respectively. The unmodified Actilox 200 SM was more difficult to compound as visible in higher extrusion pressure and load at 20 wt% less filler content in comparison to Actilox 200 HS1. In addition compounding with the unmodified material was unstable above 30 wt% filler content and generally lead to stronger yellowing and brittleness of the compounded material. The modified filler could be compounded at a content of 50 wt% without difficulties. For both materials melt flow rate (MFR) is reduced, more severely for unmodified Actilox 200 SM.

5.4.1.2 Laboratory Line Trials

Both masterbatches were used in trials on the laboratory line according to the EVAPORE® process. The materials were diluted with HDPE (Alathon L5906) to a filler content of 20 wt% and 40 wt%. In the case of Actilox 200 SM 40 wt% could not be achieved and the compounded material was processed pure instead (30 wt% filler content). Similar to the compounding tests, Actilox 200 SM showed higher load in the extrusion system (46 % load for Actilox 200 HS1 vs 52 % load for Actilox 200 SM). Table 5.9 summarizes the main parameters used in the process.

Table 5.9: Overview of important laboratory line process parameters during trials with ceramic filled HDPE.

Parameter	Actilox 200 HS1 20 % filler	Actilox 200 HS1 40 % filler	Actilox 200 SM 20 % filler	Actilox 200 SM 30 % filler
Output [kg/h]	13	14	13	14
Solvent Content [%]	54	54	54	54
Chill Roll Speed [m/min]	2	2	2,1	2,5
Chill Roll Temperature [°C]	35	35	35	35
Castfilm Thickness [μm]	450-480	430-450	450-470	400-450
MD Ratio	5,5	5,5	5,5	5,5
Stretching Temperature[a] [°C]	95 / 102	95 / 102	95 / 102	95 / 102
Annealing Temperature [°C]	102	102	102	90

[a] The MDO of the laboratory line consist of two drawing rolls.

When higher amounts of filler are used, output and/or speed need to be adjusted to counteract lower thickness due to less polymeric material. In all cases extrusion and MD stretching was successfully done without difficulties. With Actilox 200 SM contact to chill roll resulted in spots due to sticking of the film to the roll. This effect increased with higher filler content of Actilox 200 SM and could be slightly reduced by increasing chill roll speed. Optical appearance of all films were visibly whiter compared to pure HDPE.

5.4.1.3 KARO IV Trials

MD samples produced on the laboratory line were stretched in TD on the KARO IV laboratory stretching machine. The parameters used in these trials are summarized in Table 5.10.

Table 5.10: KARO IV parameters used for TD stretching of ceramic filled HDPE film samples from the laboratory line.

Parameter	Filled Samples
Stretching Temperature [°C]	70
Pre Heating Time [s]	3
Stretching Ratio TD	5.0
Stretching Speed [%/s]	20
Annealing Temperature [°C]	100
Annealing Time [s]	60

Samples were easily stretchable even at low pre heating times of 3 s. Film porosity and Gurley values are shown in Figure 5.35 and Figure 5.36. Porosity is calculated by taking the density of the ceramic filler and filler content into account.

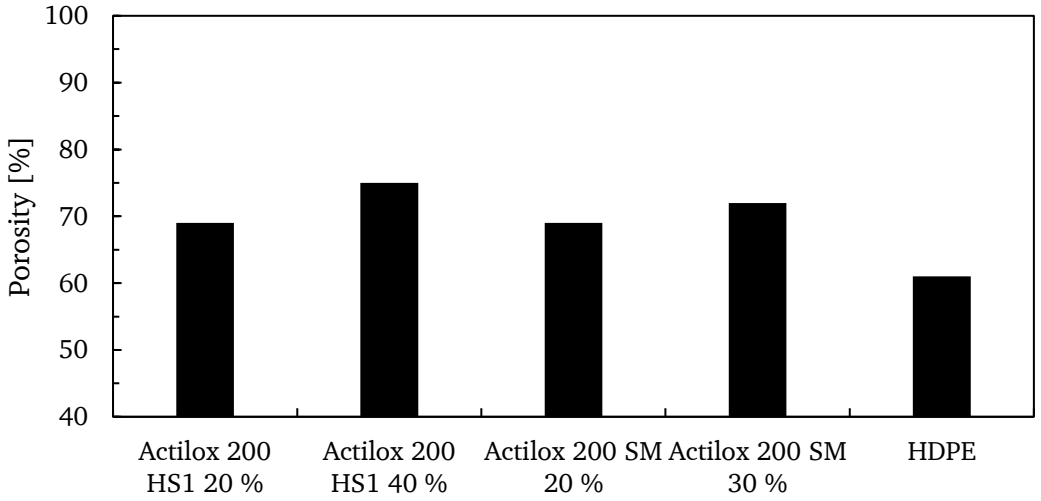

Figure 5.35: Comparison of porosity of ceramic filled laboratory line samples stretched in TD to 5.0 on the KARO IV.

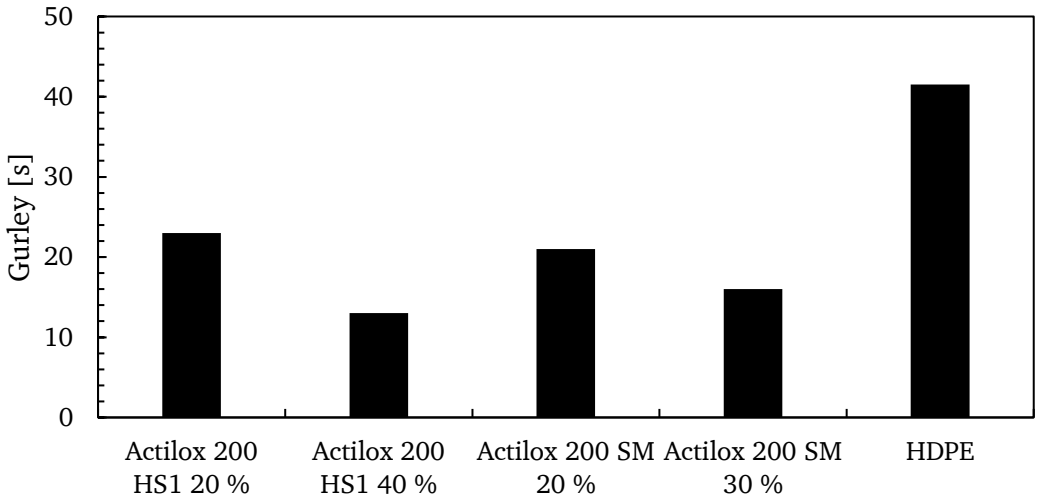

Figure 5.36: Comparison of Gurley of ceramic filled laboratory line samples stretched in TD to 5.0 on the KARO IV.

From Figure 5.35 it can be gathered that porosity is increased significantly when fillers are embedded into the polymer matrix. An unfilled sample will reach porosities around 60 % while filled samples will reach values of 70-75 % depending on the amount of filler content. It is evident, that an increase in filler content will increase porosity as well, although there is no clear distinction between Actilox 200 HS1 and Actilox 200 SM filler types. The increase in porosity correlates well with Gurley values shown in Figure 5.36. Lowest Gurley values can be found for those samples having highest porosity.

One of the goals of these trials was the increase of temperature stability and, therefore, reduction of the shrinkage value. Figure 5.37 shows shrinkage values in TD direction of KARO IV stretched samples.

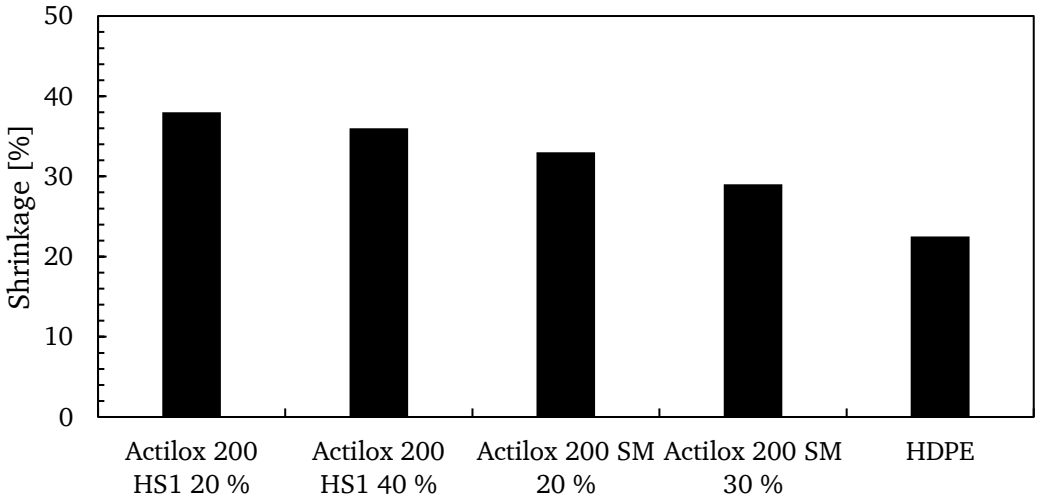

Figure 5.37: Comparison of Shrinkage of ceramic filled laboratory line samples stretched in TD to 5.0 on the KARO IV.

The results clearly show that in this case shrinkage values were not reduced and in fact higher than for samples made of unfilled HDPE samples. Although an increase of filler content in either case shows a decrease of shrinkage.

Finally mechanical strength is a concern when using fillers. Tensile strength and puncture strength are shown in Figure 5.38 and Figure 5.39.

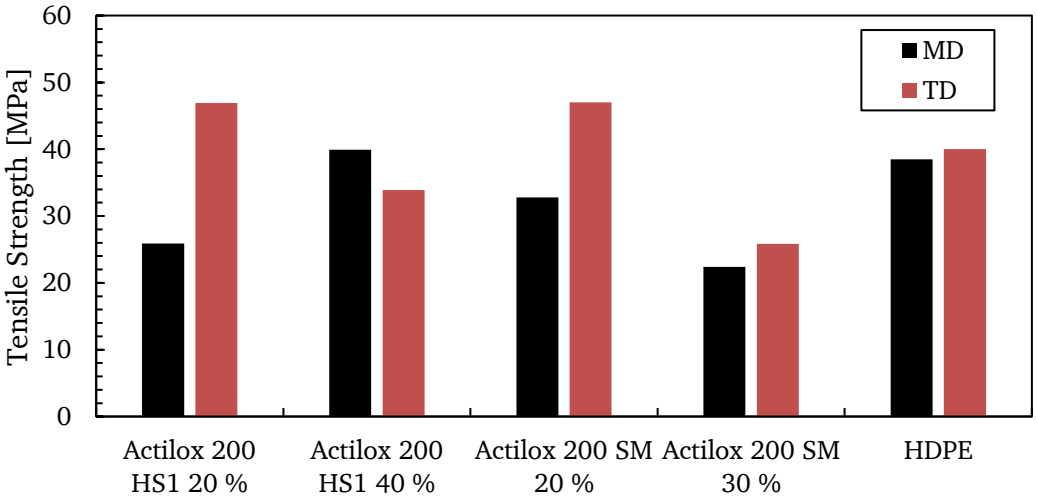

Figure 5.38: Comparison of Tensile Strength of ceramic filled laboratory line samples stretched in TD to 5.0 on the KARO IV.

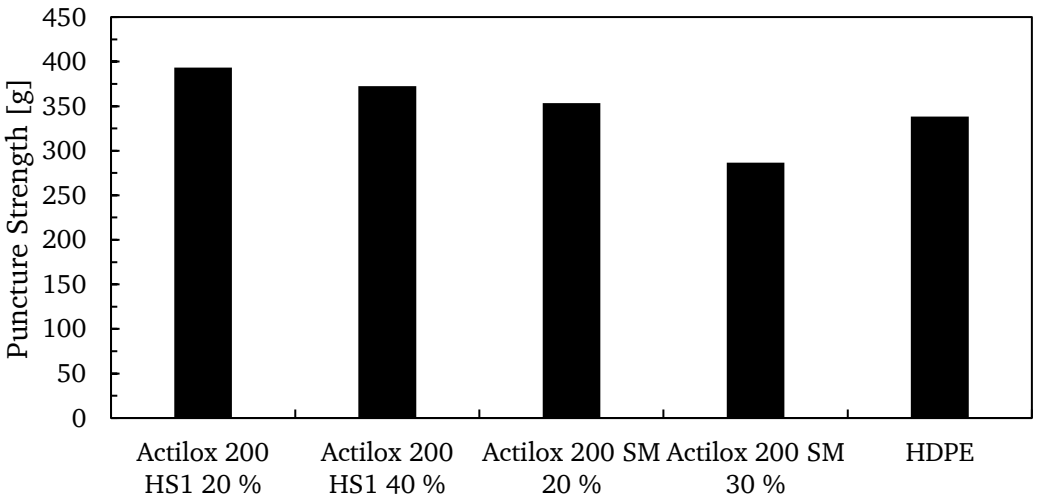

Figure 5.39: Comparison of Puncture Strength of ceramic filled laboratory line samples stretched in TD to 5.0 on the KARO IV. Values are normalized to a thickness of 20 μm and a porosity of 50 %.

Figure 5.38 shows that tensile strength is dependent on filler content with higher filler content resulting in a decrease in tensile strength. This effect is more pronounced for unmodified Actilox 200 SM with lower MD and TD tensile strength when using 30 % filler content compared to 40 % of Actilox SM HS1. These results correlate to the puncture strength shown in Figure 5.39. Higher filler content results in a decrease in

puncture strength, which is more severe for Actilox 200 SM. SEM images of surfaces of filled film samples are shown in Figure 5.40.

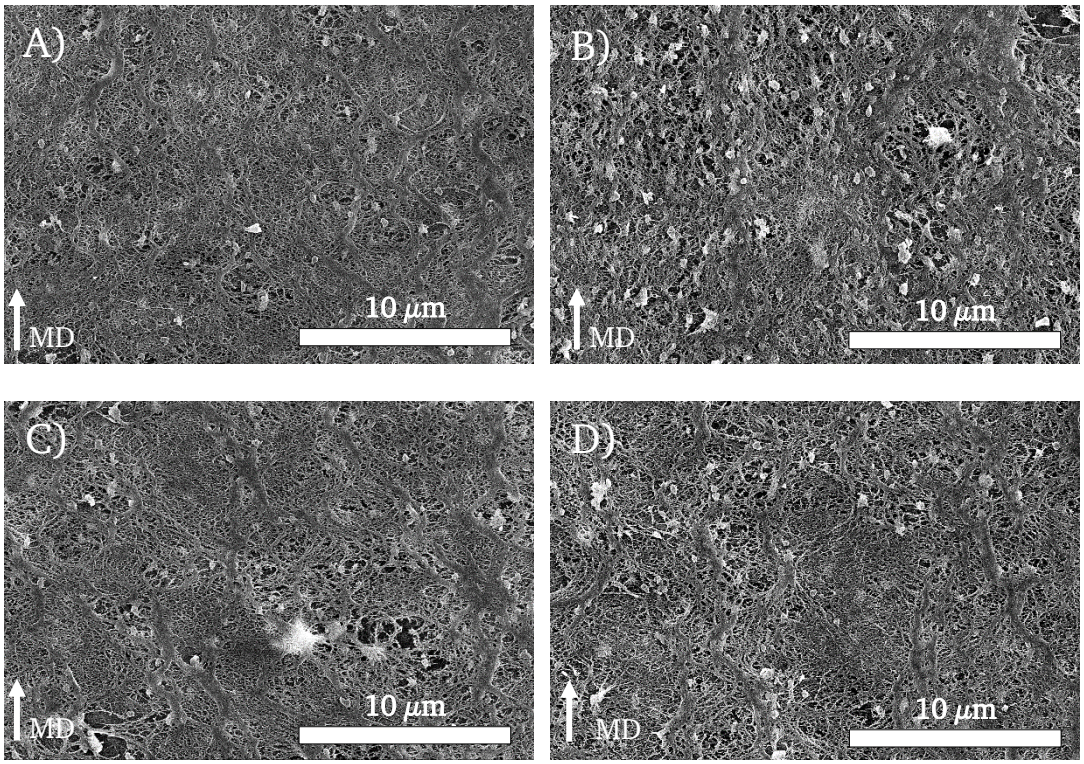

Figure 5.40: SEM images of film surfaces of stretched films containing different amounts of filler. A) Actilox 200 HS1 20 %. B) Actilox 200 HS1 40 %. C) Actilox 200 SM 20 %. D) Actilox 200 HS1 30 %.

In both cases, when higher amounts of filler are used, the morphology is visibly rougher with higher porosities on the film surface as is also evidenced by porosity measurements. The difference due to filler type is only small, with Actilox 200 SM exhibiting a slightly rougher surface morphology and higher porosity judging by the images. As the filler particles are an order of a magnitude larger than the average pore size (typically in the range of 50-70 nm), the filler cannot be completely incorporated into the polymer matrix and in many cases particles are not so much connected to the polymer than rather freestanding in one or more directions with a pore opening up around the particle.

5.4.1.4 Discussion

Compounding of Boehmite into the Alathon L5906 HDPE is easily possible, especially with surface modified particles to increase compatibility. While for unmodified material the filling degree is limited to about 30 %, as much as 50 % of the modified grade can be incorporated into the polymer matrix. This is not only evident from discoloration, but also from extrusion pressure and torque needed during compounding as well as during the laboratory line trials (see Table 5.8). The silane modification is increasing the hydrophobicity of the particles and thus the material can be mixed easier with the polymer as expected. Stretching of MD oriented films, comprising different amounts of filler, on the KARO IV machine resulted in highly porous films with correspondingly low Gurley values, compared to pure HDPE, which can be attributed to the formation of vacuoles at the polymer-particle interface[122-124]. These vacuoles form due to concentrated stress at the polymer-particle interface during stretching which leads to loss of cohesion and subsequently formation of pores or vacuoles. The extent of this mechanism is dependent on the interaction between polymer and filler type. In this case, the silane modified Boehmite should theoretically be less prone to the formation of vacuoles compared to the unmodified Boehmite due to the increased compatibility of the silane surface to the polymer matrix. While this is not directly evident by the porosity and Gurley measurements, the lower mechanical strength of Actilox 200 SM filled samples, especially for a filler content of 30 %, suggests a weakening of the polymer matrix due to the weak interaction with the filler material, possibly due to the formation of larger pores compared to Actilox 200 HS1. In all cases however, shrinkage is found to be much larger compared to the unfilled HDPE film sample, undermining the goal of achieving increased thermal stability. The increased shrinkage can mainly be attributed to the increased porosity of the film and the disruption of the polymer matrix as seen in the SEM images. Still, a higher amount of filler reduces shrinkage slightly, especially for Actilox 200 SM, which is most likely an increase in steric hindrance for the movement of the polymer chains due to the increased filling ratio[124]. The lower shrinkage of Actilox 200 SM can be explained in terms of particle size, as the D50 value is lower compared to Actilox 200 HS1 due to the fact that no additional surface coating has been applied to these particles. Therefore, particles of this type can, at the same weight ratio, be more evenly dispersed into the polymer matrix, contributing more to the steric hindrance effect.

In light of these results, and especially due to the increasing shrinkage, no further experiments were carried out in this direction. It is possible that a further increase in

filling content could lead to a more thermally stable separator as shown by Zhang et al.[124] and Takemuar et al.[35], but these are usually produced using a phase separation process such as TIPS or NIPS or even using inorganic filled non-wovens such as Evoniks Separion®[125]. At this stage it seems unlikely that an inorganic filler can increase thermal stability on a biaxial stretching process such as the EVAPORE® process.

5.4.2 POLYPROPYLENE

Three grades of development polypropylenes were tested on the pilot line and KARO IV laboratory stretcher as well as in Thermomicroscopy experiments similar to those presented in chapter 5.3.3.3. One of these materials is a bimodal grade and the remaining two differ only with regard to alpha-nucleating agents, which are added into one of those. Due to confidentiality agreements neither manufacturer nor specifics about the materials can be disclosed. Further the materials will be named as follows.

Table 5.11: Types of Polypropylenes used on the Laboratory Line.

Material	Type	Notes
PP-A	Homopolymer, isotactic	Bimodal
PP-B	Homopolymer, isotactic	Standard grade
PP-C	Homopolymer, isotactic	Same as PP-B, but contains alpha-nucleating agents

As previously described (see chapter 5.3.3.3), mixtures of polypropylene grade HP5225 H and hydrocarbon Exxsol D80 are not suitable for the process as the produced material is very brittle. With these three materials an effort was made to find out whether a change in polymer properties can counteract this behavior and lead to processable films.

5.4.2.1 Thermomicroscopy

Microscopic analysis of crystallization of PP mixtures with Exxsol D80 as well as neat PP were carried out similar to those describe previously in chapter 5.3.3.3. The content of solvent was fixed to 50 wt%. A comparison of microscopic images captured during cooling and crystallization are shown in Figure 5.41.

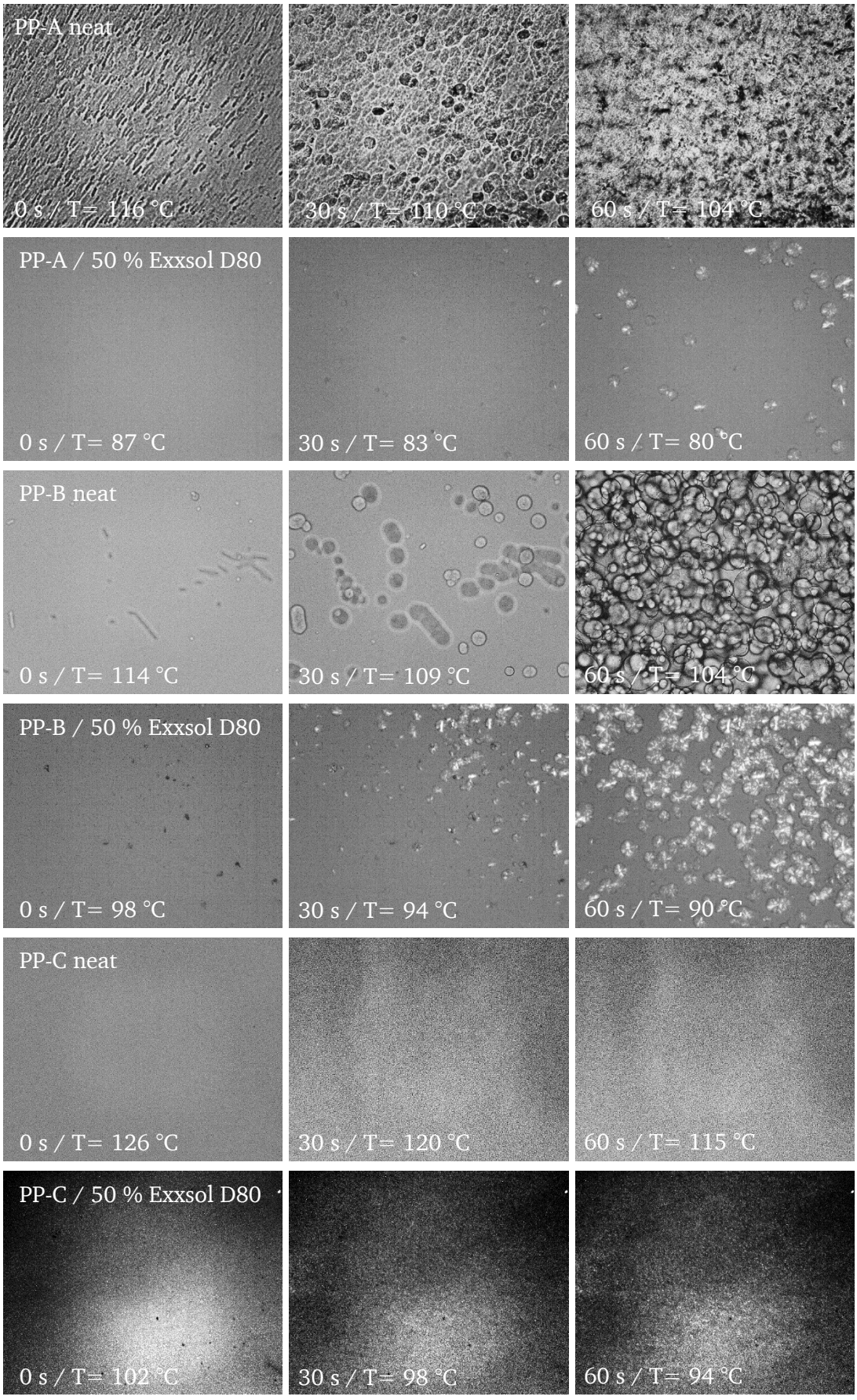

Figure 5.41: Microscopic images of polymer crystallization. The onset is defined as the first appearance of spherulitic nucleation and is marked with 0 s.

For materials PP-A and PP-B without additional nucleating agents it is clear that in mixtures with solvent Exxsol D80 crystallization is slowed significantly and the onset is shifted to lower temperatures. The extent of slowing of crystallization rate is more pronounced for the bimodal material PP-A. For PP-C, while crystallization onset temperature is lowered due to the addition of solvent, rate of crystallization is not affected. In fact for pure PP-C and mixtures of PP-C with Exxsol D80 an increase in nucleation sites and, therefore, crystallization rate is clearly evident.

5.4.2.2 Laboratory Line

All three materials were tested on the laboratory line using solvent SiSol D70 (Staub & Co. Silbermann, Germany). SiSol D70 is similar in its composition of aliphatic hydrocarbons and exhibits slightly lower boiling points than Exxsol D80. A summary of parameters used during the trials is given in Table 5.12.

Table 5.12: Overview of important laboratory line process parameters during trials with polypropylene materials.

Parameter	PP-A	PP-B	PP-C
Output [kg/h]	12	12	12
Solvent Content [%]	54	25 54	54
Chill Roll Speed [m/min]	2.1	2.1	2.1
Chill Roll Temperature [°C]	35	35	35
Castfilm Thickness [μm]	-	-	430
MD Ratio	-	-	5.5
Stretching Temperature[a] [°C]	-	-	95 / 102 100 / 126
Annealing Temperature [°C]	-	-	90 115

[a] The MDO of the laboratory line consists of two drawing rolls.

As Table 5.12 already suggests, trials with PP-A and PP-B were not successful. PP-A was not extrudable with these parameters, while PP-B produced brittle cast films as suggested by the microscopic analysis of crystallization. However, alpha-nucleated PP-C produced stable cast films that were successfully stretched in MD direction on the laboratory line.

5.4.2.3 KARO IV Trials

Using MD film made from nucleated PP-C, stretching trials were carried out on the KARO IV machine using the parameters in Table 5.13.

Table 5.13: KARO IV parameters used for TD stretching of nucleated polypropylene film samples from the laboratory line.

Parameter	Filled Samples
Stretching Temperature [°C]	60-80
Pre Heating Time [s]	2-45
Stretching Ratio TD	5.0
Stretching Speed [%/s]	50
Annealing Temperature [°C]	120
Annealing Time [s]	30

Film samples could only be stretched to a ratio of about 4.0 which was not sufficient. When a higher stretching ratio was used films would break into many pieces and exhibit very brittle behavior. Adjusting the stretching temperature between 60 and 80 °C as well as changing the pre-heating time between 2 and 45 s did not lead to any improvements in stretchability.

5.4.2.4 Discussion

As discussed earlier (see chapter 5.3.3.4), standard grade polypropylene HP522H is not processable in conjunction with the EVAPORE® process due to brittleness of the crystalline cast films. By adding solvent to the polymer, the number of nuclei is reduced and, consequently, crystallization rate is lowered while total crystallinity and spherulite size is increased. This leads to the formation of large spherulites with weak interspherulitic boundaries as seen by SEM analysis of the cross-section of a cast film made from HP522H and 50 % of solvent (see Figure 5.34). An effort was made with a small variation of alternative PP materials to check for processability in the EVAPORE® process. To that end a bimodal grade as well as an alpha-nucleated and unnucleated standard grade were used. Thermomicroscopic analysis revealed that with the standard and bimodal grade, crystallization rate is lowered by the addition of solvent

due to the inhibition of nuclei. With the bimodal grade PP-A, compared to the standard grade PP-B the number of nuclei is increased when crystallized in neat condition, while for solvent filled samples, the analysis shows that more nuclei are formed with standard grade instead. This might be attributed to the broader molecular weight distribution expected from a bimodal grade. As a higher amount of low molecular weight chains are present in the neat bimodal grade, viscosity can be expected to be reduced, and the formation of randomly aligned nuclei is facilitated. On the other hand, in the solvent filled sample, the effect of these low molecular weight chains is mitigated due to the addition of solvent, leading to the inhibition of nuclei formation.

For the alpha-nucleated PP-C, a high crystallization rate along with a high amount of small spherulites is evident in both neat and solvent filled samples. While not affecting crystallization rate in a significant degree, the onset temperature of crystallization is lowered by about 24 °C by the addition of solvent. The addition of alpha-nucleating agents is therefore promoting the formation of nuclei of neat as well as solvent filled polymer mixtures. Compared to the unnucleated PP-B, the onset of crystallization is found to be at higher temperatures for both mixtures, indicating the facilitating effect of the nucleating agent.

Due to the former results it is expected that the extrusion of unnucleated grades PP-A and PP-B will again lead to brittle cast films, while a stable cast film can be gained from PP-C. While for the bimodal grade PP-A extrusion was not possible due to an unstable melt flow at the die exit, preventing the forming of dimensional stable cast films, the extrusion of PP-B and PP-C showed the above described behavior. Cast films made from PP-B were very brittle and unstretchable in MD. On the other hand, cast films made from PP-C were stable and could be stretched in MD, but showed significant brittleness during the TD stretching, which stems most likely from an increase in crystallinity caused by the nucleating agent and facilitated by the subsequent MD orientation.

Due to the limiting processability and as the increase in thermal stability from PP is not expected to be significantly higher than PE (Melting Point of 137 °C and 167 °C for PE and PP respectively) and an alternative dry process using beta-nucleated PP is available, no further trials with PP were carried out. A variation of different nucleating agents as well as contents in combination with differing PP materials might lead to further increased processability. The manufacturing of these specialized material grades requires many resources on a trial and error basis and can only be done by the supplier or manufacturer. It is therefore outside the scope of this work.

5.4.3 POLYMETHYLPENTENE (TPX™)

Three grades of Polymethylpentene (PMP), sold under the brand name TPX™ by Mitsui Chemical (Japan), were tested using the laboratory method presented in chapter 5.1 and extruded on the laboratory extrusion line. Suitable materials were also tested on the pilot line using extruded cast film from the laboratory line. Finally a PMP/HDPE blend was attempted as well. Specifications for the tested grades are given in Table 5.14.

Table 5.14: Types of PMP grades tested for the EVAPORE® process.

Property	RT31	DX845	MX002
Density [g/cm³]	0.833	0.833	0.833
MFR[a] [g/10min]	21	9	21
Melting Point [°C]	232	232	224
E-Modulus [MPa]	1900	1900	900

[a] MFR measurement at 5kg / 260°C.

PMP exhibits a considerable higher MFR than the standard HDPE used in the EVAPORE® process (HDPE Alathon L5906: 0.13 g/10min at 230 °C / 2.16 kg). It also needs to be kept in mind that commercial grades of PMP are copolymers or mixtures with copolymers containing various amounts of $C_{2\text{-}22}$ α-olefins to increase processability[126-129]. Unfortunately, the exact amounts remain proprietary to the manufacturer. Therefore, it is not possible to calculate crystallinity from melting enthalpy as no reliable heat of fusion is available. In addition, as density of amorphous and crystalline phase are similar[71], growth of spherulites cannot be observed using a light microscope.

As a solvent, aliphatic hydrocarbons from the range of Exxsol D80 to D140 were used for mixing PMP in the laboratory method as well as for extrusion.

5.4.3.1 Laboratory Method

PMP cast films produced via the laboratory method were stretched in MD using PET covers both on top and below the film using varying stretching and annealing conditions as listed in Table 5.15.

Table 5.15: KARO IV parameters used for MD stretching of PMP film samples from the laboratory method.

Parameter	Setting
Stretching Temperature [°C]	110 - 150
Pre Heating Time [s]	40
Stretching Ratio TD	5.5
Stretching Speed [%/s]	100
Annealing Temperature [°C]	120 - 200
Annealing Time [s]	10 - 60

Keeping annealing conditions constant, stretching temperature was varied from 110 °C to 150 °C as estimated by preceding DSC measurements. SEM images of the film surface are shown in Figure 5.42.

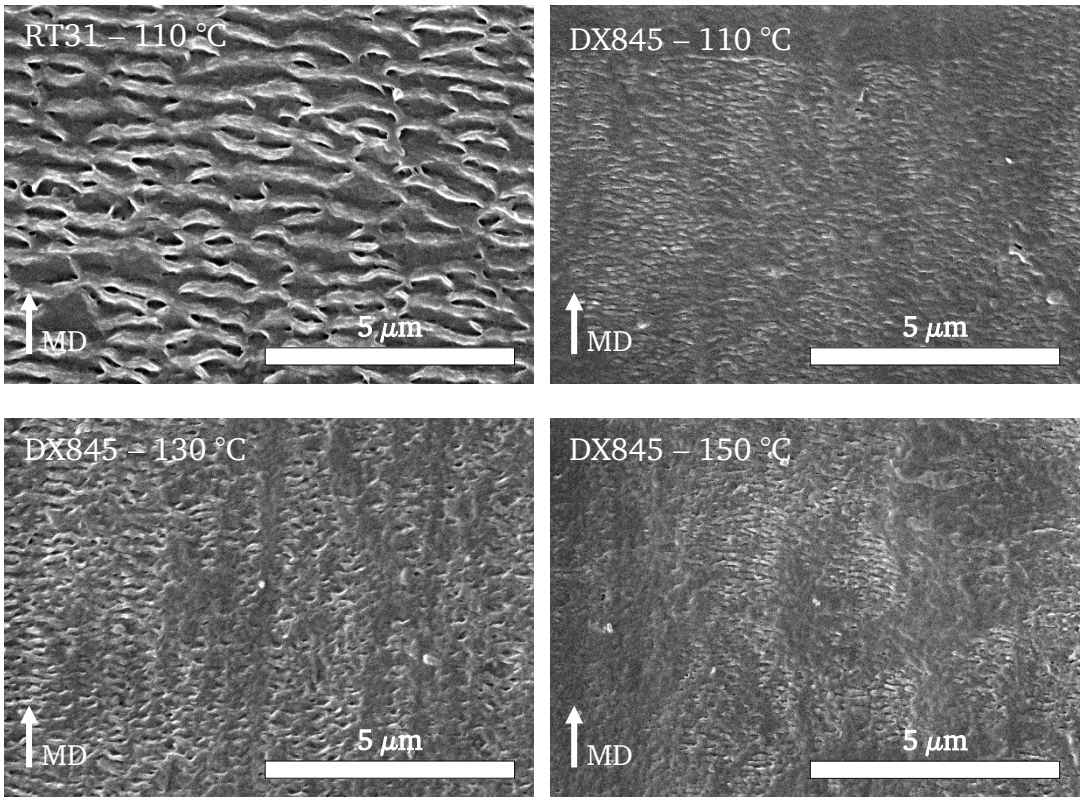

Figure 5.42: SEM images of MD stretched PMP films using RT31 and DX845 at stretching temperatures between 110 °C and 150 °C. Annealing temperature 200°C, Annealing time 30 s.

While RT31 shows significant lamellar structure at stretching temperatures as low as 110 °C, DX845 exhibits only small lamellae that are imperfectly aligned. With increasing temperature the lamellar structure becomes less pronounced.

The effect of annealing temperature on the crystalline morphology was investigated in the range of 120 °C to 200 °C. SEM images are shown in Figure 5.43.

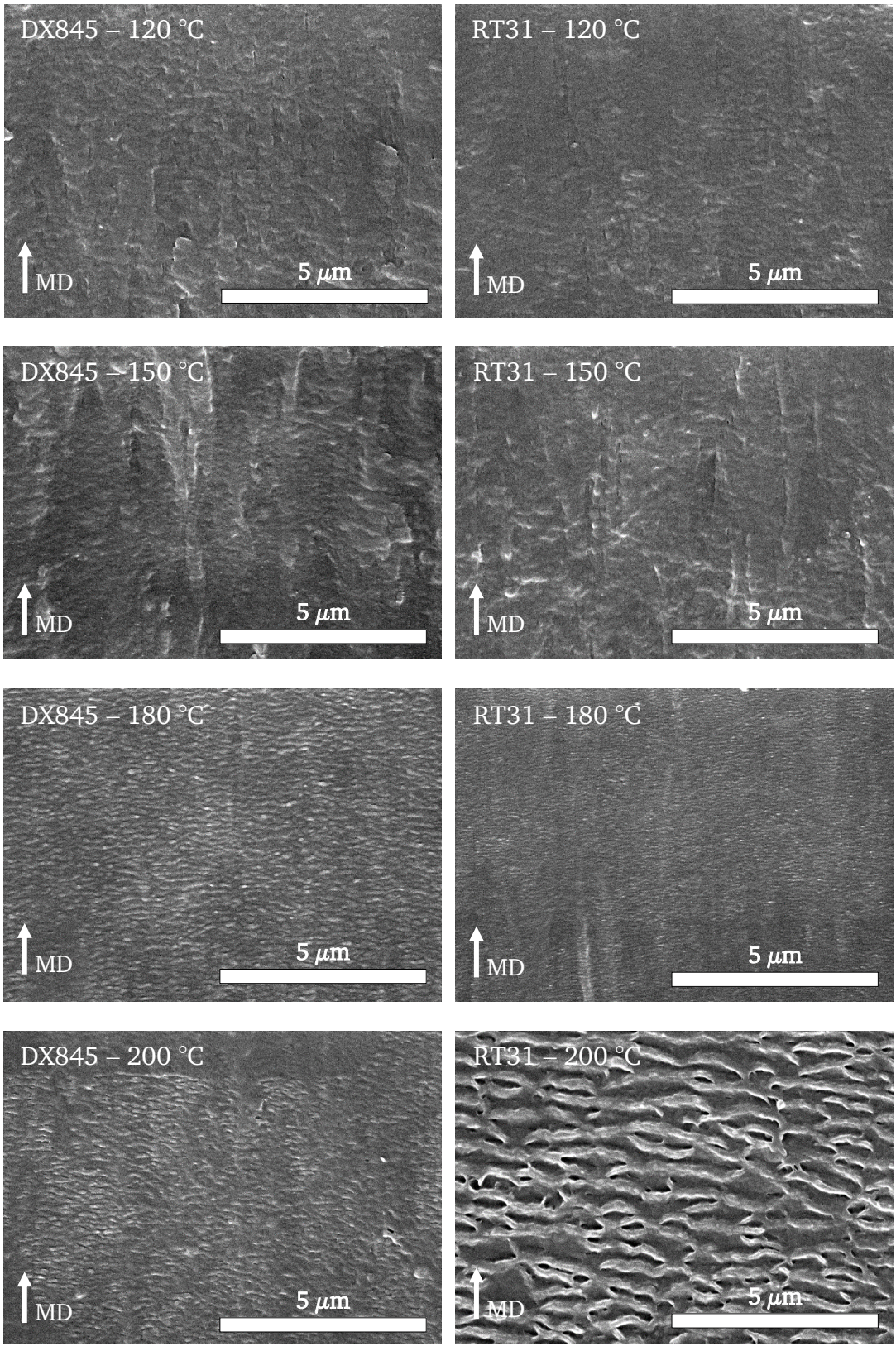

Figure 5.43: SEM images of MD stretched PMP films using RT31 and DX845 at annealing temperatures between 120 °C and 200 °C. Stretching temperature 110 °C, Annealing time 30 s.

No stacked lamellar structure can observed at annealing temperature below 180 °C. With increasing temperature, the morphology is more pronounced for RT31, while being less pronounced for DX845. The effect of annealing time in the range of 10 s to 60 s is shown in Figure 5.44.

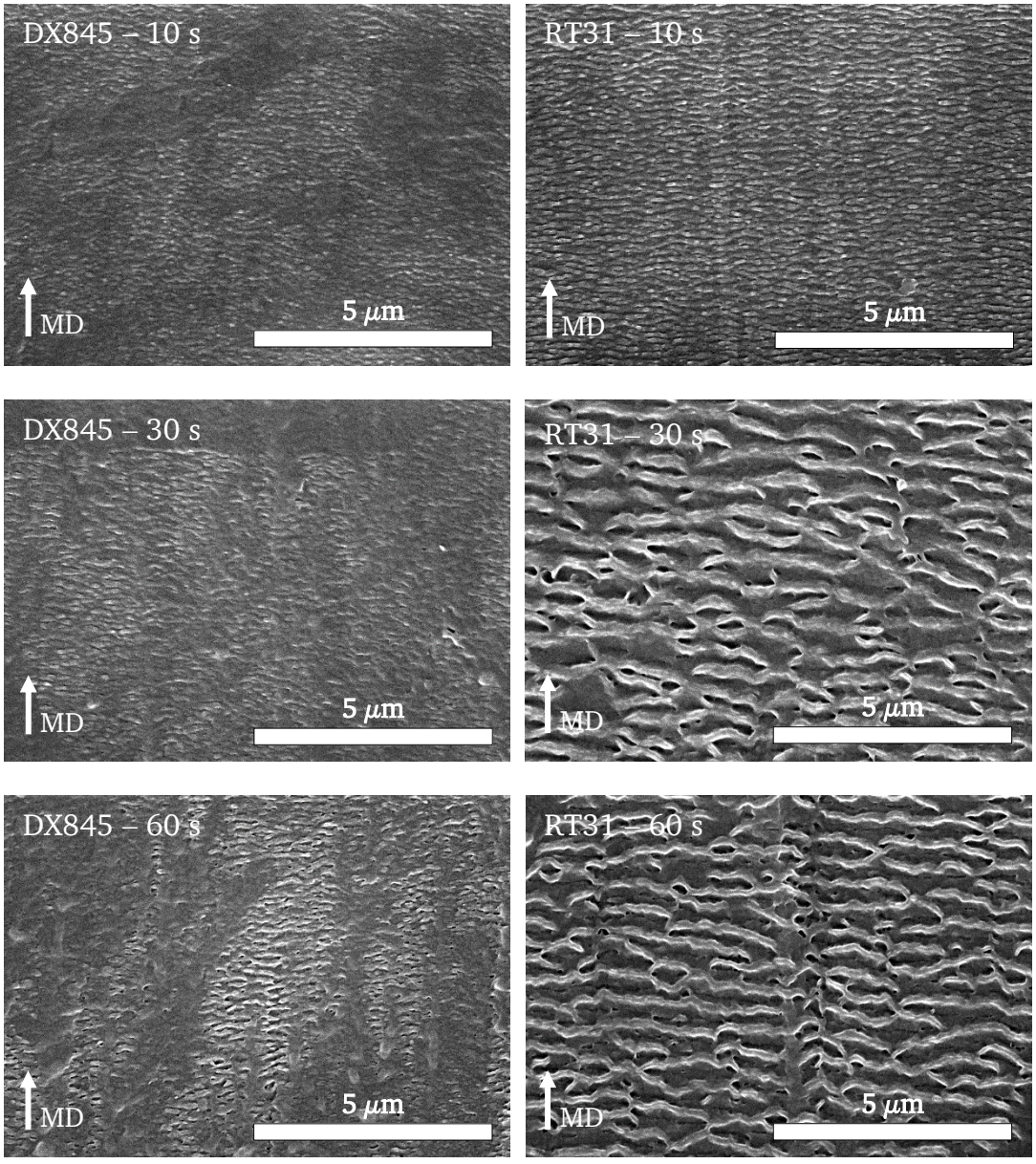

Figure 5.44: SEM images of MD stretched PMP films using RT31 and DX845 at annealing times between 10 s und 60 s. Stretching temperature 110 °C, Annealing temperature 200 °C.

Similar to an increase in temperature, the morphology becomes more pronounced for RT31, showing thicker lamellar crystals. With DX845, the increase in annealing time does not lead to a significant thickening of lamellar crystals.

5.4.3.2 Laboratory Extrusion

Three different grades of PMP and two solvents were processed on the laboratory line with the goal of producing cast films with sufficient quality. The main process parameters are listed in Table 5.16.

Table 5.16: Overview of laboratory line process parameters during trials with polymethylpentene materials.

Parameter	RT31	DX845	MX002
Solvent Type[a]	Shellsol T	Exxsol D140	Exxsol D140
Output [kg/h]	12	12	12
Solvent Content [%]	54	50	50
Chill Roll Speed [m/min]	-	2.1	2.1
Chill Roll Temperature [°C]	-	35	35
Castfilm Thickness [μm]	-	415-460	415-460

[a] An overview of solvent types can be found in 4.1.

The combination of RT31 with Shellsol T is not processable due to the lower boiling range of approximately 190 °C to 215 °C and foaming of the mixture upon exit at the die. Unfortunately, most of the material was used up during the test. DX845 and MX002 were extruded with Exxsol D140 instead, which has a boiling range of 260 °C to 370 °C. The inherently low viscosity of PMP was further lowered due to the mixture with solvent as can be seen from the melt flag at the die exit in Figure 5.45. Acceptable cast films could be produced with DX845 and MX002.

Figure 5.45: Pictures of PMP melt flag at the die exit of the laboratory line (left) and of cooled cast film after the casting unit (right).

A comparison of melt volume rate and melting enthalpy of both grades and dried cast films is given in n Figure 5.46.

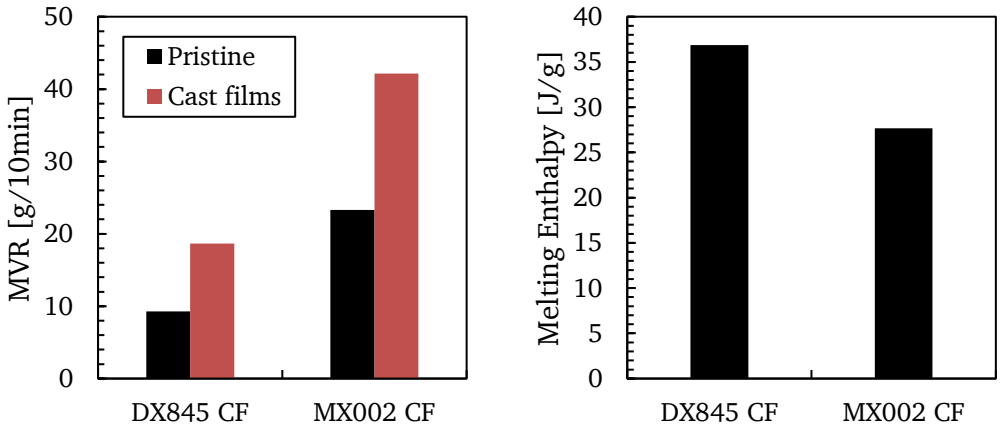

Figure 5.46: Melt Volume Rate (left) and Melting Enthalpy (right) of dried PMP cast films made of DX845 and MX002. MVR measured at 260 °C / 5 kg.

Melt volume rate is significantly higher for MX002 with approximately 9 g/10min for pristine DX845 and 23 g/10min for MX002. When processed into a cast film and stripped of its solvent by drying, melt volume rate increases further to approximately 19 g/10min for DX845 and 42 g/min for MX002, a near twofold increase in MVR compared to pristine material. DSC measurements also revealed a lower melting enthalpy of 27.7 J/g for MX002 compared to 36.9 J/g for DX845. Due to the huge range of reported heat of fusion values for PMP of 65 J/g to 119 J/g[130-132], a reliable degree of crystallinity could not be calculated.

5.4.3.3 MD Stretching

Cast films produced on the laboratory line were stretched on the KARO IV labstretcher using the conditions outlined in Table 5.17. A PET cover was used on both sides according to the laboratory method to avoid evaporation of solvent.

Table 5.17: KARO IV parameters used for MD stretching of PMP film samples from the laboratory line.

Parameter	Setting
Stretching Temperature [°C]	110 - 140
Pre Heating Time [s]	40
Stretching Ratio TD	3.5 – 5.5
Stretching Speed [%/s]	100
Annealing Temperature [°C]	160 - 220
Annealing Time [s]	30 - 300

Based on the results obtained from the stretching trials of compression molded samples, annealing temperatures were varied between 160 and 220 °C to further narrow the optimal processing window. In conjunction, annealing times as well as stretching temperatures and stretching ratios were tested as well.

The influence of annealing temperature on the morphology is shown in Figure 5.47.

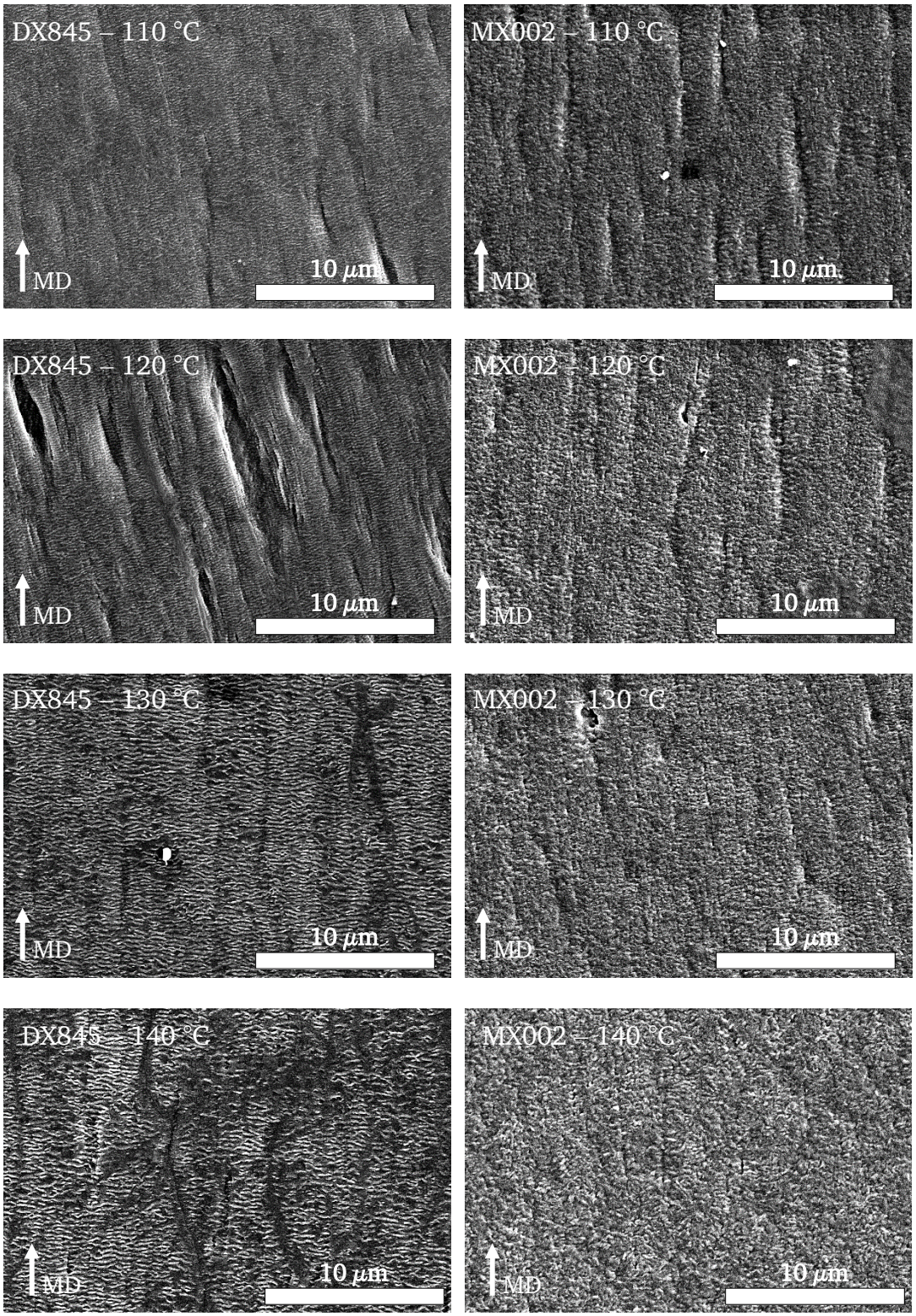

Figure 5.47: SEM images of MD stretched PMP films using DX845 and MX002 at stretching temperatures between 110 °C and 140 °C. Annealing temperature 180 °C, Annealing time 30 s, ratio 4.5.

As can be seen from the SEM images, DX845 readily develops a lamellar shish-kebab morphology at stretching temperatures as low as 110 °C with a significant increase in lamellar thickness at temperatures of 130 °C and higher. In contrast, MX002 does not develop a discernible shish-kebab morphology in the tested temperature range.

The effect of annealing temperature is further summarized in Figure 5.48 using a stretching temperature of 110 °C.

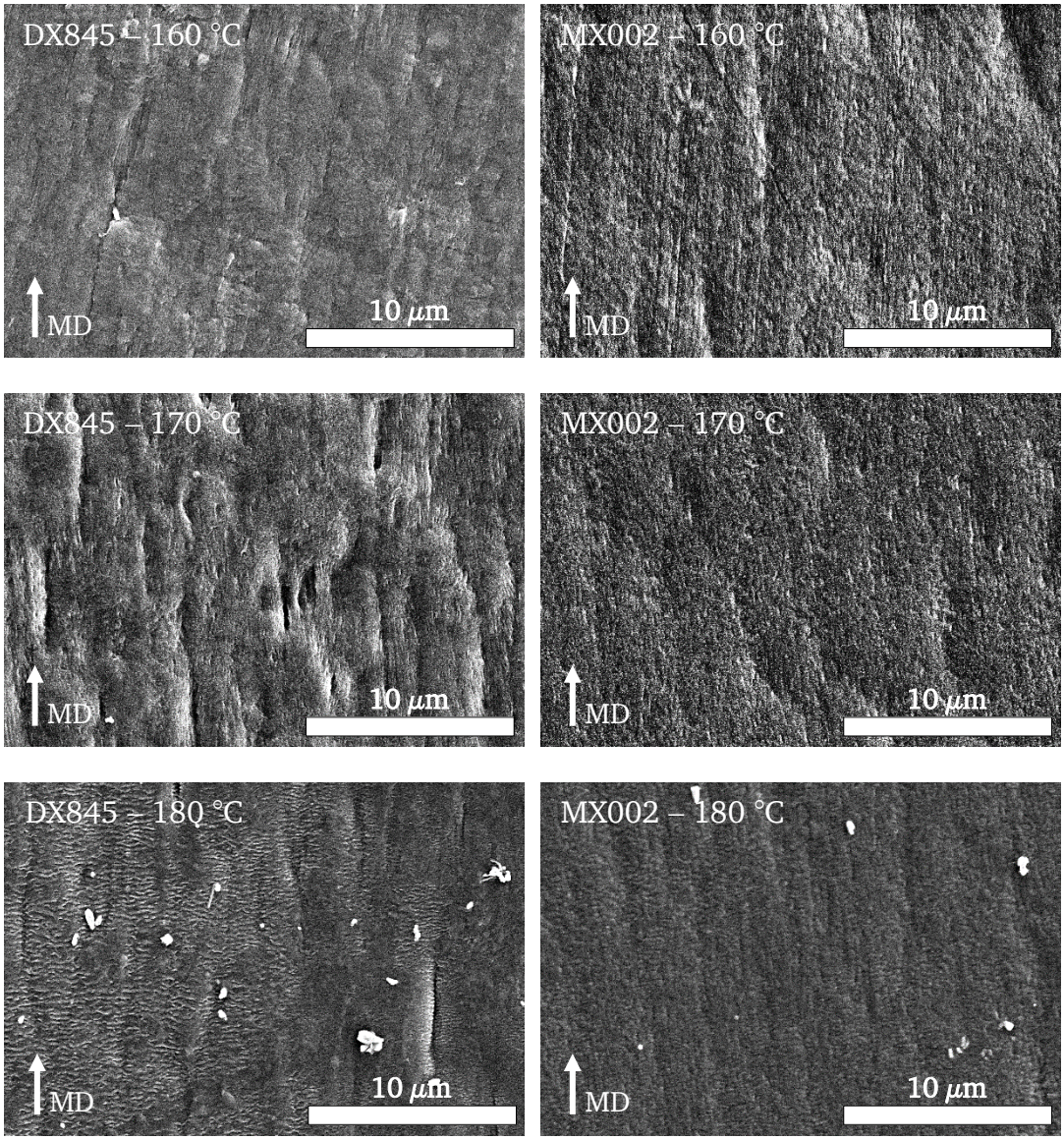

Figure 5.48: SEM images of MD stretched PMP films using DX845 and MX002 at annealing temperatures between 160 °C and 180 °C. Stretching temperature 110 °C, Annealing time 30 s, ratio 4.5.

It is evident from the results that a shish-kebab morphology will develop only at temperatures higher than 180 °C, confirming earlier results for the laboratory method

(see Figure 5.43). On the other hand, this kind of crystal structure does not develop for MX002 even at temperatures as high as 180 °C.

To find the upper limit for the formation of a stacked lamellar structure, annealing temperatures of 200 °C and 220 °C were applied to DX845. SEM images are given in Figure 5.49.

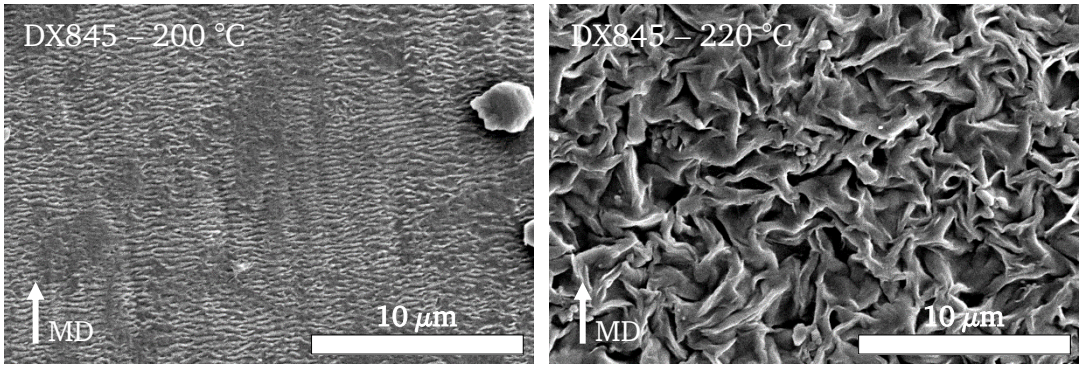

Figure 5.49: SEM images of MD stretched PMP films using DX845 at annealing temperatures 200 °C and 220 °C. Stretching temperature 110 °C, Annealing time 30 s, ratio 4.5.

At 200 °C an increase in lamellae thickness can be observed, while at 220 °C crystals have lost all alignment and are randomly dispersed on the surface. The thickness of the flake-like lamellar structure has increased in comparison to the morphology obtained using an annealing temperature of 200 °C.

Further experiments were done evaluating the effect of annealing time as well as stretching ratios on the crystalline structure. SEM images are shown in Figure 5.50.

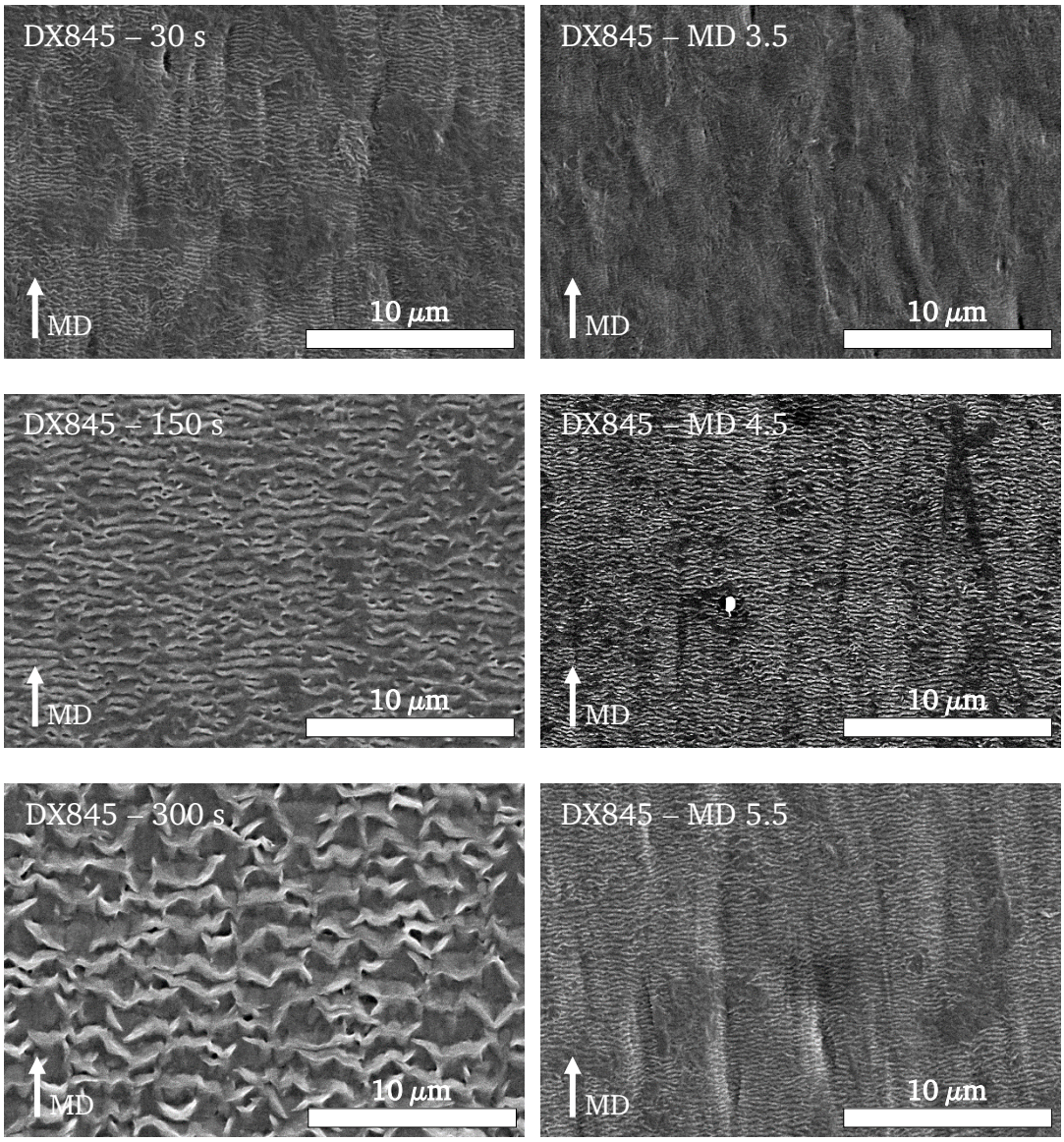

Figure 5.50: SEM images of MD stretched PMP films using DX845 at annealing times between 30 s and 300 s (left) and MD ratios between 3.5 and 5.5 (right). Stretching temperature 130 °C, Annealing temperature 180 s, ratio 4.5 (left), annealing time 30 s (right).

Longer annealing times lead to a thickening of the lamellar crystal overgrowth as well as the beginning of misalignment most visible after 300 s of annealing. With the increase in MD ratio from 3.5 to 4.5 a significant increase of shish-kebab morphology can be achieved. However, no differences can be found for MD ratios 4.5 and 5.5.
DSC measurements were done for dried MD stretched films to find optimal stretching conditions based on the formation of a shish-kebab crystal morphology. The melting enthalpies plotted against stretching temperatures are shown in Figure 5.51.

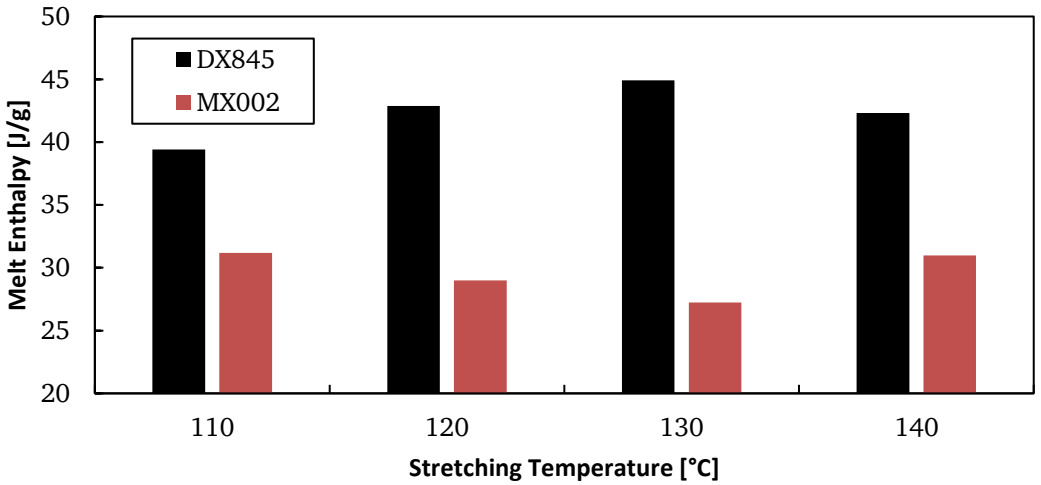

Figure 5.51: Melting enthalpy of MD stretched PMP films stretched at temperatures between 110 °C and 140 °C.

Melting enthalpies for DX845 increase with a rise in stretching temperature from 39.4 J/g at 110 °C to 44.9 J/g at 130 °C. At 140 °C a slightly lower enthalpy of 42.3 J/g was found. For MX002, rather than increasing enthalpy, higher stretching temperatures actively lowered the enthalpy from 31.2 J/g at 110 °C to 27.2 J/g 130 °C.

5.4.3.4 TD Stretching

Using a stretching temperature of 130 °C and an annealing temperature of 180 °C, MD samples were produced on the KARO IV and subsequently stretched in TD using the following settings.

Table 5.18: KARO IV parameters used for TD stretching of PMP film samples from the laboratory line.

Parameter	Setting
Stretching Temperature [°C]	90 - 150
Pre Heating Time [s]	40
Stretching Ratio TD	4.0
Stretching Speed [%/s]	25 - 100
Annealing Temperature [°C]	90 – 150
Annealing Time [s]	60

The aim of these trials were to obtain homogeneous porous films by finding optimal stretching conditions. The focus was again set on stretching temperatures as well as preheating times and stretching speed. Annealing temperature, having only a minor role in pore formation, was set to the stretching temperature in each experiment. Typical samples obtained by these trails are shown in Figure 5.52.

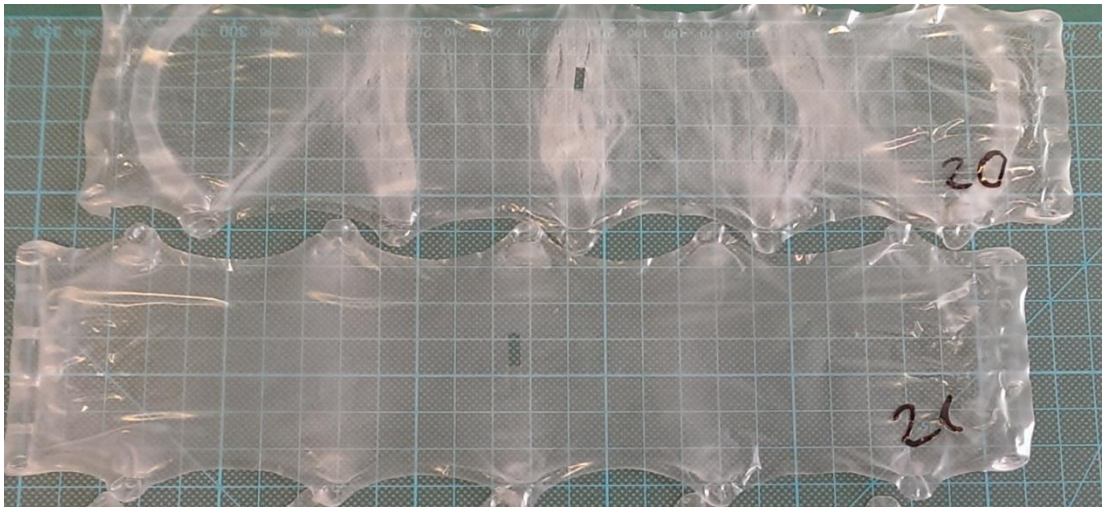

Figure 5.52: Typical optical appearance of TD stretched PMP films produced in this study. Stretching temperature 130 °C. Top: Preheating time 20 s. Bottom: Preheating time 10 s.

Depending on the stretching temperatures and preheating times two different types of films were obtained: more homogeneous transparent films, and inhomogeneous, locally opaque films with thinned out transparent regions in between. In all cases no homogeneous porous films could be achieved, as evidenced by failed Gurley measurements.

Stretching forces recorded during the experiments are shown in Figure 5.53 and Figure 5.54 in a comparison of stretching temperature and preheating temperature respectively.

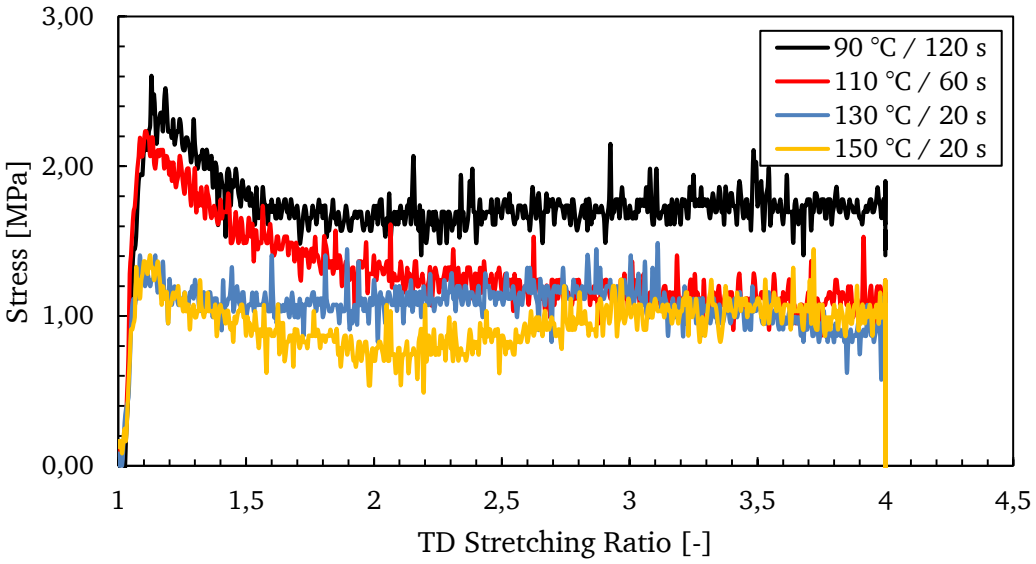

Figure 5.53: Comparison of stretching stress during TD stretching of PMP MD films at temperatures between 90 °C and 150 °C.

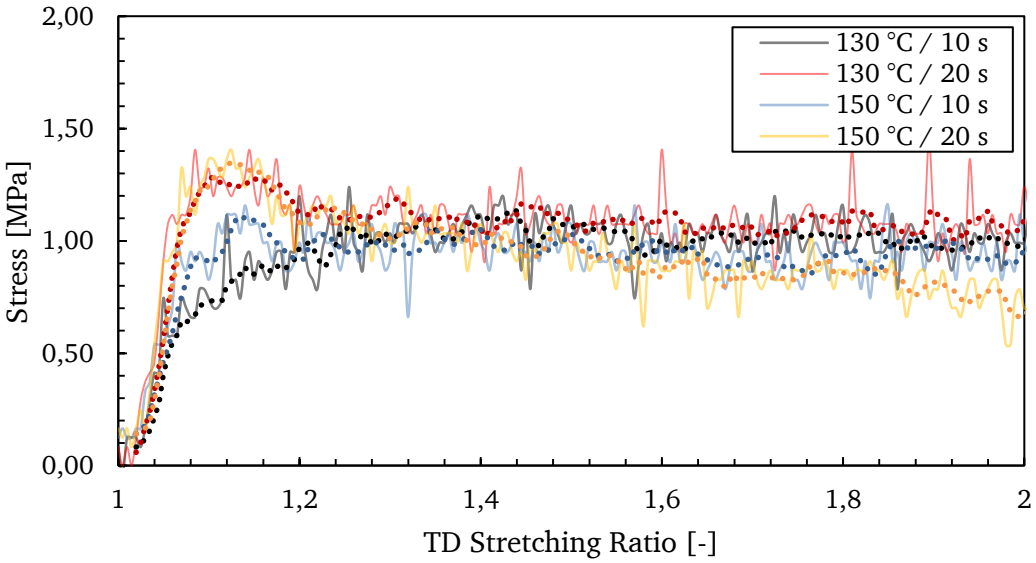

Figure 5.54: Comparison of stretching stress during TD stretching of PMP MD films at temperatures of 130 °C and 150 °C at 10 s and 20 s preheating times. Dotted lines represent moving average.

As expected, Figure 5.53 shows a decrease in stretching forces with increasing temperature and a reduction of the prominent forces of approximately 2,2 MPa associated with the yield point at temperatures below 130 °C. A comparison of preheating times from Figure 5.54 also reveals a reduction in yield force with increasing preheating time at a given temperature. While the yield point at 20 s preheating time can be found to be around a ratio of 1.12 (12 % strain) it is much more difficult to pinpoint the yield point for preheating times as low as 10 s.

SEM images of the stretched film samples were taken at a location near the labstretcher clips, where opaqueness appeared most prominent. The influence of stretching temperature on the morphology is summarized in Figure 5.55.

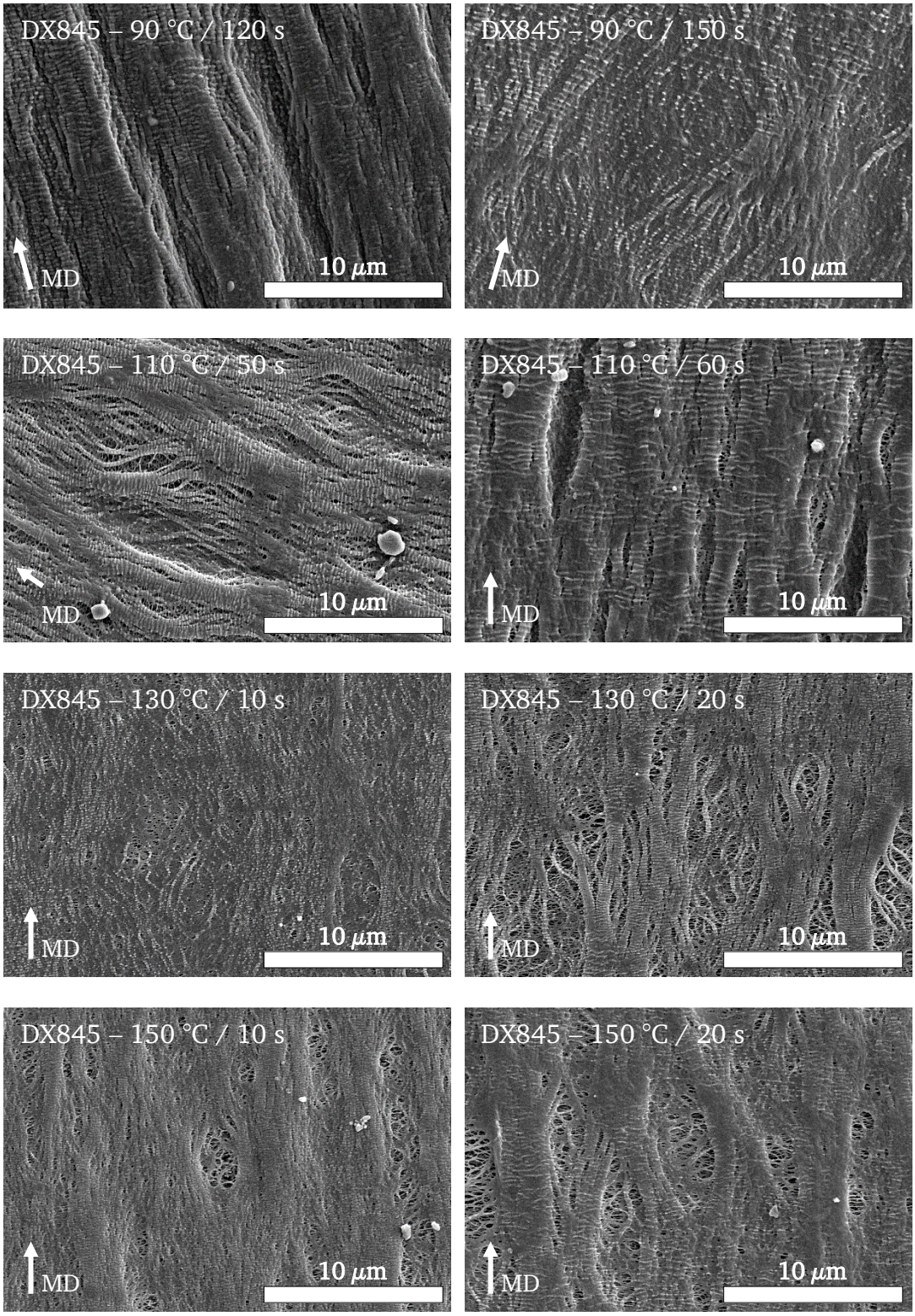

Figure 5.55: SEM images of TD stretched PMP films using DX845 at stretching temperatures between 90 °C and 150 °C at various preheating times. Annealing was done at stretching temperature for 60 s. Stretching ratio was 4.0 at a rate of 50 %/s.

In all cases fibrillation of the crystal structure is visible with additional pores becoming apparent at temperatures of 110 °C and higher. Preheating times and stretching temperature have a significant effect on the formation of pores, with high preheating times leading to a more dense surface morphology as evidenced by films stretched at 90 °C and 110 °C. On the other hand, short preheating in the case of stretching temperatures of 130 °C and 150 °C also leads to less pore formation. Based on these images an optimum seems to be a stretching temperature of 130 °C at 20 s preheating time. However, even in the best cases, only a low amount of pores have been formed with no measurable Gurley value of the films.

Using the optimized settings, further trials were done focusing on stretching rate. SEM images of the surface of these films are shown in Figure 5.56.

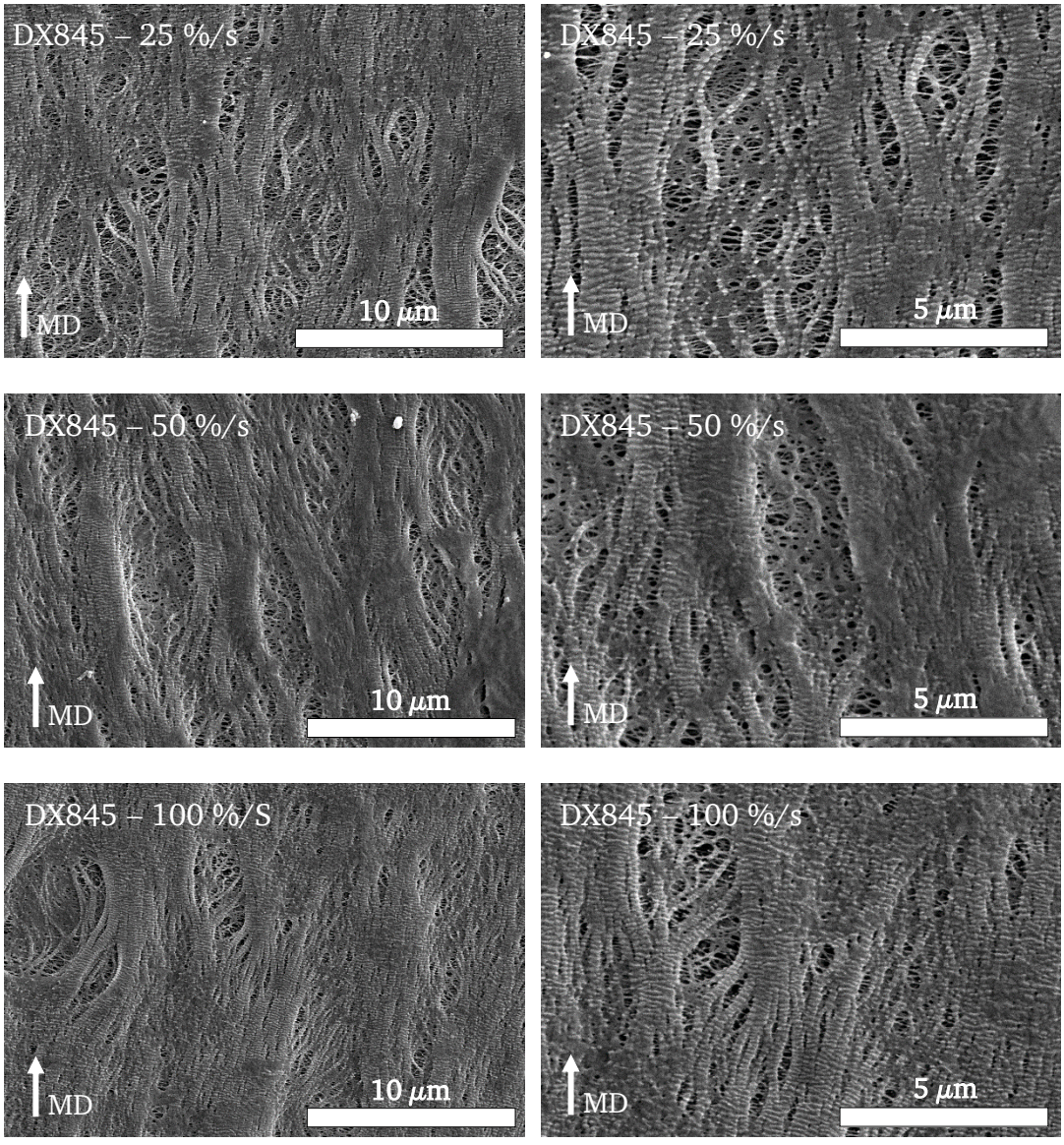

Figure 5.56: SEM images of TD stretched PMP films using DX845 at stretching rates between 25 %/s and 100 %/s. Stretching temperature 130 °C. Preheating time 20s.

The images show that a stretching speed of 25 %/s leads to a more porous surface with increased fibrillation of the crystalline phase. Even at these settings, large crystalline regions are still intact and unstretched.

To further evaluate the inhomogeneous stretched samples, SEM images were taken at different spots along the TD direction of the film, sampling opaque as well as transparent regions. The result is summarized in Figure 5.57.

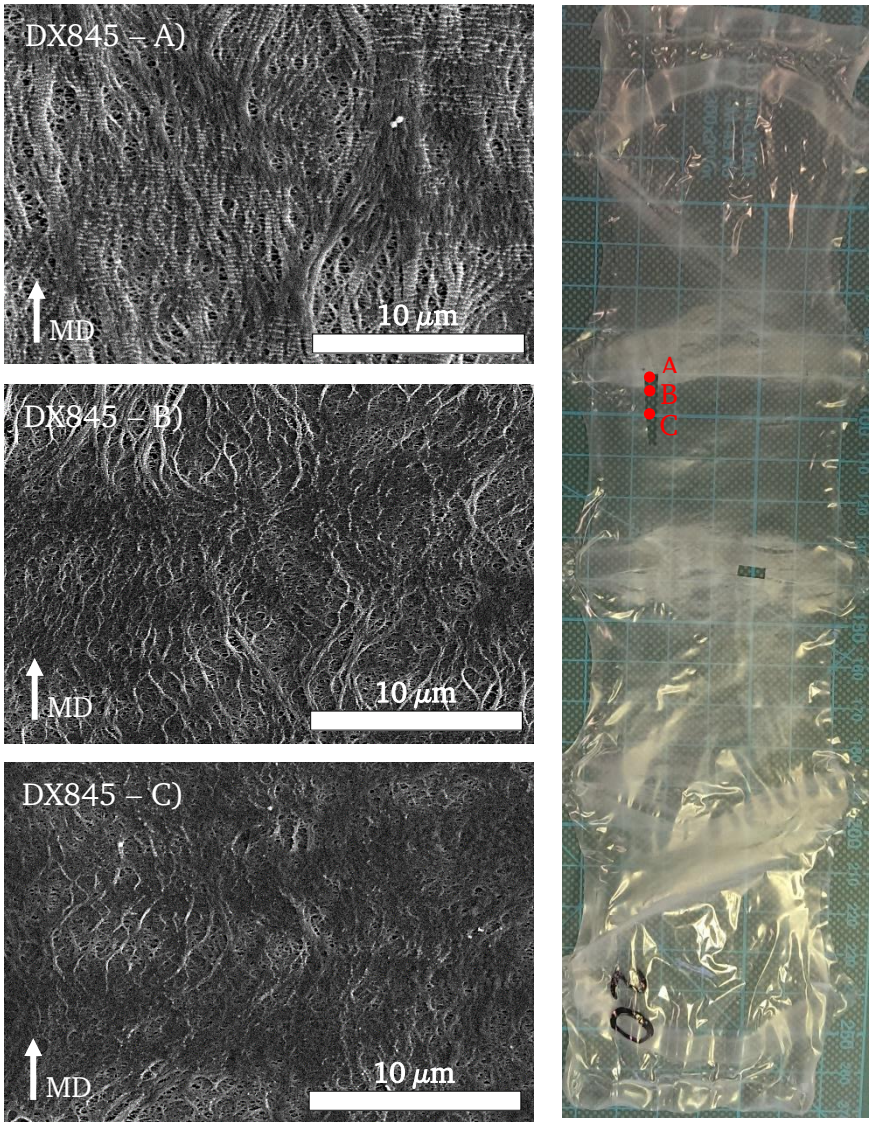

Figure 5.57: SEM images of TD stretched sample of PMP film at different positions (left). Photograph of a TD stretched sample (right). SEM sampling positions are indicated in the photograph. Stretching temperature 130 °C at a stretching ratio of 50 %/s.

With increasing distance from opaque regions towards transparent regions a significant change in surface morphology can be observed. While in the opaque regions

crystalline fibrillation and pore formation can be observed, the transparent regions show a dense surface with small crystalline fragments.

5.4.3.5 BAL Offline

The processability of PMP was tested offline (roll-to-roll) on the pilot line using cast film rolls produced on the laboratory line. The MDO was setup as described in Table 5.19.

Table 5.19: MDO settings during offline stretching trials of PMP film on the pilot line.

Parameter	Setting
Speed [m/min]	1,5
Stretching Temperature [°C]	125
Stretching Ratio TD	3.5 / 4.5
Annealing Temperature [°C]	150[a]

[a] Temperature limit of pilot line MDO.

Unfortunately the temperature limit of the MDO is reached at 150 °C while 180 °C are needed for the formation of a shish-kebab morphology. Still, some additional difficulties concerning processability could be observed. Figure 5.58 shows photographs of the first annealing roll set to 150 °C and the winding roll after the MDO.

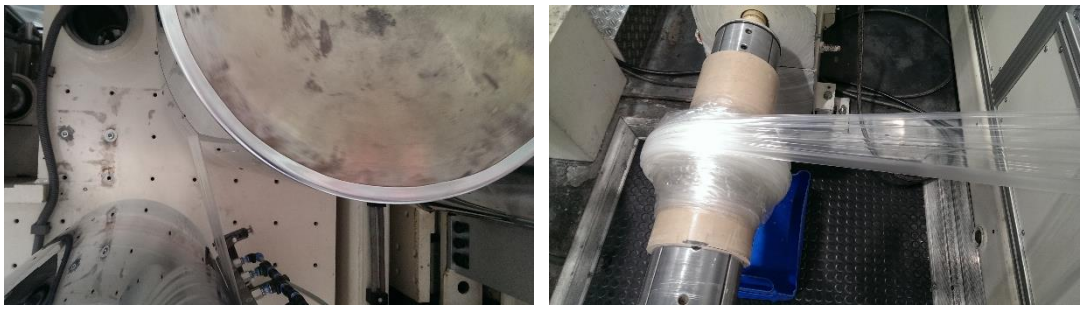

Figure 5.58: Photographs of MDO annealing rolls during pilot line offline stretching trials of PMP cast film (left) and winding of stretched PMP MD film (right).

One of the difficulties in stretching PMP is its elasticity, making it stick easily to the rolls at elevated temperatures as seen to the left of Figure 5.58. Additionally, winding of the sample turned out to be difficult as the material began to be deformed by the tension applied by the winder.

5.4.3.6 HDPE/PMP Blend

To counteract low viscosity and elasticity of PMP a blend with HDPE was tried to increase temperature resistance of HDPE. 10 % to 20 % of PMP were added to the extrusion. DSC measurement of the extruded blends are shown below.

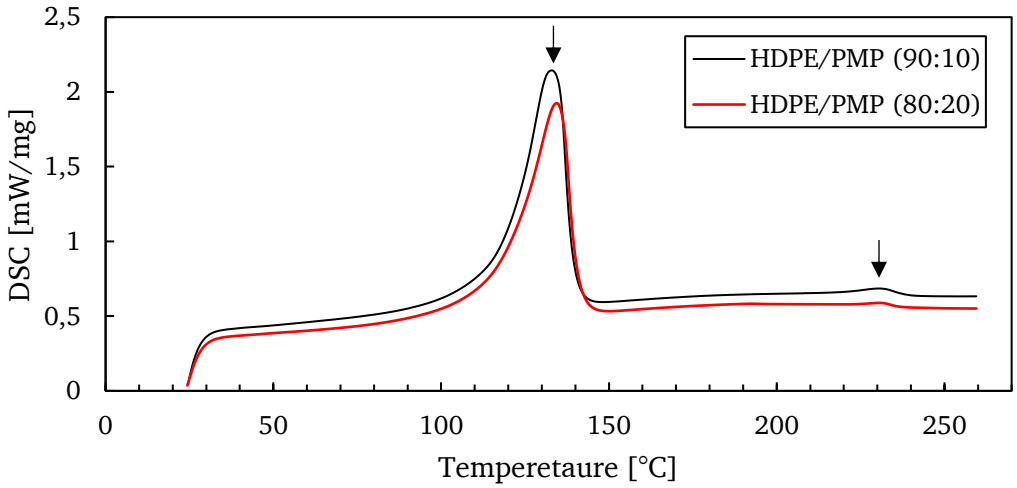

Figure 5.59: DSC analysis of HDPE/PMP blended cast films. PMP content 10 % and 20 %. Melting point of HDPE (137 °C) and PMP (230 °C) are marked.

From the thermograms both HDPE and PMP show their distinct signals corresponding to their individual melting points, with increasing melting enthalpy of PMP as expected by an increase in content. Additionally, photographs of the melt at the die exit are shown in Figure 5.60.

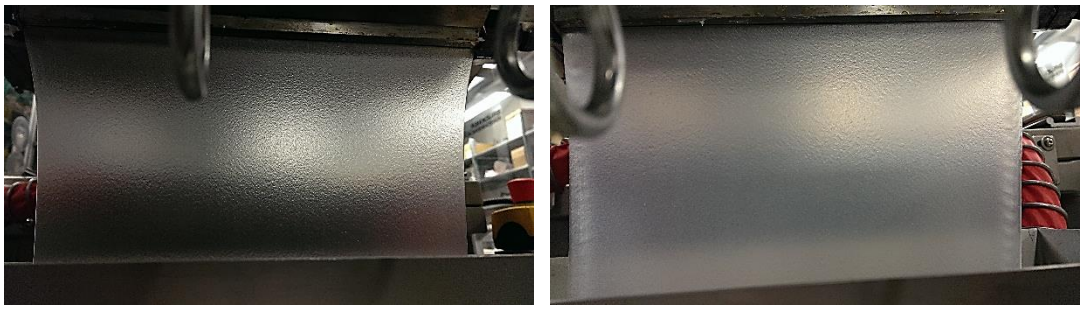

Figure 5.60: Photographs of HDPE/PMP blend melt flags at the exit of the extrusion die of the laboratory line. Left: HDPE/PMP (90:10). Right: HDPE/PMP (80/20).

In both cases a homogeneous melt could not be achieved. The surface of the melt exhibited a rough surface with many imperfections, making it unsuitable for the production of battery separator film.

5.4.3.7 Discussion

In order to find a suitable process window for pore formation, several trials were carried out using the laboratory method as well as the laboratory extrusion line to analyze crystallization behavior of PMP. To that end, stretching as well as annealing conditions were varied in a large range on the KARO IV labstretcher to achieve a shish-kebab morphology similar to HDPE stretched using EVAPORE® conditions. It was found that for DX845 a critical minimum annealing temperature of approximately 180 °C is necessary for the formation of the shish-kebab morphology as seen by Figure 5.43 and Figure 5.48. Increasing the annealing temperature and time further leads to a thickening of the lamellar crystals (see Figure 5.48 to Figure 5.50). However, at temperatures as high as 220 °C, randomly aligned crystals are formed, as a larger fraction of the polymer transfers to the molten state, resulting in a loss of molecular orientation. Stretching ratio is another key aspect in regards to the formation of a shish-kebab morphology. This type of crystallization is only possible at sufficient molecular orientation of the polymer chains. During stretching, stress-relaxation of polymer chains reduces the effect of orientation, making a minimum stretching ratio necessary. It was found that a MD stretching ratio of 4.5 is sufficient for significant growth of stacked lamellar crystals, while at a ratio of 3.5 no lamellar structure is observed. In general, the onset of the formation of a stacked lamellar morphology can be reduced by increasing molecular weight, as the stress-relaxation phenomena is tied to the viscosity and therefore chain length of the polymer solution.

While not as important as the annealing temperature, stretching temperature was found to be optimized at 130 °C, as judged by the SEM images in Figure 5.47 and from DSC analysis as shown in Figure 5.51. A high amount of crystallinity is beneficial to the formation of the shish-kebab morphology. In the range of 110 to 140 °C, stretching at 130 °C lead to the highest measured melting enthalpy, corresponding to a higher degree of crystallinity.

In contrast to DX845, MX002 did not show any significant stacked lamellar morphology even at annealing temperatures as high as 200 °C. This can be attributed to an overall lower crystallinity of the material as evidenced by the DSC analysis of pristine material, cast films and MD stretched films (see Figure 5.46 and Figure 5.51). In all three cases, enthalpy measured was significantly lower for MX002 than for DX845. When stretched in MD, enthalpy for the MX002 material did not increase in comparison to the cast film. Both measurements showed an enthalpy of about 27 J/g. For DX845 on the other hand, an increase from about 37 J/g for the cast film to about

45 J/g for the MD stretched films were measured. The increase can be attributed to the stretching and orientation of the polymer chains as well as to thickening of lamellar crystals during annealing. MX002 did not show any increase in enthalpy, corresponding well to the images taken by SEM analysis. Both MX002 and DX845 showed an increase in MVR value of the cast films compared to the pristine material. As told by the manufacturer, a certain amount of decomposition during the extrusion of the material is to be expected due to chain cleavage resulting from high temperature and shear in the extrusion system. The lower melting enthalpy and higher MVR values of MX002 compared to DX845 indicate an increased fraction of $C_{2\text{-}22}$ α-olefins in the copolymer, resulting in an increased hindrance for crystallization. The MX002 material is specially marketed for increased stretchability, for which a decreased crystallinity can be helpful. In the case of battery separators, high crystallinity is a key requirement for pore formation according to the EVAPORE® process. For that reason, the material MX002 was disqualified for further use.

Lastly, the material RT31 was tested as well, using the laboratory method. RT31 showed similar tendencies than DX845 regarding stretching and annealing conditions, with increased crystal thickness compared to DX845. Unfortunately the material ran out during the laboratory line trials, when tested with the unsuitable solvent ShellSol T. Therefore, only DX845 was used for TD stretching trials.

As pore formation primarily occurs during the TD stretching of the film, most focus was set to the stretching conditions. Annealing, used only to fix the molecular structure and to evaporate remaining solvent, was set to the same temperature as stretching. The morphology of the samples was analyzed by SEM. Unfortunately no homogeneous and porous sample could be achieved. Therefore, Gurley as well as porosity could not be determined. The stretching conditions were varied in terms of temperature and preheating times, the latter controlling the amount of residual solvent during stretching, which is an important parameter for pore formation. The stress-strain curves shown in Figure 5.53 and Figure 5.54 show the influence of temperature and preheating time on the measured stress. At lower temperatures up to 110 °C a distinct yield point can be observed, that is subsequently reduced when stretching temperature is raised to 130 °C and above. This is typical for the stretching of a thermoplastic material, as the additional energy is needed for crystal deformation in semi-crystalline materials. Directly after the yield point, stretching stress is decreasing rapidly, as the first crystals have already yielded and the film starts to thin, transitioning into a distinct necking of the material starting from a stretching ratio of about 1.5 to 2.0 as indicated

by a nearly constant value for stretching stress. This strong necking behavior can also be inferred from the optical appearance of the stretched samples as seen in Figure 5.52. The sample stretched at 130 °C preheated for 20 s shows whitening at the clips, with transparent and much thinner areas visible in between. Once the stretching stress has reached a constant value, the thinner transparent areas are the ones that are primarily stretched, as much less force is needed compared to the regions directly at the clips. This can be somewhat homogenized, when preheating time is lowered to 10 s. The samples are overall more transparent and thinning in between the clips is less pronounced. Also, as seen from Figure 5.54, no clear yield point is visible with decreased preheating times. This behavior can be attributed to the plasticization by the solvent. However, a transparent appearance of the samples generally infers that a sufficient pore structure has not been formed, due to the lack of optical refraction at pore walls. This was confirmed by SEM analysis as seen in Figure 5.55. For these measurements, samples were taken out of the center of the film samples at a location in between clips. From the images, the formation of pores can be confirmed, with a stretching temperature of 130 °C and 20 s preheating time showing the most open porous surface between oriented crystalline branches. As discussed before, a preheating time of 10 s on the other hand, did not lead to significant pore formation and the crystalline structure is barely visible, leading to the conclusion that the increased residual amount of plasticizer lowers the onset of plastic deformation of the crystals. Unfortunately, even at optimized preheating conditions, no homogeneous porous sample could be obtained. Judging by the images taken in the SEM, pore formation is initiated by micro cracks in between the crystalline structure, similar to HDPE. In contrast to HDPE, however, pore formation is soon halted as the stretching forces are diverted to the thinned regions, leading to pronounced necking of the samples. The initial stage of pore formation is therefore never overcome. The change in morphology along the sample is presented in Figure 5.57 and shows more dense surfaces with visibly less crystalline phases when transitioning from the opaque regions to the thinned out transparent regions. A change in stretching rate did not change the general necking behavior and still produced inhomogeneous results.

As samples were only stretched on the KARO IV machine using the laboratory method, a first trial on the pilot line MD orientation device was made using cast films produced on the laboratory line. During these trials some problems regarding elasticity and stickiness of the material arose that limited the processability. The problems can most likely be explained by the high MVR value exhibited by typical PMP materials, which

is a function of copolymer composition. As the MD annealing temperature on the pilot line is limited to 150 °C compared to at least 180 °C needed for sufficient recrystallization into a shish-kebab morphology, scale-up of the laboratory method was not possible in the given time frame.

Finally, to overcome the problems with pore formation, a blend of HDPE and PMP was tested on the laboratory line to combine both, the low MVR and melt strength of the HDPE and the higher temperature stability of PMP. While DSC analysis showed that the cast films exhibited crystalline phases of both HDPE and PMP, quality of the melt at the die exit was insufficient for separator production (see Figure 5.60). The reason for the incompatibility of HDPE and PMP is most likely the difference in viscosities of both materials, with PMP having much lower viscosity compared to HDPE. It is therefore difficult to produce homogeneous mixtures.

5.4.4 CONCLUSION

Compounding of HDPE using a ceramic filler proved successful in term of processable film as it could be mixed in concentrations up to 40 %. Incorporation of an inorganic filler such as Boehmite resulted in increased porosity during TD stretching due to the formation of vacuoles in the vicinity of the particles. This is attributed to the weak interface between HDPE and the particle itself, although this was improved slightly by silane surface modification of the Boehmite particles. However, while having a positive influence on the performance characteristics of a separator, shrinkage was affected negatively, as higher values were observed compared to pristine HDPE. The incorporation of an inorganic filler proved unsuitable in this study to achieve higher thermal stability.

Using PP for the EVAPORE® process was difficult due to the brittleness of cast films produced by a mixture of PP and solvent. Several approaches were taken to reduce the brittleness of the mixture and achieve stable films. The only successful approach was the addition of alpha-nucleating agents into the polymer itself, as stable cast films as well as MD films could be produced. However, MD films containing this material became very brittle and TD stretching was not possible. It is expected, that optimization of the nucleating agent type and content is necessary to find a suitable process window for both cast film production as well as film stretching.

Regarding PMP, it could be proven, that choosing the right conditions, PMP material DX 845 can behave similar to HDPE in regards to the formation of a shish-kebab morphology while also showing similar tendencies during the deformation of MD stretched films to form pores. In contrast to HDPE, however, pore formation does not exceed the initial stages of micro cracking as distinct necking is prevalent during TD stretching, resulting in overall much denser and transparent films. The material MX002 on the other hand is not suitable for battery separator production as the crystallinity of the samples is not high enough, most likely due to the higher content of $C_{2\text{-}22}$ α-olefins in the copolymer. While RT31 could not be tested further on the laboratory line in the given time frame due to material shortage, this could be an interesting candidate, as the results from the MD stretching showed increased lamellar thickness compared to DX845, indicating a higher crystallinity of RT31 processed at the same conditions as DX845.

Blending of HDPE and PMP is not suitable for the EVAPORE® process, as the melt quality suffers significantly by the addition of PMP into HDPE. The differences in melt viscosity of HDPE and PMP can be regarded as the main reason for unsuccessful blending of the materials.

5.5 ULTRA HIGH MOLECULAR WEIGHT POLYETHYLENE (UHMWPE) SEPARATOR

Several different grades of UHMWPE were evaluated in laboratory and pilot scale. Laboratory line trials were used to find suitable extrusion conditions and to evaluate final film properties. The best results were transferred to the pilot line. Table 5.20 presents an overview of the tested UHMWPE material grades.

Table 5.20: Overview of UHMWPE materials used in this study.

Property	GUR 4018	GUR 4012	GUR 4120	GUR 2122	HiZex 145M
Manufacturer	Celanese	Celanese	Celanese	Celanese	Mitsui
MW [Mg/mol]	0.7	1.8	5.0	5.0	1.15
Bulk Density [g/cm³]	0.4	0.4	0.4	0.2	0.49
Particle size D50 [μm]	120	120	120	120	150
Particle shape	Spherical	Spherical	Spherical	Sponge	Spherical

Molecular weight was varied between 0.7 Mg/mol and 5 Mg/mol with particle size D50 remaining at a comparable level. GUR2122 exhibits a different particle shape, with a much rougher and porous surface. This is also evident in its lower bulk density. The advantage of this material might be better solubility during mixing in the extrusion system. Due to a material shortage, HiZex 145M was tested on the pilot line only.

5.5.1 LABORATORY LINE

The laboratory line was used to evaluate the processability of ultra-high molecular weight materials in the extrusion by optimizing solvent content and machine parameters. In many cases a blend of UHMWPE with HDPE was necessary to reduce viscosity and increase processability. Whenever a blend was used, a powdered HDPE with a molecular weight of 0.3 Mg/mol (Asahi Sunfine SH800) was mixed with the UHMWPE beforehand and dosed into the extrusion with one dosing unit. The main line parameters found to be acceptable for BSF are listed in Table 5.21.

Table 5.21: Overview of laboratory line process parameters during trials with UHMWPE materials.

Parameter	GUR 4018	GUR 4012	GUR 4120	GUR 2122
Solvent Type	SiSol D60	SiSol D60	SiSol D60	SiSol D60
HDPE Content [%]	-	0-50	50	50
Solvent Content [%]	60-65	65-75	65-70	65
Output [kg/h]	12	8	8	8
Chill Roll Speed [m/min]	2.1	1.2	1.4	1.3
Chill Roll Temperature [°C]	35	35	35	35
Castfilm Thickness [μm]	420-440	420-475	430	400-440
MD Ratio	3.5-5.5	3.5-5.5	3.5-5.5	3.5-5.5
Stretching Temperature[a] [°C]	85 / 104	85 / 104	85 / 104	85 / 104
Annealing Temperature [°C]	98	98	98	98

[a] The film is stretched between two individually heated rolls

The solvent content needed to be increased to 65 % in general to obtain a smooth melt and cast film surface and to overall increase homogeneity. In all cases except for GUR2122 small spots were observed in the melt and on cast films and MD oriented films. Several MD oriented films were produced for further evaluation on the KARO IV labstretching system. The stretching conditions were kept at values similar to the stretching of HDPE separator films. During stretching of the MD oriented samples, the settings described in Table 5.22 have been used.

Table 5.22: KARO IV parameters used for TD stretching of UHMWPE film samples from the laboratory line.

Parameter	Setting
Stretching Temperature [°C]	60-80
Pre Heating Time [s]	5-10
Stretching Ratio TD	1.5 – 5.5
Stretching Speed [%/s]	10
Annealing Temperature [°C]	120
Annealing Time [s]	60

Different preheating times were needed to optimize porosity and optical appearance of stretched films. To evaluate the influence of stretching ratio, five different ratios have been used between 1.5 and 5.5.

5.5.1.1 Influence of Molecular Weight

One of the supposed key advantages of UHMWPE for BSF is its higher mechanical strength induced by the increased molecular weight of the material. The following results compare three different types of UHMWPE in terms of its molecular weight. When possible, a blend with HDPE was avoided to allow for highest mechanical strength. Figure 5.61 compares porosity of final separator film made of three different materials using 65 % of solvent during cast film production.

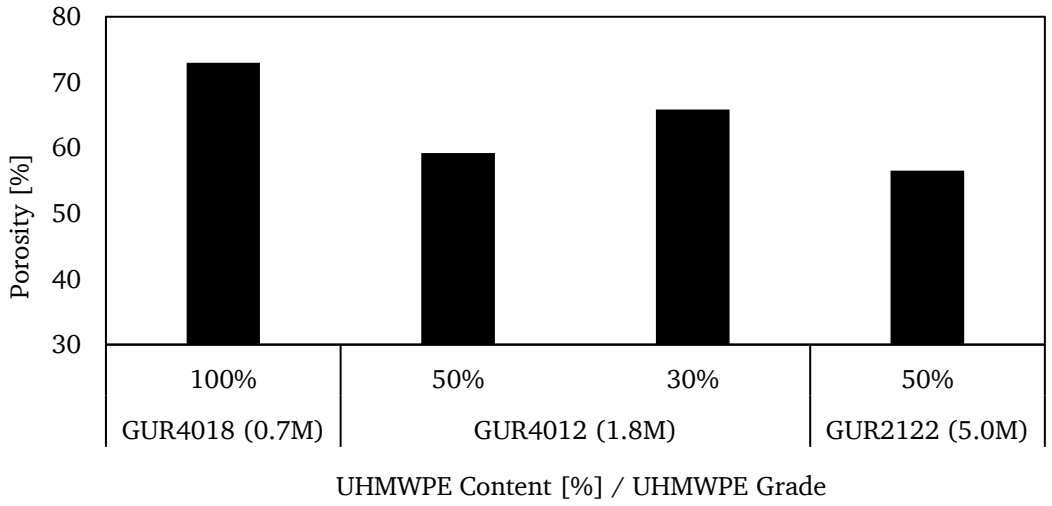

Figure 5.61: Porosity of TD stretched films containing UHMWPE grades of molecular weight between 0.7 to 5 Mg/mol.

It is clear from the results that an increase in molecular weight leads to a reduction in porosity from very high values of 73 % for GUR4018 to 57 % for GUR2122. Not surprisingly, a reduction in UHMWPE content in a blend of GUR4012 with HDPE lead to an increase in porosity from 59 % to 66 %. Despite the measured high porosity values, no measurable Gurley value was obtained.

While porosity is an important requirement for BSF, the main focus was set on the mechanical strength of the materials. Tensile strength and normalized puncture strength are compared in Figure 5.62 and Figure 5.63.

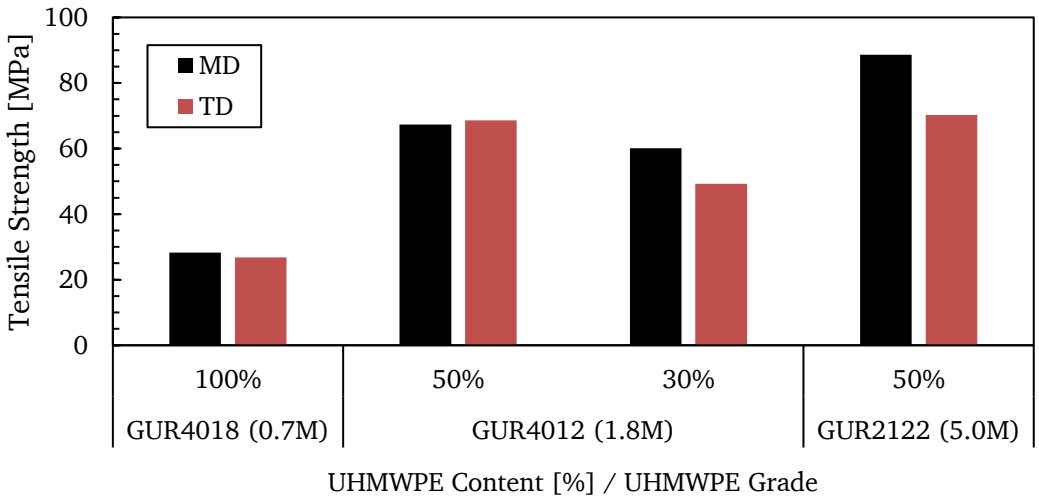

Figure 5.62: Tensile Strength of TD stretched films containing UHMWPE grades of molecular weight between 0.7 to 5 Mg/mol.

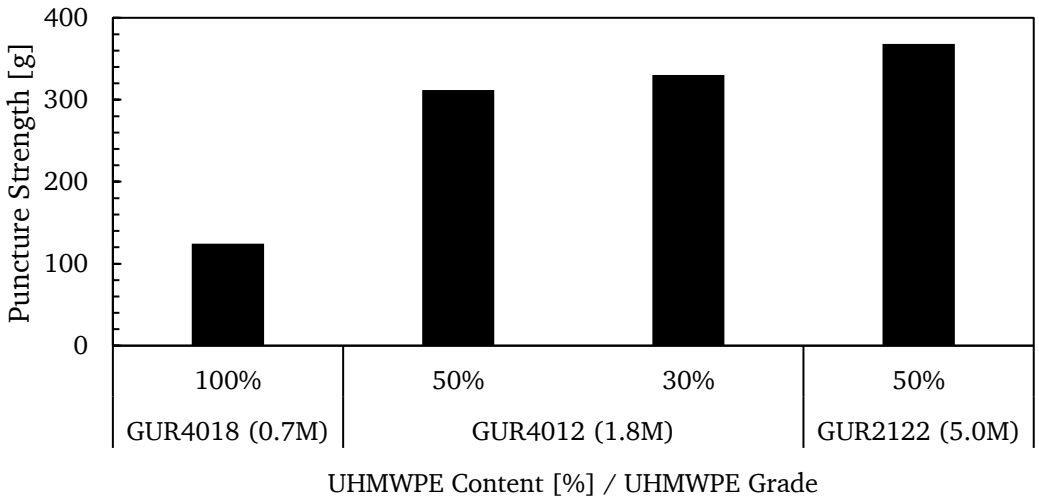

Figure 5.63: Puncture Strength of TD stretched films containing UHMWPE grades of molecular weight between 0.7 to 5 Mg/mol. Values are normalized to a thickness of 20 μm and a porosity of 50 %.

While the overall tensile strength is relatively low compared to typical values for BSF, the influence of molecular weight is still evident. As expected, an increase in molecular weight results in heightened tensile strength, most significant for the change from GUR4018 with tensile strength of about 28 MPa to GUR4012 (50 %) with tensile strength of about 67 MPa. While reducing the content of UHMWPE reduces tensile strength to about 60 MPa for GUR4012 (30 %) it is only slightly increased to 89 MPa when GUR2122 is used.

The same trend can be observed with the puncture strength, as tensile strength is directly correlated. An increase in molecular weight results in higher puncture strength ranging from 124 g for GUR4018 to 311 g for GUR4012 (50 %) and a slightly higher 368 g for GUR2122. In contrast to the tensile strength, a reduction in UHMWPE content did not lead to change in puncture strength.

5.5.1.2 Influence of MD stretching ratio

To further study the behavior of UHMWPE, the effect of varying MD ratios on film properties was investigated. For this the material GUR4012 was used in different combinations, as it exhibited a good compromise between processability while still showing significant increase in mechanical properties (see chapter 5.5.1.1). Figure 5.64 shows porosity of TD oriented samples, comparing the influence of MD ratio on different cast film compositions.

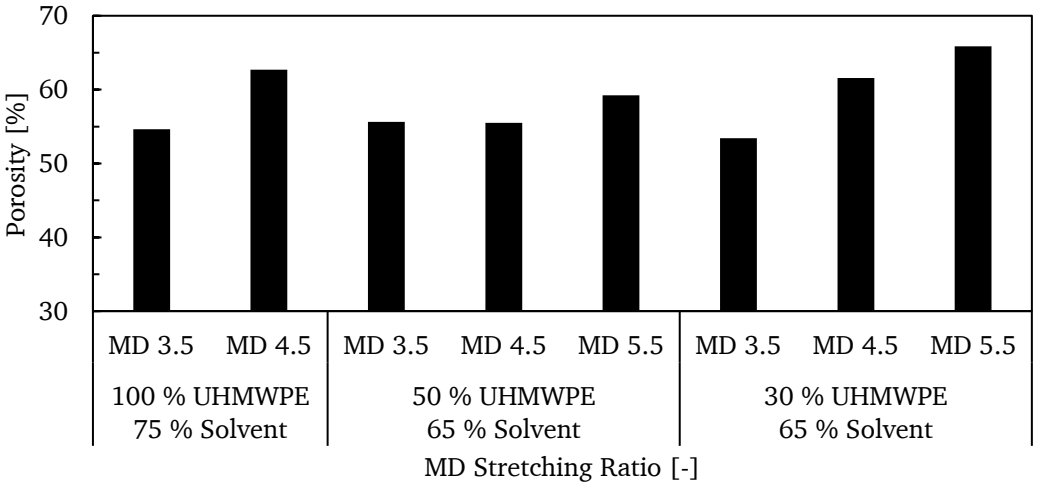

Figure 5.64: Porosity of TD stretched films containing UHMWPE GUR4012 (1.8 Mg/mol) at various MD ratios.

In general, an increase in porosity can be observed with increasing MD ratio, while slightly higher values of 66 % are obtained when the UHMWPE content is lowered to

30 % as compared to a porosity of 59 % using an UHMWPE content of 50 %. When using a mixture of 100 % UHMWPE with a necessary 75 % of solvent, porosity is higher than for a blend of 50 % UHMWPE at a solvent content of 65 %.

The mechanical properties are summarized in Figure 5.65 and Figure 5.66.

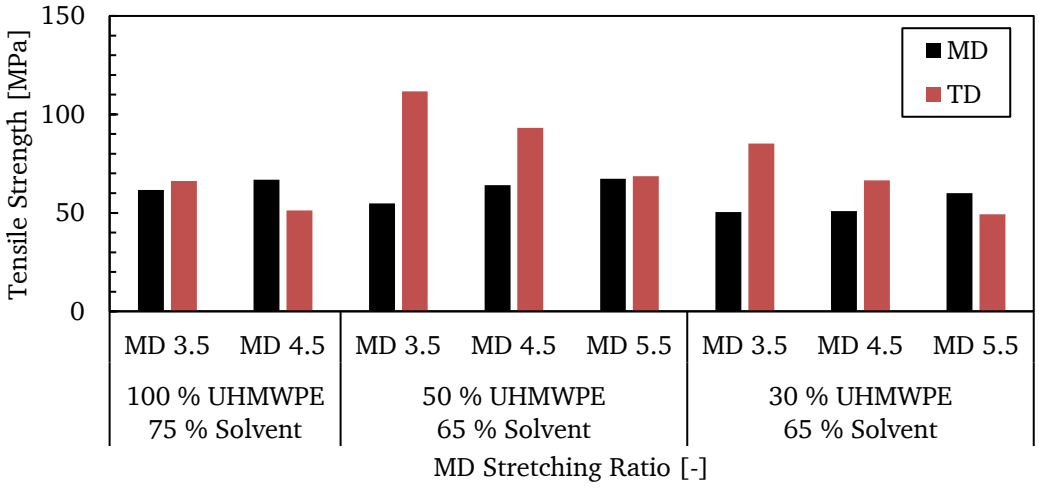

Figure 5.65: Tensile strength of TD stretched films containing UHMWPE GUR4012 (1.8 Mg/mol) at various MD stretching ratios.

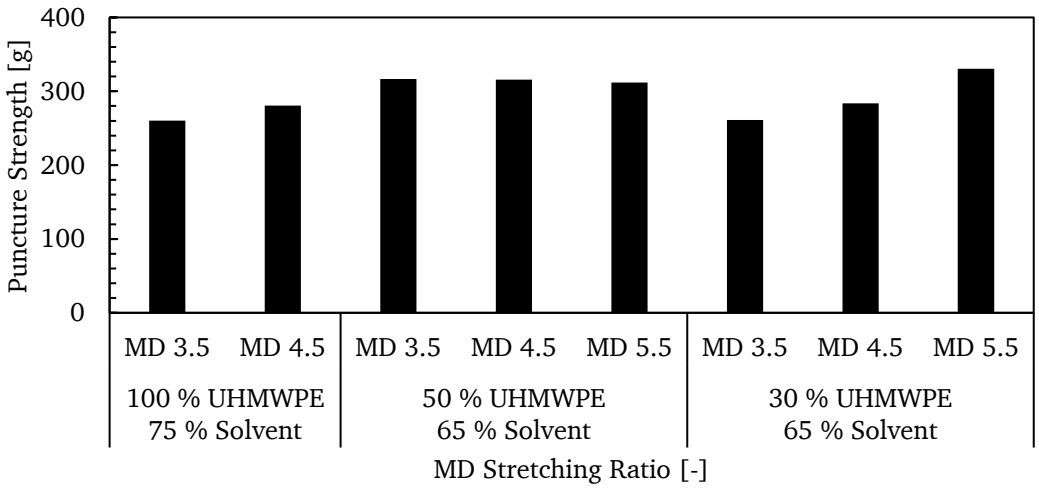

Figure 5.66: Puncture Strength of TD stretched films containing UHMWPE GUR4012 (1.8 Mg/mol) at various MD stretching ratios.

In all cases, an increase in MD stretching ratio slightly increases tensile strength in MD while significantly and negatively affecting tensile strength in TD. For example, while MD tensile strength is increased from 55 MPa to 67 MPa for a composition of 50 % UHMWPE at ratios of 3.5 and 5.5, TD tensile strength is reduced from 112 MPa to 69 MPa.

Comparing the results from Figure 5.66, it is evident that an increase in MD stretching ratio has a positive effect on puncture strength, albeit only on a small scale. Most significant an increase from 261 g to 330 g can observed for a composition of 30 % UHMWPE. Overall tensile strength as well as puncture strength is highest for a composition of 50 % UHMWPE.

Finally the influence on shrinkage of the films is compared in Figure 5.67.

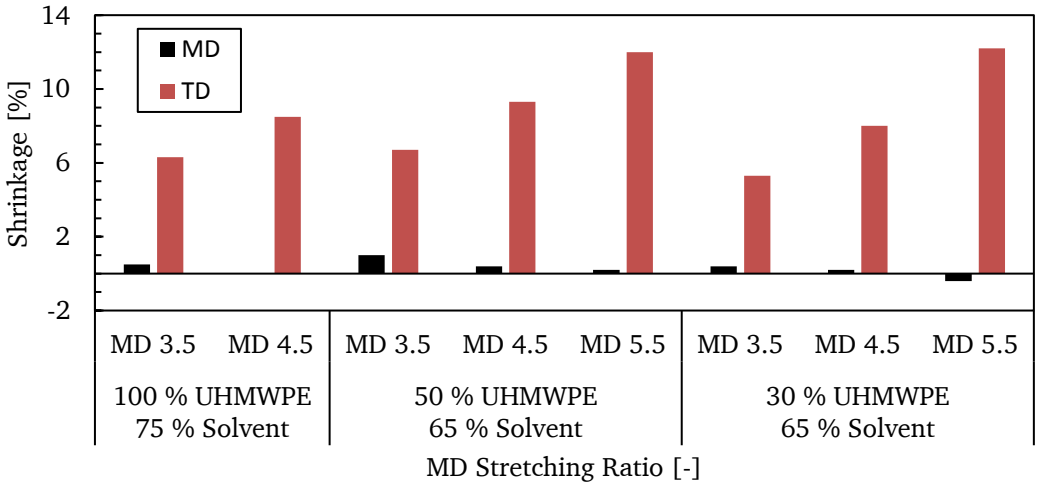

Figure 5.67: Shrinkage of TD stretched films containing UHMWPE GUR4012 (1.8 Mg/mol) at various MD stretching ratios.

While MD shrinkage is negligible due to the sample size limitation from the KARO IV machine, a clear influence of MD stretching ratio on TD shrinkage can be observed. With all compositions used in these trials, an increase in shrinkage from about 5-6 % to 12 % is evident with increasing MD stretching ratio from 3.5 to 5.5.

5.5.1.3 Influence of TD stretching ratio

In conjunction with the analysis of MD stretching ratio (see chapter 5.5.1.2), TD stretching ratio was varied between 1.5 and 5.5 with a fixed MD stretching ratio of 5.5. The influence of TD stretching ratio on the porosity of films with varying compositions is shown in Figure 5.68.

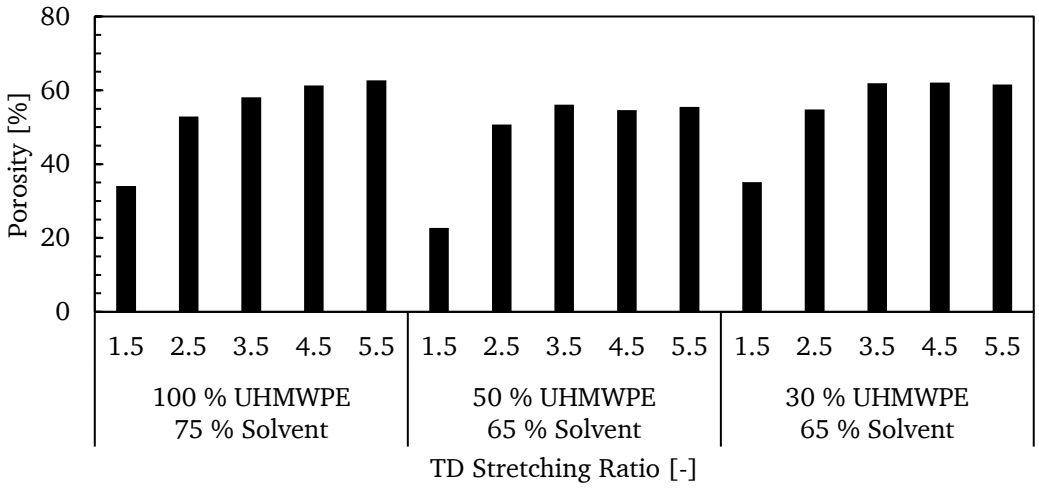

Figure 5.68: Porosity of TD stretched films containing UHMWPE GUR4012 (1.8 Mg/mol) at various TD stretching ratios.

It can be observed, that an increase in TD stretching ratio is beneficial for reaching higher porosities at ratios ranging from 1.5 to about 3.5, where porosity reaches a plateau. Comparing the compositions slightly higher porosities can be observed for materials with less UHMWPE or with higher solvent content.

The tensile strength and puncture strength of films stretched at ratios of 3.5 to 5.5 are summarized in Figure 5.69 and Figure 5.70 respectively.

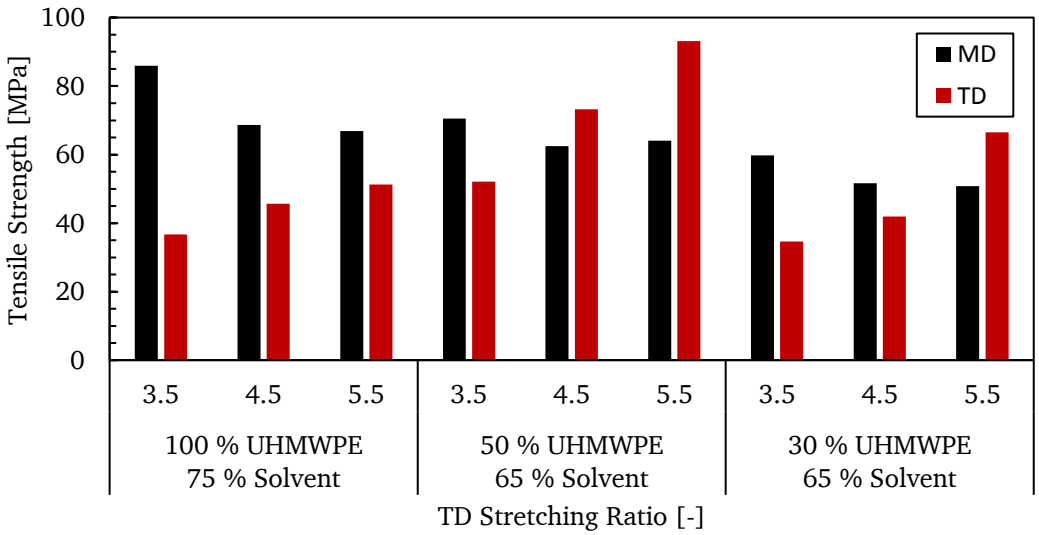

Figure 5.69: Tensile Strength of TD stretched films containing UHMWPE GUR4012 (1.8 Mg/mol) at various TD stretching ratios.

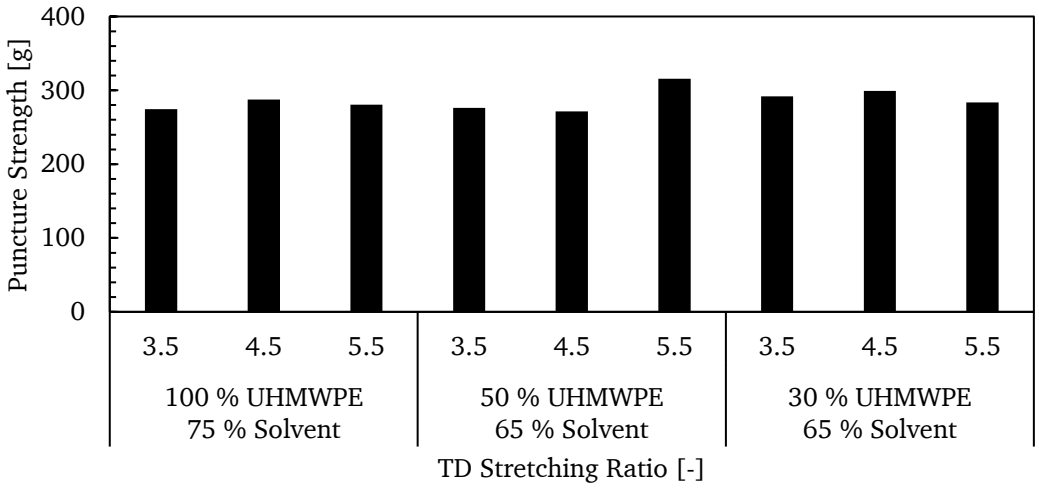

Figure 5.70: Puncture Strength of TD stretched films containing UHMWPE GUR4012 (1.8 Mg/mol) at various TD stretching ratios.

While MD tensile strength is slightly reduced with increasing stretching ratio, tensile strength is significantly increased in TD. The highest TD tensile strength can be observed for a composition of 50 % UHMWPE with 52 MPa at a ratio of 3.5 and 93 MPa at a ratio of 5.5. While TD stretching ratio has an observable effect on tensile strength, puncture strength remains largely unaffected, with only a slight increase for a composition of 50 % UHMWPE from 276 g to 315 g at ratios of 3.5 and 5.5 respectively. Figure 5.71 summarizes the effect of TD stretching ratio on shrinkage.

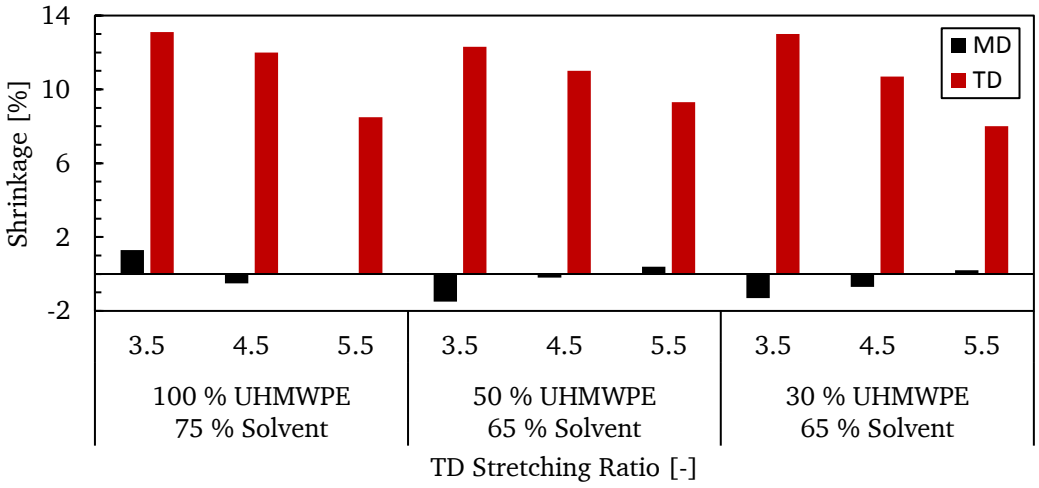

Figure 5.71: Shrinkage of TD stretched films containing UHMWPE GUR4012 (1.8 Mg/mol) at various TD stretching ratios.

Similar to the results presented before, MD shrinkage is negligible due to the sample size limitations of the KARO IV machine. However, TD shrinkage is effectively lowered

with increasing stretching ratio, with similar values of 8-9 % shrinkage achieved with all three compositions at a stretching ratio of 5.5

5.5.1.4 Influence of solvent content

Finally the effect of solvent content in the initial cast film composition was investigated with regards to the influence on the properties of films stretched at various TD stretching ratios. Figure 5.72 shows the effect of solvent content on the porosity of stretched separator films.

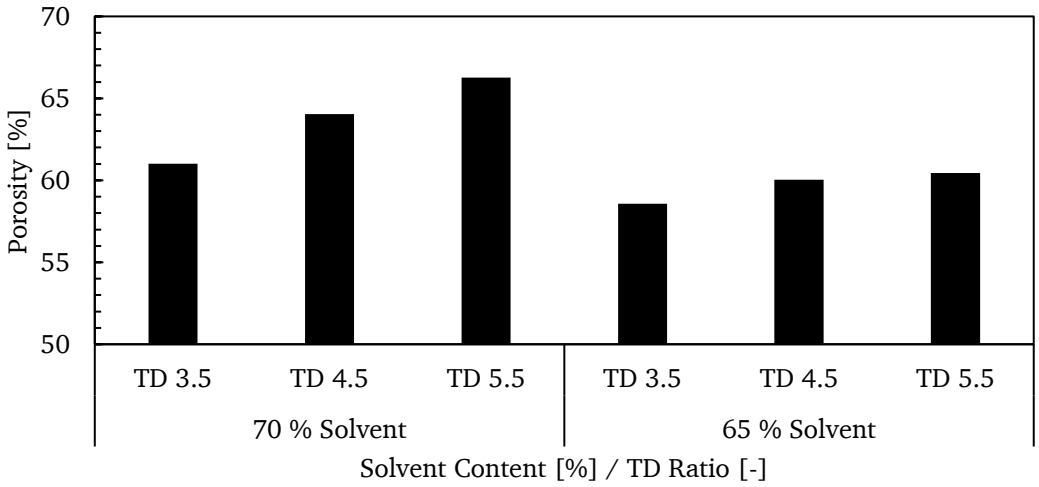

Figure 5.72: Porosity of TD stretched films containing UHMWPE GUR4012 (1.8 Mg/mol) at different Solvent content.

The results indicate that an increase in solvent content leads to a significant increase in porosity. While porosities of 61 to 66 % were achieved with compositions containing 70 % of solvent, only 59 to 60 % were obtained for compositions using 65 % of solvent. The effect of TD stretching ratio is similar to the results shown previously (see chapter 5.5.1.3).

The influence on mechanical properties in regards to solvent content are summarized in Figure 5.73 and Figure 5.74.

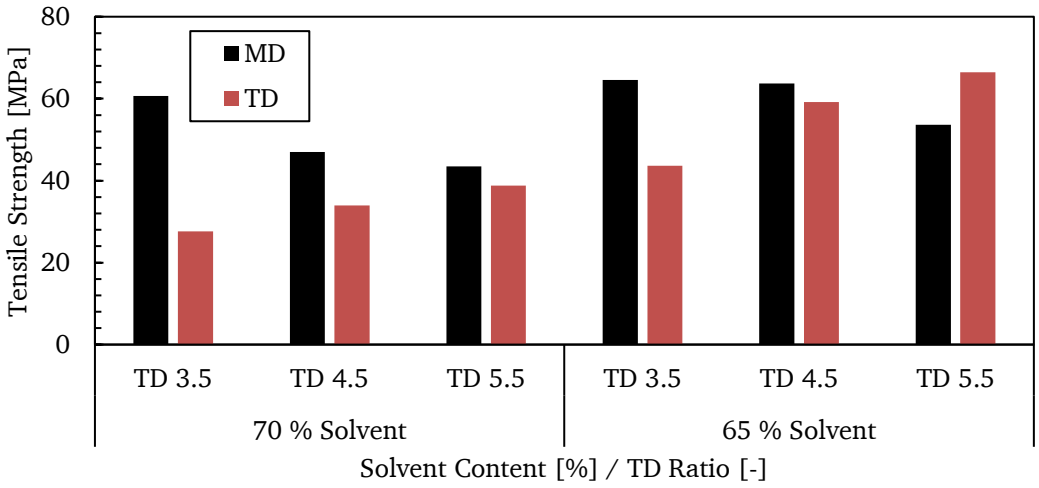

Figure 5.73: Tensile Strength of TD stretched films containing UHMWPE GUR4012 (1.8 Mg/mol) at different Solvent content.

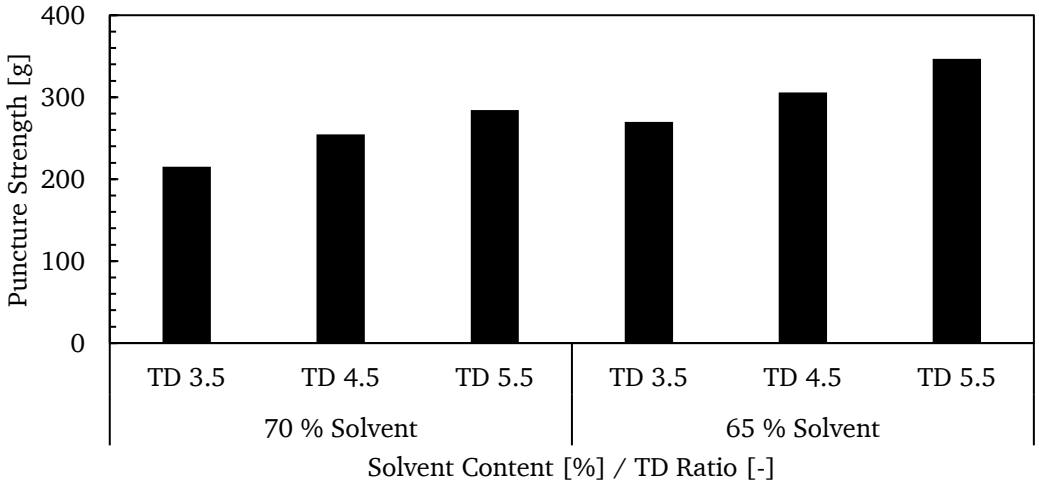

Figure 5.74: Puncture Strength of TD stretched films containing UHMWPE GUR4012 (1.8 Mg/mol) at different Solvent content.

Comparing the results for both compositions at a given TD stretching ratio, lower tensile strength in MD and TD as well as lower puncture strength can be observed for compositions containing 70 % of solvent. While films produced using 65 % of solvent exhibit tensile strength values in MD and TD of 54 MPa and 66 MPa at a stretching ratio of 5.5, the tensile strength only reaches 43 MPa and 39 MPa for a composition using 70 % solvent stretched under the same conditions. In terms of puncture strength, values of 347 g and 284 g are reached for 70 % and 65 % respectively.

The influence of solvent content on film shrinkage is shown in Figure 5.75.

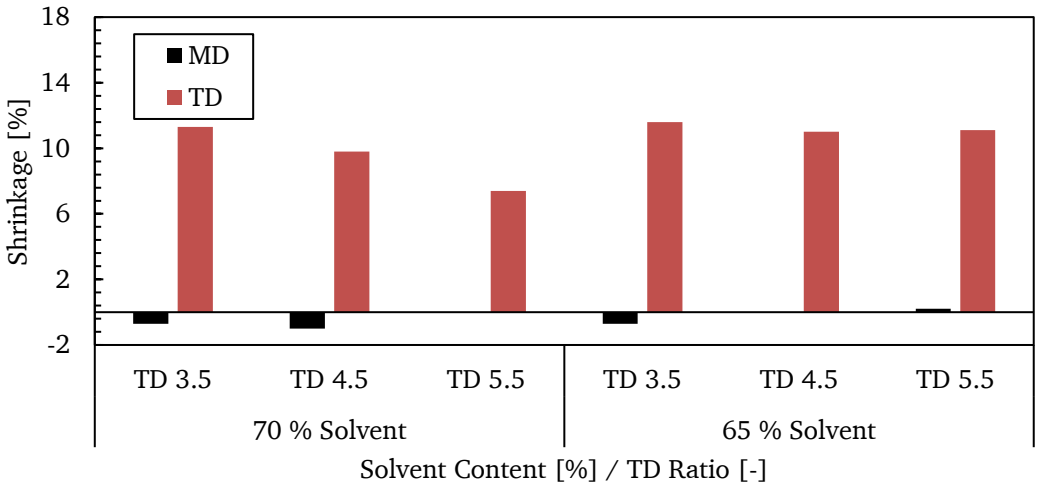

Figure 5.75: Shrinkage of TD stretched films containing UHMWPE GUR4012 (1.8 Mg/mol) at different Solvent content.

With MD shrinkage being negligible (see chapter 5.5.1.2 and 5.5.1.3), a higher shrinkage of about 11 % compared to 10 % and 7 % can be observed at stretching ratios 4.5 and 5.5 respectively for compositions containing 65 % of solvent.

To evaluate the effect of the initial solvent content on the crystallization of the melt upon cooling in the casting unit, DSC cooling thermograms of solvent filled cast films were evaluated after the material has been completely molten. As the solvent content of cast films is typically reduced during the processing compared to the initial amount dosed into the extrusion, four cast films were compared based on the real solvent content measured beforehand in drying experiments. The reduction of solvent content during processing is partly dependent on line configuration, therefore films from laboratory line and pilot line were compared. The results are summarized in Table 5.23.

Table 5.23: Influence of Solvent Content and Molecular Weight on Crystallinity of cast films containing 50 % of HDPE. Cooling at 10 K/min.

Line	Solvent Content [%]	Crystallinity [%] GUR4012	Crystallinity [%] GUR2122
Laboratory Line	55	68,3	62,3
Pilot Line	45	55,6	52,8

The results indicate that a reduction in solvent content as well as an increase in molecular weight reduces overall crystallinity of the solidified composition. Much higher crystallinity of about 68 % can be achieved using GUR4012 with a solvent content of 55 % compared to about 53 % crystallinity of GUR2122 containing 45 % of solvent.

5.5.2 PILOT LINE

To scale up the trials made on the laboratory line and KARO IV machine, compositions of 50 % HDPE and UHMWPE with the exception of GUR4018 were used on the pilot line using similar extrusion and stretching conditions. The main settings are briefly summarized in Table 5.24.

Table 5.24: Overview of important line parameters during pilot line trials using UHMWPE materials.

Parameter	GUR4018	GUR4012	GUR2122	HiZex 145M
HDPE Content [%]	-	50	50	50
Solvent Type	SiSol D60	SiSol D60	SiSol D60	SiSol D60
Output [kg/h]	24	21	21	21
Solvent Content [%]	65	65	65	65
Chill Roll Speed [m/min]	2.2	2.2	1.9	1.9
Chill Roll Temperature [°C]	40	40	40	40
MD Stretching Temperature [°C]	100 / 102	100 / 102	100 / 102	100 / 102
MD Annealing Temperature [°C]	86 / 82	90 / 86	90 / 86	90 / 86
TD Stretching Temperature [°C]	52-78	52-78	52-78	52-78
TD Annealing Temperature [°C]	124	124	124	122
Stretching Ratio	5 x 5.4	5 x 5.4	5 x 5.4	5 x 5.4
TD Relaxation	4.3	4.4	4.6	4.6

As the solvent content has a significant influence on film properties, in all cases 65 % of solvent were used during extrusion. In addition to the materials used on the laboratory line, an additional UHMWPE from Mitsui was tested using similar settings. The line could be run stable for all four materials and film rolls of about 90 cm width could be produced and were extensively characterized. The optical appearance, a critical point for separator quality, is shown in photographs of the best roll for each material in Figure 5.76

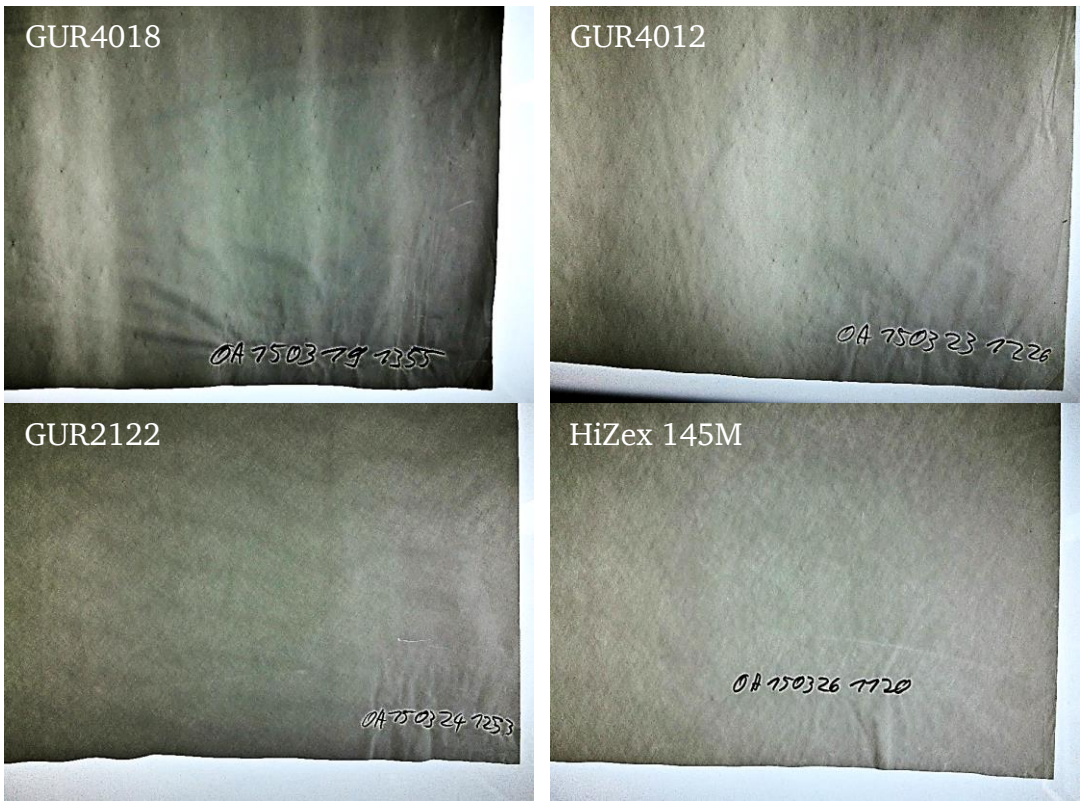

Figure 5.76: Photographs of UHMWPE Separator film produced on the Pilot Line.

Similar to the trials on the laboratory line, GUR4018 as well as GUR4012 exhibited small dark spots on the entirety of the film. Additionally GUR4018 has several stripes along the machine direction that are associated with the automatic thickness control system optimizing cast film thickness based on end film thickness profile variations. In the other three cases, this automatic system was switched off. Still, the optical appearance of GUR2122 and HiZex 145M is far from optimal, as the films exhibit an inhomogeneous cross-hatched appearance, visible most prominent for HiZex 145M. The formation of this appearance can be traced back to the die exit, where the melt briefly shows inhomogeneity shortly before being immersed into the cooling bath.

All four materials used were further compared based on the achieved film properties to find trends regarding the different material grades used. Figure 5.77 and Figure 5.78 shows the porosity and Gurley of the films produced on the pilot lines with regard to the UHMWPE material used.

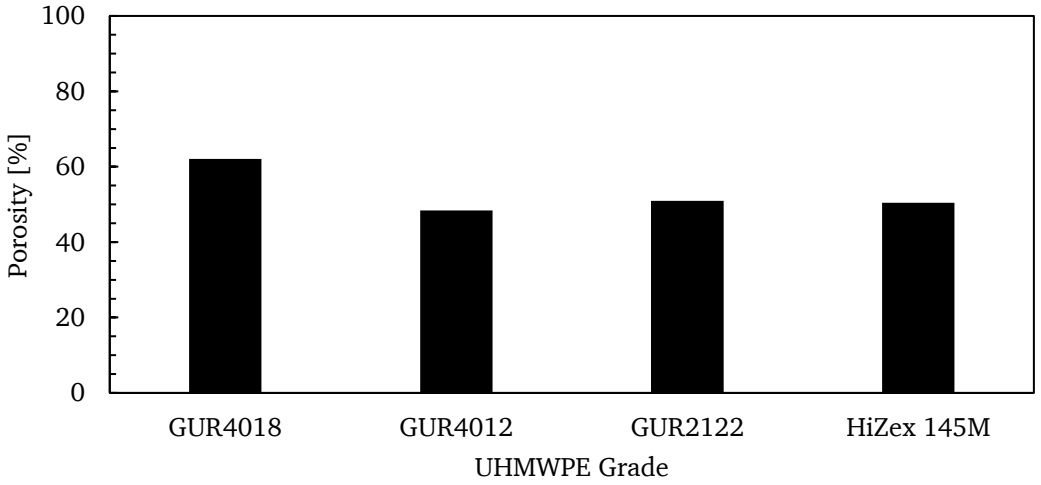

Figure 5.77: Influence of UHMWPE Grade on Porosity of Pilot line Separator film.

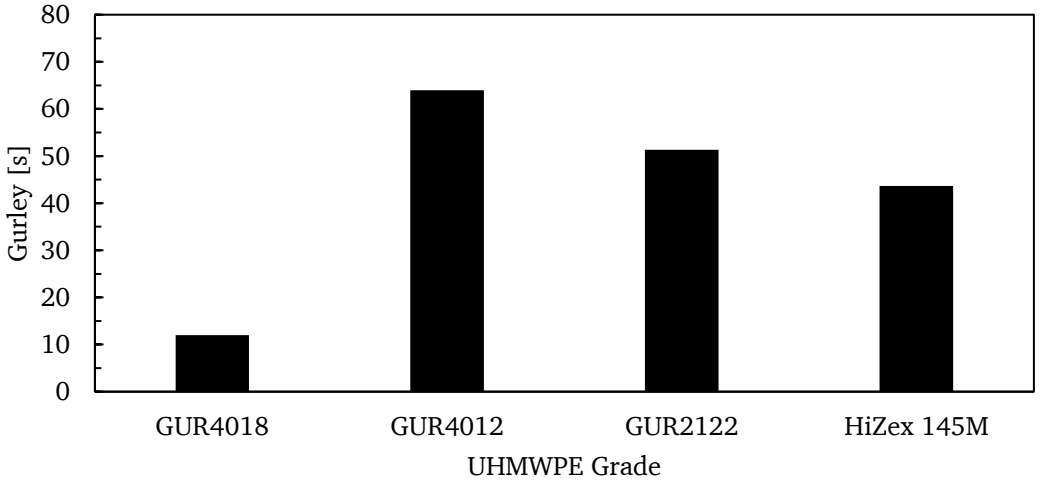

Figure 5.78: Influence of UHMWPE Grade on Gurley value of Pilot line Separator film. Volume used for measurement: 10 ml.

The only remarkable result from this comparison is the higher porosity of GUR4018 of 62 % compared to about 50 % of the other materials. In fact, the difference in molecular weight between the latter three materials does not have a significant effect on the porosity of the final film. Values of 50 % are typical for films produced on the pilot line and are at the upper range of acceptable porosities.

Contrary to the laboratory line and KARO IV trials, a Gurley value was measurable for the samples produced on the pilot line. In general, GUR4018, exhibiting the highest porosity, showed the lowest Gurley at 12 s for 10 ml. For the materials using higher molecular weight PE, Gurley values are in the range of 44 to 64 s for HiZex 145M and GUR4012 respectively.

The most important aspect of these trials was to increase the mechanical properties of the films using compositions containing UHMWPE. Figure 5.79 and Figure 5.80 show tensile strength and puncture strength of the obtained films.

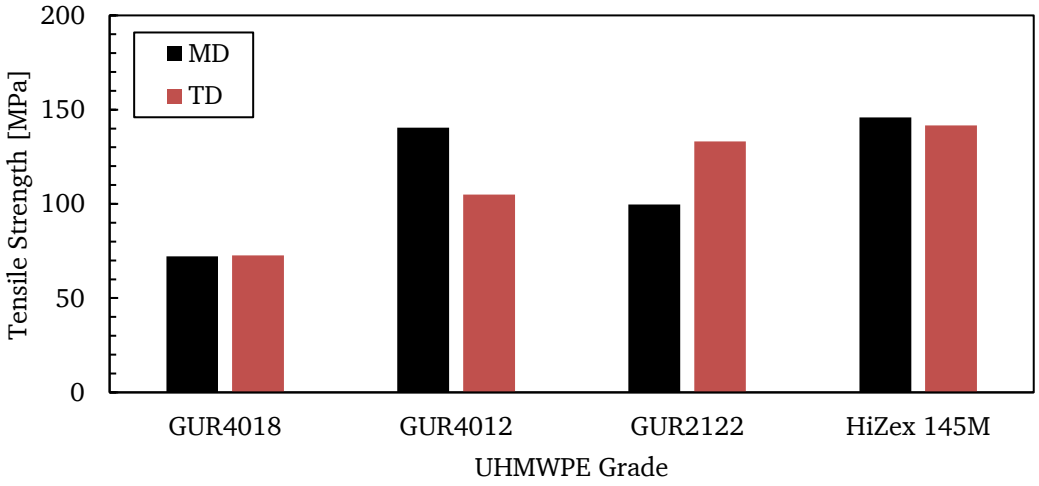

Figure 5.79: Influence of UHMWPE Grade on Tensile Strength of Pilot line Separator film.

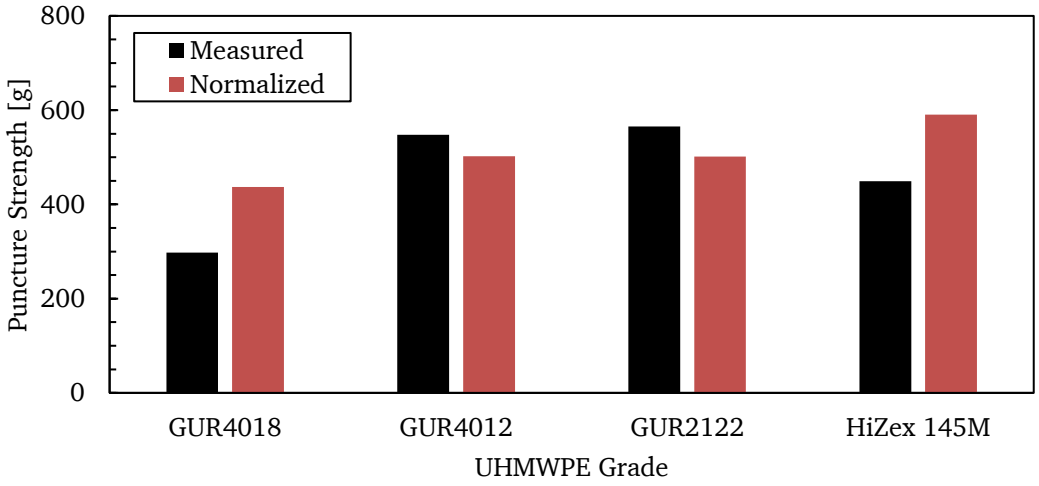

Figure 5.80: Influence of UHMWPE Grade on Puncture Strength of Pilot line Separator film. Puncture strength normalized to 20 μm and 50 % porosity.

As expected, tensile strength is lowest for GUR4018 and increases for the grades having higher molecular weight. In terms of tensile strength the highest values of about 140 MPa are reached using HiZex 145M compared to about 70 MPa achieved with

GUR4018. The same observations can be made for the normalized puncture strength, as HiZex 145M exhibits the highest value at 590 g compare to GUR4018 at 437 g, although the puncture strength of GUR4018 is not that far from GUR4012 at 502 g. Lastly, using the pilot line, reliable data for film shrinkage can be gained. The results are shown in Figure 5.81.

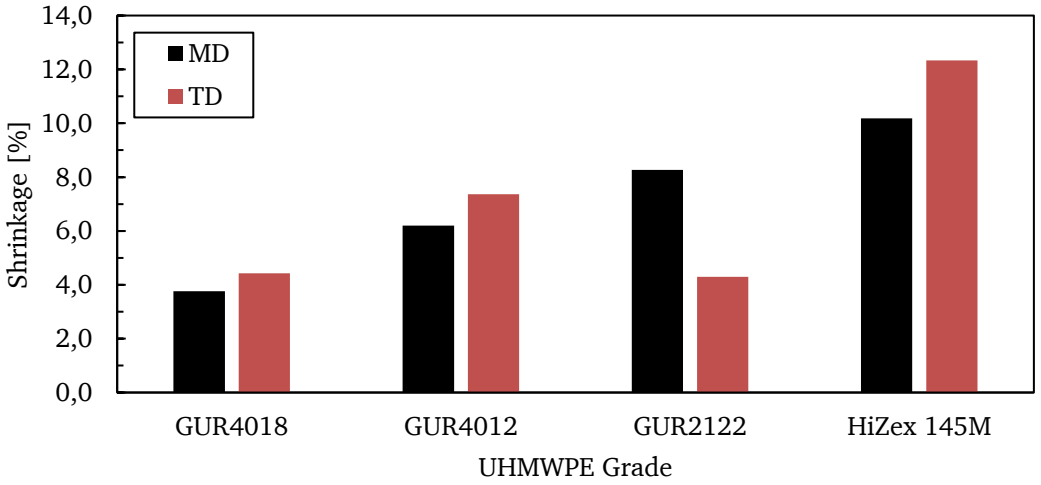

Figure 5.81: Influence of UHMWPE Grade on Shrinkage of Pilot line Separator film.

The results indicate an increase in shrinkage with increasing molecular weight in regards to the different GUR grades, with highest shrinkage of 10 % and 12 % in MD and TD being obtained for HiZex 145M and lowest at about 4 % in each direction for GUR4018. With the exception of GUR2122, TD shrinkage is 1 to 2 % higher than MD shrinkage.

5.5.3 DISCUSSION

A variation of different UHMWPE material grades were tested on the laboratory and pilot line to evaluate the suitability for the EVAPORE® process and characterize film properties when stretched at different conditions. Foremost, mechanical strength, as characterized by tensile strength and puncture strength, were the main focus, as the main advantage of UHMWPE over HDPE is increased polymer chain length, which contributes to increased mechanical integrity. When testing UHMWPE grades between 0.7 Mg/mol to up to 5 Mg/mol, a significant increase in tensile strength and puncture strength could be observed when comparing GUR4018 (0.7 Mg/mol) and GUR4012 (1.8 Mg/mol), even when GUR4018 was used without blending with a HDPE (see Figure 5.62 and Figure 5.63). A decrease in UHMWPE content to 30 % for the

GUR4012 blend seemingly reduced tensile strength of the film sample, while puncture strength remained nearly constant. The lower tensile strength compared to a blend comprising 50 % of UHMWPE can be explained in terms of its porosity. Tensile strength measurements only take total film sample thickness into account, disregarding porosity. A higher porosity sample, such as the one having 30 % of UHMWPE (see Figure 5.61), therefore shows lower tensile strength at a constant thickness. With normalized puncture strength, however, porosity is factored into the final value, showing that a reduction in UHMWPE content changes puncture strength only slightly. While the same reasoning can be applied to the tensile strength results for GUR4018, having the highest porosity, the normalized values still shows a significantly lower puncture strength for GUR4018. Finally, when comparing GUR4018 (1.8 Mg/mol) to GUR2122 (5 Mg/mol) only a small increase was evident. As processability of highly viscous materials becomes more difficult, GUR4012 was chosen for further trials as it already shows a significant increase in mechanical integrity.

The influence of both MD and TD stretching ratio is a key aspect for pore formation as well as for achieving desired mechanical strength. During pore formation, crystallinity plays an important role, as the stretching of the film transforms the oriented crystalline phase into a porous network. The prerequisites for pore formation are high crystallinity in the cast films and a high orientation with sufficient annealing during MD stretching. It is therefore not surprising that an increase in MD stretching ratio as seen in Figure 5.64 leads to an increase in final porosity of the film. The increased porosity for samples using a higher solvent content of 75 % or lower content of UHMWPE of 30 %, are indicative of a higher crystallinity during the initial solidification of the melt in the casting unit. During TD stretching however, the crystalline phases are deformed and change into a porous structure, that need a minimum stretching ratio of about 3.5 until a sufficient porosity can be achieved (see Figure 5.68). Further increase in TD stretching ratio does not affect porosity significantly.

The second aspect of stretching ratio is tensile strength and puncture strength, which are tied directly to the orientation of the molecular structure. As can be seen from Figure 5.65 and Figure 5.69 stretching increases the tensile strength in the corresponding direction while lowering tensile strength perpendicular to the stretching direction. Tensile strength is largely tied to the orientation of the polymer chains and the overall film crystallinity. Polymer orientation on the other hand corresponds to the material viscosity, as lower viscosity allows for increased chain movement and

therefore increased stress-relaxation during the orientation step. This is evident from Figure 5.65 and Figure 5.69 as a higher amount of UHMWPE (50 % compared to 30 %) at the same solvent ratio, leads to a significant increase in tensile strength. However, a UHMWPE content of 100 % shows lower tensile strength, due to a higher solvent ratio, which reduces viscosity and allows for increased chain movement. Puncture strength is somewhat more difficult to compare, as it is primarily tied to the tensile strength in both directions. As tensile strength is increased in parallel to the stretching direction, but suffers perpendicular to it, no clear influence of either MD or TD stretching ratio can be gained from Figure 5.66 and Figure 5.70. While for the variation in MD direction, a small increase in puncture strength is indicated, the variation of TD ratio does lead to similar results in all cases. Most likely, the loss in MD tensile strength compensates the increase in TD tensile strength, leading to a nearly constant puncture strength.

Film shrinkage is a function of stress frozen into the sample during processing and therefore controlled by polymer chain orientation. While higher MD stretching ratios lead to an increase in TD shrinkage, TD stretching itself reduces shrinkage in TD at higher ratios. MD shrinkage on the other hand is in all cases very negligible, which seems to be an effect of the KARO IV labstretching machine, as much higher MD shrinkage values are generally achieved on the pilot line. During stretching on the KARO IV machine the sample is only gripped at five positions and free to neck-in in between, effectively reducing stress build up in the sample. The higher TD shrinkage as a function of MD stretching ratio can be explained in terms of increased orientation of the crystalline phase, requiring higher forces during TD stretching and thereby increasing stress in the sample. On the other hand, an increase in TD stretching ratio decreases TD shrinkage significantly, which is likely caused by the ongoing deformation of the crystalline structure, resulting in an overall less oriented morphology.

Finally, the effect of solvent content was evaluated as it has a significant influence on many important film properties as discussed briefly before. Comparing Figure 5.72 to Figure 5.75 the effect of an increased solvent content is evident in increased porosity as well as lowered mechanical strength and lowered shrinkage values. This can be linked to the crystallinity of the cast films and the overall viscosity of the polymer-solvent mixture. A higher viscosity of the mixture, either by increased molecular weight of the polymer or by a reduction of solvent content, directly leads to a decreased crystallinity as proven by the results presented in Table 5.23. Generally, lower viscosity

allows for increased chain movement in the mixture, which is required for sufficient rearranging into crystalline folds. Lower viscosity also allows for increased stress-relaxation during stretching, resulting in less shrinkage and lower mechanical strength. The high crystallinity achieved this way leads to the formation of a highly porous network, increasing overall porosity.

After a first evaluation of processability and film properties, trials on the pilot line were done to scale up the process of film stretching from the KARO IV labstretching machine. In addition to the materials tested on the laboratory line, a new material HiZex 145M was tested as well, as it exhibits a favorable molecular weight of 1.1 Mg/mol. Firstly, with highly viscous materials, processability becomes a challenge, therefore, special focus was set on the homogeneity of melt and final film optical appearance and defects. It was found that for GUR4018 and GUR4012, spots were visible on the whole sample that most likely correspond to unmixed particles of UHMWPE (see Figure 5.76). However, for GUR2122 and HiZex 145M spot-free samples could be produced. For GUR2122, even though the molecular weight is higher compared to GUR4012, the difference in particle form (GUR4012 dense spheric; GUR2122 sponge) indicates an increased miscibility with the solvent due to the highly increased specific surface of the sponge-like particles. Unfortunately, even with GUR2122 and HiZex 145M, markings on the whole film surface were visible in both the melt as well as the final stretched film. These V-shaped markings contribute to the overall inhomogeneous optical appearance of the film samples, and are linked to the onset of the sharkskin effect. With the increased viscosity of the UHMWPE materials, a continuous defect is produced on the melt surface at the die exit. These defects are small enough to not significantly alter the stability of the process, but large enough to lead to unacceptable optical appearance in regards to the separator market.

While the increase in viscosity of the polymer-solvent mixtures leads to decreased porosities and subsequently lower Gurley values of the samples (see Figure 5.77 and Figure 5.78), tensile as well as puncture strength are significantly increased compared to GUR4018 (0.7 Mg/mol), while further increase in molecular weight shows no significant effect, confirming the results gained from the laboratory line and KARO IV trials. (see Figure 5.79 and Figure 5.80). However, comparing normalized puncture strength values, HiZex 145M shows slightly higher mechanical strength even though molecular weight is lower compared to GUR4012 and GUR2122.

The values for shrinkage compare well to the tensile strength of the samples, with highest shrinkage for the HiZex 145M material.

5.5.4 Conclusion

It could be proven, that by using Polyethylene with a molecular weight greater than 1 Mg/mol an increase in tensile as well as puncture strength can be achieved when compared to a material with a molecular weight of 0.7 Mg/mol. This is attributed to an increased chain orientation of the highly viscous materials, leading to less stress-relaxation due to hindered chain movement and subsequently to increased tensile strength. Unfortunately, shrinkage is also affected, as the build-up stress that is then frozen in the sample is increased. Lastly the solvent content and overall viscosity of the polymer-solvent mixture has a profound effect on the crystallinity of the film, which in turn governs pore formation as well as orientation of the polymer chains. Lower viscosity of the mixture leads to an increased crystallinity and higher porosities. Overall, when taking processability into account, HiZex 145 M showed the best combination of properties ranging from good spot-free processability, to the highest achieved puncture strength. Further trials on the pilot line have to be done, to optimize film properties as well as extrusion conditions. A critical challenge is the reduction of the sharkskin defect to gain films with sufficient homogeneous optical appearance.

6 CONCLUSION & OUTLOOK

6.1 DEVELOPMENT OF LABORATORY METHOD

During this study, a laboratory method for the EVAPORE® process was developed that could be used to produce porous stretched films in a cost and time efficient way. The method utilizes a heated press using molds to form a premixed sample of polymer/solvent into a cast sheet of a thickness of about 700 μm, similar to the thickness of cast films extruded on the pilot line. These molded sheets could then be stretched similar to cast films on the KARO IV machine and showed similar results when compared directly with SEM analysis. While this method was successfully developed, it is not without its drawbacks. The most significant limitations, as expected, is the mixing of the polymer and the solvent. Using this method, both materials are heated in a sealed test tube above the melting point of the polymer and then crystallized rapidly to produce a mixed sample. As this method can never compete to the industrially used twin-screw extrusion process, the mixture was proven to be inhomogeneous. As such, only a certain range of solvent content was processable for some polymers, while the blending of different polymers proved impossible. Another difference to the pilot line process is the anisotropy of the molded films. On the pilot line, extruding through a die imparts a shear into the material that results in a measurable anisotropy of the cast film when comparing machine direction and transverse direction. The molded films, however, do not show this anisotropy, which is attributed to the molding of the film in the heat press. In conclusion, while the laboratory method has its limits, it is a helpful tool to evaluate basic parameters of the stretching and pore forming process.

6.2 STUDY OF THE PORE FORMATION PROCESS

Using the laboratory method, the KARO IV machine as well as cast films produced on the pilot line, a study of the effect of MD stretching and annealing conditions on HDPE was done. It could be shown that the stretching and annealing temperatures have a pronounced effect on the surface and bulk morphology of the stretched samples, with higher annealing temperatures leading to the development of a shish-kebab morphology as well as increasing porosity and lowering Gurley value. This is attributed

to the orientation of the molecular chains at a given minimum stretching ratio and temperature, resulting in the formation of nuclei that promote lateral growth of lamellar crystals. The temperatures needed for an even mixture of HDPE and solvent were derived from DSC measurements and are dependent on the melting range of the mixture. While the performance characteristics of the separator could be improved with higher annealing temperatures, the surface showed a coarse and unsuitable morphology; in contrast, a homogeneous surface is generally required in Li-ion batteries. The effect of molecular weight was also investigated during this study. It was found, that the longer chains of the GUR2122 UHMWPE promoted orientation of the crystals and lead to significantly reduced Gurley values.

With these results, a deeper understanding of the stretching process in the MDO was achieved, with the DSC being a suitable tool for analyzing the temperature window necessary during stretching and annealing. However, as the MD orientation is only one step of the complex EVAPORE® process, much more work is necessary to understand all of the machine parameters and especially their interaction to one another, as a difference in solvent content could potentially require the optimization of all further process steps. In general, several areas could be identified that need additional research, including the crystallization of the melt in the casting unit, the influence of evaporation of solvent during MD and TD stretching as well as the TD stretching process itself.

6.3 DEVELOPMENT OF A HIGH TEMPERATURE STABLE SEPARATOR

With the main aim of producing a thermally stable battery separator film, many commercial materials have been evaluated in regards to their chemical stability in electrolyte, miscibility with chosen solvents, crystallinity and material cost. As a suitable material combination has to fulfill all of these criteria, most of the materials used in this study were subsequently disqualified for the EVAPORE® process. Materials such as PET and EVOH that managed to be stable in battery electrolyte, were difficult to dissolve under shear due to significant degradation of the polymer, while COC was disqualified due to its amorphous nature. Fluorinated polymers on the other hand are stable in electrolyte as expected, but cannot compete in cost to the currently used HDPE. In the end, PMP was the only candidate left that exhibits a sufficiently high melting point and was soluble in aliphatic hydrocarbons as well as cost efficient. In contrast to PP, which also showed good solubility, stable cast films could be produced

with PMP. A wide range of stretching and annealing conditions were evaluated on the KARO IV machine to narrow down the process window necessary for pore formation. While many similarities to the HDPE morphology were observed, including the onset of the formation of a porous network, a homogeneous porous film sample with sufficient air permeability could not be produced. The scale-up from the laboratory method to the pilot line also proved difficult with higher annealing temperatures needed during MD stretching than the pilot line could provide. In addition, stickiness of the film onto the heated rolls was a severe problem for line stability and winding of the stretched film proved impossible under the given circumstances.

In conclusion, while the aim set for this study could not be achieved in its entirety, the potential for PMP as an alternative material for the EVAPORE® process was presented. As other work in this field, especially on the proprietary EVAPORE® process is scarce, with the main separator manufacturers focusing on the wet and dry processing of HDPE and PP, much more work has to be done to find a suitable way to form a homogeneous pore network with a PMP material. In that regard, with PMP being a copolymer, solutions to this problem may not only include the evaluation of a more diverse range of polymer/solvent mixing ratios but also the optimization of the PMP copolymer by the manufacturer.

6.4 DEVELOPMENT OF A HIGH MECHANICAL STRENGTH SEPARATOR

Another important aspect of this study, was the achievement of higher mechanical strength of the separator. For that reason UHMWPE was chosen as a similar material to the currently used HDPE. The increased chain length of the material is expected to promote molecular orientation during stretching and subsequently achieve higher mechanical strength as expressed in tensile strength and more importantly puncture strength. Several different material grades with varying chain length between 0,7 Mg/mol up to 5 Mg/mol were evaluated on the laboratory and pilot line. It was found that an increase in molecular weight from 0.7 Mg/mol to 1.8 Mg/mol lead to a significant increase in puncture strength, while further increase to 5 Mg/mol was negligible. Due to the increased viscosity of UHMWPE compared to HDPE, processability is a critical challenge, especially regarding the appearance of the sharkskin effect that is promoted by higher viscosity. For that reason UHMWPE was mixed with 50 % of a HDPE powder while solvent content was increased to 65 %. Even with these settings, the effect could not be entirely avoided on the pilot line, resulting

in an inhomogeneous optical appearance unsuitable for battery manufacturers. Another drawback of UHMWPE is increased shrinkage of the materials comprised of higher molecular weight, making optimization necessary.

In conclusion, UHMWPE is a promising material to increase the mechanical integrity of the battery separator produced by the EVAPORE® process. The materials evaluated within this study only represent a small amount of UHMWPE grades available on the market, with some being especially advertised for Li-Ion batteries. Further material evaluations, as well as film optimization on the pilot line is necessary to increase overall quality of the film.

7 BIBLIOGRAPHY

[1] J. Li, C. Daniel, D. Wood, *Journal of Power Sources* **2011**, *196*, 2452-2460.

[2] E. M. Erickson, C. Ghanty, D. Aurbach, *J. Phys. Chem. Lett.* **2014**, *5*, 3313-3324.

[3] T. Horiba, *Proc. IEEE* **2014**, *102*, 939-950.

[4] Y. Hu, X. Sun, *J. Mater. Chem. A* **2014**, *2*, 10712-10738.

[5] N. Alias, A. A. Mohamad, *J. Power Sources* **2015**, *274*, 237-251.

[6] A. Farmann, W. Waag, A. Marongiu, D. U. Sauer, *J. Power Sources* **2015**, *281*, 114-130.

[7] X. Huang, *Journal of Solid State Electrochemistry* **2010**, *15*, 649-662.

[8] H. Lee, M. Yanilmaz, O. Toprakci, K. Fu, X. Zhang, *Energy Environ. Sci.* **2014**, *7*, 3857-3886.

[9] L. Ye, W. Lv, J. Cui, Y. Liang, P. Wu, X. Wang, H. He, S. Lin, W. Wang, J. H. Dickerson, W. He, *ChemElectroChem* **2015**, *2*, 312-323.

[10] B. Scrosati, J. Garche, *J. Power Sources* **2010**, *195*, 2419-2430.

[11] H. Budde-Meiwes, J. Drillkens, B. Lunz, J. Muennix, S. Rothgang, J. Kowal, D. U. Sauer, *Proc. Inst. Mech. Eng., Part D* **2013**, *227*, 761-776.

[12] J.-J. Hwang, J.-S. Hu, C.-H. Lin, *International Journal of Hydrogen Energy* **2015**, *40*, 11704-11712.

[13] G. L. Soloveichik, *Annu. Rev. Chem. Biomol. Eng.* **2011**, *2*, 503-527.

[14] J. B. Goodenough, *Energy Environ. Sci.* **2014**, *7*, 14-18.

[15] N. Imanishi, M. Matsui, Y. Takeda, O. Yamamoto, *Electrochemistry* **2014**, *82*, 938-945.

[16] P. G. Bruce, L. J. Hardwick, K. M. Abraham, *MRS Bull.* **2011**, *36*, 506-512.

[17] H.-G. Jung, J. Hassoun, J.-B. Park, Y.-K. Sun, B. Scrosati, *Nat. Chem.* **2012**, *4*, 579-585.

[18] J. Hassoun, B. Scrosati, *Adv. Mater.* **2010**, *22*, 5198-5201.

[19] A. Manthiram, S.-H. Chung, C. Zu, *Adv. Mater.* **2015**, *27*, 1980-2006.

[20] D. Bresser, S. Passerini, B. Scrosati, *Chem. Commun.* **2013**, *49*, 10545-10562.

[21] G. Xu, B. Ding, J. Pan, P. Nie, L. Shen, X. Zhang, *J. Mater. Chem. A* **2014**, *2*, 12662-12676.

[22] L. Chen, L. L. Shaw, *J. Power Sources* **2014**, *267*, 770-783.

[23] B. L. Ellis, L. F. Nazar, *Curr. Opin. Solid State Mater. Sci.* **2012**, *16*, 168-177.

[24] V. Palomares, M. Casas-Cabanas, E. Castillo-Martinez, M. H. Han, T. Rojo, *Energy Environ. Sci.* **2013**, *6*, 2312-2337.

[25] H. Pan, Y.-S. Hu, L. Chen, *Energy Environ. Sci.* **2013**, *6*, 2338-2360.

[26] X. Huang, *Journal of Power Sources* **2011**, *196*, 8125-8128.

[27] D. Ihm, J. Noh, J. Kim, *Journal of Power Sources* **2002**, *109*, 388-393.

[28] M. Kim, G. Y. Han, K. J. Yoon, J. H. Park, *Journal of Power Sources* **2010**, *195*, 8302-8305.

[29] S.-J. Gwon, J.-H. Choi, J.-Y. Sohn, Y.-E. Ihm, Y.-C. Nho, *Nuclear Instruments and Methods in Physics Research Section B: Beam Interactions with Materials and Atoms* **2009**, *267*, 3309-3313.

[30] E. J. Cairns, P. Albertus, *Annu. Rev. Chem. Biomol. Eng.* **2010**, *1*, 299-320.

[31] P. Arora, Z. Zhang, *Chemical Reviews* **2004**, *104*, 4419-4462.

[32] S. S. Zhang, *Journal of Power Sources* **2007**, *164*, 351-364.

[33] D. McCombs, S. Casey, Asahi Kasei to Buy Polypore to Expand Battery Business, http://www.bloomberg.com/news/articles/2015-02-23/asahi-kasei-agrees-to-acquire-polypore-in-3-2-billion-deal (accessed July 1, 2015).

[34] Business Wire, Asahi Kasei Completes Acquisition of Polypore, http://www.businesswire.com/news/home/20150826005700/en/Asahi-Kasei-Completes-Acquisition-Polypore (accessed February 25, 2016).

[35] D. Takemura, S. Aihara, K. Hamano, M. Kise, T. Nishimura, H. Urushibata, H. Yoshiyasu, *Journal of Power Sources* **2005**, *146*, 779-783.

[36] S. Zhang, K. Xu, T. Jow, *Journal of Power Sources* **2005**, *140*, 361-364.

[37] ICCNexergy, Custom Battery Systems, http://www.iccnexergy.com/battery-systems/ (accessed July 22nd, 2015).

[38] W. Schalkwijk, A, B. Scrosati, *Advances in Lithium-Ion Batteries*, Kluwer Academic Publishers, New York, **2002**.

[39] C. Daniel, J. O. Besenhard, *Handbook of Battery Materials, Vol. 2*, 2nd ed., Wiley-VCH, Weinheim, **2011**.

[40] S. F. Lux, I. T. Lucas, E. Pollak, S. Passerini, M. Winter, R. Kostecki, *Electrochemistry Communications* **2012**, *14*, 47-50.

[41] H. Yang, G. V. Zhuang, P. N. Ross, *Journal of Power Sources* **2006**, *161*, 573-579.

[42] K. Tasaki, K. Kanda, S. Nakamura, M. Ue, *Journal of The Electrochemical Society* **2003**, *150*, A1628.

[43] B. Ravdel, K. M. Abraham, R. Gitzendanner, J. DiCarlo, B. Lucht, C. Campion, *Journal of Power Sources* **2003**, *119-121*, 805-810.

[44] S. Tan, Y. J. Ji, Z. R. Zhang, Y. Yang, *ChemPhysChem* **2014**, *15*, 1956-1969.

[45] M. Hu, X. Pang, Z. Zhou, *Journal of Power Sources* **2013**, *237*, 229-242.

[46] K. Satoru, S. Yutaka, O. Keiji, US2011189529, 2011.

[47] L. Jean, S. Jongmoon, K. Yongkyoung, US2011033743, 2011.

[48] N. Satoshi, WO2008149895, 2008.

[49] S. Hiroyuki, O. Shini, O. Satoshi, EP2151322, 2010.

[50] L. Jean, S. Jongmoon, K. Yongkyoung, EP2260523, 2010.

[51] W. Hanhui, L. Shishuo, EP2077594, 2009.

[52] J. R. Weon, K. G. Gwon, J. I. Hwa, WO2011090356, 2011.

[53] T. Kotaro, K. Shintaro, WO2007117042, 2007.

[54] S. Yasuyuki, Y. Norihiro, S. Yasuo, WO2010116729, 2010.

[55] M. Nobuaki, K. Hideaki, S. Yoshinori, WO2010104127, 2010.

[56] M. Hiroshi, I. Hidenori, N. Hirosuke, WO2008149986, 2008.

[57] S. H. Yoo, C. K. Kim, *Industrial & Engineering Chemistry Research* **2009**, *48*, 9936-9941.

[58] Y. S. Chung, S. H. Yoo, C. K. Kim, *Industrial & Engineering Chemistry Research* **2009**, *48*, 4346-4351.

[59] J. Nentwig, *Kunststofffolien*, 3 ed., Carl Hanser Verlag, München, **2006**.

[60] I. M. Ward, *Structure and Properties of Oriented Polymers*, 2nd ed., Chapman & Hall, London, **1997**.

[61] H. Greif, A. Limper, G. Fattmann, S. Seibel, *Technologie der Extrusion*, Carl Hanser Verlag, München, **2004**.

[62] P. H. Gilbert, A. J. Giacomin, *Polymer Engineering & Science* **2015**, *55*, 2042-2049.

[63] R. J. Koopmans, J. Molenaar, *Polym. Eng. Sci.* **1998**, *38*, 101-107.

[64] T. Yoo, D. H. Kim, Y. Son, *J. Appl. Polym. Sci.* **2012**, *126*, E322-E329.

[65] M. Ansari, Y. W. Inn, A. M. Sukhadia, P. J. DesLauriers, S. G. Hatzikiriakos, *Polymer* **2012**, *53*, 4195-4201.

[66] E. Miller, J. P. Rothstein, *Rheologica Acta* **2004**, *44*, 160-173.

[67] Y. Woo Inn, *J. Rheol.* **2013**, *57*, 393-406.

[68] M. Ansari, S. G. Hatzikiriakos, A. M. Sukhadia, D. C. Rohlfing, *Polym. Eng. Sci.* **2012**, *52*, 795-804.

[69] C. Dubrocq-Baritaud, E. Darque-Ceretti, B. Vergnes, *J. Non-Newtonian Fluid Mech.* **2011**, *166*, 847-858.

[70] D. R. Arda, M. R. Mackley, *Journal of Non-Newtonian Fluid Mechanics* **2005**, *126*, 47-61.

[71] H. Domininghaus, *Kunststoffe*, 7 ed., Springer-Verlag, Berlin, **2008**.

[72] A. Keller, *Reports on Progress in Physics* **1968**, *31*, 623-704.

[73] L. Lin, A. S. Argon, *Journal of Materials Science* **1994**, *29*, 294-323.

[74] P. J. Barham, R. A. Chivers, A. Keller, J. Martinez-Salazar, S. J. Organ, *Journal of Materials Science* **1985**, *20*, 1625-1630.

[75] R. J. Samuel, *Structured Polymer Properties*, John Wiley & Sons, New York, **1974**.

[76] R. H. Somani, B. S. Hsiao, A. Nogales, S. Srinivas, A. H. Tsou, I. Sics, F. J. Balta-Calleja, T. A. Ezquerra, *Macromolecules* **2000**, *33*, 9385-9394.

[77] R. H. Somani, L. Yang, L. Zhu, B. S. Hsiao, *Polymer* **2005**, *46*, 8587-8623.

[78] M. Derakhshandeh, S. G. Hatzikiriakos, *Rheologica Acta* **2011**, *51*, 315-327.

[79] W. W. Adams, D. Yang, E. L. Thomas, *Journal of Materials Science* **1986**, *21*, 2239-2253.

[80] F. Sadeghi, *Journal of Plastic Film and Sheeting* **2005**, *21*, 199-216.

[81] A. Rozanski, A. Galeski, *International Journal of Plasticity* **2013**, *41*, 14-29.

[82] A. Pawlak, *Colloid and polymer science* **2013**, *291*, 773-787.

[83] A. Rozanski, A. Galeski, *Macromolecules* **2011**, *44*, 7273-7287.

[84] A. Pawlak, A. Galeski, *Polimery* **2011**, *56*, 627-636.

[85] A. Pawlak, A. Galeski, *J. Polym. Sci., Part B: Polym. Phys.* **2010**, *48*, 1271-1280.

[86] A. Pawlak, A. Galeski, *Polymer* **2010**, *51*, 5771-5779.

[87] A. Galeski, A. Rozanski, *Macromolecular Symposia* **2010**, *298*, 1-9.

[88] A. Pawlak, A. Galeski, *Macromolecules* **2008**, *41*, 2839-2851.

[89] R. Lv, W. Xu, B. Na, Q. Zhang, Q. Fu, *Journal of Polymer Science Part B: Polymer Physics* **2008**, *46*, 1202-1206.

[90] A. Pawlak, *Polymer* **2007**, *48*, 1397-1409.

[91] N. E. Zafeiropoulos, R. J. Davies, K. Schneider, M. Burghammer, C. Riekel, M. Stamm, *Macromol. Rapid Commun.* **2006**, *27*, 1689-1694.

[92] A. Pawlak, A. Galeski, *Macromolecules* **2005**, *38*, 9688-9697.

[93] J. M. Brady, E. L. Thomas, *Journal of Materials Science* **1989**, *24*, 3311-3318.

[94] B. Z. Jang, D. R. Uhlmann, J. B. Vander Sande, *Polym. Eng. Sci.* **1985**, *25*, 98-104.

[95] H. R. Brown, E. J. Kramer, *J. Macromol. Sci., Phys.* **1981**, *B19*, 487-522.

[96] Beuth Verlag GmbH, DIN EN ISO 1133-1:2012-03, http://www.beuth.de/de/norm/din-en-iso-1133-1/145217616 (accessed February 25, 2016).

[97] ASTM International, ASTM D882 - 12, http://www.astm.org/Standards/D882.htm (accessed February 25, 2016).

[98] Beuth Verlag GmbH, DIN 53370:2006-11, http://www.beuth.de/de/norm/din-53370/92244621 (accessed February 25, 2016).

[99] Brückner Maschinenbau, KARO IV, http://www.brueckner-maschinenbau.com/de/brueckner-maschinenbau/technologie-shyzentren/laborreckrahmen/ (accessed February 25, 2016).

[100] B. V. GmbH, BS ISO 5636-5:2013-10-31, http://www.beuth.de/de/norm/bs-iso-5636-5/197447356 (accessed February 25, 2016).

[101] B. Fortunato, P. Mirone, G. Fini, *Spectrochim. Acta, Part A* **1971**, *27*, 1917-1927.

[102] Y. Wang, Z. Jiang, L. Fu, Y. Lu, Y. Men, *Macromolecules* **2013**, *46*, 7874-7879.

[103] A. Rozanski, A. Galeski, *Int. J. Plast.* **2013**, *41*, 14-29.

[104] M. Minelli, M. G. De Angelis, *Fluid Phase Equilib.* **2014**, *367*, 173-181.

[105] S. S. Hosseini, S. Taheri, A. Zadhoush, A. Mehrabani-Zeinabad, *J. Appl. Polym. Sci.* **2007**, *103*, 2304-2309.

[106] D. E. Duvall, *Polym.-Plast. Technol. Eng.* **1995**, *34*, 227-242.

[107] M. E. Cagiao, F. J. Balta Calleja, C. Vanderdonckt, H. G. Zachmann, *Polymer* **1993**, *34*, 2024-2029.

[108] S. Wilken, P. Johansson, P. Jacobsson, *Solid State Ionics* **2012**, *225*, 608-610.

[109] G. Gachot, S. Grugeon, M. Armand, S. Pilard, P. Guenot, J.-M. Tarascon, S. Laruelle, *Journal of Power Sources* **2008**, *178*, 409-421.

[110] ICIS, OUTLOOK '15: Asia fatty alcohol market faces uncertainty in H1, http://www.icis.com/resources/news/2014/12/23/9848893/outlook-15-asia-fatty-alcohol-market-faces-uncertainty-in-h1/ (accessed February 25, 2016).

[111] Institut für Arbeitsschutz der Deutschen Gesetzlichen Unfallversicherung, GESTIS Stoffdatenbank, http://gestis.itrust.de/ (accessed February 25, 2016).

[112] S. Net, S. Rabodonirina, R. Ben Sghaier, D. Dumoulin, C. Chbib, I. Tlili, B. Ouddane, *Sci. Total Environ.* **2015**, *521-522*, 152-159.

[113] T. Cirillo, G. Latini, M. A. Castaldi, L. Dipaola, E. Fasano, F. Esposito, G. Scognamiglio, F. D. Francesco, L. Cobellis, *J. Agric. Food Chem.* **2015**, *63*, 3303-3310.

[114] C. Hansen, Hansen Solubility Parameters in Practice, http://hansen-solubility.com/HSPiP.html (accessed February 25, 2016).

[115] N. Li, C. Xiao, R. Wang, S. Zhang, *Journal of Applied Polymer Science* **2012**, *124*, E169-E176.

[116] S. H. Yoo, C. K. Kim, *Journal of Applied Polymer Science* **2008**, *108*, 3154-3162.

[117] H. Matsuyama, K. Hayashi, T. Maki, M. Teramoto, N. Kubota, *Journal of Applied Polymer Science* **2004**, *93*, 471-474.

[118] H. Matsuyama, M.-M. Kim, D. R. Lloyd, *Journal of Membrane Science* **2002**, *204*, 413-419.

[119] M. Zhang, C.-f. Zhang, Z.-k. Yao, J.-l. Shi, B.-k. Zhu, Y.-y. Xu, *Chinese Journal of Polymer Science* **2010**, *28*, 337-346.

[120] H. Ding, Y. Tian, L. Wang, B. Liu, *Journal of Applied Polymer Science* **2007**, *105*, 3355-3362.

[121] H. Matsuyama, S. Berghmans, D. R. Lloyd, *Journal of Membrane Science* **1998**, *142*, 213-224.

[122] A. Qaiss, H. Saidi, O. Fassi-Fehri, M. Bousmina, *J. Appl. Polym. Sci.* **2012**, *123*, 3425-3436.

[123] S. Saengerlaub, M. Boehmer, C. Stramm, *J. Appl. Polym. Sci.* **2013**, *129*, 1238-1248.

[124] C. Zhang, Y. Xia, K. Zuo, Y.-P. Zeng, *J. Appl. Polym. Sci.* **2014**, *131*, 40724/40721-40724/40726.

[125] Litarion GmbH, Separion, http://separion.com/ (accessed November 02, 2015).

[126] T. Uekusa, K. Okamoto, T. Katsumasa, K. Koichi, JP2015007179 (A), 2013.

[127] T. Uekusa, JP2014214227 (A), 2013.

[128] U. Takayuki, M. Okamoto, Y. Tamo, CN103588917 (A), 2010.

[129] T. Tanaka, Y. Houtani, A. Morita, US20110144224 (A1), 2009.

[130] G. Charlet, G. Delmas, *J. Polym. Sci., Part B: Polym. Phys.* **1988**, *26*, 1111-1125.

[131] M. B. Johnson, G. L. Wilkes, *Journal of Applied Polymer Science* **2002**, *83*, 2095-2113.

[132] F. E. Karasz, H. E. Bair, J. M. O'Reilly, *Polymer* **1967**, *8*, 547-560.

8 APPENDIX

8.1 LATTICE PARAMETER OF XRD TEXTURE ANALYSIS

Presented herein are the lattice parameters corresponding to the XRD analysis described in chapter 5.2.

Table 8.1: Lattice parameters, crystallite size and micro strain of all investigated samples of containing GUR4012 and GUR2122 measured along the film surface. The lattice parameters of polyethylene from the Cambridge Crystallographic Data Centre (#QILHUO01) are also given.

Sample	Annealing Temp. [°C]	a [Å]	b [Å]	c [Å]	V [Å³]	Crystal Size [nm]	Strain (ε_0) [%]
PE-CCDC	-	7.400	4.930	2.534	92.45	-	-
GUR4012	100	7.429	4.967	2.558	94.4	24	0.37
GUR2122	100	7.438	4.971	2.550	94.3	23	0.35
GUR4012	110	7.431	4.971	2.558	94.5	24	0.35
GUR2122	110	7.437	4.975	2.553	94.5	24	0.37
GUR4012	120	7.427	4.967	2.549	94.0	29	0.30
GUR2122	120	7.429	4.968	2.547	94.0	29	0.32

Table 8.2: Lattice parameters, crystallite size and micro strain of all investigated samples of containing GUR4012 and GUR2122 measured along the MD cross-section. The lattice parameters of polyethylene from the Cambridge Crystallographic Data Centre (#QILHUO01) are also given.

Sample	Annealing Temp. [°C]	a [Å]	b [Å]	c [Å]	V [Å³]	Crystal Size [nm]	Strain (ε_0) [%]
PE-CCDC	-	7.400	4.930	2.534	92.45	-	-
GUR4012	100	7.424	4.964	2.547	93.9	24	0.30
GUR2122	100	7.424	4.963	2.555	94.1	24	0.35
GUR4012	110	7.423	4.965	2.556	94.2	26	0.33
GUR2122	110	-	-	-	-	-	-
GUR4012	120	7.417	4.964	2.556	94.1	31	0.29
GUR2122	120	7.410	4.959	2.548	93.6	29	0.25

Table 8.3: Lattice parameters, crystallite size and micro strain of all investigated samples of containing GUR4012 and GUR2122 measured along the TD cross-section. The lattice parameters of polyethylene from the Cambridge Crystallographic Data Centre (#QILHUO01) are also given.

Sample	Annealing Temp. [°C]	a [Å]	b [Å]	c [Å]	V [Å³]	Crystal Size [nm]	Strain (ε_0) [%]
PE-CCDC	-	7.400	4.930	2.534	92.45	-	-
GUR4012	100	7.438	4.973	2.555	94.5	16	0.12
GUR2122	100	7.442	4.964	2.552	94.3	18	0.07
GUR4012	110	7.442	4.980	2.554	94.7	18	0.06
GUR2122	110	7.443	4.980	2.555	94.7	21	0.08
GUR4012	120	7.445	4.995	2.557	95.0	24	0.08
GUR2122	120	7.449	4.963	2.553	94.4	18	0.07

8.2 SUPPLEMENTARY ATR-FTIR DATA

Presented herein is additional ATR-FTIR data corresponding to chapter 5.3.1.2.

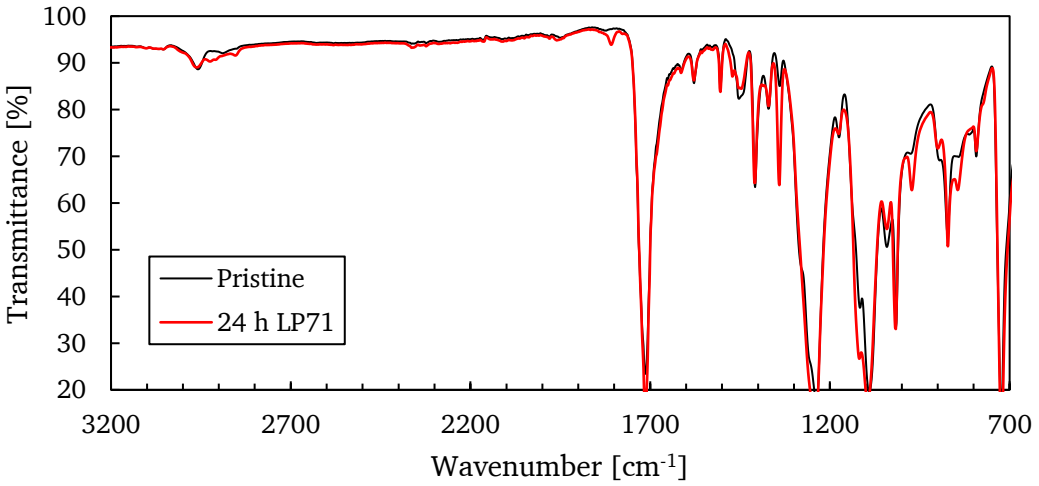

Figure 8.1: ATR-FTIR Spectra of PET before and after submersion in LP71 for 24 h at 60 °C.

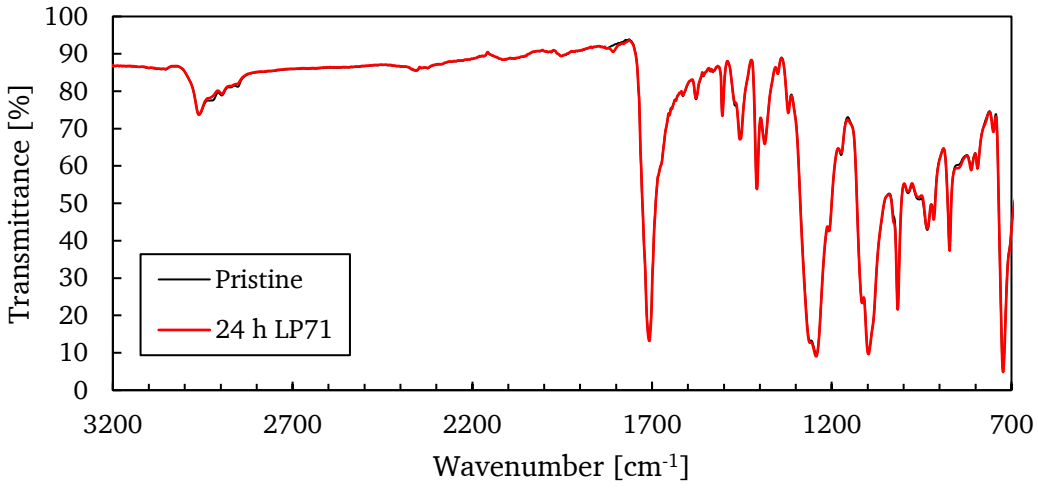

Figure 8.2: ATR-FTIR Spectra of PBT before and after submersion in LP71 for 24 h at 60 °C.

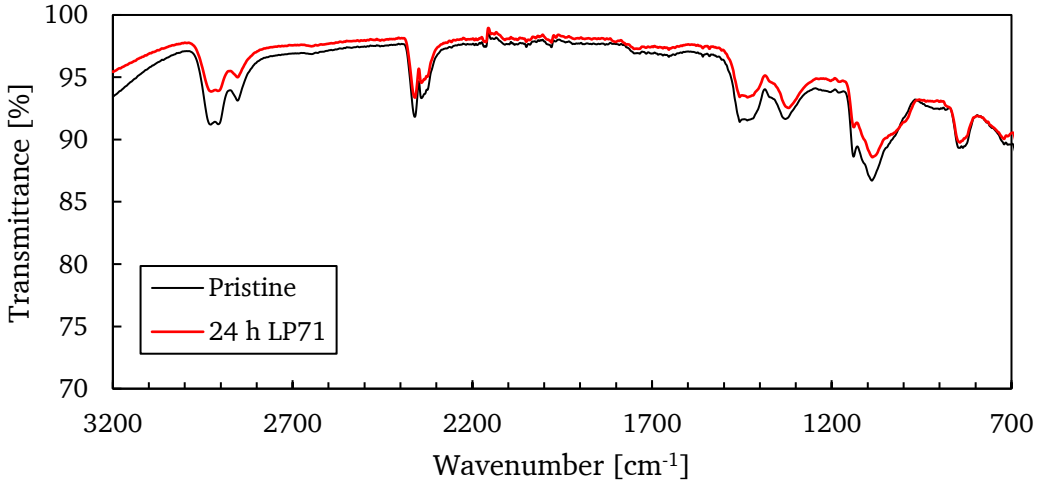

Figure 8.3: ATR-FTIR Spectra of EVOH before and after submersion in LP71 for 24 h at 60 °C.

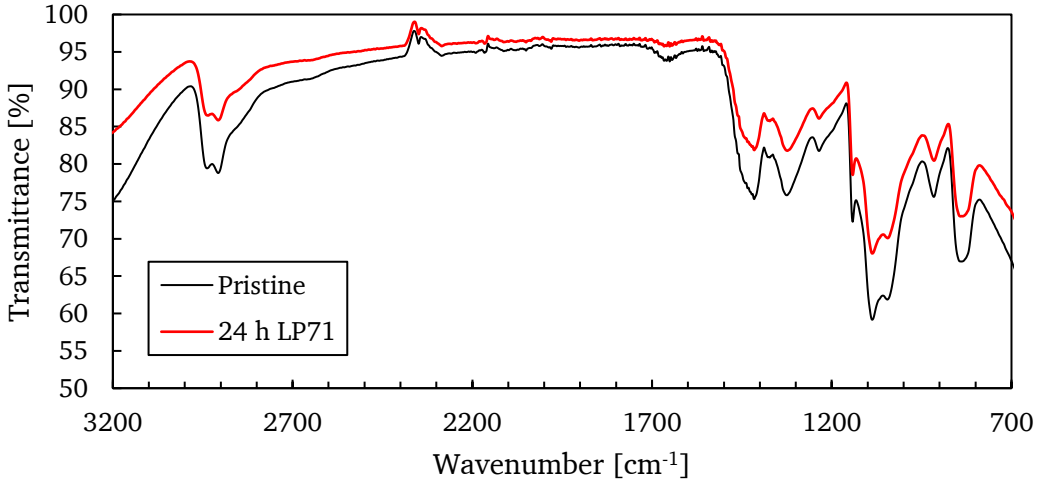

Figure 8.4: ATR-FTIR Spectra of PVOH before and after submersion in LP71 for 24 h at 60 °C.

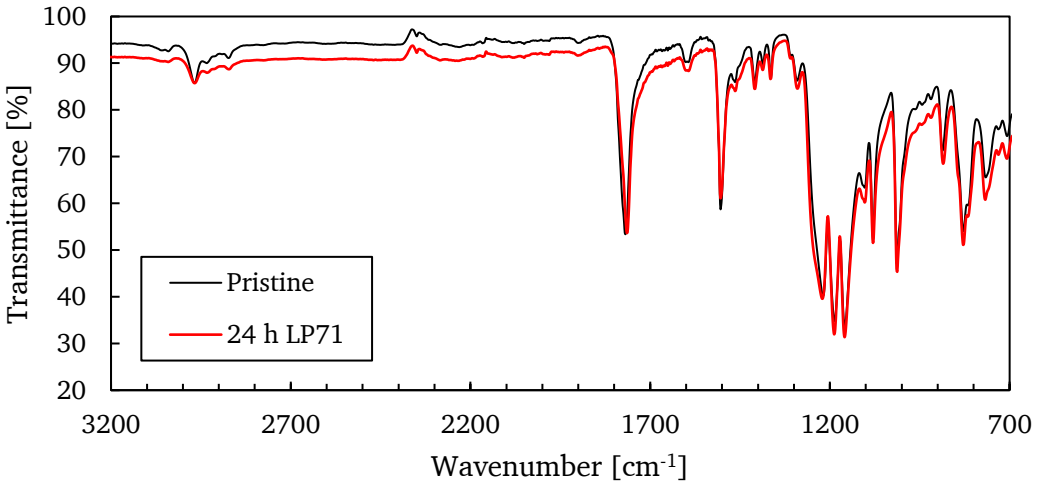

Figure 8.5: ATR-FTIR Spectra of PC before and after submersion in LP71 for 24 h at 60 °C.

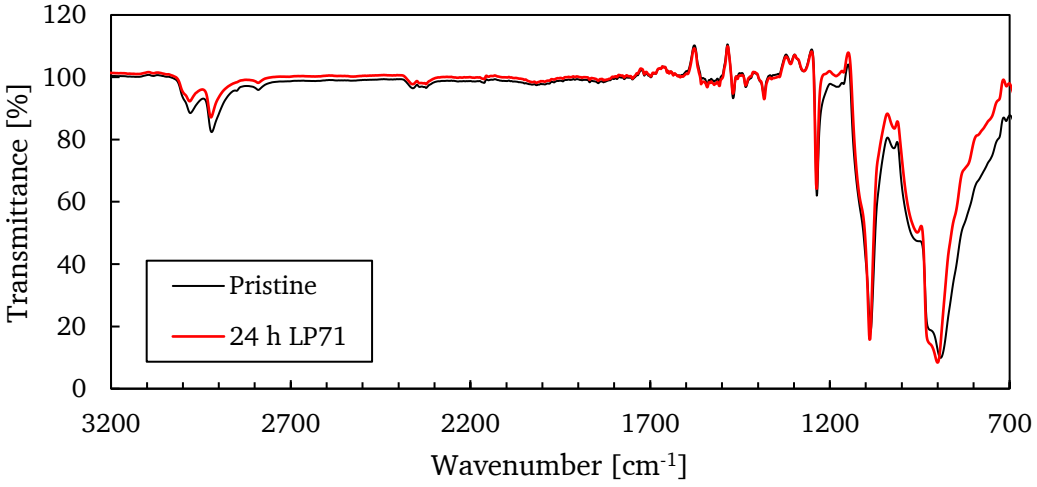

Figure 8.6: ATR-FTIR Spectra of POM before and after submersion in LP71 for 24 h at 60 °C.

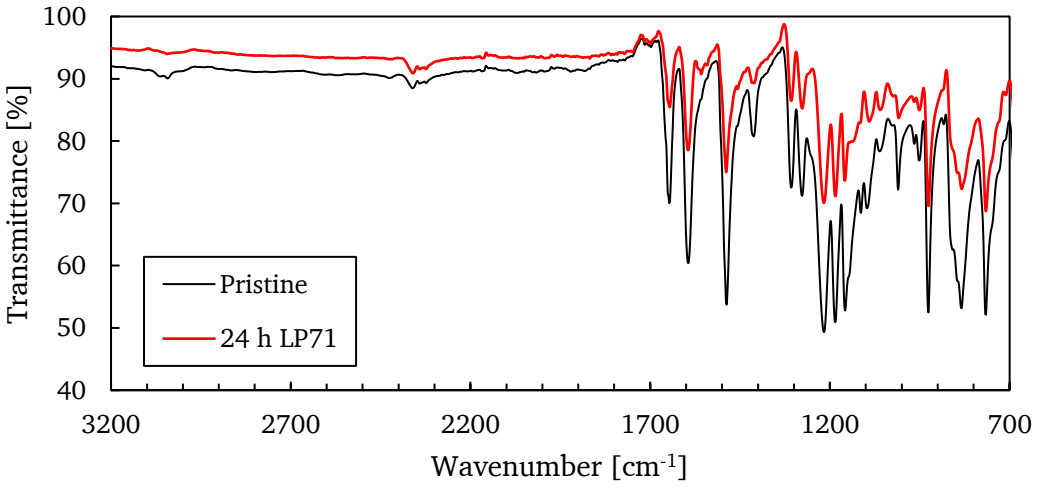

Figure 8.7: ATR-FTIR Spectra of PEEK before and after submersion in LP71 for 24 h at 60 °C.

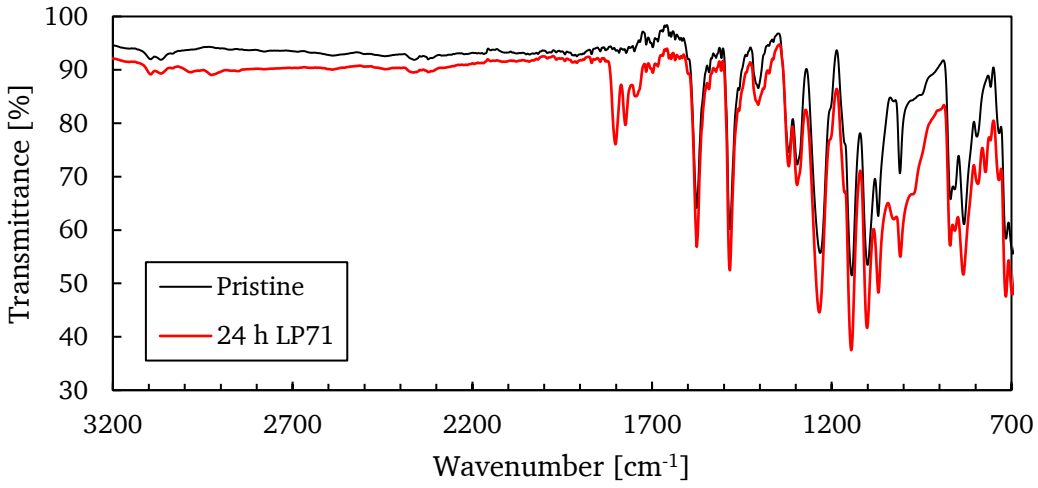

Figure 8.8: ATR-FTIR Spectra of PES before and after submersion in LP71 for 24 h at 60 °C.

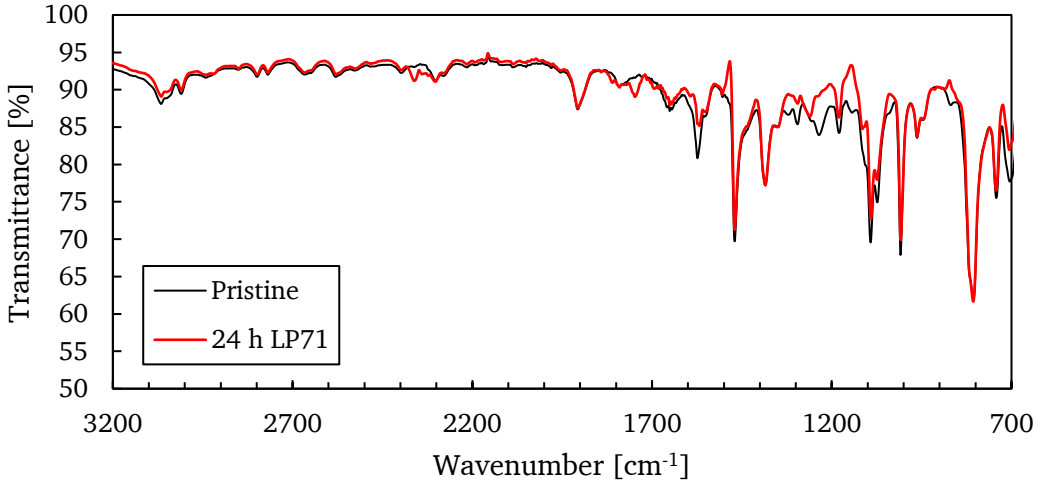

Figure 8.9: ATR-FTIR Spectra of PPS before and after submersion in LP71 for 24 h at 60 °C.

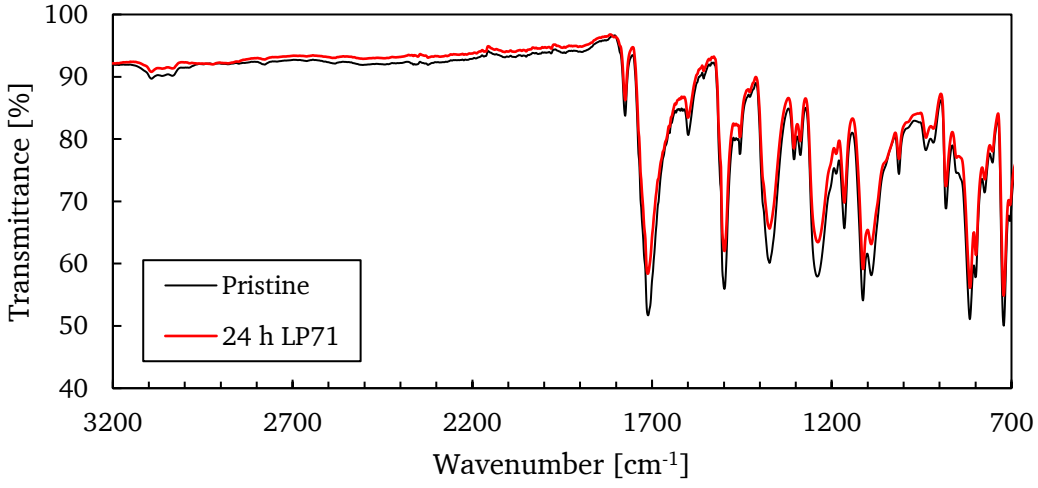

Figure 8.10: ATR-FTIR Spectra of PI before and after submersion in LP71 for 24 h at 60 °C.

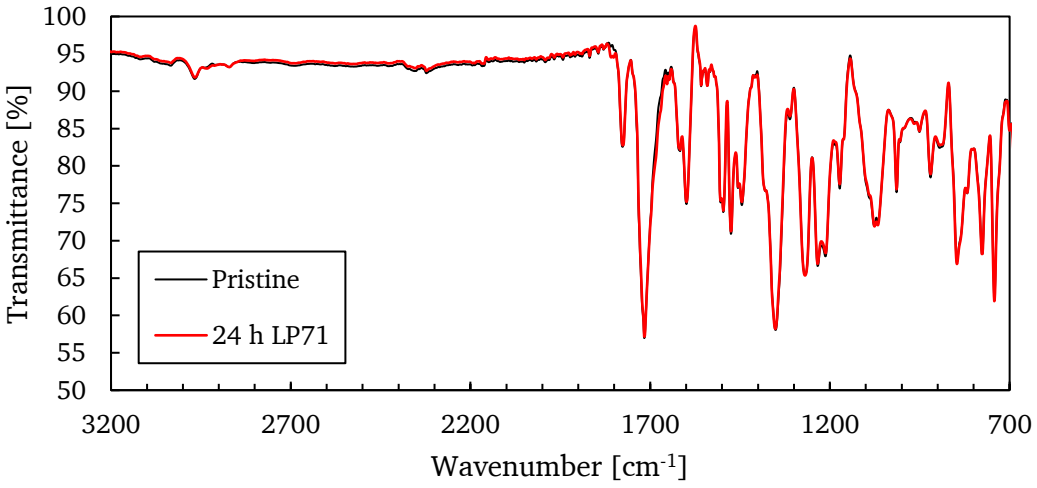

Figure 8.11: ATR-FTIR Spectra of PEI before and after submersion in LP71 for 24 h at 60 °C.

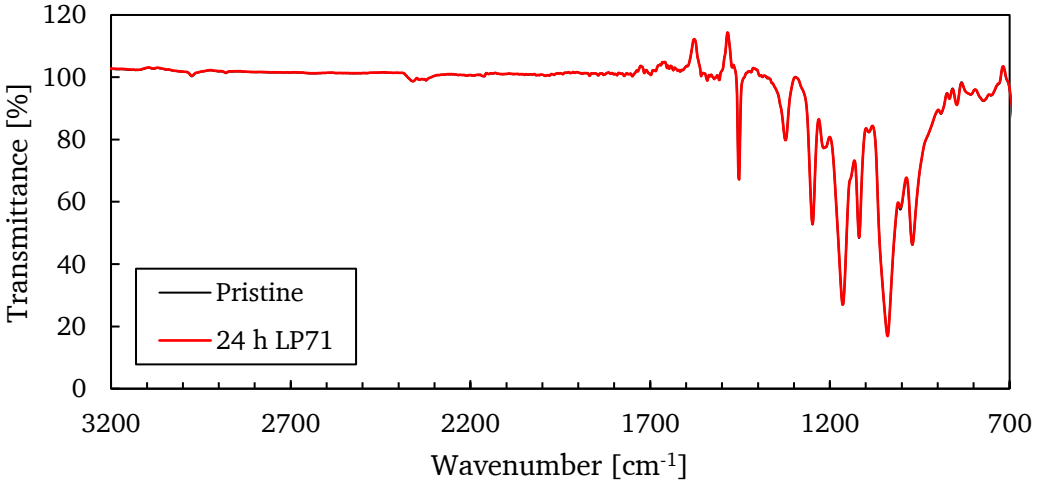

Figure 8.12: ATR-FTIR Spectra of FEP before and after submersion in LP71 for 24 h at 60 °C.

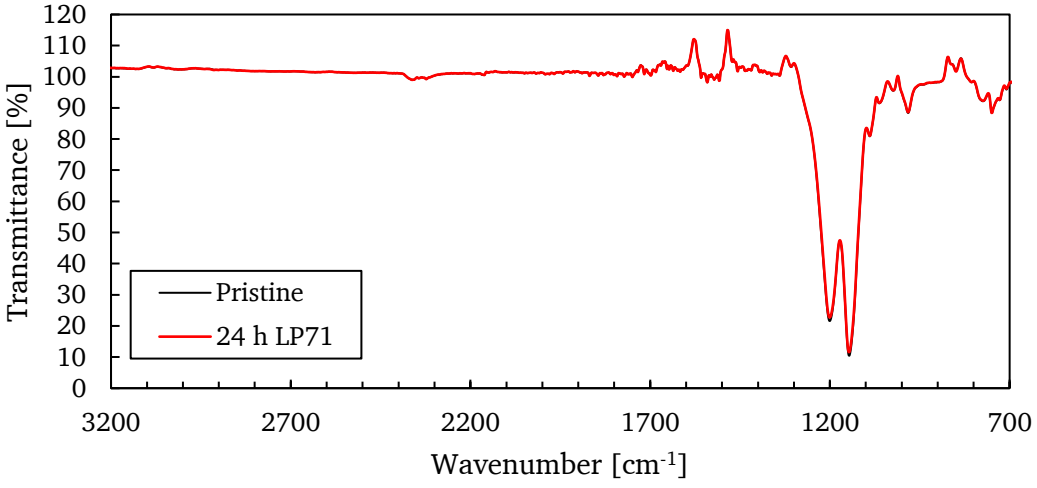

Figure 8.13: ATR-FTIR Spectra of ETFE before and after submersion in LP71 for 24 h at 60 °C.

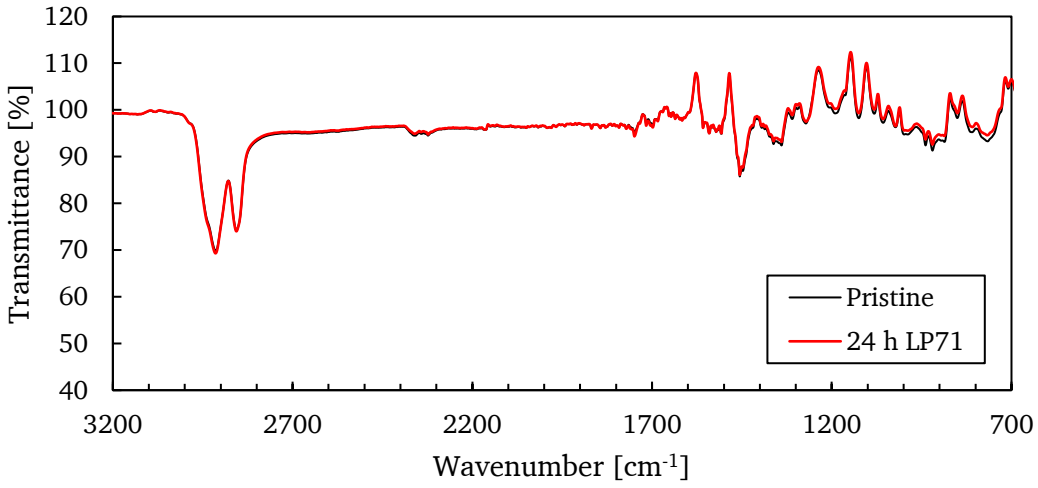

Figure 8.14: ATR-FTIR Spectra of COC before and after submersion in LP71 for 24 h at 60 °C.

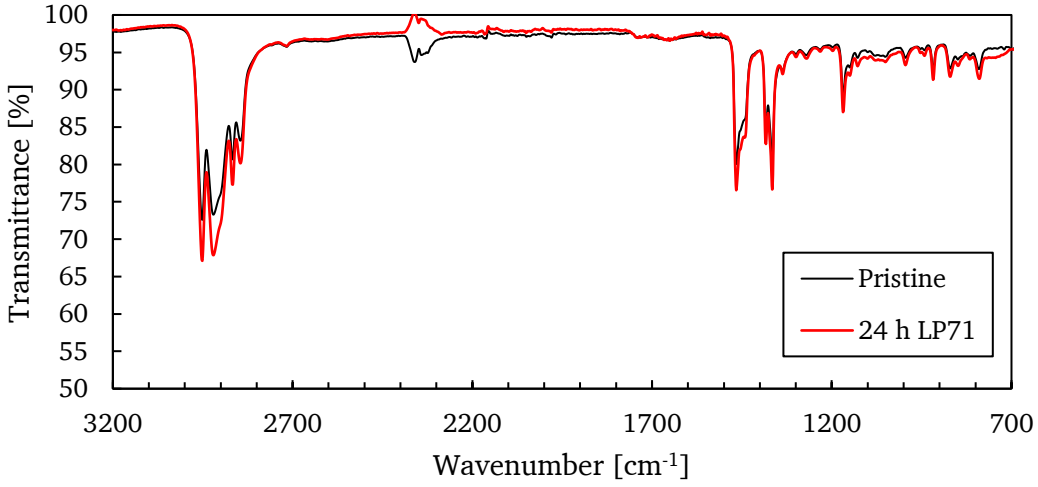

Figure 8.15: ATR-FTIR Spectra of PMP before and after submersion in LP71 for 24 h at 60 °C.

8.3 MATERIAL TECHNICAL DATA SHEETS

When available Technical Data Sheets are given for the materials used in this study.

Alathon

L5906

High Density Polyethylene
HMW Film Grade
Melt Index: 0.075 Density: 0.960

Applications

Alathon L5906 is a high molecular weight high density polyethylene homopolymer with a broad bimodal molecular weight distribution. This resin exhibits excellent stiffness, very high tensile strength, and low gels. L5906 is selected by customers for use in draw tapes and paper replacement applications as well as other mono-and multi-layer films requiring both stiffness and toughness.

Regulatory Status

L5906 meets the requirements of the Food and Drug Administration regulation, 21 CFR 177.1520. This regulation allows the use of this olefin polymer in "...articles or components of articles intended for use in contact with food..." Specific limitations or conditions of use may apply. Contact your Equistar product safety representative for more information.

Processing Techniques

Specific recommendations for processing L5906 can only be made when the processing conditions, equipment and end use are known.

Typical Properties

Property	Nominal Value	Units	ASTM Test Method
Melt Index	0.075	g/10 min	D1238
Density	0.960	g/cc	D1505
Film Properties*			
Dart Drop Impact Strength, F_{50}	390	g	D1709
Elmendorf Tear Strength, MD (TD)	20 (60)	g	D1922
Tensile Strength @ Yield, MD (TD)	5800 (5200)	psi	D882
Tensile Strength @ Break, MD (TD)	12,800 (10,000)	psi	D882
Elongation @ Break, MD (TD)	340 (340)	%	D882
Secant Modulus, MD (TD)	180,000 (189,000)	psi	D882

***Data Obtained Under the Following Extrusion Conditions:**
Alpine 200 mm 3 Layer Die (40/35/25); 3 Extruders: 65 mm / 75 mm / 50 mm; Die Gap = 1.5 mm;
Film Thickness = 0.8 mil; 500 lbs/ hr; Internal Bubble Cooling; Neck Height = 8 x DD; Blow Up Ratio = 4:1

These are typical values and not to be construed as specification limits.

Figure 8.16: Technical Data Sheet of HDPE Alathon L5906.

Table 1a: Standard grades

Grade	Et.Cont. (mol%)	Density*1 (g/cm³)	MFR*2 (g/10min)	Tm (ºC)	Tg*3 (ºC)	OTR*4 (cm³.20µm/m².day.atm)	Application
F101B	32	1.19	1.6	183	69	0.4	bottle, sheet, film, tube
F171B	32	1.19	1.8	183	57	0.4	bottle, sheet, film, tube
T101B	32	1.17	1.7	183	69	0.5	thermoforming, sheet, film
H171B	38	1.17	1.7	172	53	0.7	film
E105B	44	1.14	5.7	165	53	1.5	sheet, film

*1: 20ºC *2:190ºC, 2160g *3: dry *4: OTR, 20ºC, 65% RH (ISO 14663-2)

Table 1c: Special grades

Grade	Et.Cont. (mol%)	Density*1 (g/cm³)	MFR*2 (g/10min)	Tm (ºC)	Tg*3 (ºC)	OTR*4 (cm³.20µm/m².day.atm)	Application
M100B	24	1.22	2.2*5	195	60	0.1	ultra high-barrier
L171B	27	1.20	4.0*5	191	60	0.2	high-barrier
J102B	32	1.17	2.0	183	69	0.6	deep thermoforming, sheet, film
C109B	35	1.17	9.3	177	53	0.6	extrusion coating
G156B	48	1.12	6.9	160	50	3.2	oriented shrink film

*1: 20ºC *2:190ºC, 2160g *3: dry *4: OTR, 20ºC, 65% RH (ISO 14663-2) *5: 210ºC, 2160g

Figure 8.17: Technical Data Sheet of EVOH EVAL F101B and G156B.

Product Specification

Polyester Chips

INVISTA™

PET for
Film Application

INVISTA Resins & Fibers GmbH
Technical Service APP
Ludwig-Herrmann-Str. 100
86368 Gersthofen
Tel.: +49 (0) 821 479 31 58
Fax: +49 (0) 821 479 27 21

4027

Issue date: 18.01.2008
replaces earlier versions

Character	Value (Mixture)	Method
Intrinsic Viscosity (IV)*	0.612 ± 0.007	1 % solution in Dichloroacetic acid
Fines**	< 100 ppm	
Carboxylic Endgroups	13 – 25 meq/kg	Potentiometric Titration in o/m-Cresol
Diethylene Glycol	0.8 – 1.2 wt.%	Alkaline Methanolysis and GC
Chip Size (4 mm) Chips/10g Bulk Density	 270 - 320 ca. 0.8 g/cm³	optical DIN 53466
Moisture Content**	≤ 0.1 wt.%	Karl-Fischer-Titration
L* b*	57 – 66 5 - 13	Minolta Chromameter CR 310

Figure 8.18: Technical Data Sheet of PET Invista RT4027.

lyondellbasell

Moplen HP522H

Polypropylene, Homopolymer

Product Description

"Moplen" HP 522 H is a polypropylene homopolymer designed for the production of biaxially oriented polypropylene films (BOPP). The product is particularly suitable for both plain and coextruded structures for metallization. It does not contain any slip or antiblocking agents and is Calcium Stearate free. BOPP films made of "Moplen" HP 522 H are widely used in the food packaging industry.
"Moplen" HP 522 H is suitable for food contact.

Product Characteristics

Status	Commercial: Active
Test Method used	ISO ASTM
Availability	Europe, Africa-Middle East
Processing Method	BOPP
Features	Homopolymer
Typical Customer Applications	Film, BOPP, Food Packaging Film, Barrier Film

Typical Properties	Method	Value Unit
Physical		
Density	ISO 1183	0.900 g/cm³
Melt flow rate (MFR) (230°C/2.16Kg)	ISO 1133	2.0 g/10 min
Mechanical		
Tensile Modulus (1 mm/min)	ISO 527-1, -2	1500 MPa
Tensile Stress at Yield (50 mm/min)	ISO 527-1, -2	34.0 MPa
Tensile Strain at Break (50 mm/min)	ISO 527-1, -2	410 %
Tensile Strain at Yield (50 mm/min)	ISO 527-1, -2	11 %
Hardness		
Shore hardness (Shore D)	ISO 868	71
Thermal		
Heat deflection temperature B (0.45 MPa) Unannealed	ISO 75B-1, -2	93.0 °C
Vicat softening temperature (A50 (50°C/h 10N))	ISO 306	152 °C

Additional Properties

Typical Film Properties of monolayer film produced on T.M. Long equipment, a laboratory simultaneous film stretcher (7x7@150°C):
Haze, ASTM D 1003, 20 µm: 0.6%
Tensile Tangent Modulus (0-1%), MA 18068, 5 mm/min, 20 µm: 2500 MPa
Stress at Break, MA 18068, 50 mm/min, 20 µm: 114 MPa
Elongation at Break, MA 18068, 50 mm/min, 20 µm: 25%

Figure 8.19: Technical Data Sheet of PP Moplen HP522H.

SUNFINE™ GRADE LIST

HMW-HDPE/UHMWPE POWDER

AsahiKASEI
ASAHI KASEI CHEMICALS

	Grade			SH810	SH800
	Properties	Unit	Method		
Powder Characteristics	Mv : x10⁴ Average of Molecular Weight	g/mol	Viscosity Method *1)	20	30
	Molecular Weight Distribution (Mw/Mn) *5)	-	DSC	N.A.	7.1
	Intrinsic Viscosity	dl/g	Asahi-Kasei Method *2)	2.4	3.2
	Bulk Density	g/cm³	ISO 60:1977	0.50	0.50
	Density	kg/m³	JIS K 7112-1999	955	955
	Particle Size Peak Top	μm	Asahi-Kasei Method *3)	75-150	75-150
	D50 *4)	μm	Asahi-Kasei Method *3)	90	90
	Melting Temperature	℃	JIS K 7121-1987	136	136
	Major Application			battery separators, porous products	battery separators, porous products

*1) $Mv=5.34x\{\eta\}^{1.4925}$
*2) Based on ISO 1628-3:2010
*3) Based on JIS K 0069-1992
*4) D50 values are calculated by integration from small particle size.
*5) Values calculated from limited number of samples, only for reference use.

Figure 8.20: Technical Data Sheet of UHMWPE Sunfine SH800.

Available Grades of HI-ZEX MILLION™

Test Item	Unit	Test Method	Grade						
			030S	145M	240S	240M	320MU	340M	630M
Average molecular weight (Solution viscosity method)	x10⁴	MPC Method	50	115	200	240	320	340	590
Density	kg/m³	ASTM D1505	950	940	940	935	935	935	930
Average particle size	μm	MPC Method	130	150	120	160	150	155	155
Bulk specific gravity		ASTM D1895	520	490	475	435	420	460	430
Dynstat impact	kJ/m²	MPC Method	74	107	112	85	80	76	62
Kinetic coefficient of friction	—	MPC Method	0.2	0.2	0.2	0.2	0.2	0.2	0.2
Sand abrasion wear	mg	MPC Method	18	6	6	10	3	3	3

※Note: Figures shows here are typical values, not guaranteed specifications.

Figure 8.21: Technical Data Sheet of UHMWPE Hi-Zex 145M.

Physical Properties				Type	High-Modulus				Intermediate-Modulus	Low-Modulus		
	List	Measured Condition	Unit	Grade	RT18, RT31	DX845	DX231	DX820	MX004	MX002	MX0020	DX310
				Methodology								
Basic Properties	Density	Density Gradient Method	kg/m³ lb/in³	MCI Method	833 0.030	833 0.030	832 0.030	832 0.030	833 0.030	834 0.030	834 0.030	834 0.030
	MFR	Applied Force= 5kgf, 260℃	g/10min	MCI Method	26 (RT18) 21 (RT31)	9	100	180	25	21	21	100
	Melting Point	DSC Method	℃ ℉	ASTM D3418	232 449.6	232 449.6	232 449.6	232 449.6	228 442.4	224 435.2	224 435.2	226 438.8
	Water Absorption		%	ASTM-D570	<0.01	<0.01	<0.01	<0.01	<0.01	<0.01	<0.01	<0.01
Thermal Properties	Vicat Softening Temperature	Injection Molded Specimen (2㎜ thick) x 2pcs Heat Speed: 50℃/hour Applied Load: 10N	℃ ℉	ASTM-D1525	168 334.4	168 334.4	178 352.4	172 341.6	164 327.2	149 300.2	149 300.2	145 293.0
	Heat Distortion Temperature	Injection Molded Specimen (1/4 inch thick) Heat Speed: 120℃ /hour Applied Stress: 0.45MPa	℃ ℉	ASTM-D648	127 260.6	127 260.6	126 259.8	132 269.6	100 212.0	93 199.4	93 199.4	80 176.0
	Coefficient of Linear Expansion	TMA Method Measured Range: -10℃~ 150℃ Applied Force: 3g Nitrogen Flow: 100mL/min	cm/cm℃	MCI Method	1.17×10^{-4}	1.17×10^{-4}	1.17×10^{-4}	1.17×10^{-4}	1.17×10^{-4}	1.17×10^{-4}	1.17×10^{-4}	1.17×10^{-4}
Mechanical Properties	Yield Stress	Injection Molded Specimen (ASTM-4) Cross-Head-Speed: 50㎜/㎜ Chuck Distance: 65㎜	MPa PSI	ASTM-D638	30 4350	30 4350	29 4205	32 4640	25 3625	21 3045	21 3046	20 2900
	Fractured Stress		MPa PSI	ASTM-D638	25 3625	25 3625	25 3625	25 3625	20 2900	10 1450	10 1450	10 1450
	Fractured Strain		%	ASTM-D638	22	19	19	7	27	87	87	52
	Tensile Modulus		MPa PSI	ASTM-D638	1900 275500	1900 275500	1860 269700	1950 282750	1300 188500	900 130500	900 130500	850 122250
	Flexural Modulus	Injection Molded Specimen (3.2㎜ thick) Cross-Head-Speed: 1.3㎜/㎜ Span Length: 51㎜	MPa PSI	ASTM-D790	1450 210250	1500 217500	1450 210250	1600 232000	750 108750	480 69600	480 69600	490 71050
	Flexural Strength		MPa PSI	ASTM-D790	36 5220	40 5800	37 5365	40 5800	25 3625	18 2610	18 2610	18 2610
	Izod Impact Strength	Injection Molded Specimen (Machined Notch)	J/m ft-lbs/in	ASTM-D256	24 0.45	25 0.47	13 0.24	10 0.19	27 0.51	30 0.56	30 0.56	19 0.36
		Injection Molded Specimen (w/o Notch)	kJ/m² ft-lbs/in²	ASTM-D4812	10 4.8	10 4.8	8 3.8	9 4.3	22 10.5	NB	NB	29 13.9
	Rockwell Hardness	Injection Molded Specimen R scale	—	ASTM-D785	83	86	88	90	66	< 50[**]	< 50[**]	< 50[**]
Optical Properties	Haze	Injection Molded Specimen C Illuminant	%	ASTM-D1003	0.7	0.7	1.7	2.1	0.7	1.3	0.7	1.7
	Transmittance		%	ASTM-D1003	94	94	93	92	94	93	94	93
	Refractive Index	Injection Molded Specimen (3㎜ thick) Wave Length: 589㎚	—	ASTM-D542	1.462	1.462	1.462	1.461	1.462	1.463	1.463	1.463
Electrical Properties	Volume Resistivity	Injection Molded Specimen (2㎜ thick)	Ω • cm	ASTM-D257	$>10^{16}$	$>10^{16}$	$>10^{16}$	$>10^{16}$	$>10^{16}$	$>10^{16}$	$>10^{16}$	$>10^{16}$
	Dielectric Breakdown	Injection Molded Specimen (2㎜ thick)	KV/mm V/mil	ASTM-D149	32 812	32 812	32 812	32 812	32 812	32 812	32 812	32 812
	Relative Dielectric Constant	Injection Molded Specimen (2㎜ thick), Frequence: 1MHz	—	ASTM-D150	2.11	2.11	2.11	2.14	2.14	2.15	2.15	2.15
Moldability	Spiral Flow	Injection Temperature: 310-320℃ Mold Temperature: 73℃	cm	MCI Method-1	51	50			53	56	56	
	Molding shrinkage	Injection Molded Specimen (2㎜ thick) MD	%	MCI Method-2	1.6	1.5			1.7	1.6	1.6	
		Injection Molded Specimen (2㎜ thick) TD	%	MCI Method-2	1.3	1.4			1.4	1.3	1.3	
Processing Method	Injection Molding		◎ : Recommended ○ : Applicable		◎	○	○	○	◎	◎	◎	○
	Extrusion-Coating						◎	◎		○		◎
	Extrusion-T-Die Casting				○	◎			◎	◎	◎	
	Extrusion-Profile type, Mandrel, Pipe				○	○			◎	◎	○	
	Extrusion-Fiber Spinning				○	○	○	◎	○	○	○	○
	Direct Blow Molding					○			○	○	○	

Figure 8.22: Technical Data Sheet of PMP (RT31, DX845, MX002).

EXXSOL D GRADE DEAROMATISED HYDROCARBONS

Our Exxsol D-Series products from ExxonMobil Chemical offer users a wide selection of dearomatised hydrocarbon fluids, with a typical Aromatic content below 1%. These fluids maintain good solvency characteristics for many applications. Because of their relatively high OELs, they often serve as replacements for more conventional solvents that might not meet health or environmental regulations. Heavier Exxsol D grades have boiling ranges between 140° and 310° C.

	Exxsol D30	Exxsol D155/170	Exxsol D40	Exxsol D180/200 SP	Exxsol D60	Exxsol D80	Exxsol D220/240	Exxsol D100	Exxsol D100S	Exxsol D120	Exxsol D140
Alternate Name	N/A	N/A	N/A	N/A	N/A	N/A	N/A	N/A	N/A	N/A	N/A
CAS No	N/A	N/A	N/A	64742-48-9	64742-48-9	64742-47-8	64742-47-8	64742-47-8	64742-47-8	64742-47-8	64742-46-7
Distillation Range (°C)	143 – 165	160 – 174	160 – 190	188 – 202	187 – 216	205 – 237	224 – 252	240 – 267	240 – 266	263 – 297	285 – 318
Flash Point (°C)	29	41	42	63	63	76	90	102	102	120	138
Aromatic Content (wt %)	0.001	0.006	0.003	0.03	0.06	0.06	0.2	0.4	0.07	0.6	1.0
Aniline Point (°C)	64	66	67	69	70	76	76	78	78	83	88
Density (@ 15°C)	0.762	0.771	0.775	0.789	0.792	0.804	0.810	0.817	0.816	0.828	0.834
Evap Rate (nButAc=100)	44	21	14	4.9	3.4	<1	<1	<1	<1	<1	<1

Figure 8.23: Technical Data Sheet of ExxSol hydrocarbon grades.

8.4 TECHNICAL DATA SHEET OF COMMERCIAL SEPARATORS

Celgard® High Performance Battery Separators

Celgard is a recognized leader among lithium battery material suppliers, with:

- Unparalleled Product Availability
  Broadest Portfolio in the Separator Industry
- Proven Performance and Reliability
  Over 30 Years of Experience in Separator Design, Manufacturing and Distribution
- Technical Leadership & Expertise
  R&D Teams with Experience in Lithium Battery and Battery Separator Technology
- Strong Global Presence
  Manufacturing Facilities in China, Korea, and the USA;
  Sales and Technical Service Staff throughout Asia, Europe, and North America

Commercial Trilayer Products

Comparison of Typical Properties

Product	2340	2325	C500	C480	2320	C300	C250	C200	C212	M825	M824
Thickness; µm	38	25	25	21.5	20	20	18	17	16	16	12
JIS Gurley; seconds	780	620	515	320	530	560	500	450	435	460	425
Porosity	45%	39%	35%	50%	39%	36%	35%	35%	35%	39%	38%
PP Pore Size; µm	0.035	0.028	0.041	0.038	0.027	0.032	0.032	0.032	0.032	0.026	0.026
TD Shrinkage @ 90° C / 1 hour	0.0%	0.0%	0.0%	0.0%	0.0%	0.0%	0.0%	0.0%	0.0%	0.0%	0.0%
MD Shrinkage @ 90° C / 1 hour	<7.0%	<5.0%	<5.0%	<5.0%	<5.0%	<4.0%	<5.0%	<5.0%	<2.5%	<1.0%	<1.5%
Puncture Strength; grams	>550	>380	>320	>400	>360	>300	>300	>245	>220	>300	>225
TD Tensile Strength; kgf/cm²	165	150	170	140	165	185	175	190	180	150	155
MD Tensile Strength; kgf/cm²	1630	1700	1680	2195	2050	1800	1800	1900	2085	2100	2200

Commercial Monolayer & Specialty Products

Comparison of Typical Properties

	Monolayer PP			Coated PP		Laminated to PP Nonwoven Fabric		Laminated & Coated
Product	2400	2500	A273	3400/ 3401	3500/ 3501	4550 PP/PE/PP	4560 PP	5550 PP
Thickness; laminated film; µm	-	-	-	-	-	110	110	110
Thickness; base film; µm	25	25	16	25	25	38	25	25
JIS Gurley; seconds	620	200	345	620	200	780	200	200
Porosity	41%	55%	40%	41%	55%	45%	55%	55%
PP Pore Size; µm	0.043	0.064	0.039	0.043	0.064	0.035	0.064	0.064
TD Shrinkage @ 90° C / 1 hour	0.0%	0.0%	0.0%	0.0%	0.0%	0.0%	0.0%	0.0%
MD Shrinkage @ 90° C / 1 hour	<5.0%	<5.0%	<3.0%	<5.0%	<5.0%	<7.0%	<5.0%	<5.0%
Puncture Strength; grams	>450	>335	>300	>450	>335	>550	>335	>335
TD Tensile Strength; kgf/cm²	140	135	130	140	135	165	135	135
MD Tensile Strength; kgf/cm²	1420	1055	1600	1420	1055	1630	1055	1055

Figure 8.24: Technical Data Sheets of Celgards Battery Separator portfolio.

8.5 LIST OF PUBLICATIONS

Parts of this dissertation were publicized in:

Articles

T. Knoche, R. Lund, O. Prymak, M. Epple, M. Ulbricht
Effect of annealing temperature on pore formation in preparation of advanced polyethylene battery separator membranes
Polymer, submitted

Poster

06/2013, Italy	T. Knoche, M. Ulbricht Influence of stretching parameters on lamellae orientation and Pore formation in mono-and bi-axially stretched HDPE films *European Polymer Congress*

8.7 CURRICULUM VITAE

This section was removed for the pdf-version of this document.